

# DISSERTATION

## DILUTION REFRIGERATION OF MULTI-TON COLD MASSES

ausgeführt zum Zwecke der Erlangung des akademischen Grades eines  
Doktors der Technischen Wissenschaften

betreut von Univ.Prof. Dr.phil. Dr.h.c. Harald W. Weber  
Atominstitut der Österreichischen Universitäten (E141)  
Technische Universität Wien

eingereicht an der Technischen Universität Wien  
Fakultät für Physik

von  
Dipl.-Ing. Patrick Wikus  
Matrikelnummer: 9825134  
22, chemin des Jargilières  
01210 Ferney Voltaire  
Frankreich

Diese Arbeit wurde unterstützt von CERN und dem Österreichischen  
Bundesministerium für Bildung, Wissenschaft und Kultur.

Wien, am 23.04.2007

## **Gutachter**

*Technische Universität Wien, Atominstitut (E141)*

Univ.Prof. Dr.phil. Dr.h.c. Harald W. Weber

*Technische Universität Wien, Institut für Festkörperphysik (E138)*

Ao.Univ.Prof. Dipl.-Ing. Dr.techn. Gerfried Hilscher

## Acknowledgements

I would like to express my gratitude to Dr. Tapio O. Niinikoski of CERN and Prof. Harald W. Weber of the Atomic Institute of the Austrian Universities, who have both acted as supervisors for this thesis. I would also like to thank Prof. Gerfried Hilscher for providing a reviewer's report and Prof. Christian Fabjan for his constant support.

This work would not have been possible without the help of CERN's Cryolab team: Mrs. Laetitia Dufay, Mrs. Gaëlle Ratcliffe, Mr. Agostino Vacca, Mr. Laurent LeMao, Mr. Sebastien Prunet and Mr. Hervé Vigier have spent a lot of time building the dilution refrigerator whose design is presented in chapter 2 of this thesis.

I would like to acknowledge the contributions of my colleagues Gerhard Burghart, Nuno Alexandre Elias, Ana Sofia Torrento Coello and Dr. Friedrich Haug, with whom I have shared a great time of collaboration. The measurements presented in chapters 3 and 4 would not have been possible without Gerhard, who dedicated a lot of time to the operation of our dilution refrigerator. I am indebted to all members of the EURECA collaboration who let me participate in their most interesting experiment. The preliminary design of the EURECA detector unit in chapter 6 is based on discussions I had with Dr. Vitaly Kudryavtsev and Dr. Wolfgang Seidel.

I am obliged to Prof. Giorgio Frossati, Prof. Massimo Cerdonio and Prof. Odylio Aguiar for the information about the gravitational wave antennas they either operate or plan to build. Prof. Frossati let me know his thoughts concerning the heat load on the MiniGRAIL sphere, which proved to be very helpful for the compilation of residual heat sources in chapter 4 of this thesis. Dr. Richard Schmitt of Fermilab has recommended literature concerning the cryogenic dark matter search CDMS. Prof. Franz Sauerzopf of the Atomic Institute of the Austrian Universities has taught me both about SQUIDS and many practical things about cryogenics.

Working at Cryolab has been tremendously interesting and I would like to thank all my colleagues for the great time we shared. My deep gratitude goes to my future wife Sarah for her invaluable support throughout the last years.

## Zusammenfassung

$^3\text{He}/^4\text{He}$  Verdünnungskryostaten stellen die einzige technische Möglichkeit zur kontinuierlichen Kühlung bei Temperaturen unter 250 mK dar. Derzeit in Planung befindliche Experimentanlagen erfordern die Kühlung von Massen in der Größenordnung mehrerer Tonnen und benötigen leistungsfähige Kühlsysteme, deren Kühlleistung unter 10 mK die Möglichkeiten heutiger Systeme beträchtlich übersteigt. Diese Arbeit beschäftigt sich mit der Entwicklung solcher Systeme.

Eine neuartige, numerische Methode zur Berechnung der Kühlleistung eines Verdünnungskryostaten bekannten Designs wurde im Rahmen der vorliegenden Arbeit entwickelt. Diese Methode zieht nicht nur die Unterschiede zwischen realen und den in der Theorie üblicherweise behandelten idealen Wärmetauschern in Betracht, sondern ermöglicht auch die Berücksichtigung zusätzlicher Wärmelasten am Wärmetauscher und die Simulation transienten Verhaltens. Dieses numerische Modell wurde mittels experimenteller Daten verifiziert, die aus dem Betrieb eines vom Autor entwickelten Verdünnungskryostaten gewonnen wurden. Weiters wird die Bestimmung der minimalen Wärmelast, die von einem Kühlsystem eines Tieftemperaturperiments abgeführt werden muß, behandelt. Die Ergebnisse dienen der Berechnung der erforderlichen Kühlleistung zukünftiger Großexperimente.

Basierend auf der im Bau und Betrieb des Verdünnungskryostaten gewonnenen Erfahrung wurden Konstruktionsregeln für derartige Kühlsysteme abgeleitet. Diese wurden bei der Auslegung eines Kühlsystems für EURECA, eines europäischen Detektors für dunkle Materie, angewandt, wobei zusätzlich den Forderungen nach geringem radioaktivem Hintergrund und den aus dem Betrieb in unterirdischen Laboratorien resultierenden Einschränkungen Rechnung getragen wurde.

Diese Arbeit wurde von CERN und vom Österreichischen Bundesministerium für Bildung, Wissenschaft und Kultur finanziert.



## **Abstract**

Dilution refrigeration is the only means to provide continuous cooling at temperatures below 250 mK. Future experiments featuring multi-ton cold masses require a new generation of dilution refrigeration systems, capable of providing a heat sink below 10 mK at cooling powers which exceed the performance of present systems considerably. This thesis presents some advances towards dilution refrigeration of multi-ton masses in this temperature range.

A new method using numerical simulation to predict the cooling power of a dilution refrigerator of a given design has been developed in the framework of this thesis project. This method does not only allow to take into account the differences between an actual and an ideal continuous heat exchanger, but also to quantify the impact of an additional heat load on an intermediate section of the dilute stream. In addition, transient behavior can be simulated. The numerical model has been experimentally verified with a dilution refrigeration system which has been designed, built and tested at CERN in the framework of this doctoral thesis project. Furthermore, the determination of the residual heat load to the cold mass of a very low temperature (VLT) experiment is addressed. The results of this analysis can be used to predict the required cooling power for large future experiments.

Based on the experience gained with the dilution refrigeration system at CERN, design rules for large dilution refrigerators have been derived. They are consequently used in a design and feasibility study of a refrigeration system, which is tailored for the future cryogenic dark matter search EURECA and meets the requirements of low-background experiments and operation in remote underground laboratories.

This doctoral thesis project has been funded CERN and by the Austrian Federal Ministry for Education, Science and Culture.

## Contents

<i>Acknowledgements</i>	<i>ii</i>
<i>Zusammenfassung / Abstract</i>	<i>iii</i>
<i>Contents</i>	<i>v</i>
<i>Nomenclature</i>	<i>vii</i>
<i>1. Introduction</i>	<i>1</i>
1.1 Gravitational Wave Antennas	1
1.2 Cryogenic Dark Matter Searches	3
1.3 Dilution Refrigeration	4
1.4 Cooling Power and Temperature	5
<i>2. Design of a Dilution Refrigeration System</i>	<i>12</i>
2.1 The CERN Cryolab Dilution Refrigerator (CCDR)	12
2.2 The 4 Kelvin System and Inner Vacuum Chamber (IVC)	14
2.3 The 1 Kelvin Subsystem	15
2.4 The Still and Film Burner	17
2.5 The Heat Exchanger	19
2.6 The Mixing Chamber	21
2.7 The Gas Handling System	24
2.8 Vibration Isolation System	25
2.9 Electrical System and Data Acquisition (DAQ)	27
<i>3. Numerical Simulation of Dilution Refrigerators</i>	<i>29</i>
3.1 Numerical Thermal Simulation	29
3.2 The Numerical Model of a Dilution Refrigerator	33
3.3 The Numerical Model of the CCDR	39
3.4 Comparison of Steady State Simulations with Experimental Results	40
3.5 Comparison of Transient Simulations with Experimental Results	44
3.6 The Efficiency of Sintered Sponges	45

<i>4. Residual Heat Loads in Very Low Temperature Systems</i>	50
4.1 Measurements of the Residual Heat Load on the CCDR	50
4.2 Thermal Conduction	52
4.3 Residual Heat from Typical Construction Materials	55
4.4 Heat Dissipation in Vibrating Structures	68
4.5 Heat Transport by Residual Gas	77
4.6 Radiative Heat Transfer at Very Low Temperatures	84
4.7 Heat Load due to Cosmic Rays	89
4.8 Summary and Scaling Laws	91
 <i>5. Principles of Dilution Refrigerator Design</i>	 95
5.1 Design of Precooling Heat Exchangers	95
5.2 Heat Transfer in the 1 K Pot and the Still	100
5.3 Optimization of Sintered Heat Exchangers	102
5.4 Optimum Pump Line Dimensions	107
5.5 Mechanical Design Principles	113
 <i>6. A Dilution Refrigerator for a Multi-Ton Cold Mass</i>	 117
6.1 The European Dark Matter Search EURECA	117
6.2 System Engineering	119
6.3 The EURECA System Concept	121
6.4 Preliminary Temperature and Heat Load Requirements	122
6.5 Dilution Refrigerator Design Parameters	127
6.6 The Refrigeration Unit	128
6.7 Connecting Pipe and Main Heat Exchanger	135
6.8 The Mixing Chamber	137
6.9 Gas Handling System and Proximity Cryogenics	138
6.10 Design Risks and Alternatives	141
 <i>7. Conclusions and Outlook</i>	 144
7.1 Summary	144
7.2 Suggestions for Future Work	144
 <i>Appendices</i>	 146
A. Thermal Simulation Model for the CCDR	146
B. Thermal Simulation Model for Sintered Sponges	153
 <i>Bibliography</i>	 156

## Nomenclature

### SYMBOLS USED IN EQUATIONS

Symbol	Name	Unit
$A$	Surface area	$\text{m}^2$
	Amplitude	N/A
$a$	Speed of Sound	m/s
$B$	Field Strength	T
$c$	Viscous Damping Constant	(N·s)/m
$C$	Integral Thermal Conductivity	W/K
$c_p$	Specific Heat	J/(kg·K)
$d$	Diameter	m
$E$	Energy	J
	Young's Modulus	N/m <sup>2</sup>
$f$	Frequency	Hz
$H$	Enthalpy	J/mol
$k$	Spring Constant	N/m
Kn	Knudsen Number	[1]
$l$	Length	m
$L$	Length	m
$M$	Thermal Mass	J/K
	Molecular Mass	kg/mol
	Spectral Specific Radiated Energy	W/(m <sup>2</sup> ·Hz)
$m$	Mass	kg
$\dot{m}$	Mass Flow Rate	kg/s
$N$	Number of Particles	[1]
$\dot{n}$	Flow rate	mol/s
Nu	Nusselt Number	[1]
$p$	Pressure	Pa
	Perimeter	m
Pr	Prandtl Number	[1]
$Q$	Heat (Energy)	J
$\dot{Q}$	Heat load	W
$\bar{Q}$	Quality factor	[1]
$\dot{q}$	Specific Heat Flux	W/m <sup>2</sup>
$R$	Electrical Resistance	$\Omega$
$r$	Radius	m
Re	Reynolds Number	[1]

Symbol	Name	Unit
$S$	Kapitza Conductance	$\text{W}/(\text{m}^2 \cdot \text{K}^4)$
$T$	Temperature	K
	Half Life	s
$t$	Time	s
$V$	Volume	$\text{m}^3$
	Molar Volume	$\text{m}^3/\text{mol}$
$\dot{V}$	Volumetric Flow Rate	$\text{m}^3/\text{s}$
$w$	Velocity	$\text{m}/\text{s}$
$x$	Concentration	[1]
	Displacement	m
$Z$	Flow Impedance	$\text{m}^{-3}$
$\alpha$	Absorptivity	[1]
	Heat Transfer Coefficient	$\text{W}/(\text{m}^2 \cdot \text{K})$
	Van der Waals Constant	$\text{J} \cdot \text{m}^3/\text{mol}^2$
	Linear Thermal Expansion Coefficient	$\text{K}^{-1}$
	Accommodation Coefficient	[1]
$\varepsilon$	Emissivity / Efficiency	[1]
	Strain	$\text{m}/\text{m} = [1]$
$\gamma$	Heat Transfer Parameter	$\text{W}/\text{m}$
$\eta$	Dynamic viscosity	$\text{Pa} \cdot \text{s}$
$\Theta$	Debye Temperature	K
$\theta$	Thermal Conductivity Integral	$\text{W}/\text{m}^2$
$\kappa$	Specific Heat Ratio	[1]
$\lambda$	Thermal Conductivity	$\text{W}/(\text{m}^2 \cdot \text{K})$
	Wavelength	m
$\nu$	Kinematic Viscosity	$\text{m}^2/\text{s}$
	Poisson's Ratio	[1]
$\xi$	Molecular Diameter	m
	Friction Factor	[1]
	Thermal Penetration Depth	m
$\rho$	Density	$\text{kg}/\text{m}^3$
	Specific Resistance	$\Omega \cdot \text{m}$
$\sigma$	Stress	$\text{N}/\text{m}^2$
$\tau$	Relaxation Time	s
$\mathcal{G}$	Damping Ratio	[1]
$\varphi$	Phase Shift	[1]
$\psi$	Filling Factor	[1]
$\Omega$	Solid Angle	sr
$\omega$	Angular Frequency	$\text{s}^{-1}$



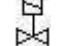






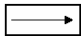

## SUBSCRIPTS

Symbol	Name	Symbol	Name
<i>A</i>	Adsorption	<i>L</i>	Condensation
<i>b</i>	Bulk	<i>m</i>	Mixing Chamber
<i>C</i>	Concentrated Stream / Critical	<i>n</i>	Natural / Normal
<i>D</i>	Dilute Stream	<i>o</i>	Outer
<i>e</i>	Electron	<i>r</i>	Radiation
<i>f</i>	Flow	<i>s</i>	Surface, Still
<i>F</i>	Force / Fermi	<i>sat</i>	Saturation
<i>g</i>	Gas	<i>turb</i>	Turbulent
<i>i</i>	Inlet / Inner	<i>W</i>	Wall
<i>l</i>	Linear	<i>X</i>	Displacement
<i>lam</i>	Laminar	3	<sup>3</sup> He
<i>liq</i>	Liquid	4	<sup>4</sup> He

## PHYSICAL CONSTANTS

Symbol	Name	Unit	Value [53]
<i>c</i>	Vacuum speed of light	m/s	299 792 458
<i>e</i>	Euler's number	[1]	2.71828
<i>E<sub>0</sub></i>	Permittivity of free space	F/m	$8.854187817 \cdot 10^{-12}$
<i>h</i>	Planck constant	J·s	$6.62606876 \cdot 10^{-34}$
$\hbar$	Reduced Planck constant	J·s	$1.054571596 \cdot 10^{-34}$
<i>k<sub>B</sub></i>	Boltzmann constant	J·K <sup>-1</sup>	$1.3806503 \cdot 10^{-23}$
<i>L<sub>0</sub></i>	Lorentz number	W·Ω/K <sup>2</sup>	$2.44301 \cdot 10^{-8}$
$\pi$	Pi	[1]	3.14159
<i>R</i>	Ideal gas constant	J/(mol·K)	8.314472
$\sigma$	Stefan-Boltzmann constant	W/(m <sup>2</sup> ·K <sup>4</sup> )	$5.6704 \cdot 10^{-8}$

## SYMBOLS USED IN HYDRAULIC DIAGRAMS

Symbol	Description	Symbol	Description
	Manually Actuated Valve		Oil Mist Filter
	Electrically Actuated Valve		Pressure Indicator
	Safety Release Valve		Pressure Transducer
	Primary Pump		Pressure Switch
	Roots Blower		Flowmeter
	Turbomolecular Pump		

## ABBREVIATIONS

AISI	American Iron and Steel Institute
BET	Brunauer Emmett and Teller (an adsorption model)
CCDR	CERN Cryolab Dilution Refrigerator
CCS	Carbon Ceramic Resistor
CDMS	Cryogenic Dark Matter Search
CERN	European Organization for Nuclear Research
CFD	Computational Fluid Dynamics
CRESST	Cryogenic Rare Event Search with Superconducting Thermometers
DAQ	Data Acquisition
DFT	Discrete Fourier Transform
DR	Dilution Refrigerator
ECR	Experiment Cryogenics
EDELWEISS	Expérience pour Detecter les WIMPs en Site Souterrain
EURECA	European Underground Rare Event Calorimetric Array
FEM	Finite Element Methods
FFT	Fast Fourier Transform
FS	Full Scale
GPIB	General Purpose Interface Bus
GRAIL	Gravitational Wave Antenna in Leiden
H/X	Heat Exchanger
INFN	Istituto Nazionale di Fisica Nucleare (Italy)
INPE	Instituto Nacional De Pesquisas Espaciais (Brazil)
IVC	Inner Vacuum Chamber
MACHO	Massive Compact Halo Object
MiniGRAIL	Mini Gravitational Wave Antenna in Leiden
MoS	Margin of Safety
NIST	National Institute of Standards and Technology
NMR	Nuclear Magnetic Resonance
PE	Polyethylene
POM	Polyoxymethylene
PSD	Power Spectral Density
R&D	Research and Development
RMS	Root Mean Square
SPE	Solar Particle Event
SQUID	Superconducting Quantum Interference Device
SSITER	Steady State Iteration
SMC	Spin Muon Collaboration
SUSY	Supersymmetry
TAK	Thermal Analysis Kit
TLS	Two Level System
VLT	Very Low Temperature
WIMP	Weakly Interacting Massive Particle

## 1. Introduction

Several frontier experiments in physics – such as gravitational wave antennas, cryogenic dark matter detectors or precision observations of other rare events such as the suspected neutrinoless double-beta decay – are in need of dilution refrigerators to reach the required very low temperatures (VLT), which typically lie in the range of 10 mK. The increasing size and mass of the VLT parts of some of these experiments renders research towards high performance dilution refrigeration systems<sup>1</sup> necessary.

In this introduction, present and future experiments requiring large cooling powers at low temperatures will briefly be described. Dilution refrigeration and the models which are currently used to predict the cooling power and base temperature of such machines are reviewed.

### *1.1 Gravitational Wave Antennas*

Gravitational wave antennas are designed to detect bursts of gravitational waves produced by sources in our galaxy and the local group. Gravitational waves are perturbations of the space-time moving with the speed of light and are predicted by Einstein's theory of general relativity. Gravitational radiation interacts very weakly with matter and could thus be detected by measuring the vibration caused in a large mass by impinging gravitational waves. The benefit of cooling gravitational wave antennas to cryogenic temperatures is two-fold, as thermal noise can be reduced by cooling the mass to sufficiently low temperatures while the quality factor of the antenna material increases at the same time. Currently, there are three gravitational wave experiments operating at very low temperatures.

NAUTILUS [11] has been the first new-generation gravitational resonant antenna and has started operation in 1994. NAUTILUS is located in the Frascati INFN Laboratories. It consists of a 3 m long aluminum bar with a mass of 2350 kg which is

---

<sup>1</sup> A high performance dilution refrigerator shall be defined somewhat arbitrarily as a system whose cooling power exceeds 5  $\mu$ W at a mixing chamber temperature of 10 mK.



cooled to 90 mK. Initially, a temperature of 50 mK had been planned,<sup>2</sup> but couldn't be reached due to the unexpectedly large heat load on the bar. The same group currently studies a spherical detector with a mass between 40 and 100 tons operated in the range of 20 mK, which is called SFERA [28]. A single sphere is capable of detecting gravitational waves from all directions and polarizations and has, at constant resonant frequency, a larger mass than a bar detector; this translates into improved sensitivity. AURIGA [25] operates at very low temperature since 1997 in the INFN Legnaro Laboratories. The cold mass of this experiment is very similar to the one used by NAUTILUS; the oscillator used to search for gravitational waves is a 2330 kg aluminum bar operated at 100 mK. Currently, a successor for AURIGA is being planned: The DUAL gravitational wave antenna<sup>3</sup> will make use of two oscillators by measuring their difference in position. The advantage of such a system is an enhanced signal with respect to the single oscillator response. The oscillators will most likely consist of two concentric cylinders with a total cold mass of 30 tons. MiniGRAIL [35] is the first spherical gravitational wave antenna which has actually been put to operation. A copper sphere with a diameter of 68 cm and a mass of 1350 kg is cooled to 60 mK.<sup>4</sup> The Dutch group operating MiniGRAIL proposed a bigger spherical antenna named GRAIL [51, 52] with a mass of 30 tons and a diameter of 3 m, which will be cooled to 10 mK. The required cooling power has been estimated to 100  $\mu$ W. As the GRAIL project currently lacks funding, no work is in progress. The spherical antenna Mario Schenberg is located in Brazil. It has a mass of 1150 kg and is operated at 6 K. It is planned to use a dilution refrigerator to cool the sphere to at least 100 mK during future science runs.<sup>5</sup>

The sensitivity of gravitational wave antennas can be increased by lowering the temperature of the oscillator and by increasing its mass [51]. The three experiments SFERA, DUAL and GRAIL, which are currently in their research and development phase, will need dilution refrigerators capable of cooling large heat loads in the range of several tens of  $\mu$ W at temperatures between 10 and 100 mK.

---

<sup>2</sup> Private communication from Dr. Tapio O. Niinikoski (CERN), 2005

<sup>3</sup> Private communication from Prof. Massimo Cerdonio (INFN, University of Padova), 2006

<sup>4</sup> Private communication from Prof. Giorgio Frossati (Leiden University), 2006

<sup>5</sup> Private communication from Prof. Odylio Aguiar (INPE), 2006

## ***1.2 Cryogenic Dark Matter Detectors***

Astrophysical observations suggest that galaxies may contain considerably more mass than one would estimate from visual observations. The amount of this non-luminous mass, or dark matter, can be calculated from the orbital velocity of a spiral galaxy's disk, which in turn can be determined as a function of radius by measuring the Doppler shift of the spectral lines in the light reaching the earth. The rotation curves yielded by these measurements suggest that most galaxies are immersed in dark halos which outweigh the luminous components by about a factor of ten [69].

A certain amount of this dark matter is of baryonic nature. Stellar remnants, such as black holes or neutron stars consist of baryonic matter. Brown dwarfs, which are stars with a mass smaller than 0.08 solar masses, are also dark as they never ignite and shine only very dimly due to gravitational contraction. All objects mentioned above are classified as Massive Compact Halo Objects (MACHOs). They can be detected by gravitational lensing. The MACHO collaboration succeeded in putting an upper limit of 20 % to the galactic halo mass fraction accounted for by MACHOs [3]. Other candidate particles, such as the neutralino, are introduced by supersymmetric (SUSY) theories. The neutralino classifies as a Weakly Interacting Massive Particle (WIMP). Other, non-supersymmetric candidate particles are axions and neutrinos [69].

So far, dark matter has not been directly detected. It was however possible to exclude some WIMP candidates by ruling out particles of given mass and interaction cross-section. Ongoing experiments searching for dark matter have been able to extend the exclusion plot to regions as low as  $2.5 \cdot 10^{-7}$  picobarn. Results of some cryogenic dark matter searches are shown in Figure 1 on the following page.

The experiments CRESST [127], EDELWEISS [85] and CDMS use  $\text{CaWO}_4$ , Ge and Si crystals to search for dark matter. The crystals are cooled to temperatures of some mK, where the specific heat of the absorber material is very low. The tiny energy deposited in the crystal by a collision with a WIMP thus causes a measurable temperature rise, which can be determined with high-impedance thermistors or superconducting transition-edge sensors. Discrimination between electron and nuclear recoils can be effected by measuring the crystals' ionization (Ge) or by means of scintillation ( $\text{CaWO}_4$ ). Target masses are rather small and typically lie in the range between several hundred grams and a few kilograms.

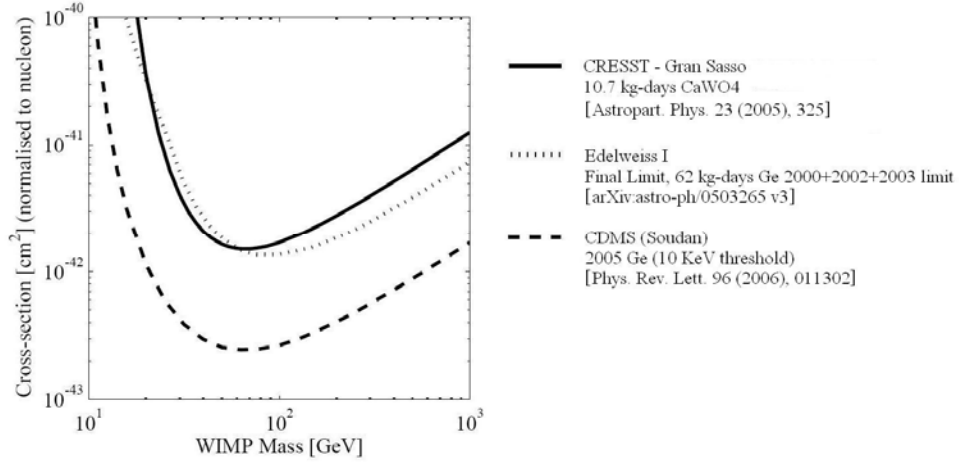


**Figure 1: A typical WIMP exclusion plot. The vertical scale gives the elastic scattering cross-section of the postulated WIMP on the target nucleus (Image: R. Gaitskell and V. Mandic), Source: [2, 7, 120]**

The probability to detect an impacting WIMP depends on the amount of target material and the duration of the data-taking phase. The groups involved in CRESST and EDELWEISS thus formed a European collaboration to perform research and development towards a considerably larger detector: EURECA [78, 79, 80] will feature a target mass in the range of one ton with a cold volume of up to 2 m<sup>3</sup>. The target needs to be held at a temperature of 10 mK. EURECA sets out to explore cross-sections in the range of 10<sup>-9</sup> to 10<sup>-10</sup> picobarn.

### 1.3 Dilution Refrigeration

Dilution refrigeration is the only means to provide continuous cooling in the low millikelvin range. Descriptions of the operating principle are given in [43, 91, 109]. Using the enthalpy of mixing  $\Delta H$  of <sup>3</sup>He and <sup>4</sup>He for cooling was first suggested by London, Clarke and Mendoza in 1962 [87]. The first dilution refrigerator was built by Das, De Bruyn and Taconis at Leiden University in 1965 [34]. Hall [63] and Neganov [96] independently succeeded in realizing a design capable of continuous refrigeration below 100 mK in 1966. Previously, such temperatures could only be reached by adiabatic demagnetization of paramagnetic salts, which is a discontinuous process. Today, dilution refrigeration is the most important cooling technique for temperatures between 600 mK and 5 mK. Dilution refrigeration is also used as a base from which lower temperatures can be reached. Various methods to cool to very low temperatures are shown in Figure 2.

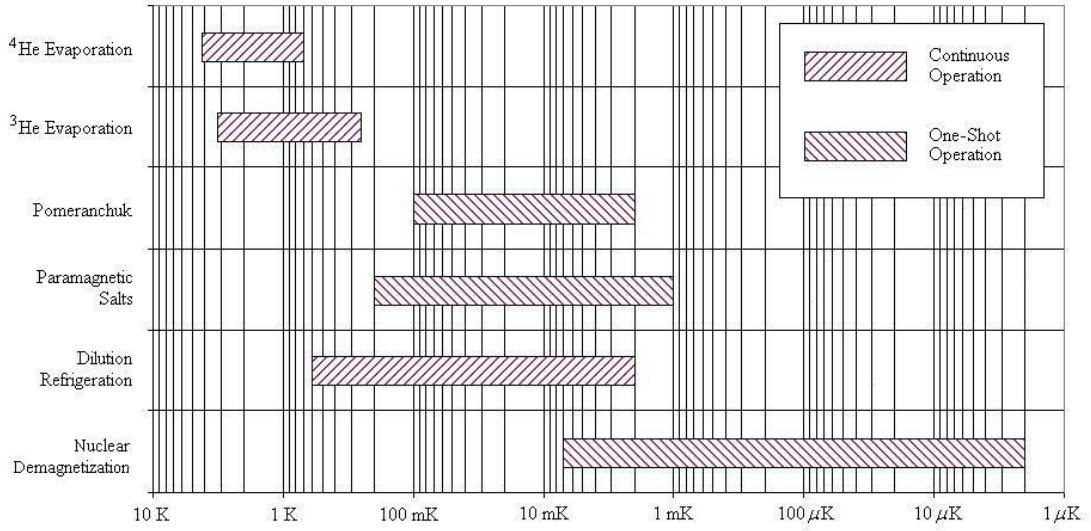


**Figure 2: Cooling methods at VLT**

The invention of sintered metal heat exchangers, and especially the use of silver sinters, greatly enhanced the performance of dilution refrigerators. The minimum temperature obtained with a dilution refrigerator is 1.9 mK, achieved by Frossati and co-workers [133]. One of the highest cooling powers is achieved with the SMC dilution refrigerator at CERN and amounts to 350 mW at 300 mK [38].

### 1.4 Cooling Power and Temperature

The cooling power  $\dot{Q}$  and sample temperature  $T_{\text{Sample}}$  are the two most important requirements imposed on a dilution refrigerator by an experiment. Various models have been derived to predict the cooling power for a dilution refrigerator of a certain design as a function of the mixing chamber temperature  $T_m$ , which can be determined from the required sample temperature  $T_{\text{Sample}}$  by characterizing the thermal link between the sample and the liquid inside the mixing chamber.

The cooling power  $\dot{Q}$  of the dilution process can be calculated as a function of the temperature  $T$  and the <sup>3</sup>He dilution rate  $\dot{n}_3$  by subtracting the enthalpy  $H_C(T)$  of the concentrated phase from the enthalpy  $H_D(T)$  of the dilute phase:

$$\dot{Q}(T) = \dot{n}_3 \cdot [H_D(T) - H_C(T)]. \quad [1.1]$$

With numerical data for the enthalpies below 50 mK, namely  $H_D = a \cdot T^2$  and  $H_C = b \cdot T^2$ , with  $a = 95 \text{ J}/(\text{mol} \cdot \text{K}^2)$  and  $b = 11 \text{ J}/(\text{mol} \cdot \text{K}^2)$ , equation [1.1] yields the following relation for the cooling power of the dilution process:

$$\dot{Q}(T) = (a - b) \cdot \dot{n}_3 \cdot T^2 = 84 \cdot \dot{n}_3 \cdot T^2 \frac{\text{J}}{\text{mol} \cdot \text{K}^2}. \quad [1.2]$$

This cooling power can only be reached in single-shot operation, where the incoming flow of  $^3\text{He}$  is stopped. In continuous operation, some of the available cooling power is put to cooling the incoming  $^3\text{He}$  to the temperature of the mixing chamber. This hints already at the great importance of the heat exchanger in a dilution refrigerator. If the incoming  $^3\text{He}$  is at a higher temperature  $T_i$  than that of the mixing chamber  $T_m$ , the cooling power is calculated from

$$\dot{Q}(T_m, T_i) = \dot{n}_3 \cdot [H_D(T_m) - H_C(T_i)]. \quad [1.3]$$

In the extreme case of no cooling power being available, i.e.  $\dot{Q} = 0$ , equation [1.3] yields the maximum temperature at which the  $^3\text{He}$  may enter into the mixing chamber:

$$T_i(T_m) = \sqrt{\frac{a}{b}} \cdot T_m \approx 3 \cdot T_m. \quad [1.4]$$

If the  $^3\text{He}$  flow rate is set too low, an insufficient number of atoms crosses the phase boundary to provide sufficient cooling. If the  $^3\text{He}$  flow rate is set too high, the concentrated stream is not cooled sufficiently in the heat exchanger and introduces too much heat into the mixing chamber. As a consequence, there is an optimum  $^3\text{He}$  flow rate. It can be calculated by setting  $d\dot{Q}/d\dot{n}_3 = 0$  in equation [1.3] and solving for  $\dot{n}_3$  at constant mixing chamber temperature  $T_m$ , still temperature  $T_s$  and  $^4\text{He}$  contamination  $X_4$ . The result is

$$\text{opt}\{\dot{n}_3\} = \frac{H_D(T_m) - H_C(T_i)}{c_{p,3}(T_i) \cdot (dT_i/d\dot{n}_3)_{T_m, T_s, X_4}}, \quad [1.5]$$

where  $c_{p,3}$  is the specific heat of the concentrated stream per mole of  $^3\text{He}$ . The temperature  $T_i$  depends on the performance of the countercurrent heat exchanger. Niinikoski [99] was the first to derive a theoretical model of dilution refrigeration

which takes into account the finite efficiency of heat exchangers. The derivation starts from the equation which describes the gradient of the concentrated stream temperature  $T_C$  along the axial coordinate  $z$  of the heat exchanger:

$$\frac{dT_C}{dz} = \frac{A}{L} \cdot \frac{\gamma(T_C, T_D)}{\dot{n}_3 \cdot c_{p,3}} - \frac{A_{Cross,C}}{\dot{n}_3 \cdot c_{p,3}} \cdot \left[ \lambda_C \cdot \frac{d^2 T_C}{dz^2} + \frac{d\lambda_C}{dz} \cdot \left( \frac{dT_C}{dz} \right) \right] - \frac{\eta_C \cdot V_C^2 \cdot \dot{n}_3}{c_{p,3}} \cdot \frac{dZ_C}{dz}, \quad [1.6]$$

where  $A$  is the heat exchange surface area in the concentrated stream,  $L$  the length of the stream,  $\gamma(T_C, T_D)$  the heat transfer parameter between the concentrated and dilute stream and  $\dot{n}_3$  the  $^3\text{He}$  flow rate.

The second term on the right hand side of equation [1.6] represents the reduction of the temperature gradient due to axial thermal conduction in the fluid. The thermal conductivity of the concentrated stream is  $\lambda_C$ , and  $A_{Cross,C}$  is the cross-section of the concentrated stream. The third term in equation [1.6] accounts for frictional heating, whose magnitude is influenced by the flow impedance  $Z_C$  of the concentrated stream, the dynamic viscosity  $\eta_C$  of  $^3\text{He}$  and its molar volume  $V_C$ .

In a good design, both axial conduction and frictional heating are sufficiently small to render these effects negligible. The corresponding terms can thus be removed from equation [1.6], which reduces to

$$\frac{dT_C}{dz} = \frac{A}{L} \cdot \frac{\gamma(T_C, T_D)}{\dot{n}_3 \cdot c_{p,3}(T_C)}. \quad [1.7]$$

The heat transfer parameter  $\gamma(T_C, T_D)$  between the concentrated and dilute stream is dominated by the Kapitza conductance. Heat transfer between two bodies in contact occurs due to phonon transmission. The phonon velocity in liquid helium is more than one order of magnitude smaller than in solids. Due to this acoustic mismatch, the majority of phonons cannot pass the liquid/solid interface. The analogue phenomenon in optics is total internal reflection. Acoustic mismatch is the most severe obstacle for a good thermal contact at temperatures below 1 K. The heat transfer between two substances at low temperatures  $T_1$  and  $T_2$  with contact surface  $A$  can be described by the following equation:

$$\dot{Q}(T_1, T_2) = A \cdot S \cdot (T_1^4 - T_2^4). \quad [1.8]$$

Typical values for  $S$  are  $20 \text{ W}/(\text{m}^2 \cdot \text{K}^4)$  between pure  $^3\text{He}$  and copper and  $25 \text{ W}/(\text{m}^2 \cdot \text{K}^4)$  between dilute solution and copper. For the two serial thermal contacts between the concentrated stream and the heat exchanger (surface area  $A_C$ ) and the heat exchanger and the dilute stream (surface area  $A_D$ ), respectively, the heat transfer parameter may be written as

$$\gamma(T_C, T_D) = S_C \cdot T_C^4 \cdot \frac{1 - (T_D/T_C)^4}{1 + (S_C \cdot A_C)/(S_D \cdot A_D)}. \quad [1.9]$$

If a dilution refrigerator is running at optimum  $^3\text{He}$  flow, the concentrated stream temperature is approximately twice as high as the dilute stream temperature, i.e.  $T_D/T_C = 0.5$  [99]. The heat transfer parameter thus no longer depends on  $T_D$  and can be calculated from

$$\gamma(T_C) = S_C \cdot T_C^4 \cdot \frac{0.9375}{1 + (S_C \cdot A_C)/(S_D \cdot A_D)} = S \cdot T_C^4. \quad [1.10]$$

The constant  $S$  can easily be calculated from the properties of the main heat exchanger. This relation for the  $\gamma(T_C, T_D)$  may now be substituted in equation [1.7]. After some further short calculations, the following result is obtained:

$$c_{p,3}(T_i) \cdot (dT_i/d\dot{n}_3)_{T_m, T_s, X_4} = \frac{A \cdot \gamma(T_i)}{\dot{n}_3^2}. \quad [1.11]$$

This can now be combined with equations [1.3] and [1.5] to obtain the optimum  $^3\text{He}$  flow rate  $opt\{\dot{n}_3\}$  and the maximum cooling power  $\max\{\dot{Q}\}$  of a dilution refrigerator with a perfectly continuous heat exchanger. If the enthalpies of the dilute and concentrated solutions are approximated by the functions given above, and if the heat transfer parameter  $\gamma$  can be described by [1.10], the following two important relations are obtained:

$$\max\{\dot{Q}\} = A_C \cdot \gamma(T_i) = \left(\frac{a}{2b}\right)^2 \cdot A_C \cdot S \cdot T_m^4, \quad [1.12]$$

$$opt\{\dot{n}_3\} = \frac{A \cdot \gamma(T_i)}{H_D(T_m) - H_C(T_i)} = \frac{a}{2b^2} \cdot A_C \cdot S \cdot T_m^2 \text{ (K}^2 \cdot \text{mol/J)}. \quad [1.13]$$

The functions which have been used to describe the enthalpies of concentrated and dilute solution are only valid in a limited temperature range, so that equations [1.12] and [1.13] only hold below a certain mixing chamber temperature  $T_m < 50$  mK. A more general solution covering the full temperature range must be obtained numerically.

Frossati [48, 49, 50] derived a formula for the mixing chamber temperature as a function of  $A$ ,  $S$ ,  $\dot{Q}$  and – in contrast to Niinikoski – also the  $^3\text{He}$  flow rate  $\dot{n}_3$ . In the following, the derivation of his theory will briefly be discussed. Frossati also uses equations [1.7] and [1.8] as a starting point.

He proceeds by deriving a relation between the temperature of the concentrated stream  $T_C$  and the temperature of the dilute stream  $T_D$ . All heat given by the concentrated phase must be absorbed by the dilute phase, i.e.

$$c_{p,3}(T_C) \cdot dT_C = c_{p,D}(T_D) \cdot dT_D. \quad [1.14]$$

The heat capacities of Fermi liquids are proportional to temperature. Below 50 mK, the heat capacities of concentrated and dilute solution can thus be fitted with  $c_{p,3} = i \cdot T_C$  and  $c_{p,D} = j \cdot T_D$ , where  $i = 25$  J/(mol·K<sup>2</sup>) and  $j = 107$  J/(mol·K<sup>2</sup>). Equation [1.14] thus changes to

$$i \cdot T_C^2 = j \cdot T_D^2. \quad [1.15]$$

By combining [1.7], [1.8] and [1.15], Frossati obtains a differential equation which describes the temperature profile along the concentrated stream for the case of a negligibly small heat load on the mixing chamber.

$$\frac{dT_C(z)}{T_C(z)^3} = \frac{A \cdot S}{L \cdot \dot{n}_3} \cdot \frac{1 - (i/j)^2}{i} \cdot dz. \quad [1.16]$$

Integrating this equation with the boundary condition  $T_C(L) = \infty$  yields the temperature  $T_i = T_C(0)$  of the concentrated stream entering the mixing chamber. With equation [1.4],  $T_i$  can easily be related to the mixing chamber temperature  $T_m$ :

$$T_i^2(T_m) = \frac{i \cdot \dot{n}_3}{2 \cdot A \cdot S \cdot (1 - (i/j)^2)} = \frac{a}{b} \cdot T_m^2. \quad [1.17]$$



The constant  $S$  is the same as in equation [1.10], and  $A$  the surface area of the heat exchanger. For clarity, the equation for  $T_m$  is given in its explicit form:

$$T_m = \sqrt{\frac{b}{a} \cdot \frac{i}{1 - (i/j)^2} \cdot \frac{\dot{n}_3}{2 \cdot A \cdot S}}. \quad [1.18]$$

It should be emphasized that equation [1.18] is only valid if the external heat load on the mixing chamber is small in comparison to the heat load resulting from the incoming  $^3\text{He}$ . In the contrary case, i.e. if the total heat load is dominated by external sources, the mixing chamber temperature must be calculated from equation [1.2].

In Frossati's theory, the actual mixing chamber temperature is now obtained by summing the values of  $T_m^2$  obtained from equations [1.2] and [1.18]:

$$T_m^2 = \frac{b}{a} \cdot \frac{i}{1 - (i/j)^2} \cdot \frac{\dot{n}_3}{2 \cdot A \cdot S} + \frac{\dot{Q}}{(a - b) \cdot \dot{n}_3}. \quad [1.19]$$

Figure 3 on page 11 shows the dependence of the two terms on the flow rate as well as the resulting mixing chamber temperature. The graph nicely mimics the general behavior of a dilution refrigerator.

Frossati's theory has, however, one weakness: The characteristic of the heat exchanger is not correctly taken into account. This becomes obvious when calculating the mixing chamber temperature for a given heat load and flow rate with equation [1.19], and comparing the result with the temperature at which the dilute stream enters the heat exchanger, which can be obtained from equations [1.15] and [1.17]: The temperature at which the dilute stream enters the mixing chamber is not equal to the mixing chamber temperature. Furthermore, the summation of two temperatures which has been performed to obtain equation [1.19] cannot be justified from a thermodynamic point of view. Frossati's model may thus yield reasonable results for very high and very low flow rates, but not for optimum flow conditions!

Takano [131] modified Frossati's model by adding the correct boundary conditions to the differential equation which describes the temperature profile along the heat exchanger; the resulting formulas cannot be solved analytically, though, and thus do not have the advantage of yielding results quickly and straightforwardly.

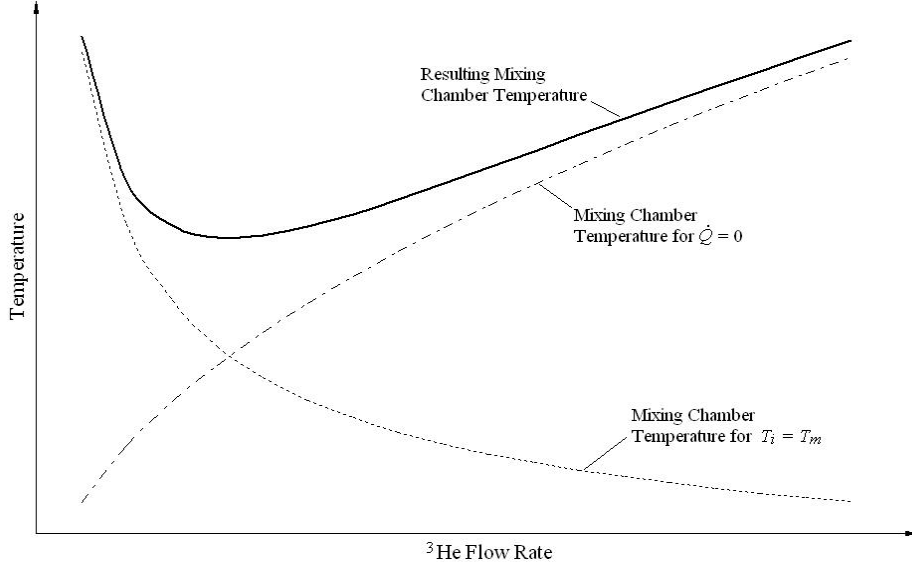


**Figure 3:** In Frossati's model, the mixing chamber temperature is obtained by summing the temperatures yielded by equations [1.2] and [1.18].

A further development of the theories for the prediction of the cooling power of a dilution refrigerator, which relies on numerical simulation, is presented in this thesis. This new method of performance prediction has the advantage of being correct from a thermodynamic point of view, while at the same time being capable of predicting the performance at non-optimum flow. Effects which cannot easily be taken into account by the analytic theory, such as axial conduction, frictional heating and the dependence of the enthalpy of the dilute stream on the mixing chamber temperature, have been included in the model.

Regardless of the calculation method used, the required cooling power  $\dot{Q}$  has to be well known.  $\dot{Q}$  consists of the heat dissipated by the experiment and the residual heat load, which slowly decreases with time and approaches a constant value. The identification of the different sources of residual heat, their magnitude and their scaling laws are also addressed in this work (see chapter 4).

In the framework of this thesis project, a dilution refrigerator has been built at the CERN Central Cryogenic Laboratory (chapter 2) to test the results of the numerical simulation (chapter 3) and to conduct first experiments on the residual heat load (chapter 4). These experiments will be continued in the future [22]. The obtained results were used for a first design of a dilution refrigeration system for the European large dark matter detector array EURECA (chapter 6).

## 2. Design of a Dilution Refrigeration System

A dilution refrigerator for operation at the CERN Central Cryogenic Laboratory (Cryolab) has been designed, built and tested. Thorough tests have been carried out to characterize the performance of this refrigerator. The experimental results of these cooling power measurements are presented in chapter 3 and the measurements of the residual heat load are described in chapter 4. All other important parameters are reported in the following along with a design description.

The refrigeration system can be cooled from room temperature to millikelvin temperatures in three to four days; approximately 28 hours are necessary to cool the IVC from room temperature to 4 K and completely fill the atmospheric  $^4\text{He}$  bath. A total of 210 l of liquid  $^4\text{He}$  is necessary for this operation. With  $\text{H}_2$  as exchange gas, the parts inside the IVC can be cooled to some 30 K. It takes another 8 hours to put the 1 K pot into operation. The heat exchanger and the mixing chamber are cooled to 1 K within another 18 hours. This is achieved by circulating a small quantity of He in the  $^3\text{He}$  circuit. The last operation, namely condensing the He mixture, takes some 6 hours if done slowly to allow for proper purification of the gas in the nitrogen trap. If  $^4\text{He}$  is used as exchange gas inside the IVC, the parts of the dilution refrigerator can be precooled to some 10 K, which greatly reduces the time needed for cool-down at the cost of not being able to perform leak testing on the IVC.

### 2.1 The CERN Cryolab Dilution Refrigerator (CCDR)

The CCDR has been designed in view of tests to be carried out in the framework of the dilution refrigeration research program at CERN. Its overall layout is shown in Figure 4.

The maximum allowable  $^3\text{He}$  flow rate in excess of 10 mmol/s allows for future tests of new heat exchanger concepts with very high surface areas to validate their performance at mixing chamber temperatures below 10 mK with cooling powers in the range of a few  $\mu\text{W}$ . Furthermore, special features have been accommodated to facilitate the measurement of the residual heat load: The vacuum system, for instance, is equipped with shutters which can be used to almost completely eliminate the direct flux of hot molecules from hot surfaces to the mixing chamber.

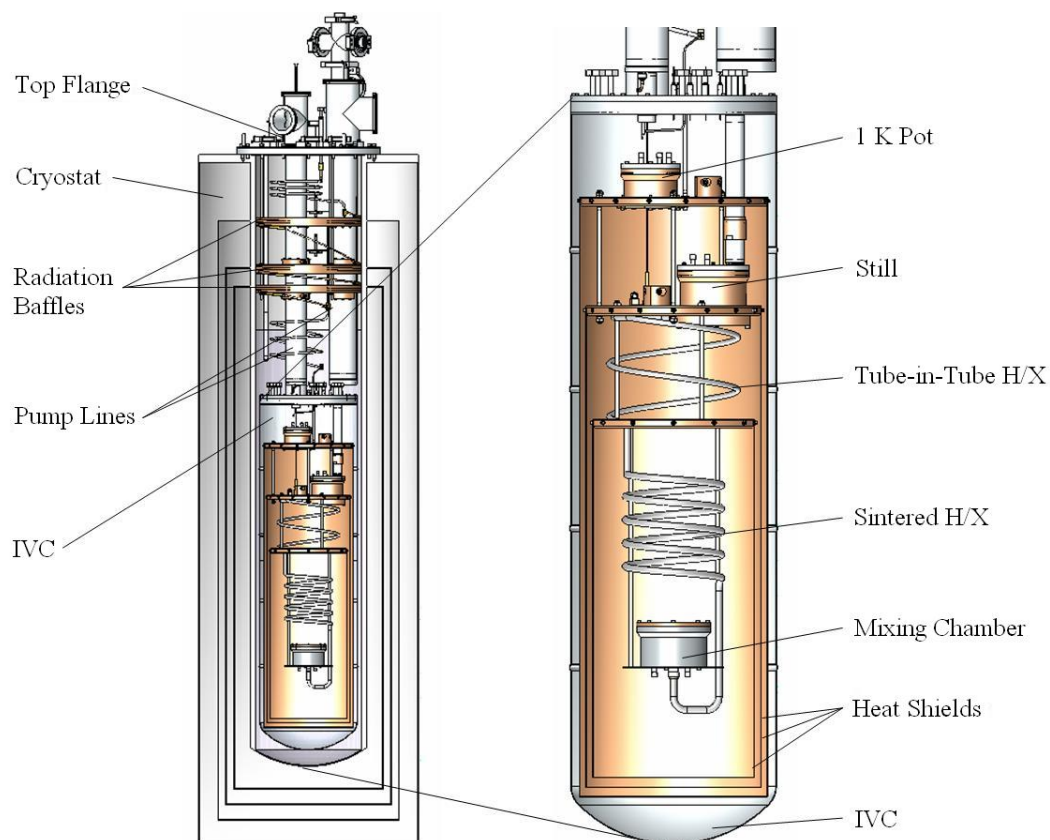


**Figure 4: Layout of the CCDR**

In addition, the cryostat was mechanically decoupled from rotating machinery and from the floor of the laboratory hall to assess the heat load due to damping of vibrations. Heaters have been placed on the mixing chamber, the heat exchanger, the still and the 1 K system to facilitate subjecting the apparatus to different combinations of heat loads. Furthermore, the volume available for the cold mass amounts to more than 20 l and thus allows for the accommodation of large material samples.

The design of the CCDR was adapted to existing equipment, which includes a hermetic Alcatel  $^3\text{He}$  pump<sup>6</sup>, a Leybold  $^4\text{He}$  pump<sup>7</sup>, and two Alcatel Roots blowers<sup>8</sup>. With this equipment, the maximum pump speed for both  $^3\text{He}$  and  $^4\text{He}$  amounts to approximately 300 m<sup>3</sup>/h. The dilution refrigerator was fitted into an existing dewar with an inner diameter of 340 mm and a depth of 1950 mm. A photograph of the complete refrigeration system is shown in Figure 5.

<sup>6</sup> Model 2060H, Alcatel Vacuum Technology (Annecy, France)

<sup>7</sup> Model Sogevac SV280, Leybold Vacuum GmbH (Köln, Germany)

<sup>8</sup> Model MIV350, Alcatel Vacuum Technology (Annecy, France)



**Figure 5: The complete CCDR dilution refrigeration system**

## ***2.2 The 4 Kelvin System and Inner Vacuum Chamber (IVC)***

The IVC is submerged in a  $^4\text{He}$  bath at atmospheric pressure and thus has a wall temperature of approximately 4.2 K. The autonomy of the dilution refrigeration system is limited by the amount of helium in this bath. The helium level should never exceed 1500 mm and must not drop below 1200 mm. The volume between these two levels amounts to some 23.4 l, which is equivalent to 732 mol of  $^4\text{He}$ . Helium is consumed by the 1 K subsystem, the precooling heat exchanger and the heat load to the 4 K bath. The heat load to the bath has been determined by measuring the boil-off rate, which amounts to 14.5 mmol/s when the helium level is high, and to 8 mmol/s when the helium level is low. The average boil-off rate is 9.7 mmol/s, which is equivalent to a heat load of 0.85 W. The amount of  $^4\text{He}$  consumed by the precooling heat exchanger and the 1 K pot depends on the  $^3\text{He}$  flow rate. At low  $^3\text{He}$  flow rates, the autonomy between two refilling operations is thus dominated by the heat load to the 4 K bath and lies in the range of 21 h. At high  $^3\text{He}$  flow rates, the autonomy might be as low as 8 h. A continuous refilling system for the bath is thus mandatory if high flow rates must be maintained over long periods of time.

The IVC contains the 1 K stage as well as the dilution refrigerator itself, which consists of the still, the mixing chamber, the main heat exchanger and the thermal

insulation system. The IVC is made up of a flange, which accommodates all fluid and electrical feed-throughs, and a vacuum jacket. The vacuum jacket is made of stainless steel and has an inner diameter of 309 mm and a length of 1100 mm. The wall thickness amounts to 1 mm. For structural reinforcement, ribs have been welded to the vacuum vessel in addition to crimped corrugations. Several charcoal traps are located inside the IVC to improve the isolation vacuum by adsorbing residual gas molecules. These traps are mounted on the vacuum shutters, which can be opened and closed during operation. They are kept open during the evacuation of the system, and closed for the remaining time to prevent hot molecules from entering the cold parts of the dilution refrigerator. The molecules which pass through the remaining gap are captured by the charcoal traps which are equipped with heaters and thermometers to control their temperature. The charcoal can be heated during cool-down to prevent it from charging rapidly in the beginning of operations. The shutters are closed by springs which ensure a good thermal contact between the shutter and its support. This is necessary to cool the charcoal traps.

### ***2.3 The 1 Kelvin Subsystem***

The main purpose of the 1 K subsystem is to provide a heat sink for the first thermal shield and for the condensation of the incoming  $^3\text{He}$ . The 1 K subsystem consists of a copper pot containing  $^4\text{He}$  at reduced pressure. The pot is mounted on a flange. The heat shield surrounding the actual dilution refrigerator is bolted to that flange.

Grooves have been machined into the bottom of the 1 K pot to enhance the contact surface between the liquid and the solid. The  $^4\text{He}$  in the pot is replenished from the atmospheric bath through an adjustable needle valve, where the pressure drop and expansion take place.

A heat exchanger inside the pump line makes use of the enthalpy of the cold gas to precool the incoming  $^4\text{He}$ . Cooling fins are used to increase the surface available for heat exchange as the heat transfer coefficient between the low pressure gas and the tube is rather low. A level gauge has been accommodated inside the 1 K pot. It is of standard length (1100 mm) and is led through the pump line. This allows for easy exchange in case of gauge failure.

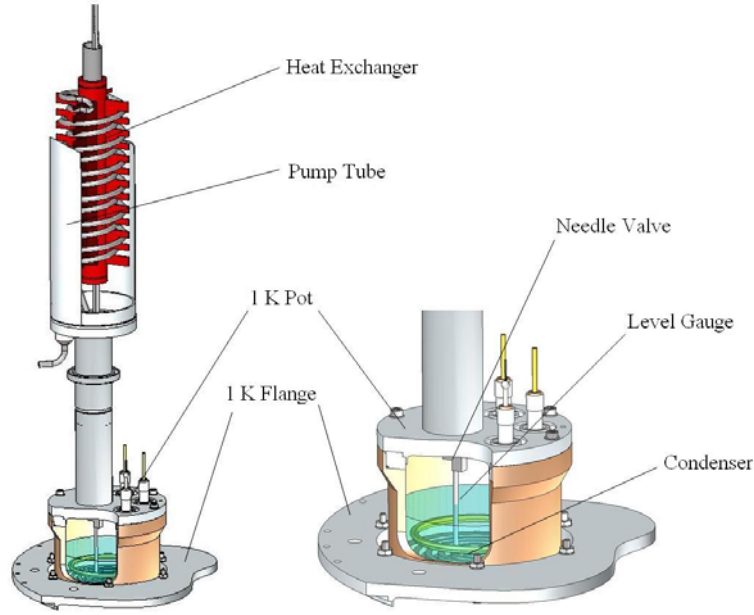


**Figure 6: The 1 K subsystem of the CCDR**

The temperature of the 1 K pot is monitored with a carbon-ceramic resistance thermometer (CCS/F1)<sup>9</sup>. Inside the 1 K pot, a copper tube with an inner diameter of 1.25 mm, an outer diameter of 1.65 mm and a length of 600 mm has been installed. It serves as condenser for the incoming <sup>3</sup>He flow. A flow constriction with an impedance  $Z$  equalling

$$Z = \frac{\Delta p}{\dot{V} \cdot \eta} = \frac{128 \cdot l}{d^4 \cdot \pi} = 5.2 \cdot 10^7 \text{ cm}^{-3}, \quad [2.1]$$

where  $l = 8 \text{ cm}$  is the length and  $d = 0.5 \text{ mm}$  the inner diameter of the capillary, has been installed downstream of the condenser to raise the condensation pressure. It lies in series with a needle valve which allows for adjustment of the condensation pressure and thus makes a larger range of flow rates accessible.

The heat load to the 1 K system can be determined from the boil-off rate of  $100 \text{ } \mu\text{mol/s}$  which has been measured at a temperature of  $1.6 \text{ K}$ . Superfluid film flow along the pump line, which has a diameter of  $26.8 \text{ mm}$ , amounts to  $60 \text{ } \mu\text{mol/s}$ , if the critical film speed amounts to  $30 \text{ cm/s}$  and the actual perimeter of the pump line is three times as large as the geometric perimeter. A heat load of  $3.7 \text{ mW}$  must be

---

<sup>9</sup> TMI Cryogenics (Oxford, UK)

present to evaporate the remaining 40  $\mu\text{mol/s}$ . If superfluid film flow is neglected, the heat load is calculated to be 9.1 mW. The minimum temperature achievable with the 1 K pot in continuous operation is 1.2 K.

## 2.4 The Still and Film Burner

The still has been designed such that the heat load to the boiling dilute solution is minimized. This is necessary to achieve small  $^3\text{He}$  flow rates. Furthermore, a film burner has been implemented to reduce the  $^4\text{He}$  contamination of the concentrated stream. The still pot is shown in Figure 7.

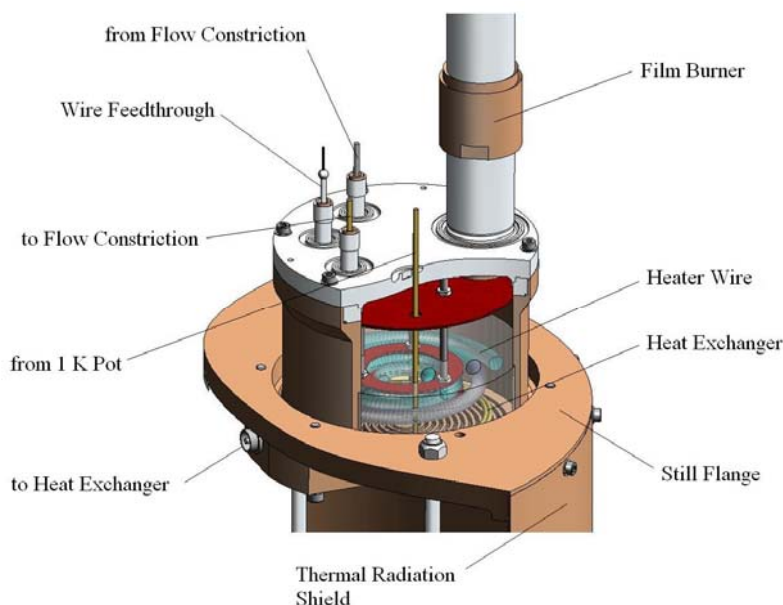


**Figure 7: The still and film burner subsystem of the CDDR**

The still is similar to the 1 K pot as it is made from high conductivity copper and bolted to a flange, which in turn is bolted to a radiation shield. Again, grooves provide an enhanced heat exchange surface area between the pot and the liquid. Inside the still, a heat exchanger has been installed to subcool the  $^3\text{He}$ . The heat exchanger consists of a copper pipe with an inner diameter of 1.25 mm and an outer diameter of 1.65 mm. Its length amounts to 700 mm. Furthermore, a heater has been installed to control the  $^3\text{He}$  flow rate. The electrical resistance of the still heater amounts to 21  $\Omega$ . It consists of a manganin wire with a diameter of 0.55 mm and a length of 9 m. The resulting heater surface area guarantees that the critical boiling heat flux of 3 mW/cm<sup>2</sup> and the maximum allowable temperature difference of 0.6 K are not exceeded.



The film burner is a heated copper piece which is located inside the  $^3\text{He}$  pump line close to the still. It is equipped with a copper tube which protrudes into the still pot as shown in Figure 8. The film burner is heated to a temperature above the  $\lambda$ -point, which “burns” away the superfluid film. The  $^4\text{He}$  vapor recondenses in the still but does not enter the pump line. This is assured by adding a  $^4\text{He}$  shield to the assembly. If the level in the atmospheric  $^4\text{He}$  bath is low, no power has to be applied to the film burner as it is then heated sufficiently by conduction along the pump line.

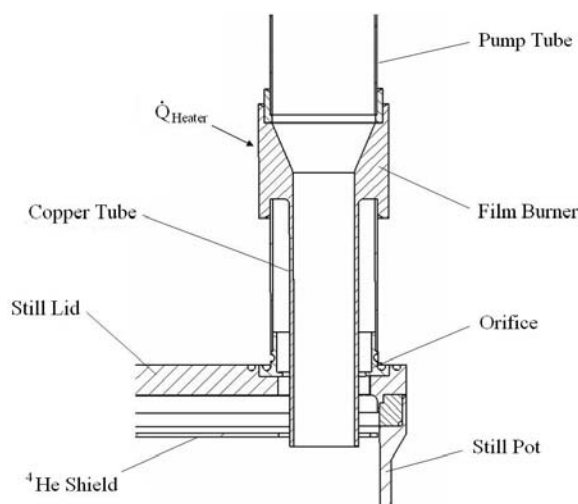


**Figure 8: The film burner**

The heat load on the still resulting from the film burner has a two-fold origin. Heat is conducted through the stainless steel pipe connecting the film burner with the still lid (as a consequence, a tube with a very small wall thickness has been chosen), and heat is introduced into the still by the recondensation of  $^4\text{He}$ .

At the beginning of a cold run - and with the film burner being switched off - the minimum flow rate of the  $^3\text{He}/^4\text{He}$  gas mixture is  $80 \mu\text{mol/s}$ . Approximately  $20 \mu\text{mol/s}$  are attributed to superfluid film creep. The minimum flow rate is determined by the heat load on the still, which lies between 2.3 mW and 4.9 mW. These lower and upper values have been obtained by assuming that either pure  $^3\text{He}$  or pure  $^4\text{He}$  evaporates. After a few weeks of operation, the heat load on the still has dropped sufficiently to allow for a minimum flow rate of some  $40 \mu\text{mol/s}$ .

The highest possible flow rate amounts to approximately  $10 \text{ mmol/s}$ . It is limited by the total pressure drop of the condensation line in the cryostat, which is mainly determined by the precooling- and the main heat exchangers. The pressure drop at maximum flow amounts to some 700 mbar.

## 2.5 The Heat Exchanger

The design chosen for the sintered heat exchanger has already proven its suitability in many dilution refrigerators [98, 99, 100]. The heat exchanger is made of three short sintered copper elements with a length of 40 mm each and nine longer elements with a length of 80 mm each. The copper tubes used for the manufacturing of the sintered elements have an inner diameter of  $d_i = 2$  mm and an outer diameter of  $d_o = 3$  mm. The elements are joined together with thin-walled CuNi connection tubes to minimize axial conduction. Sintered copper elements and the cross-section of the heat exchanger are shown in Figure 9.

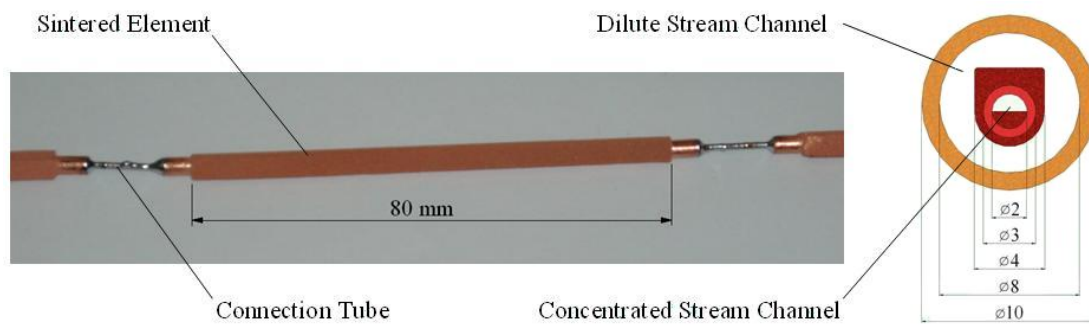


**Figure 9: Three sintered copper elements soldered together and the cross-section of the H/X**

Copper powder was sintered to the inside and outside surfaces of the tube. The volume of the sintered sponge inside a sintered element with a length of 80 mm amounts to  $125 \text{ mm}^3$  in the concentrated stream, and to  $737 \text{ mm}^3$  in the dilute stream. This is equal to a surface area of  $167 \text{ cm}^2$  in the concentrated stream channel of a sintered element, and to  $983 \text{ cm}^2$  in the dilute stream channel. The total surface amounts to  $1750 \text{ cm}^2$  in the concentrated stream and to  $1 \text{ m}^2$  in the dilute stream. These values have been calculated from the grain size and the filling factor of the copper powder, which amount to  $18 \text{ }\mu\text{m}$  and 0.4, respectively. These numbers are furthermore supported by the performance tests carried out with the CCDR.

The thickness of the sintered layer does not exceed 1 mm in the concentrated stream and 1.5 mm in the dilute stream to maximize the fraction of the total surface participating in heat transfer, which is limited by the temperature dependent thermal penetration depth of sintered sponges. To improve the contact between the sintered sponge and the tube, the metal surface to which the sintered sponge adheres has been roughened. A thin saw blade proved useful for the inside surface of the tube.

After soldering all sintered elements together, they were inserted into a brass tube of low thermal conductivity which forms the dilute flow channel. A tube with  $d_o = 10$  mm and  $d_i = 8$  mm has been used. Figure 10 shows the design of the CCDR main heat exchanger.

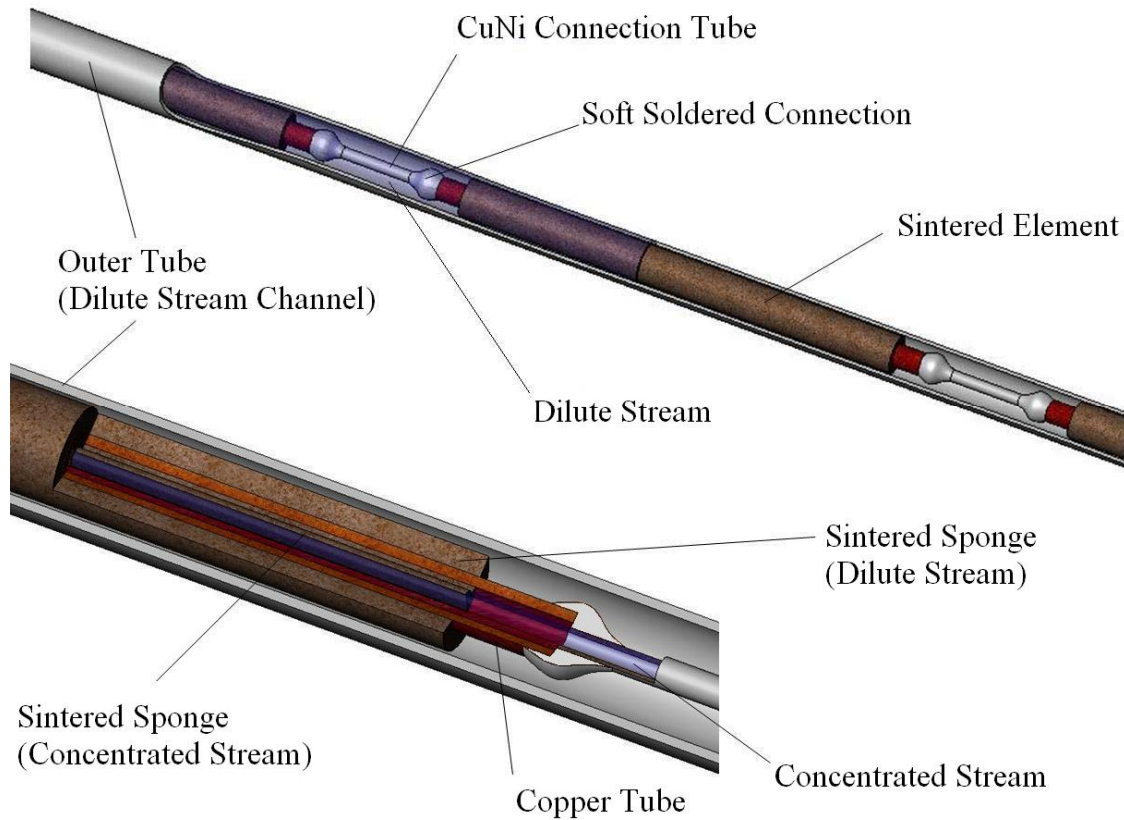


**Figure 10: The sintered copper heat exchanger in the CCDR**

In order to precool the concentrated stream to temperatures where sintered heat exchanger elements can be effective, a straight and a coiled tube-in-tube heat exchanger have been incorporated. A cupronickel tube with an inner diameter of 0.65 mm and an outer diameter of 1.0 mm confines the concentrated stream. The dilute stream is confined by a brass tube with an inner diameter of 6 mm. The length of the straight tube-in-tube heat exchanger amounts to 50 cm.

The length of the coiled heat exchanger is 120 cm in the concentrated stream and 70 cm in the dilute stream. The dilute stream also serves as a heat sink for the last heat shield surrounding the mixing chamber.

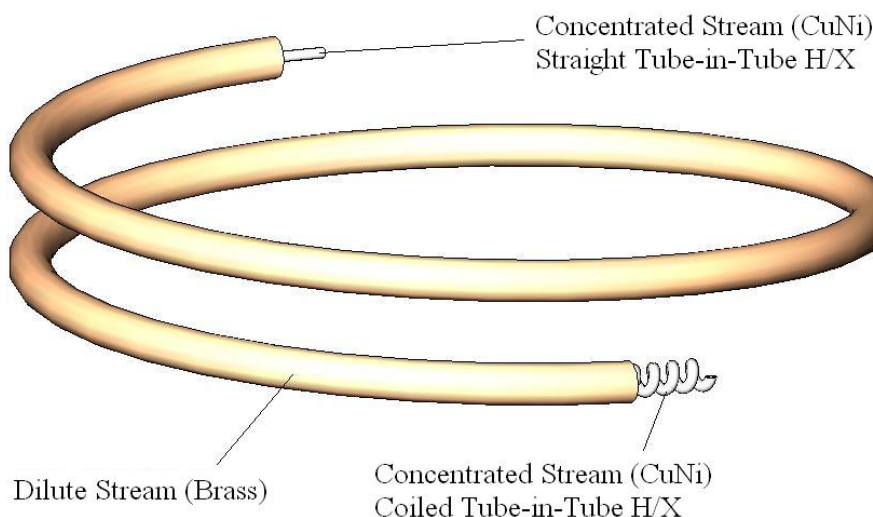


**Figure 11: The straight and coiled tube-in-tube heat exchanger**

## ***2.6 The Mixing Chamber***

The design of the mixing chamber is shown in Figure 12 on the following page. The mixing chamber body is made from stainless steel. Sealing is achieved by means of an indium gasket. The mixing chamber is held in place by three steel support rods.

The heater which is used to subject the dilution refrigerator to a well determined heat load for the cooling power measurements is located inside the mixing chamber. Heat transport in the liquid is enhanced by convection, which is driven by the temperature dependent density of the liquids. A  $^3\text{He}$  trap is used to improve convection. Pure  $^3\text{He}$  rises up from the outlet of the concentrated stream and gets caught in the trap where a phase boundary develops. The cold dilute solution originating from the phase passes by the mixing chamber heater where it warms up and rises. It subsequently drops to the bottom of the mixing chamber, forming a vortex. Depending on the quantity of  $^3\text{He}$  in the dilution refrigerator, the grooves of the  $^3\text{He}$  trap may be completely filled with concentrated solution and a second phase boundary may develop underneath the lid of the mixing chamber. The bottom of the mixing chamber has been slightly inclined to guide the dilute solution to the outlet in the center.

The mixing chamber heater consists of a manganin wire with a length of 30 m and a diameter of 0.09 mm, which is wound around a plastic support. The electrical resistance of the heater amounts to 1650  $\Omega$ .

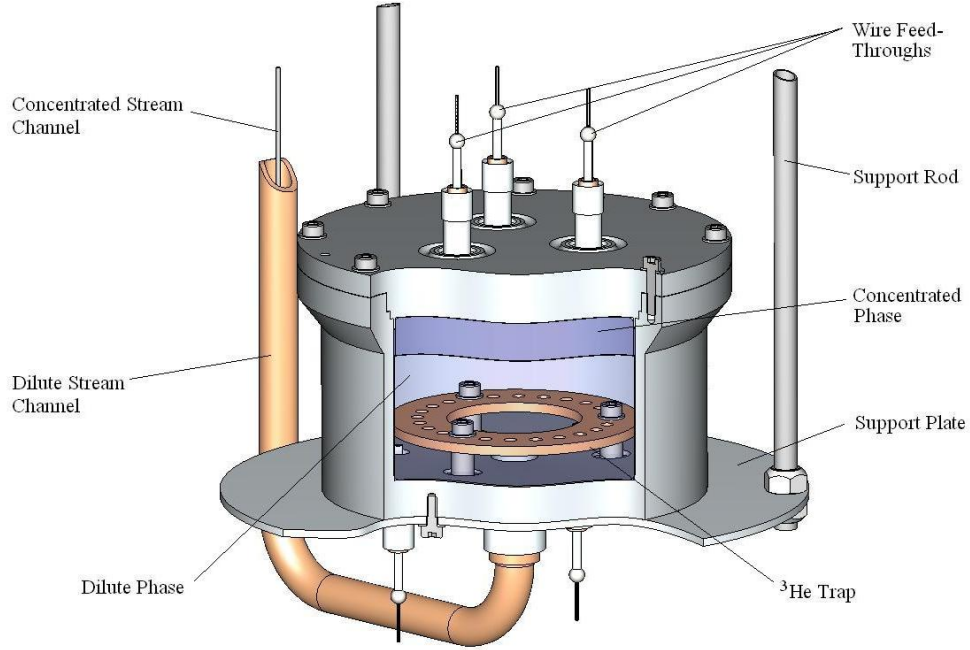


**Figure 12: The CC DR mixing chamber**

The temperature of the mixing chamber is measured by a resistance thermometer<sup>10</sup> which has been calibrated between 42 K and 40 mK by the supplier. The temperature is obtained from an equation of the form

$$T = \sum_{i=0}^{10} A_i \cdot \cos \left( i \cdot \arccos \left( \frac{(\log_{10}(R) - Z_L) - (Z_U - \log_{10}(R))}{Z_U - Z_L} \right) \right) \quad [2.2]$$

fitted to the calibration data.  $T$  is the temperature in K,  $R$  the measured resistance in  $\Omega$  and  $A_i$  the fitting coefficients given in Table 1.  $Z_U$  and  $Z_L$  are constants and amount to 3.635 and 4.8649 respectively. Temperatures lower than 40 mK were determined by extrapolation of the supplied  $R(T)$  characteristics. The resistance of RuO<sub>2</sub> thick film thermometers has successfully been fitted to an extrapolation function of the following form [18, 126, 138]:

$$R(T) = R_0 \cdot e^{\left( \frac{T_0}{T} \right)^\beta} . \quad [2.3]$$

The  $R(T)$  characteristic of the thermometer used in the mixing chamber of the CC DR obeys this law very well, with  $R_0 = 1957.8768 \Omega$ ,  $T_0 = 0.6666 \text{ K}$  and  $\beta = 0.4774$ .

<sup>10</sup> Ruthenium Oxide RX-202A-AA-0.05B, Lakeshore Inc. (Westerville, Ohio, USA)

$A_0$	0.294701	$A_6$	0.008535
$A_1$	-0.386296	$A_7$	-0.003647
$A_2$	0.201307	$A_8$	0.001454
$A_3$	-0.095691	$A_9$	-0.000541
$A_4$	0.042883	$A_{10}$	0.000108
$A_5$	-0.018858		

**Table 1: Coefficients for Chebychev fitting of thermometer  $R(T)$  characteristics (Lake Shore)**

In addition to this calibrated thermometer, off-the-shelf RuO<sub>2</sub> thick film resistors (Type RCWP-575 with 1 k $\Omega$  at 300 K) have been placed inside the mixing chamber. These resistors feature a  $R(T)$  characteristic which is more convenient at temperatures below 100 mK. They have been calibrated against the Lakeshore thermometer above 45 mK. Measurements at lower temperatures were made by extrapolating the  $R(T)$  characteristic. For temperature measurements in the range of 10 mK, Speer carbon resistors of type 1002 were used. The electrical resistance  $R$  can be fitted by

$$\ln(R) = A \cdot (\ln T)^2 + B \cdot \ln T + C, \quad [2.4]$$

where  $A$ ,  $B$  and  $C$  are constants [103]. For the Speer thermometer used in the CCDR, these constants amount to  $A = 5.75 \cdot 10^{-2}$ ,  $B = -1.59$  and  $C = 13.5$ , if the temperature  $T$  is measured in K. All thermometers inside the mixing chamber have been wired with superconducting NbTi cables to minimize heat conduction. The fitting functions for the RuO<sub>2</sub> and Speer thermometers are compared to the calibration data in Figure 13.

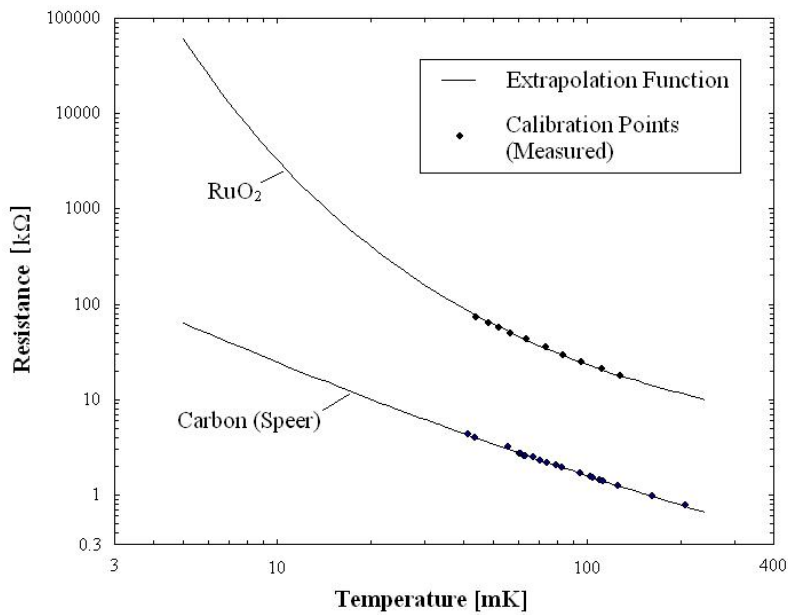


**Figure 13: Extrapolation functions and calibration points for the RuO<sub>2</sub> and Speer thermometers**

The lowest temperature ever obtained with the CCDR in continuous mode amounts to  $(9.85 \pm 0.27)$  mK. In one shot operation, a temperature of  $(5.1 \pm 0.27)$  mK was reached. This indicates that the performance of the dilution refrigerator is limited by the heat exchanger and not by the residual heat load.

## 2.7 The Gas Handling System

The layout of the gas handling system for the CCDR is outlined in Figure 14. The pumping systems for vacuum and  $^4\text{He}$  as well as the closed  $^3\text{He}$  circuit are shown.

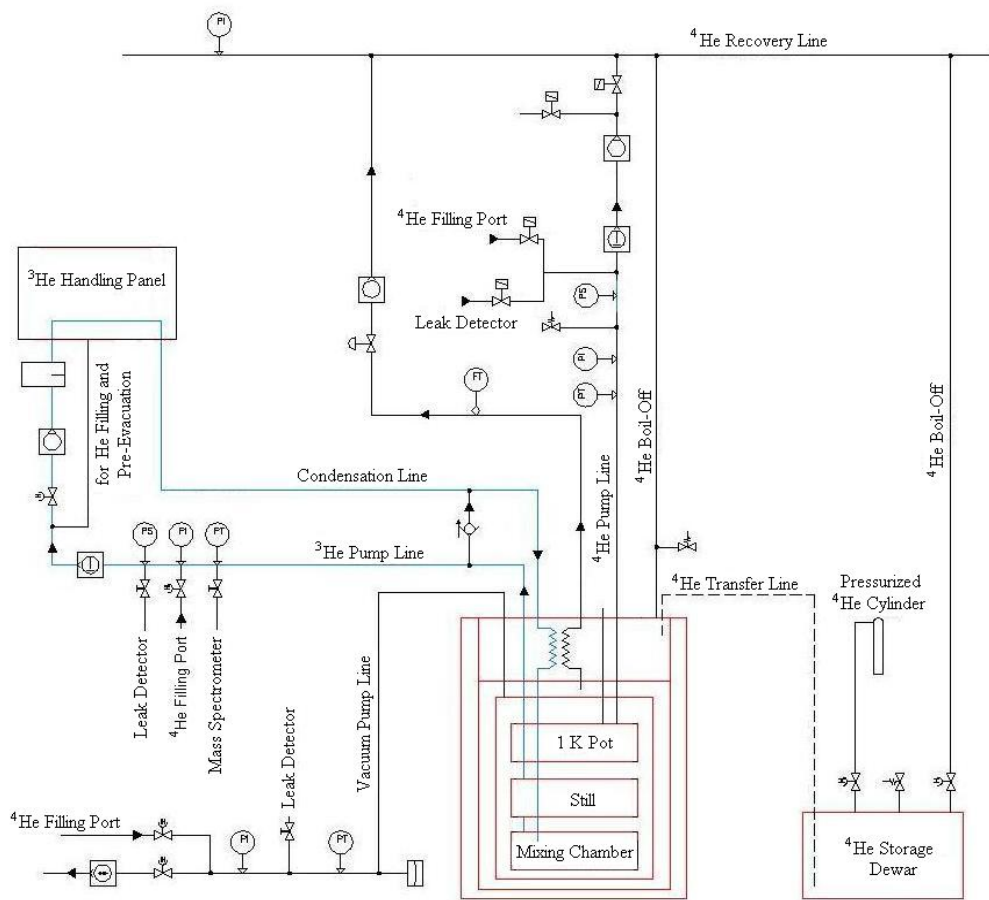


**Figure 14: CCDR synoptic diagram**

The  $^4\text{He}$  and vacuum pump lines are equipped with various pressure sensors, a  $^4\text{He}$  filling port for purging, a connection for a leak detector and a safety release valve. The atmospheric  $^4\text{He}$  bath inside the cryostat is replenished from a 500 l storage dewar. The liquid helium is forced out of the dewar into the transfer line by pressurizing the storage vessel with gaseous  $^4\text{He}$  from a cylinder. The  $^3\text{He}$  circuit



features a port for a leak detector, a port for filling the He isotopes and a port for a mass spectrometer to determine the  $^4\text{He}$  contamination. A safety valve which opens into the reservoir is part of the gas handling rack.

The synoptic diagram and a photograph of the  $^3\text{He}$  Handling Rack are shown in Figure 15. The  $^3\text{He}$  rack houses two charcoal traps, one at ambient temperature and one at liquid nitrogen temperature. The gas handling system may be improved by adding two charcoal traps in parallel to the existing ones. These redundant traps would allow for regeneration without having to interrupt the operation of the dilution refrigerator. Furthermore, two gas reservoirs for  $^3\text{He}$  (50 l) and  $^4\text{He}$  (410 l) respectively are connected to the  $^3\text{He}$  circuit.

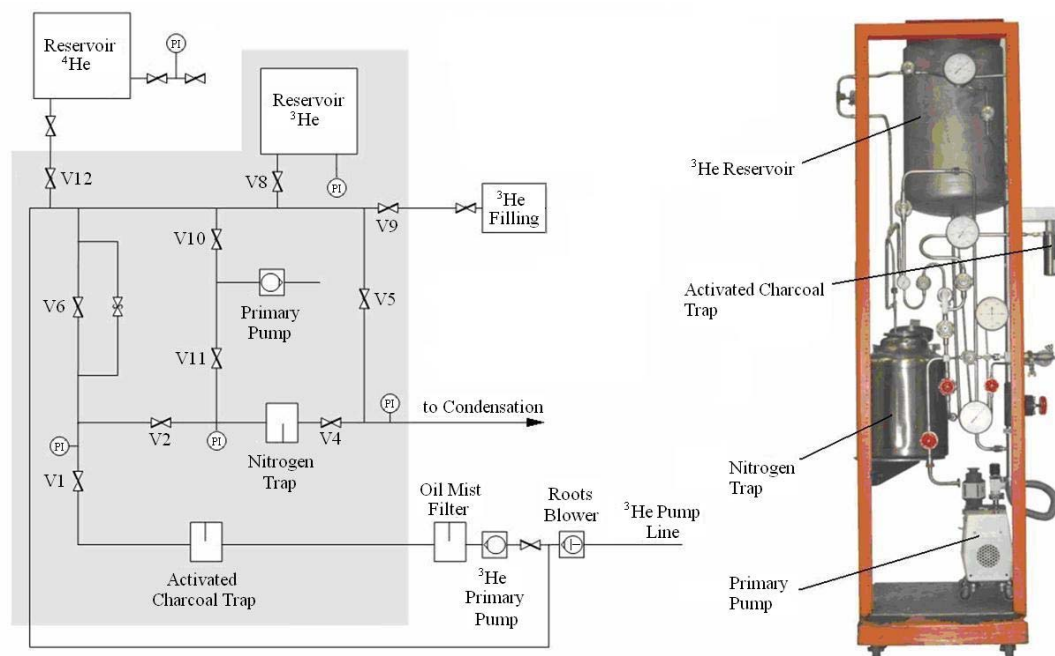


Figure 15: Layout of the  $^3\text{He}$  handling rack

## 2.8 The Vibration Isolation System

Vibrations have to be kept away from the dilution refrigerator to improve the signal to noise ratio of electrical signals which deteriorates if wires are moving. Furthermore, vibrations can lead to an increased heat load due to structural damping and eddy current heating.

The pump lines acoustically couple the vibrating pumps with the cryostat, which requires damping. Both the  $^4\text{He}$  and  $^3\text{He}$  lines are clamped to a concrete block as



shown in Figure 16. Two bellows are incorporated in each pump line; one between the pump and the concrete block, and a second one between the block and the cryostat. At a later stage, the bellows can be replaced by a longer section of flexible tubing.

Acoustic decoupling between the cryostat and the laboratory building is achieved by placing the cryostat on a heavy basement. The CCDR is placed on concrete blocks with a total mass of 5000 kg. These concrete blocks have been placed on tennis balls, which are affordable and effective elastic dampers. As each tennis ball can support approximately 100 kg, a total of 64 balls has been used.

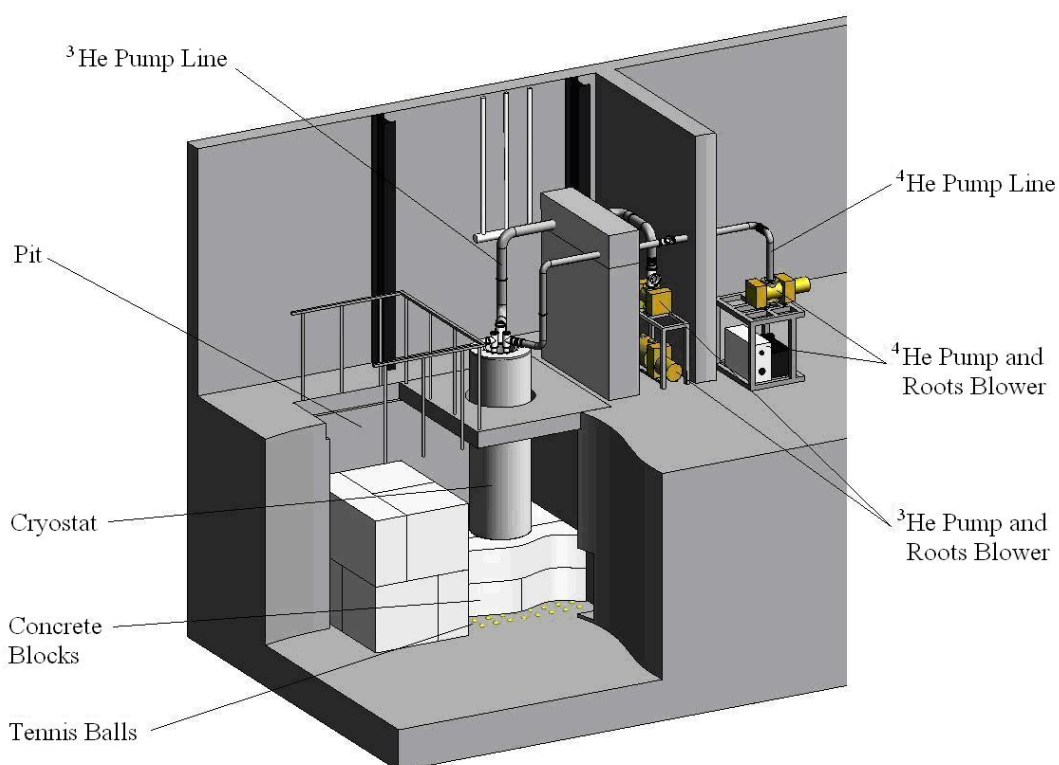


**Figure 16: Vibration damping for the CCDR**

In order to assess the performance of the vibration damping system, measurements with an accelerometer have been carried out. The accelerometer was firmly fixed on the cryostat and measurements were taken with the dilution refrigerator running, i.e. all pumps were operating. The measured vibration spectrum is shown in Figure 17 on the following page.

The peaks resulting from the pumps and roots blowers are clearly visible. It is interesting to note that the  $^3\text{He}$  and  $^4\text{He}$  Roots blowers excite the cryostat at very different frequencies, despite of them being identical. This is attributed to the transmission characteristics of the pump lines, which are of different geometry.

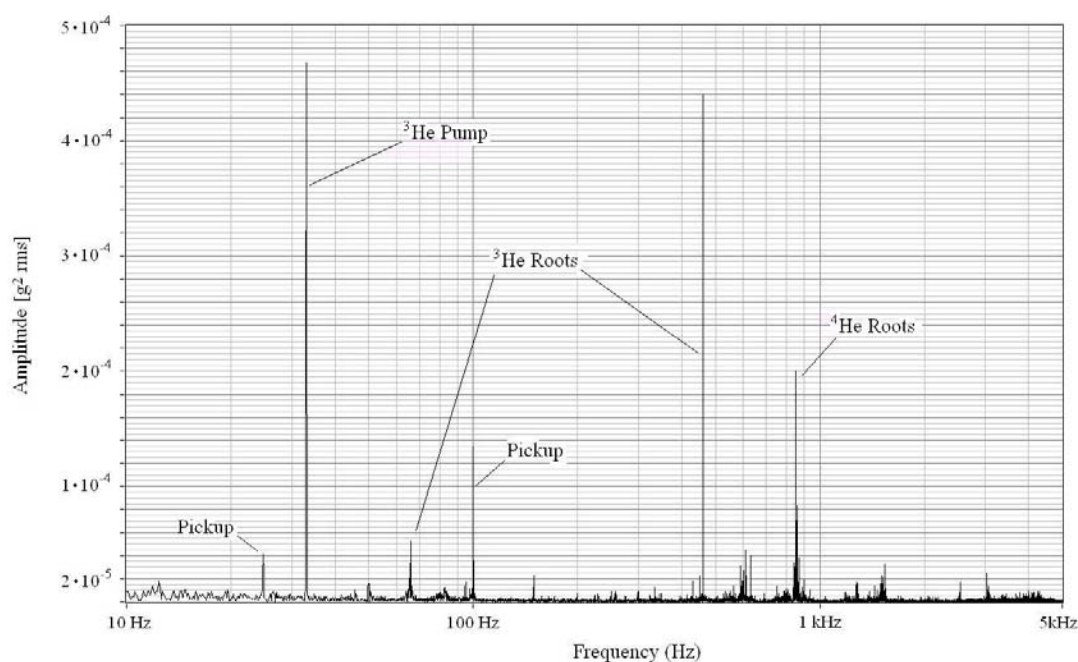


**Figure 17: Peak amplitude vibration spectrum measured on the top plate of the cryostat**

## ***2.9 Electrical System and Data Acquisition (DAQ)***

The electrical system controls and supplies power to equipment such as the pumps and heaters. Furthermore, it provides a means for data acquisition (DAQ). All control and read-out electronics have been accommodated in a 19" rack. Table 2 on page 28 lists the electrical components used in the CCDR system.

Data acquisition is effected via GPIB and a Personal Computer using a Labview<sup>11</sup> program. For safety reasons, control operations are not carried out by the Personal Computer. Temperatures are read with an AVS-46 and an AVS-47A resistance bridge<sup>12</sup>. Both units have been specially designed for use at very low temperatures. They are equipped with multiplexers and allow for scanned temperature measurements of 15 thermometers.

Low-pass filters are installed at the cable connections to the cryostat to reduce high frequency interferences which may cause heating of the temperature sensors. All cables are double shielded and grounded to the outer vacuum vessel. This facilitates

<sup>11</sup> National Instruments Corporation (Austin, Texas, USA)

<sup>12</sup> Picowatt (Vantaa, Finland)

temperature measurements at the lowest possible excitation level provided by the resistance bridges, which amounts to 3  $\mu\text{V}$ . The power supplies listed in Table 2 should be replaced for future tests where electromagnetic interferences must be further reduced, as the currently installed units proved to distort the output of the AC amplifier of the resistance bridges considerably.

Item No	Description	Device
<b>Pumps</b>		
1	$^3\text{He}$ Roots Blower	Alcatel MIV350
2	$^3\text{He}$ Primary Pump	Alcatel 2060H
3	$^4\text{He}$ Roots Blower	Alcatel MIV350
4	$^4\text{He}$ Primary Pump	Leybold Sogevac SV280
5	Pump for precooling H/X	KNF NK 1200 ED
<b>Flow Meters and Controllers</b>		
6	$^3\text{He}$ Flowmeter ( 1 – 20 mmol/s)	Hastings Flowmeter EACC-50KPGX
7	$^3\text{He}$ Flowmeter ( 0 – 3 mmol/s)	Bronkhorst F-101 E-AAD-99-V
8	Pre-Cooling HX Flow Controller	Bronkhorst F-201E-AAB-33-V
<b>Pressure and Vacuum Gauges</b>		
9	$^3\text{He}$ Pump Outlet Pressure	WIKA Tronic Line 891.13.500
10	IVC Pressure	Alcatel CF2P Penning Gauge
11	Still Pressure	Pfeiffer Vacuum TPR280 Pirani Gauge
12	1K Pot Pressure	Pfeiffer Vacuum TPR280 Pirani Gauge
<b>Level Gauges</b>		
13	$^4\text{He}$ Bath Level Gauge	Twickenham Helium Depth Indicator
14	1K Pot Level Gauge	Twickenham Helium Depth Indicator
<b>Power Supplies</b>		
15	Charcoal Trap Heater	Hameg Power Supply HM8142, max. 30V/1A
16	Still Heater	Hameg Power Supply HM8142, max. 30V/1A
17	Mixing Chamber Heater	Hameg Power Supply HM8142, max. 30V/1A
18	Film Burner Heater	Hameg Power Supply HM8142, max. 30V/1A
<b>Thermometry</b>		
19	AC Resistance Bridges	Picowatt AVS-46 and AVS-47A

**Table 2: Components used for experiment control and DAQ**

An additional modification of the electrical system which may be carried out in the future is the rearrangement of all electronic equipment in two separate racks. One rack should house all units for the control of equipment located outside the cryostat, such as the pumps and flowmeters. The second rack must be well protected from interference sources and is reserved for equipment connecting to wires which lead into the cryostat, such as the resistance bridges for the temperature measurements and the power supplies for the heaters inside the still and the mixing chamber.

### 3. Numerical Simulation of Dilution Refrigerators

#### 3.1 Numerical Thermal Simulation

Numerical thermal simulation is a useful means to simulate the thermal behavior of technical equipment. The following section explains how a dilution refrigerator can be modeled to predict its base temperature and cooling power at different flow rates. Numerical thermal simulation is mandatory for the design of a very large dilution refrigerator as it greatly reduces the risk of serious design flaws. The advantages of numerical simulation over the analytic theory of continuous heat exchangers [48, 99] is the reliable prediction of performance data if

- heat loads are not only applied to the mixing chamber but also to other heat sinks such as the dilute stream,
- the temperature dependence of dilute fluid parameters, which depends on several variables, cannot be replaced by simple analytic approximations,
- materials with different Kapitza resistances are used in the heat exchanger,
- the number of sintered elements is too small to justify the assumption of a continuous heat exchanger,
- viscous heating and axial conduction need to be accounted for correctly,
- thermal penetration in sintered powders needs to be included
- and if transient solutions are required.

A great variety of software for thermal simulation is available on the market. For this work, the “Thermal Analysis Kit (TAK) 2000 Pro V3”<sup>13</sup> has been chosen. TAK 2000 is a text-based simulation program. The thermal model is created with a text editor and then processed by one of the TAK 2000 solvers, which create output files containing the requested results, such as heat fluxes or temperatures.

A TAK 2000 model consists of nodes and conductors which connect the nodes. The two properties of a node are its temperature  $T$  and its thermal mass  $M(T)$ . The thermal mass is defined as

---

<sup>13</sup> K&K Associates (Westminster, Colorado, USA)

$$M(T) = m \cdot c_p(T), \quad [3.1]$$

where  $m$  is the mass of the node and  $c_p(T)$  the specific heat of the material of the node.  $M$  often depends on temperature  $T$ . Nodes with a thermal mass equal to zero are called arithmetic nodes. Boundary nodes have a fixed temperature. They are used to model boundary conditions, such as a boiling  $^4\text{He}$  bath at 4.2 K, for instance.

Conductors can be separated into two groups, linear conductors and radiation conductors. Linear conductors transfer a heat flux which is linearly proportional to the temperature difference of two adjacent nodes:

$$\dot{Q}_{\text{Linear}} = C(T) \cdot (T_1 - T_2). \quad [3.2]$$

Flow conductors are a special type of linear conductors and are used to simulate fluid flow. Their conductance  $C_{\text{Flow}}(T)$  is defined as

$$C_{\text{Flow}}(T) = c_p(T) \cdot \dot{m}, \quad [3.3]$$

where  $\dot{m}$  is the mass flow rate and  $c_p(T)$  the specific heat of the fluid. The specific heat can be modeled to change with temperature. Heat transport in flow conductors is only possible in one direction, which is the direction of the fluid flow, i.e. the conditions of the downstream cannot influence the upstream node.

Radiation conductors can be used to model heat transfer due to radiation. As Kapitza conduction also depends on the fourth power of temperature, radiation conductors are very suitable to model heat transfer between liquid helium and a solid body at low temperatures. The conductance  $C(T)$  of a radiation conductor can be temperature dependent:

$$\dot{Q}_{\text{Radiation}} = C(T) \cdot (T_1^4 - T_2^4). \quad [3.4]$$

Conductors with more exotic properties can be defined by implementing FORTRAN code in the model. This is necessary for sintered silver heat exchangers, where heat transfer grows with  $T^{-3}$ , for instance.

Other elements, such as controlled heaters or constant heat sources can be placed on nodes. Temperature dependent heat sources are used to model the cooling power of the dilution process, for instance.

When the thermal network has been designed and programmed, the actual process of solving the model starts. Two different types of solvers are available, namely steady state solvers and transient solvers. While the transient mode is used to simulate the time dependent behavior of a system, the “steady-state” mode is used to calculate temperatures and heat-fluxes in thermal equilibrium.

Steady state solvers (such as SSITER in TAK 2000) calculate the temperature of a node  $i$  by solving the equation

$$Q_i + \sum_{j \neq i} C_L(i, j) \cdot (T_j - T_i) + \sum_{j \text{ upstream}} C_F(i, j) \cdot (T_j - T_i) + \sigma \cdot \sum_{j \neq i} C_R(i, j) \cdot (T_j^4 - T_i^4) = 0, \quad [3.5]$$

where  $Q_i$  is the heat dissipated inside a node by a source,  $C_L(i, j)$  the conductances of the linear conductors,  $C_F(i, j)$  the conductances of the flow conductors and  $C_R(i, j)$  the conductances of the radiation conductors connecting to node  $i$  [5]. Direct matrix inversion is used to effect the solution. To account for changing matrix coefficients due to temperature dependent material properties and radiative couplings, the solution is obtained iteratively. The forth power dependence of radiative heat transfer is taken care of by linearization.

Square roots of negative numbers might be encountered when iterating the temperature of a node which is connected to both linear and radiation conductors whose numerical values are of the same order of magnitude. This is clearly the case in the heat exchanger of a dilution refrigerator, where radiation conductors are used to model the Kapitza heat transfer between the dilute stream and the concentrated stream. It is thus suggested to use a transient forward differencing solver even for obtaining steady-state solutions by simply calculating transient behavior for a sufficiently long time span, i.e. until the system is in equilibrium. Forward differencing calculates the temperatures for a time step directly and independently. The temperature  $T$  of a node  $i$  for the time level  $n + 1$  is calculated by

$$T_i^{n+1} = T_i^n + \frac{\Delta t}{C_i} \cdot \Phi_i^n, \quad [3.6]$$

where  $\Delta t$  is the time step,  $C_i$  the thermal mass of the node and  $\Phi_i^n$  the total heat flux into node  $i$  at time  $n$  [5]. Due to the large number of time steps necessary to fulfill stability criteria the forward differencing method yields the steady state solution much more slowly than a solver like SSITER does.

The TAK 2000 solver requires that the time step cannot be larger than the minimum time constant of the network. The time constant of each node is calculated by dividing its thermal mass by the sum of all conductances attached to it. TAK 2000 automatically calculates a time step which fulfills this condition. Due to the fact that a dilution refrigerator operates at temperatures rather close to absolute zero, the temperature of a node can sometimes turn out to be negative between two iterations if the time step chosen automatically by the solver is not sufficiently small. In some cases it is thus necessary to specify a maximum allowable time step. A value of 0.0001 s has proven successful for the simulation of dilution refrigerators. Smaller maximum allowable time steps are of course possible, but have a negative effect on the calculation time. The solver continues to iterate the solution for each time step until the maximum temperature change per iteration is smaller than a user specified threshold. For the simulation of the CCDR, a value of  $10^{-10}$  K was used. The temperature change per iteration approaching zero is usually not a sufficiently good condition to guarantee thermal equilibrium. As a consequence, the nodal and system-level energy balance values have to be checked. If these values exceed a few percent, the simulation results might be highly inaccurate. Problems with the rounding of numbers (which is automatically performed by TAK 2000) can be avoided by calculating in units of mK and  $\mu$ W, instead of K and W. The conversion factors for temperatures, thermal masses, conductances and heat loads are given in Table 3.

Element	SI	TAK 2000	Factor
Nodal Temperature	K	mK	$10^3$
Nodal Thermal Mass	$\frac{J}{K}$	$\frac{\mu J}{mK}$	$10^3$
Linear Conductor	$\frac{W}{K}$	$\frac{\mu W}{mK}$	$10^3$
Radiation Conductor	$\frac{W}{K^4}$	$\frac{\mu W}{(mK)^4}$	$10^{-6}$
Heat Source	W	$\mu$ W	$10^6$

**Table 3: Unit conversion factors**

For more details concerning numerical thermal simulation, modeling techniques and the TAK 2000 software, reference is made to [70].

### 3.2 The Numerical Model of a Dilution Refrigerator

The following section is dedicated to the development of a complete thermal model of a dilution refrigerator which can be used to make reliable predictions about the performance of a given design. The model is created step wise, starting with only two nodes, namely the mixing chamber and a second node which represents the inlet of the concentrated stream as shown in Figure 18. From now on, nodes are depicted as circles. Boundary nodes are represented by black dots, and heat sources are marked by the letter Q.

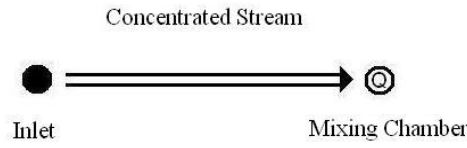


**Figure 18: A simple thermal network of the mixing chamber**

The conductor represents the flow of concentrated solution into the mixing chamber. The corresponding conductance of this flow conductor is calculated as a function of temperature:

$$C_{\text{Flow}}(T) = c_{p,c}(T) \cdot \dot{n}_3. \quad [3.7]$$

The specific heat  $c_{p,c}(T)$  of the concentrated solution is stored in an array. The data has been taken from [60]. TAK 2000 performs linear interpolation between the temperature values. It is thus useful to specify as many data points as possible. For the time being, the inlet node (which is a boundary node) represents the heat exchanger. Its fixed temperature is equal to the outlet temperature of the heat exchanger. A heat source with a negative heating rate has been assigned to the mixing chamber node. This negative heating rate represents the cooling effect of  $^3\text{He}$  atoms passing the phase boundary. The data is again temperature dependent and given in form of a doublet array. The values for the cooling power have been taken from [111].

The results of this very simple simulation are shown in Figure 19. The base temperature of the mixing chamber has been calculated as a function of inlet temperature for the hypothetical case of the external heat load on the mixing chamber equaling zero. The relation is almost perfectly linear; the constant  $T_i/T_m$  obtained by simulation is independent of the flow rate and in good agreement with the theoretical values given by Pobell [109] and Radebaugh [111] and in equation [1.4]



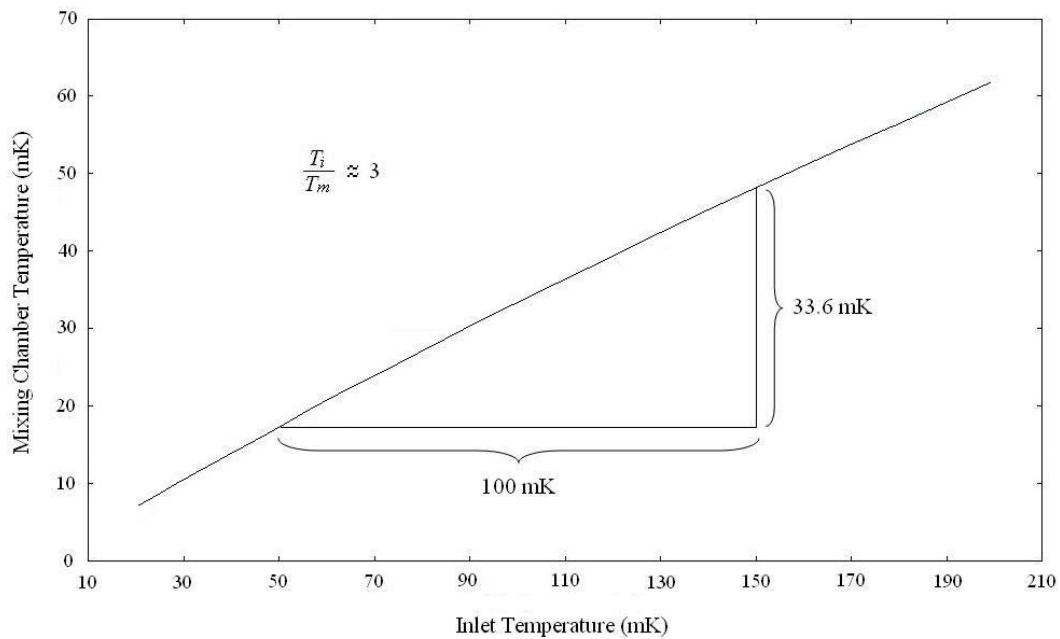


**Figure 19: Simulation results for the mixing chamber temperature as a function of concentrated stream inlet temperature in the case of no external heat load being applied**

The thermal network described above is only of limited use as the inlet temperature, the mixing chamber temperature and the flow rate are related in a real dilution refrigerator. The relation between these values is determined by the performance of the heat exchanger between the still and the mixing chamber. It can thus not be neglected and must be included in the simulation.

The heat exchanger of a dilution refrigerator usually consists of a series of sintered elements. The thermal network of such a sintered element is shown in Figure 20.

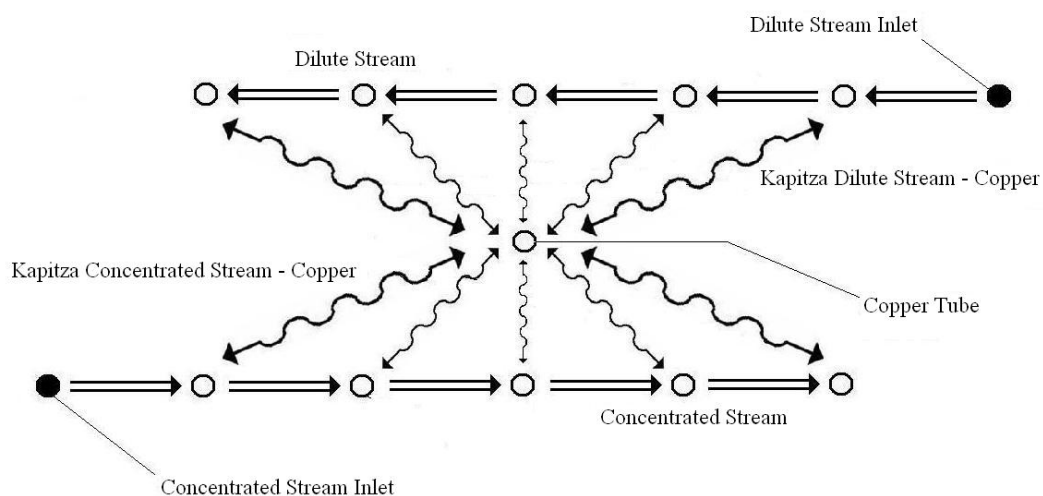


**Figure 20: The thermal network of a single sintered element**

The flow conductors simulating the dilute stream are modeled with the specific heat data for  $^3\text{He}$  in  $^4\text{He}$  given in [111]. The tube to which the metal powder has been sintered is modeled as a single node as the temperature gradient along the tube is small compared to the temperature gradient in the liquids. Kapitza resistance governs the heat transfer between the liquids and the sintered sponge. For sintered copper elements, radiation conductors can be used as the heat transfer grows with  $T^4$ .

One of the differences between ideal, continuous and real heat exchangers is addressed by modeling the copper tube with a single node: The number of discrete elements forming the heat exchanger enters into the calculation. It has to be noted that the temperature dependent efficiency of sintered sponges, which has already been briefly mentioned in section 2.5, is not taken into account by the modeling technique described above. The simulation of this effect is discussed in section 3.6.

The result of an exemplary simulation for a single element and a flow rate of  $250 \mu\text{mol/s}$  is shown in Figure 21. The surface available for heat exchange is  $492 \text{ cm}^2$  in the dilute stream and  $84 \text{ cm}^2$  in the concentrated stream. The Kapitza conductance between the concentrated solution and the sponge amounts to  $S_3 = 20 \text{ W}/(\text{m}^2 \cdot \text{K}^4)$  while the conductance between the dilute solution and the sponge amounts to  $S_4 = 25 \text{ W}/(\text{m}^2 \cdot \text{K}^4)$ .

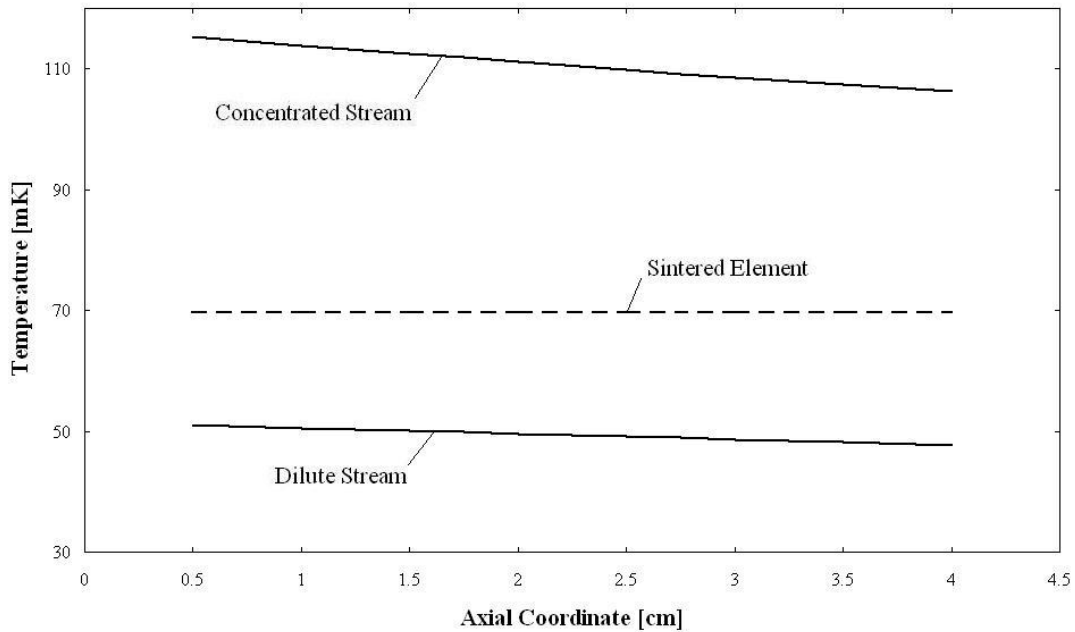


**Figure 21:** Simulation results for the temperature distribution in a single sintered element for a flow rate of  $\dot{n}_3 = 250 \mu\text{mol/s}$

The inlet temperature for the concentrated stream amounts to 115.3 mK, the inlet temperature of the dilute stream to 47.7 mK. These values correspond to the first sintered element in the H/X of the CCDR when a heat load of 10  $\mu$ W is applied to the mixing chamber and the dilution refrigerator is running at optimum flow.

The next step towards a complete thermal network model of a dilution refrigerator is the combination of a few such sintered elements with a tube-in-tube heat exchanger and a node representing the mixing chamber. The corresponding thermal network is shown in Figure 22. The total surface area in the concentrated stream shall amount to 250 cm<sup>2</sup>. A continuous tube-in-tube heat exchanger with a surface area of 18 cm<sup>2</sup> in the concentrated stream precedes the sintered elements. The still temperature has been assumed to be 800 mK, which is fixed by connecting the inlet of the tube-in-tube heat exchanger to a boundary node. Furthermore, an external heat load  $\dot{Q}$  is applied to the mixing chamber. This is effected by placing a second heat source (the first one simulates the cooling power) on the mixing chamber node.

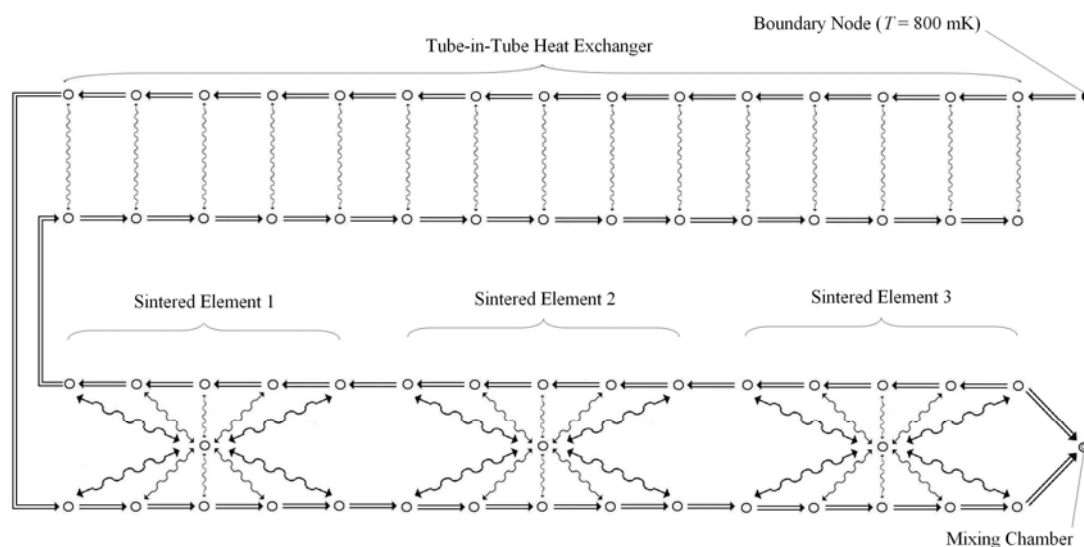


**Figure 22: The thermal network of a dilution refrigerator consisting of three sintered elements**

The dilution refrigerator represented by this thermal network does not exist in reality as it consists of only three sintered elements – in the heat exchanger of the CCDR, twelve such elements have been incorporated. However, the simulation illustrates very well the differences between ideal and real heat exchangers. The numerical modeling technique presented in this chapter allows for these differences.

Figure 23 shows the simulated temperature profiles of the dilute and concentrated streams in the sintered elements at the optimum flow rate of 110  $\mu$ mol/s. The value

for the optimum flow rate is in fairly good agreement with the analytic theory derived by Niinikoski [99]. A comparison is given in Figure 24. The temperature difference arises from the fact that the axial conduction in the sintered elements is not taken into account by the analytic theory. For the sake of completeness, values obtained with Frossati's theory [48] are also shown.

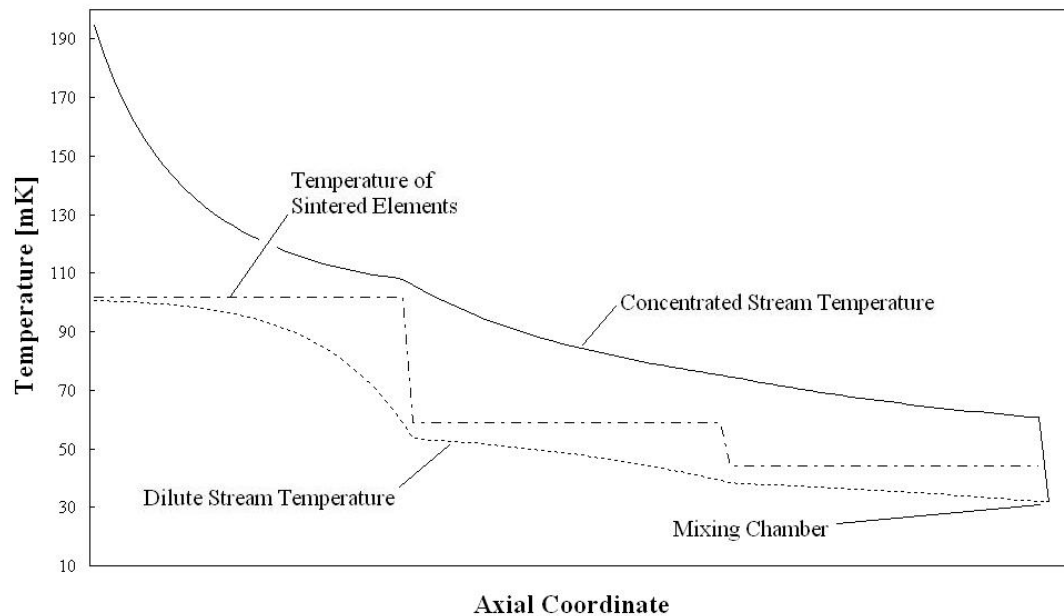


Figure 23: Simulation results for the temperature distribution along the three sintered elements for  $\dot{n}_3 = 110 \mu\text{mol/s}$  and  $\dot{Q} = 5 \mu\text{W}$

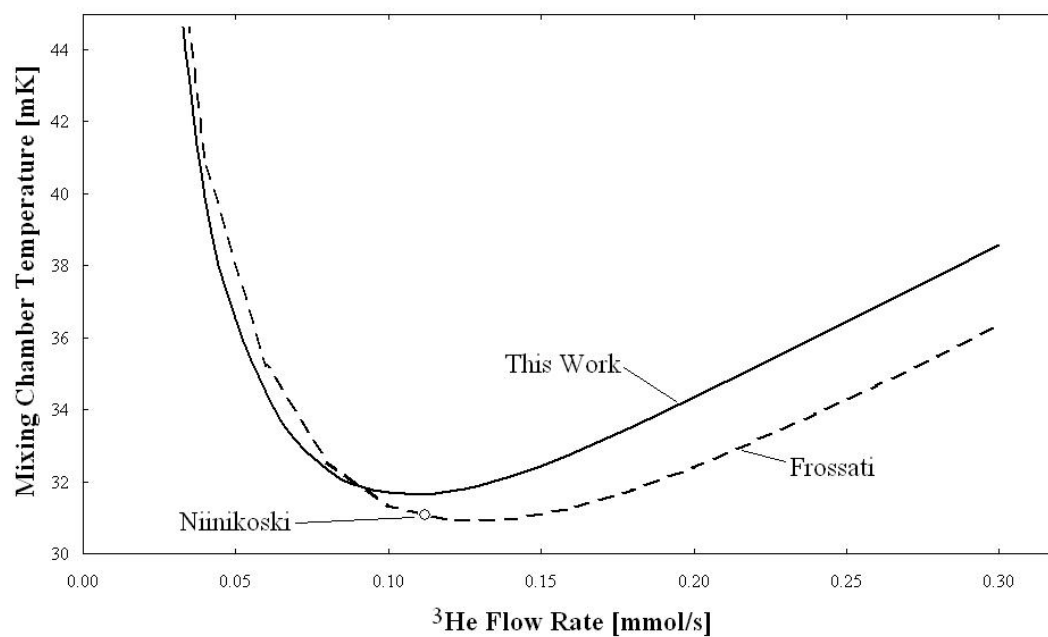


Figure 24: The mixing chamber temperatures yielded by the numerical simulation method, Niinikoski's theory and Frossati's theory for a heat load  $\dot{Q} = 5 \mu\text{W}$

The numerical model can be further improved by modeling effects such as viscous heating, axial conduction, the additional heat load due to the kinetic energy of the incoming  $^3\text{He}$  and the temperature dependent thermal penetration depth in sintered sponges. Viscous heating can be taken care of by placing heat sources on the nodes representing the heat exchanger. The heat dissipated in the nodes of the concentrated stream amounts to

$$\dot{Q}_{\text{ViscousHeating, Conc}} = \Delta p(T) \cdot \dot{V}_3 = \frac{128 \cdot \eta(T) \cdot l}{d^4 \cdot \pi} \cdot \dot{n}_3^2 \cdot V_3^2, \quad [3.8]$$

where  $\eta(T)$  is the viscosity and  $V_3$  the molar volume of the concentrated solution,  $l$  the length of the tube section represented by the node and  $d$  its hydraulic diameter.

In the dilute stream, viscous heating occurs due to the movement of the  $^3\text{He}$  through the superfluid  $^4\text{He}$ . Work on the flow properties of  $^3\text{He}$  in  $^4\text{He}$  has been conducted by Castelijns [23, 24] and Zeegers [140]. If the flow channel is sufficiently large to avoid mutual friction, the mechanical-vacuum approximation can be applied. In this model, the superfluid  $^4\text{He}$  background is treated as a vacuum while the  $^3\text{He}$  component is considered to be in gaseous form at a pressure which is equal to the osmotic pressure. In this case, equation [3.8] also applies to the dilute stream channel. The molar volume of  $^3\text{He}$  in the mixture can be assumed to be constant ( $V_3 = 415 \cdot 10^{-6} \text{ m}^3/\text{mol}$ ) and the viscosity obeys the law  $\eta(T) = \eta_0/T^2$  where  $\eta_0 = 5 \cdot 10^{-8} \text{ Pa} \cdot \text{s} \cdot \text{K}^2$  [140]. Equation [3.8] thus changes to

$$\dot{Q}_{\text{ViscousHeating, Dil}} = \frac{128 \cdot \eta_0 \cdot l}{T^2 \cdot d^4 \cdot \pi} \cdot \dot{n}_3^2 \cdot V_3^2. \quad [3.9]$$

Axial conduction in the liquids and the tube may be accounted for by modifying the arrays for the flow conductors. This modeling technique is only valid if heat transfer due to axial conduction is smaller than heat transport due to fluid flow, which will always be the case in a properly functioning dilution refrigerator. Data on the thermal conductivity of  $^3\text{He}$  is given in [1] and [33], and on the thermal conductivity of dilute  $^3\text{He}/^4\text{He}$  solutions in [1].

Viscous heating and axial conduction can be rendered negligible by carefully designing the dilute and concentrated flow channels. The thermal model of the CDDR presented in the following section takes these effects into account, however. This further enhances the accuracy of the simulation results.

### 3.3 The Numerical Model of the CCDR

In the following, the thermal model for the CERN Cryolab Dilution Refrigerator will be established. The model is based on the design described in chapter 2 of this thesis. The relevant design data is summarized in Table 4.

Straight Tube-in-Tube H/X			
Concentrated Stream Tube	Length	mm	500
	$D$	mm	0.65
	$s$	mm	0.175
	Material	N/A	CuNi
	Kapitza Conductance	$W/(m^2 \cdot K^4)$	67
Dilute Stream	Length	mm	500
	Inner Tube Diameter	mm	6
	Cross Section (Annular)	$mm^2$	27.5
	Material	N/A	Brass
Coiled Tube-in-Tube H/X			
Concentrated Stream Tube	Length	mm	1200
	$d$	mm	0.65
	$s$	mm	0.175
	Material	N/A	CuNi
	Kapitza Conductance	$W/(m^2 \cdot K^4)$	67
Dilute Stream	Length	mm	700
	Inner Tube Diameter	mm	6
	Cross Section (Annular)	$mm^2$	27.5
	Material	N/A	Brass
Sintered Heat Exchanger Elements (short)			
Amount		[1]	3
Material		N/A	Cu
Surface Area Concentrated Stream		$cm^2$	84
Kapitza Conductance in Concentrated Stream		$W/(m^2 \cdot K^4)$	20
Length		mm	40
Surface Area Dilute Stream		$cm^2$	492
Kapitza Conductance in Dilute Stream		$W/(m^2 \cdot K^4)$	25
Sintered Heat Exchanger Elements (long)			
Amount		[1]	9
Material		N/A	Cu
Surface Area Concentrated Stream		$cm^2$	167
Kapitza Conductance in Concentrated Stream		$W/(m^2 \cdot K^4)$	20
Length		mm	80
Surface Area Dilute Stream		$cm^2$	983
Kapitza Conductance in Dilute Stream		$W/(m^2 \cdot K^4)$	25
Sintered Heat Exchanger (Dilute Stream)			
Inner Diameter		mm	8
Cross Section (Annular)		$mm^2$	26.5

Table 4: CCDR design data used for the development of the thermal model

The  $^3\text{He}$  flow rate, the still temperature, the heat load on the mixing chamber and the efficiency of the sintered heat exchanger are input parameters. The following effects are taken into account by the model:

- Finite number of sintered elements
- Accurate values for material properties of  $^3\text{He}$  and dilute solution over the whole temperature range below 0.9 K
- Varying Kapitza conductance along the heat exchanger:  $67 \text{ W}/(\text{m}^2 \cdot \text{K}^4)$  between  $^3\text{He}$  and CuNi,  $20 \text{ W}/(\text{m}^2 \cdot \text{K}^4)$  between  $^3\text{He}$  and Cu
- Viscous heating of the concentrated and dilute streams
- Axial conduction in the helium liquids

The TAK 2000 code listing for the model of the CCDR is given in Appendix A. It has been used to obtain the results presented in the following two sections.

### ***3.4 Comparison of Steady State Simulations with Experimental Results***

The steady state behavior of the CCDR has been measured in the range of 0.2 mmol/s to 3 mmol/s for several different cooling powers. The resulting points, i.e. the mixing chamber temperatures for certain  $^3\text{He}$  flow rates, are displayed below for cooling powers of 500, 250, 100, 50 and 10  $\mu\text{W}$ . These rather high heating powers have been chosen to assure that the applied heat load is large compared to the residual one.

Error bars have been added to the measured points to indicate the magnitude of measurement uncertainties. The largest error originates from the  $^3\text{He}$  mass flow meter which is calibrated to  $\pm 1\%$  FS. The  $^4\text{He}$  contamination, which is certainly present, is however not taken into account in this way. It is thus suggested to perform future cold runs with a mass spectrometer connected to the  $^3\text{He}$  pump line to evaluate the true  $^3\text{He}$  flow rate. Uncertainties in the temperature measurement do not amount to more than  $\pm 0.27 \text{ mK}$ . The thermometer was only calibrated to 42 mK, and temperatures lower than that have been evaluated by extrapolating the  $R(T)$  characteristic of the resistor. The accuracy of this approach is not known.

The results from the numerical simulations are given as solid lines. They agree well with the measured values if the ratio between the effective and the geometric surface of the heat exchanger (i.e. the heat exchanger efficiency) is chosen suitably.

At low flow rates the measured values are offset from the calculated ones to the right. This is attributed to a  $^4\text{He}$  contamination of up to 20 %, which enters into the measurement of the flow rate but does not contribute to the cooling process.

The  $^4\text{He}$  contamination in the  $^3\text{He}$  circuit is also thought to be the cause of the observed scattering of the measured points. The  $^4\text{He}$  contamination is most likely not constant as the temperature of the film burner depends on the variation of the liquid level in the atmospheric  $^4\text{He}$  bath. If the level is low, the heat load to the film burner is higher. Measurements of the  $^4\text{He}$  contamination with a mass spectrometer have already been suggested above and may help to understand these phenomena.

The fact that the efficiency of the sintered heat exchanger has to be adjusted by the user is certainly not satisfying from an engineering point of view. The laws of heat transfer in sintered sponges should thus be addressed in future studies. A first effort is undertaken in section 3.6. It will be shown that the results reflect the behavior of sintered sponges qualitatively but are not sufficiently accurate to reproduce the curves in Figure 25 through Figure 29.

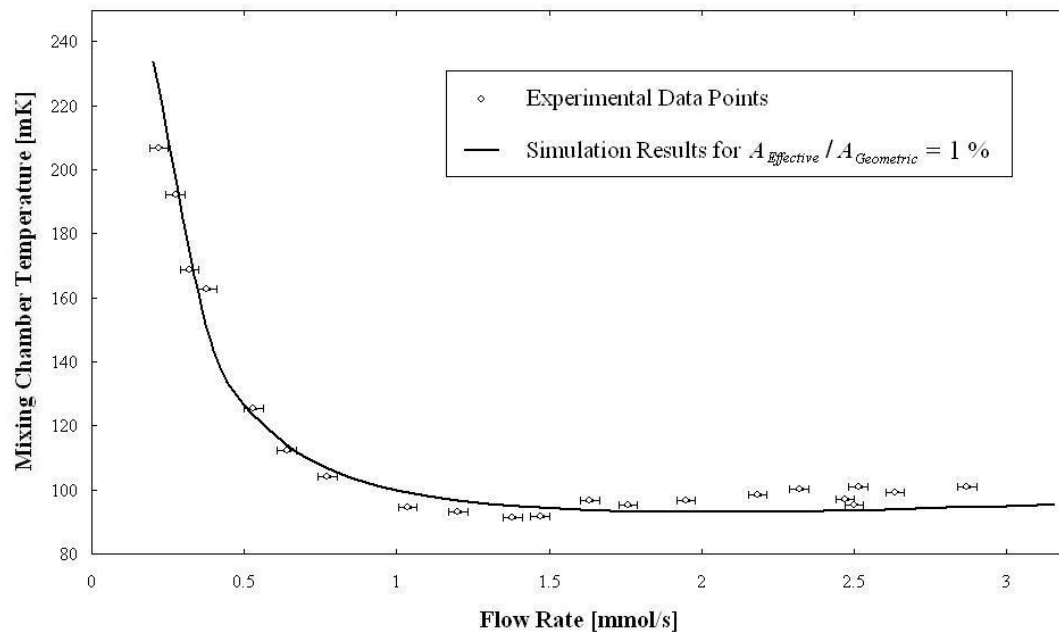


**Figure 25:** Comparison between simulation results and experimental data for the dependence of the mixing chamber temperature on the  $^3\text{He}$  flow rate at a cooling power of 500  $\mu\text{W}$



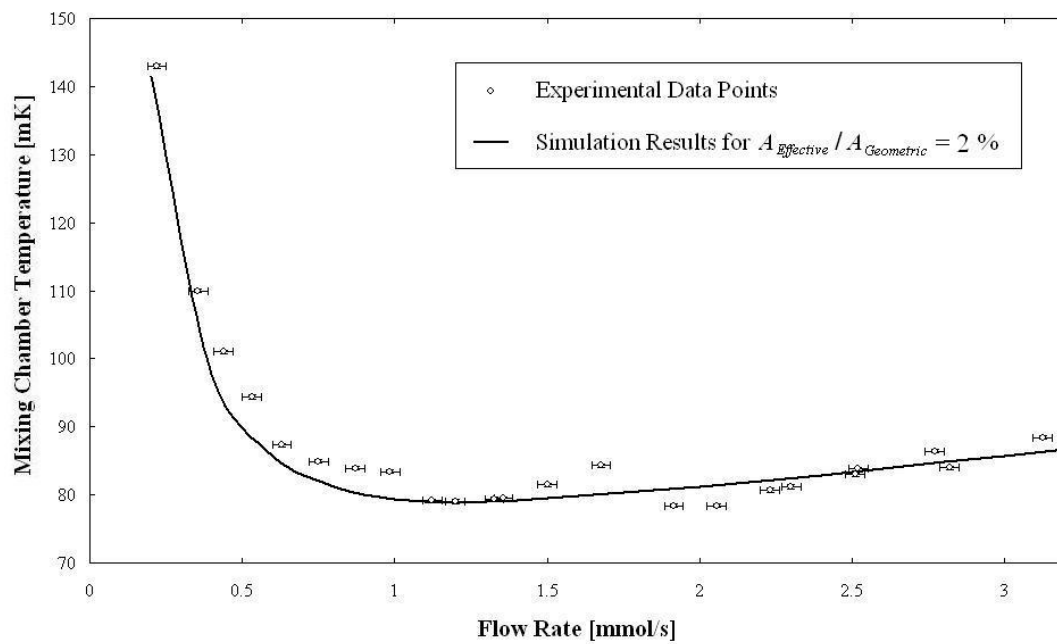


Figure 26: Comparison between simulation results and experimental data for the dependence of the mixing chamber temperature on the  $^3\text{He}$  flow rate at a cooling power of  $250\ \mu\text{W}$

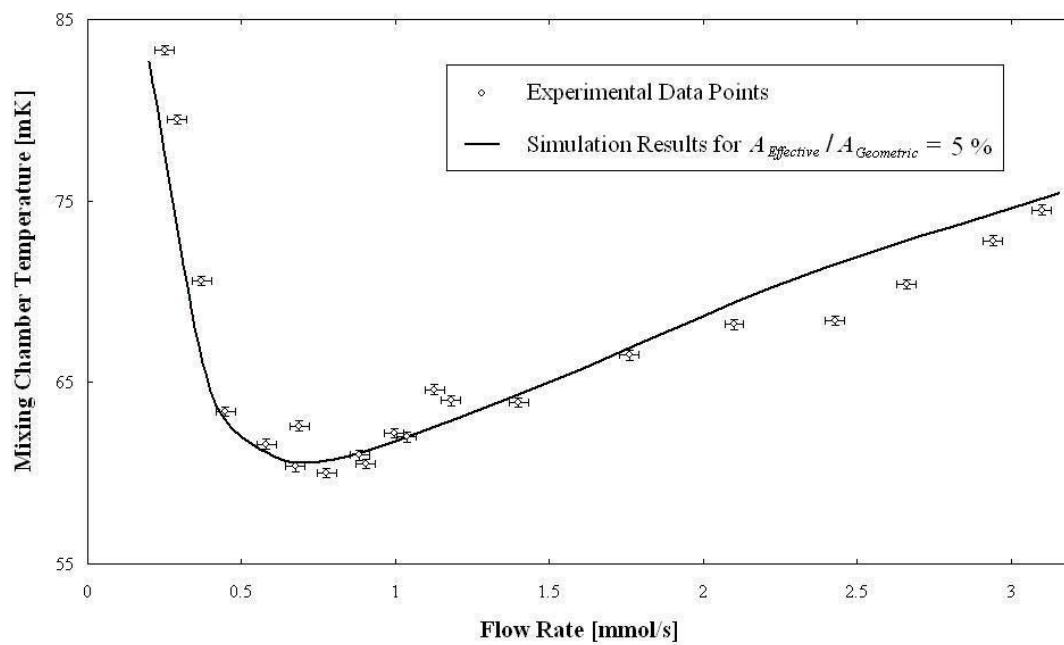


Figure 27: Comparison between simulation results and experimental data for the dependence of the mixing chamber temperature on the  $^3\text{He}$  flow rate at a cooling power of  $100\ \mu\text{W}$

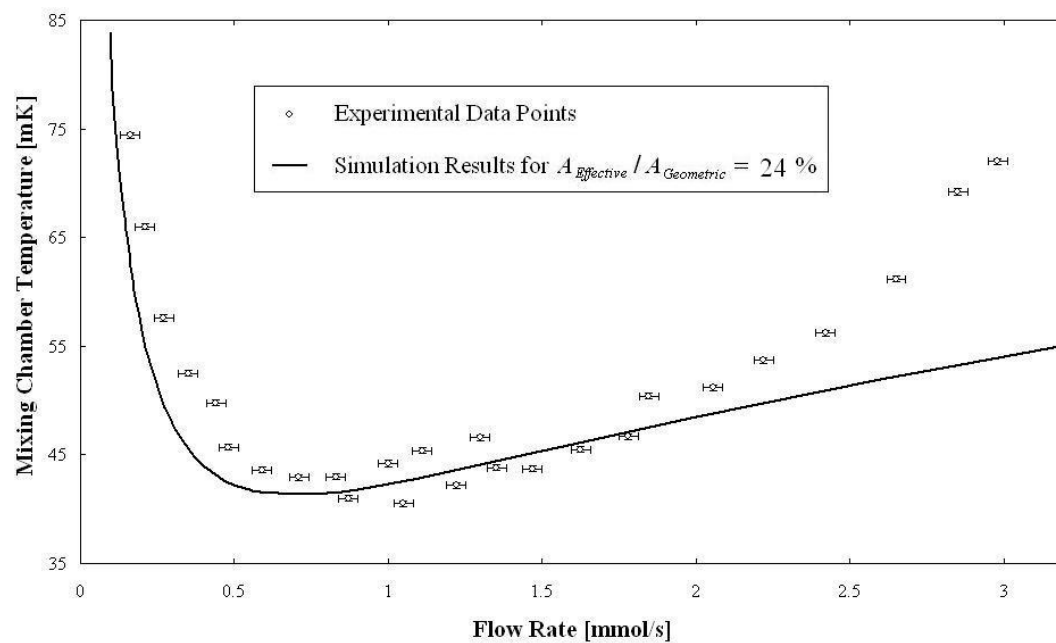


Figure 28: Comparison between simulation results and experimental data for the dependence of the mixing chamber temperature on the  $^3\text{He}$  flow rate at a cooling power of 50  $\mu$ W

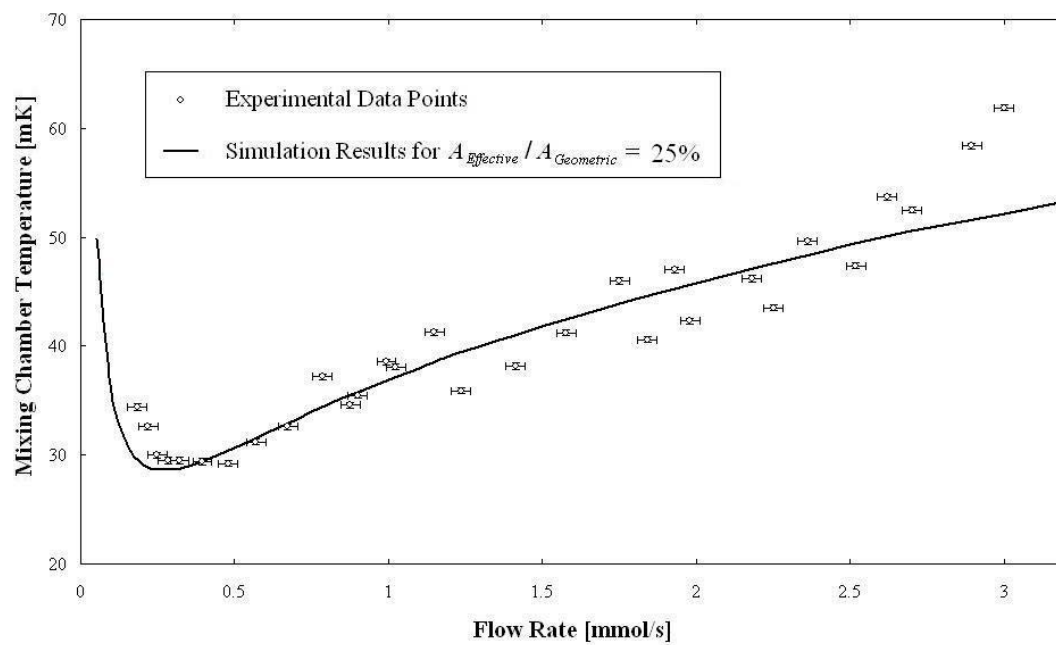
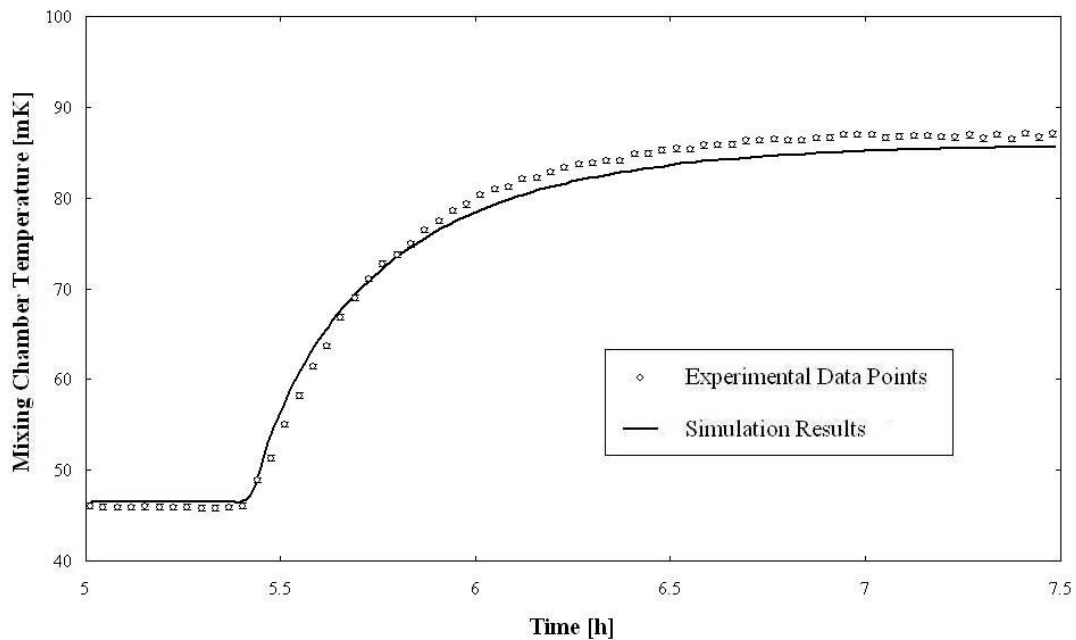


Figure 29: Comparison between simulation results and experimental data for the dependence of the mixing chamber temperature on the  $^3\text{He}$  flow rate at a cooling power of 10  $\mu$ W

### 3.5 Comparison of Transient Simulations with Experimental Results

The transient behavior can easily be simulated by the thermal model described above if thermal masses are assigned to the nodes. At low temperature, the specific heat of the solids can be neglected. Figure 30 and Figure 31 compare the results of a transient simulation with experimental results. The heat load on the mixing chamber was increased from 50  $\mu\text{W}$  to 250  $\mu\text{W}$  at a flow rate of 1.7 mmol/s. After the dilution refrigerator had achieved thermal equilibrium, the measurement was repeated with a heat load jump from 250  $\mu\text{W}$  to 50  $\mu\text{W}$ .

The simulation (represented by the solid line) is in good agreement with the measured points. The mixing chamber contains some 3.8 mol of liquid  $^3\text{He}$ , most of it in the form of concentrated solution. The data on the specific heat of  $^3\text{He}$  was taken from [60], the data on the specific heat of the dilute solution from [111]. To account for the fact that the efficiency of the sintered heat exchanger cannot be assumed to be constant for all mixing chamber temperatures it was varied linearly between the start and end temperature.



**Figure 30: Comparison between simulation results and experimental data for the transient response of the mixing chamber temperature to a step in heating power from 50 to 250  $\mu\text{W}$**

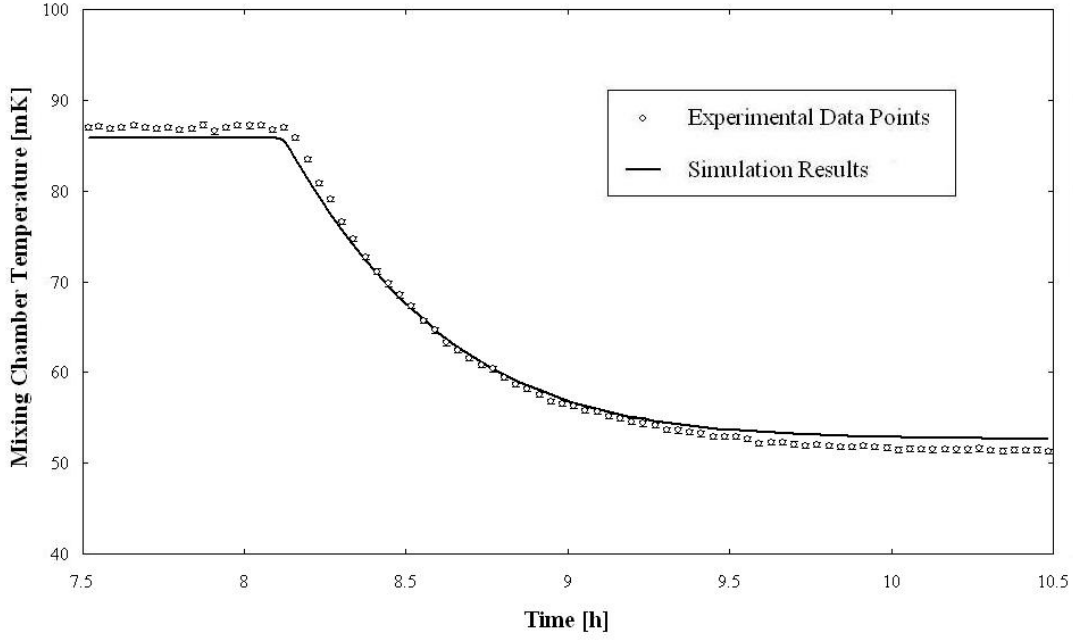


Figure 31: Comparison between simulation results and experimental data for the transient response of the mixing chamber temperature to a step in heating power from 250 to 50  $\mu\text{W}$

### 3.6 The Efficiency of Sintered Sponges

The temperature dependent efficiency of sintered sponges has already been mentioned several times in this thesis. The efficiency  $\varepsilon$  of a heat exchanger is defined as the ratio between the actual and the ideal energy transfer [14]. The ideal energy transfer can be calculated from equation [1.8] from the sponge temperature  $T_{\text{Solid}}$  and the temperature  $T_{\text{Liquid}}$  of the bulk liquid at the free surface of the sponge.

$$\varepsilon(T) = \frac{\text{Actual Energy Transfer}}{\text{Ideal Energy Transfer}} = \frac{\dot{Q}_{\text{Actual}}(T)}{A \cdot S \cdot \left( T_{\text{Solid}}^4 - T_{\text{Liquid}}^4 \right)}, \quad [3.10]$$

where  $A$  is the surface area of the sponge and  $S$  the Kapitza conductance. The data presented in section 3.4 illustrates well the phenomenon that the efficiency varies with temperature: sintered sponges become more effective heat exchangers with decreasing temperature. The temperature dependence is a geometric effect and depends on the thickness of the sponge which is proportional to the depth of the sintered pores. Furthermore, the efficiency is influenced by the cross-section of the pores, which is mainly influenced by the grain size  $d_e$  of the powder used for sintering.

A simplified model of a sintered sponge is shown in Figure 32. Liquid  $^3\text{He}$  or dilute solution fills the pores of the sintered sponge. This liquid is not in motion, and the heat transport is only due to conduction. The total cross section of this conduction path is proportional to the free surface  $A_{\text{Free}}$  of the sponge and to  $(1-\psi)$ , where  $\psi$  is the filling factor of the powder:

$$A_{\text{CrossSection}} = A_{\text{Free}} \cdot (1 - \psi). \quad [3.11]$$

The length of the conduction path is proportional to the thickness of the sintered layer. It is likely that the conduction path length is considerably larger than the sponge thickness, as the axis of the pore cannot be assumed to be completely straight and orthogonal to the free surface of the sponge.

The thermal conductivity of the He liquids at very low temperatures is considerably lower than the thermal conductivity of metals. As a consequence, a temperature gradient develops along the axial coordinate  $x$  of the pore. The temperature  $T_S$  of the sponge may be assumed to be constant in a first approximation.

Inside the pores, heat is exchanged between the walls and the liquid. As heat transfer between the liquid and the sponge is driven by  $T_{\text{Liq}}(x)^4 - T_S^4$ , more heat is passed from the liquid to the solid close to the entrance of the pores, where the temperature difference is large, than at their bottom, where the temperature difference is small.

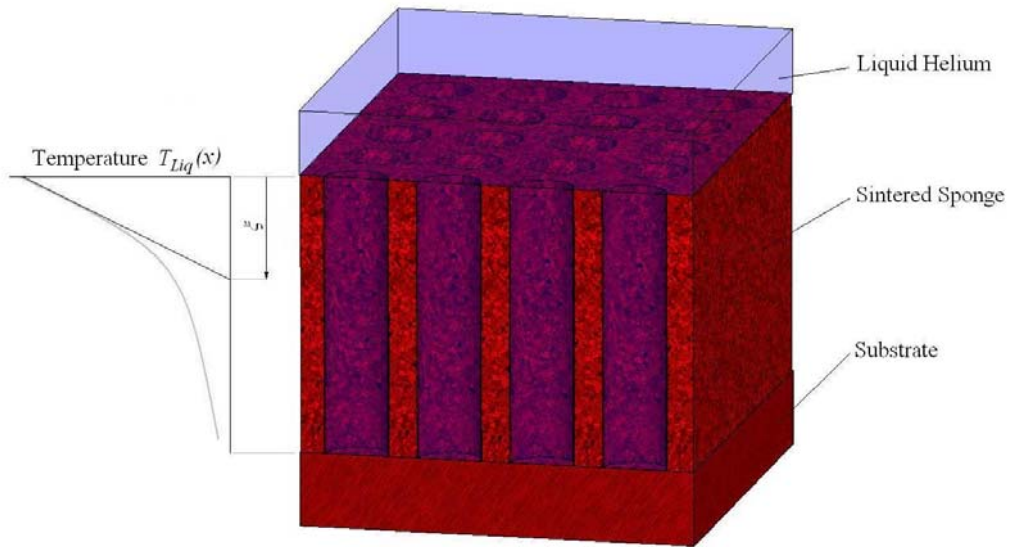


**Figure 32: A simplified model of a sintered sponge explains the geometric effect influencing the heat transfer between liquid He and sintered metals**

The characteristic pore depth for efficient heat exchange is called thermal penetration depth  $\xi$ . The concept of the thermal penetration depth has first been put forward by Das and was later refined by Krusius et al. [81] and Niinikoski, who derived a formula for  $\xi$ , which depends on the temperature  $T$  and the properties of the sponge:

$$\xi(T) = \sqrt{\frac{d_e(1-\psi)}{6\psi} \cdot \frac{\lambda(T)}{4 \cdot S \cdot T^3}}, \quad [3.12]$$

where  $\lambda(T)$  is the thermal conductivity of the liquid,  $S$  the Kapitza conductance,  $d_e$  the grain diameter and  $\psi$  the powder's filling factor. For the copper powder used in the CCDR, for instance, the thermal penetration depth in the concentrated stream amounts to 0.4 mm at 200 mK, to 1.25 mm at 100 mK, to 4.2 mm at 50 mK and to 23 mm at 20 mK. It becomes clear from these numbers that thick sintered layers should only be used close to the mixing chamber in the cold parts of the heat exchanger.

A numerical model can be established to evaluate a sintered sponge's efficiency as defined in [3.10]. The thermal network is outlined in Figure 33. As a first step, the thermal conductivity of the sintered grains is assumed to be equal to the thermal conductivity of bulk copper.

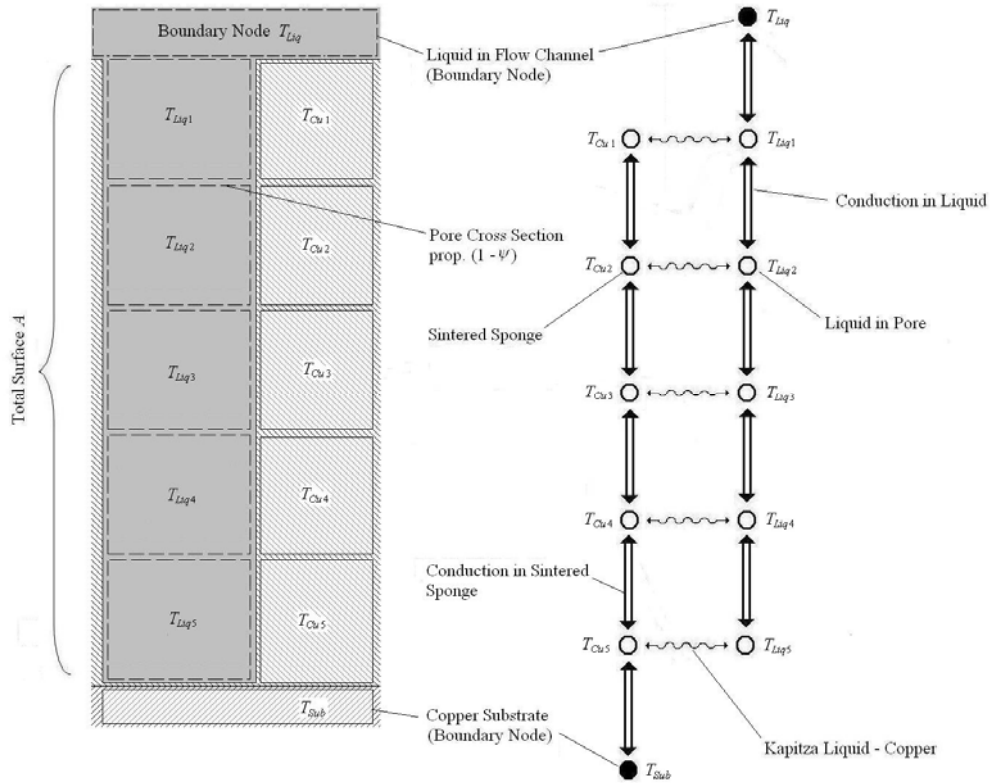


Figure 33: Thermal network for the determination of the efficiency of sintered sponges

The result yielded by this thermal model is a table which states the efficiency of a sintered sponge as a function of the temperatures of the sponge and the liquid. Table 5 and Table 6 show such results for sponges which have been sintered from copper powder with a grain size of 18  $\mu\text{m}$  and a filling factor of  $\psi = 0.4$ . The thickness of the sponges is 0.7 mm and 1.0 mm respectively.

Liquid Temperature	Sponge Temperature [mK]								
	20	30	40	50	60	70	80	90	100
40	0.978	0.977							
50	0.947	0.947	0.946						
60	0.896	0.896	0.895	0.893					
70	0.828	0.828	0.826	0.824	0.819				
80	0.742	0.742	0.740	0.737	0.730	0.720			
90	0.702	0.702	0.702	0.701	0.700	0.700	0.698		
100	0.691	0.691	0.690	0.690	0.689	0.688	0.686	0.686	
110	0.656	0.656	0.655	0.654	0.653	0.650	0.646	0.641	0.632
120	0.607	0.607	0.606	0.605	0.603	0.600	0.596	0.591	0.584
130	0.558	0.558	0.557	0.557	0.555	0.552	0.549	0.545	0.538
140	0.513	0.513	0.513	0.512	0.510	0.508	0.505	0.501	0.496
150	0.472	0.472	0.471	0.470	0.469	0.467	0.465	0.462	0.457
160	0.434	0.434	0.433	0.433	0.432	0.430	0.428	0.425	0.421

**Table 5: Calculated heat exchange efficiency between liquid  $^3\text{He}$  and a sintered copper sponge with a thickness 0.7 mm**

Liquid Temperature	Sponge Temperature [mK]								
	40	50	60	70	80	90	100	110	130
10	0.997	0.997	0.996	0.995	0.994	0.998	0.998	0.998	0.997
20	0.996	0.996	0.995	0.994	0.992	0.997	0.997	0.997	0.996
30	0.988	0.991	0.992	0.991	0.991	0.995	0.995	0.995	0.994
40		0.985	0.988	0.988	0.988	0.992	0.993	0.993	0.992
50			0.980	0.984	0.984	0.989	0.990	0.990	0.989
60				0.976	0.979	0.985	0.986	0.986	0.986
70					0.972	0.980	0.981	0.982	0.982
80						0.972	0.976	0.977	0.977
90							0.967	0.970	0.971
100								0.961	0.964
110									0.957
120									0.948

**Table 6: Calculated heat exchange efficiency between dilute solution and a sintered copper sponge with a thickness of 1.0 mm**

Such tables may be included in a thermal model of a dilution refrigerator. When this was tried for the CCDR, qualitative agreement between simulation and measurements could be achieved; the results were, however, not accurate enough for quantitative performance predictions.

Due to these discrepancies, more work on the heat exchange properties of sintered metals is necessary. In view of the large uncertainties inherent to the geometry of sintered sponges and of the unknown influence of sintering parameters, it seems desirable to address this question experimentally and perform measurements on the heat transfer between liquid helium and sintered samples of varying thickness at different temperatures and heat fluxes. Such work will be presented in [22].

If numerical simulation is to be used for the performance prediction of sintered sponges, the following effects may explain the observed deviations between simulation and experiment:

- The pore diameter may be smaller than the phonon wavelength and thus limit the conduction in the liquid filling the pore. It may thus be inappropriate to use the thermal conductivity data of bulk liquid.
- The thermal conductivity data of bulk copper, which has been used in the simulations, cannot be applied to sintered sponges.
- The thermal resistance of the interface between the sintered powder and the substrate may limit the heat transfer. This effect has not been taken into account in the present simulation.
- The actual pore depth may be much larger than the thickness of the sintered sponge. In fact, it seems very unlikely that the pores extend into the sponge straightly and orthogonally to the free surface.
- Other effects, such as the decrease of the boundary resistance due to the dominant phonon wavelength being comparable with the size of the solid [65], may also play a role and should be included in future models.

Similar calculations have been performed for the heat transfer between dilute solution and sintered silver sponges by Cousins et al. [31, 32]. They estimated that the pore depth exceeds the thickness of the sponge by a factor  $f = 3$ . Furthermore, they modified the data for the conductivity of the dilute solution to account for the fact that conduction is dominated by the  $^3\text{He}$  quasiparticle contribution. With these assumptions, they obtained results which are in good agreement with their experimental values.



## 4. Residual Heat Loads in Very Low Temperature Systems

The residual heat load is the remaining energy flux which is absorbed by a cooling system such as a dilution refrigerator in steady state when all external sources of heat are removed. This chapter takes a first step towards a complete, systematic and quantitative assessment of residual heat sources and may serve as a guideline for the prediction of residual heat loads in large cold masses. It starts with a description of the measurement of the residual heat load on the mixing chamber of the CCDR und continues with a detailed description of potential sources of residual heat.

### 4.1 Measurements of the Residual Heat Load on the CCDR

The residual heat load on the mixing chamber can be evaluated by measuring the base temperature of the dilution refrigerator and using this value along with the surface area  $A$  of the heat exchanger and the Kapitza conductance  $S$  in equation [1.12], if the refrigerator is operated at optimum flow conditions. Experimentally obtained values for the cooling power of the CCDR as a function of mixing chamber temperature are shown in Figure 34 below. The solid line shows the performance of a dilution refrigerator as given by equation [1.12]. The surface area in the concentrated stream was fitted to experimental data and amounts to  $A = 440 \text{ cm}^2$ . The Kapitza conductance  $S$  is assumed to amount to  $16.5 \text{ W}/(\text{m}^2 \cdot \text{K}^4)$ .

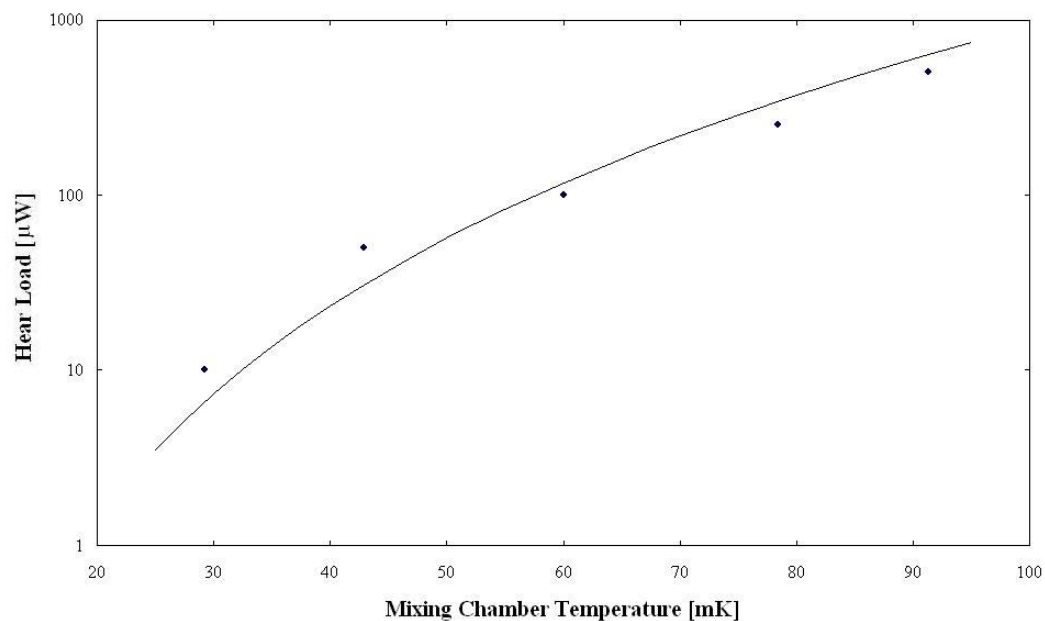


Figure 34: Experimental data points and the theoretical function for  $A = 440 \text{ cm}^2$  of the mixing chamber temperature vs. heat load for optimum flow

It has already been mentioned that the effective surface area of a sintered heat exchanger depends on temperature. This effect is responsible for the experimentally determined cooling power being lower than the theoretical value obtained from equation [1.12] at high temperatures. An equation using a constant surface area cannot yield accurate results over a large temperature range.

After a few weeks of operation, the dilution refrigerator's base temperature of  $(9.85 \pm 0.27)$  mK is achieved at the minimum  $^3\text{He}$  flow rate of  $(41.0 \pm 7)$   $\mu\text{mol/s}$ . As already mentioned above, this base temperature is limited by the accessible flow rate range and not by the heat load on the mixing chamber. As a consequence, the base temperature is not achieved at optimum flow and equation [1.12] must not be applied.

The numerical simulation method described in chapter 3 does allow for the calculation of such non-optimum conditions, however. Uncertainties arise from the fact that the surface area of the heat exchanger is not exactly known and from errors in the temperature and flow rate measurements. It is assumed that the effective surface area of the heat exchanger given in section 2.5 is correct within  $\pm 10\%$ .

Figure 35 shows the mixing chamber temperature  $T_m$  as a function of heat load  $\dot{Q}$  for various combinations of different flow rates and heat exchanger surface areas:

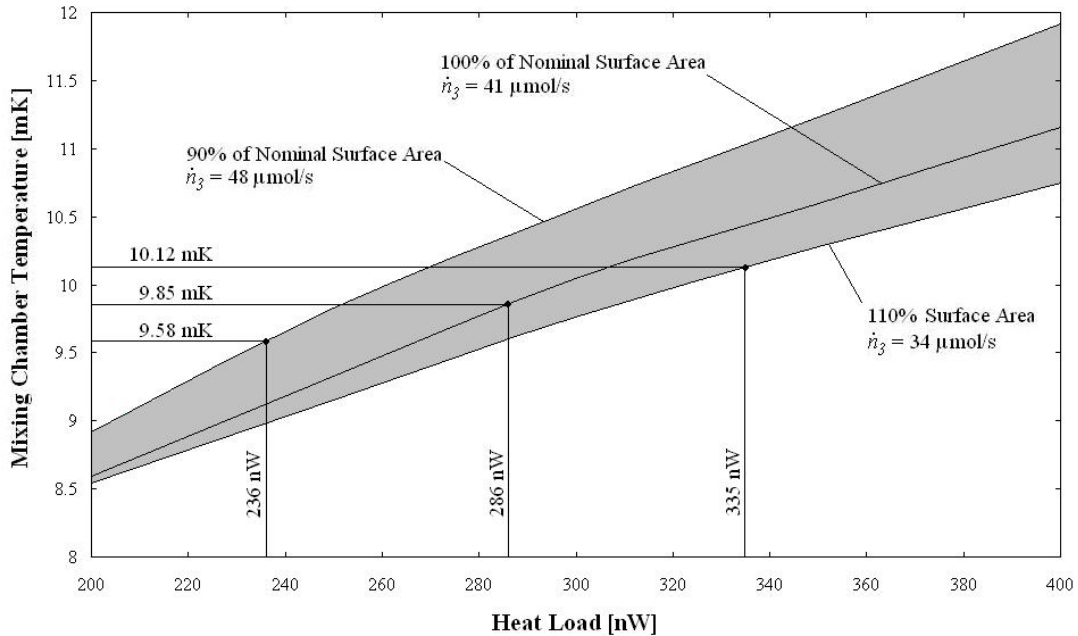


**Figure 35: Mixing chamber temperature vs. heat load for all possible combinations of flow rates between 34.0 and 48.0  $\mu\text{mol/s}$  and for heat exchange surface areas between 1575 and 1925  $\text{cm}^2$**

The grey region accommodates all possible combinations of flow and heat exchanger surface area between the thresholds defined by the uncertainties in the measurements. Figure 35 can be used to determine the heat load on the CCDR. It amounts to 286 nW after some five weeks of operation. With the uncertainties mentioned above, a lower threshold of 236 nW and an upper threshold of 335 nW can be determined. For the calculations in this chapter, the most conservative value of 335 nW will be used.

A more thorough determination of the residual heat load can be achieved by better characterizing the performance of the CCDR. This was not possible in the framework of this thesis project, as the electromagnetic interferences created by the power supply of the mixing chamber heater strongly deteriorated the temperature measurements in the mK range. These improved measurements of the residual heat load will be addressed in [22].

#### 4.1 Thermal Conduction

Thermal conduction is probably the most evident source of heat transfer to the cold parts of a very low temperature (VLT) system, even though it only amounts to a small fraction of the total heat load in a good design. The conducted heat load  $\dot{Q}$  can be easily calculated with thermal conductivity integrals  $\theta(T)$ , which take into account the temperature dependent – and thus varying – thermal conductivity along a conduction path with uniform cross-section  $A$  along its length  $l$  between the temperature  $T_1$  and the temperature  $T_2$ :

$$\dot{Q} = \frac{A}{l} \cdot [\theta(T_1) - \theta(T_2)]. \quad [4.1]$$

The thermal conductivity  $\lambda$  of many standard construction materials is experimentally known and at low temperatures often obeys a law of the following form:

$$\lambda = A \cdot (T^B), \quad [4.2]$$

where  $A$  and  $B$  are empirical constants. Values for  $A$  and  $B$  are thus determined from experimental data and are given in Table 7 for some important materials. The unit of  $T$  is K and the thermal conductivity is given in W/(K·m).

Material	A	B	Validity	Ref
Pure Copper (Impurities < 10 ppm)	1333	1	200 mK < $T$ < 600 mK	[41]
CuNi 45/55	0.065	1.1	50 mK < $T$ < 2 K	[104]
CuNi 70/30	0.093	1.23	300 mK < $T$ < 4 K	[44]
Vespel	0.0017	1.85	50 mK < $T$ < 2 K	[104]
NbTi (superconducting)	0.015	2	50 mK < $T$ < 2 K	[104]
Stainless Steel	0.145	1	100 mK < $T$ < 1 K	[61]
Nickel	32.0	1.29	4 K < $T$ < 10 K	[68]

**Table 7: The empirical constants in equation [4.2] for the thermal conductivity of standard construction materials**

It seems safe to extrapolate the values in Table 7 to temperatures in the range of a few mK. Thermal conductivity integrals can easily be obtained from relation [4.3]:

$$\theta(T_i) = \int_0^{T_i} \lambda(T) \cdot dT = A \cdot \frac{T_i^{B+1}}{B+1}. \quad [4.3]$$

The thermal conductivity  $\lambda$  and the electrical resistivity  $\rho$  of fairly pure non-magnetic metals are closely related to the flow of free electrons and are influenced by the same scattering processes. The Wiedemann-Franz law gives the relation between the two:

$$\lambda \cdot \rho = L_0 \cdot T, \quad [4.4]$$

where  $T$  is the temperature and  $L_0$  the Lorentz number. The resistivity of a material can easily be measured at room temperature and at low temperatures. The residual resistivity ratio (RRR) is defined as the ratio of the specific resistance at 300 K and at 4.2 K:

$$\text{RRR} = \frac{\rho_{300K}}{\rho_{4.2K}}. \quad [4.5]$$

The residual resistivity ratio is available for a great many construction materials as it commonly serves as a measure for the purity of a material. The Wiedemann-Franz law yields a linear temperature dependence for  $\lambda$  in the temperature range where RRR is reached. The calculated values for the thermal conductivity are usually higher than experimental data. The difference sometimes amounts to one order of magnitude at low temperatures [109]. Due to this, and to the fact that the impurity of a sample - which is not always well known - governs the thermal conductivity at low temperatures, experimental values should be used for design calculations whenever

possible. The heat load conducted along support structures can be reduced by choosing materials with low thermal conductivity, minimizing the cross-section of the structure, maximizing its length and by good heat sinking.

In addition to conduction in solids, heat can be transported through substances which have condensed on the surface of a solid body. A prominent example is the film of superfluid  $^4\text{He}$  which may cover the surfaces in a cryostat, especially if  $^4\text{He}$  is used as an exchange gas. Heat transport in  $^4\text{He}$  films at temperatures below the Lambda point is linked to the motion of the superfluid component. Kosterlitz and Thouless [76] found that vortices are key to understanding transitions between the superfluid and the normalfluid state in such two dimensional systems. Their theory predicts that above a critical temperature  $T_C$  free vortices exist, which drive the film into its normalfluid state and greatly decrease its thermal conductivity.  $T_C$  depends on the film thickness  $d$  in terms of atomic layers:

$$T_C = T_\lambda \cdot (1 - A \cdot d^{-\gamma}), \quad [4.6]$$

where  $T_\lambda$  amounts to 2.17 K,  $\gamma = 1.4$  and  $A = 1.6$  [92].  $^4\text{He}$  films in the vacuum space of a cryostat are unsaturated; their thickness  $d$  is given by

$$d = \left( \frac{\alpha}{k_B T \cdot \ln(p/p_{sat})} \right)^{1/3}, \quad [4.7]$$

where  $T$  is the film temperature,  $p$  the actual pressure,  $p_{sat}$  the saturation pressure of helium at temperature  $T$  and  $\alpha/k_B$  the van der Waals constant, which amounts to 27 if  $d$  is measured in terms of atomic layers and  $T$  in K [109].

Above  $T_C$ , Ratnam and Mochel [114] measured a film conductivity of 2130 W/(m·K) at 1.3 K and 2500 W/(m·K) at 1.4 K. In the low temperature regime above  $T_C$ , the conductivity slowly increases linearly with temperature. Below  $T_C$ , the conductivity rapidly increases by more than three orders of magnitude; films were measured to support heat fluxes of at least 1 W/cm<sup>2</sup>.

If a mobile film exists in a VLT apparatus such as a dilution refrigerator, its performance will be seriously impaired. The film creeps to the warmer regions of the machine where it evaporates. The vapor recondenses at the colder surfaces, which

creates an enormous heat load.<sup>14</sup> As a consequence, attention must be paid to minimizing the thickness of the  $^4\text{He}$  film to avoid the onset of superfluidity. The required thickness can be achieved by pumping on the vacuum space for a sufficiently long time. Another possibility is to use  $^3\text{He}$  as an exchange gas, which does not turn superfluid at temperatures typically encountered in a dilution refrigerator. The heat load conducted along superfluid films can thus be easily avoided and does not contribute significantly to the total heat load in a well designed dilution refrigerator.

The fraction of the residual heat load on the mixing chamber of the CCDR which has to be attributed to thermal conduction is calculated in the following. The mixing chamber is suspended from an intermediary flange by means of three stainless steel tubes, which have a length  $l = 235$  mm and a cross-section  $A = 7.1 \text{ mm}^2$  each. With the cryostat running at base temperature, the intermediate flange has a temperature of 55 mK. The resulting heat load to the mixing chamber is

$$\dot{Q} = 3 \cdot \frac{A}{l} \cdot [\theta(T_1) - \theta(T_2)] = 14.8 \text{ nW}. \quad [4.8]$$

Conduction along the superconducting Nb-Ti signal leads can be neglected. The thickness of the helium film covering the support rods is considered small enough to render the film immobile; conduction in the film is thus also neglected.

## 4.2 Residual Heat from Typical Construction Materials

During cool-down, heat is released by materials due to their specific heat. At temperatures below 1 K, the specific heat of diamagnetic metals is dominated by the electronic specific heat; above 10 K, the phonon specific heat dominates. Magnetic impurities also contribute to the specific heat of a material. The amount of heat  $Q$  resulting from a change in temperature from  $T_1$  to  $T_2$  can easily be calculated by

$$Q = m \cdot \int_{T_1}^{T_2} c_p(T) \cdot dT, \quad [4.9]$$

---

<sup>14</sup> Private communication from Dr. Tapio O. Niinikoski (CERN), 2007

where  $c_p$  is the specific heat of the construction material and  $m$  its mass. Problems arise if the thermal link between the part to be cooled and the heat sink is such that thermal equilibration takes place only very slowly. This may be the case for superconducting materials below  $T_C$ . In the following, the heat release from a cylindrical rod with radius  $r$  and length  $l$  is calculated. The rod shall be made of a material with specific heat  $c_p(T)$ , density  $\rho$  and thermal conductivity  $\lambda(T)$ . The distribution of the temperature  $T(x,t)$  on the rod depends on the distance  $x$  from the heat sink and the time  $t$ . The heat conducted along the rod is described by the following partial differential equation:

$$\frac{\partial T(x,t)}{\partial t} = \frac{\lambda}{\rho \cdot c_p} \cdot \frac{\partial^2 T(x,t)}{\partial x^2}. \quad [4.10]$$

The solution of this equation is a Fourier series. For bars with non-constant cross sections and material properties which change strongly with temperature, it is easier to solve the problem numerically. The heat load from an aluminum rod with a diameter of 10 mm, a length of 100 mm and an initially constant temperature of  $T(x,0) = T_C = 1.18$  K to a heat sink at 20 mK is depicted in Figure 36 for a time period of 100 days as an example. Even though the heat load is not large in absolute terms, it drops only very slowly with time and might thus be a nuisance – especially if large amounts of insulators or superconducting materials are used.

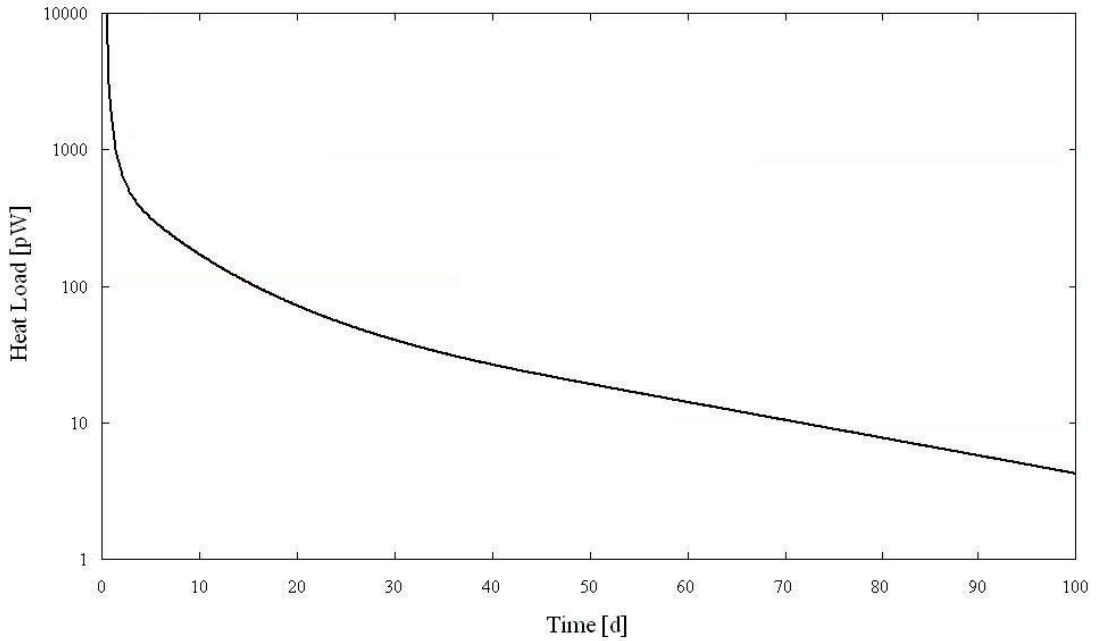


**Figure 36: Heat load due to the slow cool-down of a superconducting aluminum bar**

In the following, the residual heat load from typical construction materials, which does not result from electronic or lattice specific heats, is discussed. The values given may well be used for a preliminary assessment of the residual heat load to a VLT machine, but cannot replace experimental measurements.

### ORTHO-PARA CONVERSION OF H<sub>2</sub>

The two protons of a hydrogen molecule (H<sub>2</sub>) can be arranged in a symmetric and an antisymmetric nuclear spin state. Hydrogen molecules in the former state are called ortho-H<sub>2</sub>, in the latter state para-H<sub>2</sub>. The thermal equilibrium at room temperature is characterized by 75% of ortho-H<sub>2</sub> and 25% of para-H<sub>2</sub>. This ratio is temperature dependent and obeys the following equation [109]:

$$\frac{N_{ortho}}{N_{para}} = \frac{3 \cdot \sum_{J=1,3,\dots} (2J+1) \cdot e^{-h^2 J(J+1)/(2\theta \cdot k_B \cdot T)}}{\sum_{J=0,2,\dots} (2J+1) \cdot e^{-h^2 J(J+1)/(2\theta \cdot k_B \cdot T)}}, \quad [4.11]$$

where  $J$  is the total angular momentum quantum number of the molecule,  $\hbar$  is the reduced Planck constant  $h/(2\pi)$ ,  $k_B$  the Boltzmann constant,  $T$  the temperature and  $\theta = 4.59 \cdot 10^{-48} \text{ kg} \cdot \text{m}^2$  the moment of inertia of the H<sub>2</sub> rotator. Figure 37 gives the ratio between ortho- and para-H<sub>2</sub> as given by equation [4.11].

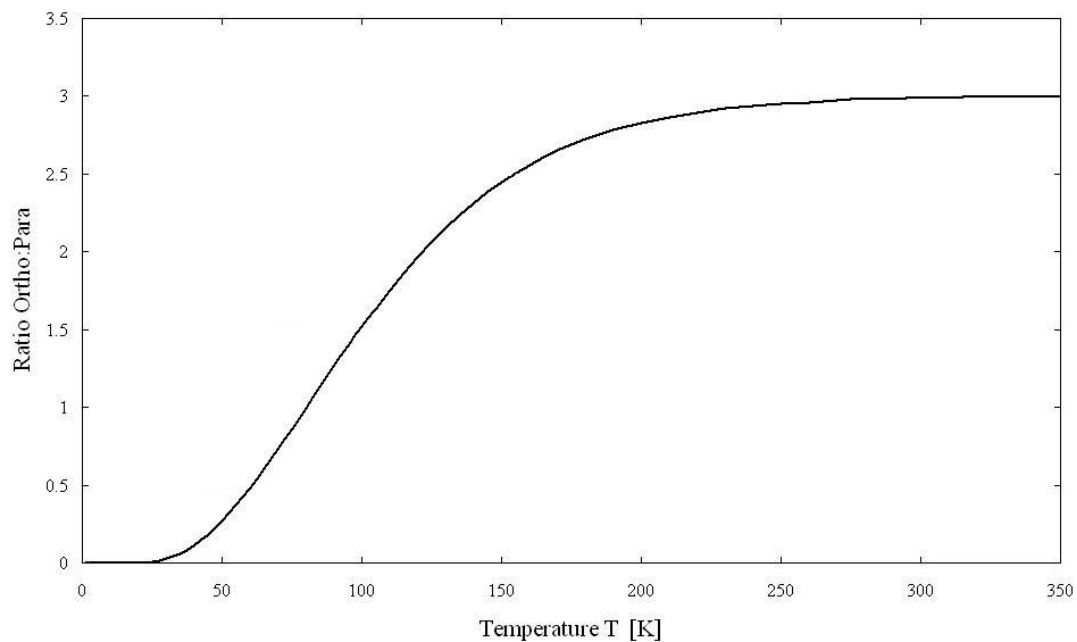


**Figure 37: Ratio of ortho-H<sub>2</sub> and para-H<sub>2</sub> as a function of temperature**



The equilibrium ratio amounts to 3 at room temperature, is unity at approximately 80 K, and at liquid helium temperature (4.2 K) there are almost 100% para-H<sub>2</sub>. It is obvious that a conversion from ortho-H<sub>2</sub> to para-H<sub>2</sub> takes place when a system is cooled to cryogenic temperatures. This conversion is an exothermic process which releases the energy of  $E = 1.42$  kJ per mole ortho-H<sub>2</sub> which converts. For an initial ratio of  $x_0 = 0.75$  ortho-H<sub>2</sub>, the heat release thus amounts to  $E = 1.063$  kJ per mole of H<sub>2</sub> if a piece is cooled from room temperature to a few K. Furthermore, the conversion process is rather slow and follows the law

$$x(t) = \frac{x_0}{1 + x_0 \cdot k \cdot t}, \quad [4.12]$$

where  $x(t)$  is the concentration of ortho-H<sub>2</sub> and  $k = 1.9 \cdot 10^{-2}$  per hour. This value has often been confirmed experimentally.

Hydrogen is introduced into metals during electrolytic production processes. It does not dissolve very well in some metals such as copper, brass or platinum, but is collected in small gas bubbles with a typical diameter between 0.1  $\mu\text{m}$  and 0.4  $\mu\text{m}$  [43]. The bubble density is in the range of  $10^{10} \text{ cm}^{-3}$ . The hydrogen concentration in commercial copper lies between 10 ppm and 100 ppm [123]. If the metal is cooled to low temperatures, the hydrogen in the bubbles becomes liquid or solid and undergoes ortho-para conversion. This results in a heat release which can be detrimental for achieving a low base temperature in a dilution refrigerator. The heat release per mole of H<sub>2</sub> can be calculated as follows:

$$\dot{Q}(t) = E \cdot \frac{dx}{dt} = E \cdot \frac{k \cdot x_0^2}{(1 + x_0 \cdot k \cdot t)^2}. \quad [4.13]$$

Schwark et al. [123] conducted measurements with hydrogen-charged copper samples. Sahling et al. [119] reported a hydrogen-induced heat release from aluminum samples. Their results are in very good agreement with the numbers presented above.

The best way to reduce the hydrogen loading of a metal structure is to anneal it in vacuum. Typical process parameters are annealing temperatures of several hundred °C and heating times of one to two hours. Such treatment typically reduces hydrogen contamination to below 0.1 ppm [109]. The heat load from a copper sample thus scales linearly with mass and depends on the hydrogen contamination of the metal.

Typical, experimentally found initial heat loads are 220 pW/g for 6.4 ppm H<sub>2</sub> contamination, 1.0 nW/g for 27 ppm H<sub>2</sub> contamination and 2.8 nW/g for 76 ppm H<sub>2</sub> contamination. The initial heat load to be expected from a copper part which has been properly annealed to 0.1 ppm lies in the range of 3.7 pW/g.

The ortho-para conversion is an autocatalytic process. In liquid hydrogen, it always follows a law as described by equation [4.12]. Schmidt, however, observed a slower conversion rate in solid hydrogen in the temperature range from 11 K to 14 K [122]. This result can be explained by the limited mobility of hydrogen molecules at low temperatures. If an ortho-H<sub>2</sub> molecule does not have a neighbor which is also in the ortho-state, it cannot undergo conversion. At higher temperature, diffusion takes care of balancing the ortho-H<sub>2</sub> distribution. At low temperatures, the rate of diffusion is small compared to the rate of conversion, which is thus reduced. Schmidt derived a set of differential equations which can be used to numerically calculate the ortho-para conversion as a function of the diffusion constant, which in turn depends on temperature. His model is supported by experimental results, which means that the assumption of a temperature independent conversion rate cannot be applied to materials where solid hydrogen fills the bubbles.

Koláč et al. [75] have also observed a temperature dependence of the relaxation time. They report that the relaxation process was much more rapid at temperatures above 10 K. The heat released from copper at very low temperatures can be greatly reduced by following a well-defined cool-down profile, where time is reserved for quick equilibration at constant temperature.

In order to calculate the heat load resulting from ortho-para conversion in the CCDR, the total amount of hydrogen has to be known. The concentration of hydrogen in the AISI 316LN stainless steel available at the CERN store has been measured by Bacher et al. [12] and typically lies between 0.5 and 0.9 µg/g. If a conservative value of 0.9 µg/g is assumed, the total amount of H<sub>2</sub> dissolved in the body of the mixing chamber can be estimated to 0.83 mmol. The resulting time dependent heat load amounts to

$$\dot{Q}(t) = \frac{3.5}{(1 + 0.01425 \cdot t)^2} \mu\text{W}, \quad [4.14]$$

where  $t$  is the time in hours. The initial heat load thus amounts to  $3.5 \mu\text{W}$ , and decays to  $1.9 \mu\text{W}$  after 24 h and to  $20 \text{ nW}$  after five weeks. It has to be noted that conversion starts immediately after precooling is started, i.e. the largest part of the total heat load is absorbed even before the  $^3\text{He}/^4\text{He}$  mixture is condensed in the dilution refrigerator after a few days.

### *TUNNELING EFFECTS IN AMORPHOUS SOLIDS*

Due to the unordered distribution of atoms in amorphous materials, atoms or groups of atoms can assume several equilibrium positions in the lattice which are characterized by different energy states separated by an energy barrier. At low temperature, transitions between these energy states are exclusively driven by tunneling effects. Tunneling states can also exist in crystalline solids with defects, which are discussed later. Good introductions into the subject of tunneling states are given in [43] and [95].

Tunneling states can be described by the two-level-system (TLS) model, which has been proposed by Phillips [107] and independently by Anderson, Varma and Halperin [6] in 1972. The TLS model assumes the existence of equally distributed, asymmetric, one-dimensional double-well potentials with a constant density of states. This assumption is generally believed to be accurate for vitreous silica.

The relaxation of tunneling states results in a time dependent heat load. Schwark et al. [124] and Nittke et al. [101] have carried out both theoretical work and measurements on the heat release due to tunneling states in amorphous materials. The heat release of a sample with volume  $V$  after it has been cooled rapidly from a temperature  $T_1$  to a non-equilibrium state at temperature  $T_2$  is predicted to be

$$\dot{Q}(t) = \frac{V \cdot \pi^2 \cdot k_B^2 \cdot \bar{n} \cdot (T_1^2 - T_2^2)}{24 \cdot t}, \quad [4.15]$$

where  $\bar{n}$  is the density of two-level tunneling states and  $t$  the time. This equation holds well for charging temperatures  $T_1 < 5 \text{ K}$ . For higher charging temperatures, Schwark et al. have developed a model with a modified distribution of tunneling states, which has to be solved numerically [124]. The tunneling state density  $\bar{n}$  has been derived from experimental results for several materials. In Suprasil, for instance,

the density of tunneling states amounts to  $10^{38} \text{ J}^{-1} \text{ cm}^{-3}$ . The heat load due to tunneling processes can in theory be identified by its  $t^{-1}$  time dependence. The relaxation times of the tunneling states extend over at least 12 orders of magnitude, from less than  $1 \mu\text{s}$  to  $10^6 \text{ s}$ . The typical heat load is in the range of  $100 \text{ pW/g}$  one day after these materials have been cooled to very low temperatures. No heat release has been observed for Teflon, graphite and  $\text{Al}_2\text{O}_3$ .

The time dependent heat load resulting from the relaxation of tunneling states in vitreous silica samples has been measured in times scales from  $10 \mu\text{s}$  to  $100 \text{ ms}$  by Loponen et al. [89, 90] and in larger time scales of several minutes and hours by Zimmermann and Weber [141]. Their results also confirm the time dependence of the heat load as given in equation [4.15] which is derived from the tunneling model for uniform state distribution.

As it is not likely that any of the above mentioned amorphous materials will be used in a large dark matter array in significant quantities, it is not considered worthwhile to pursue a more thorough characterization of their heat release. The only exception might be Polyethylene (PE), which is a candidate material for neutron shielding of dark matter detector arrays. As these PE shields might be installed at mixing chamber temperature close to the absorber crystals, the heat release of PE should be experimentally studied in detail. PE is a partly amorphous material and the existence of tunneling effects has been reported [106].

Amorphous materials can be found in the CCDD's mixing chamber at three locations: The four hermetic feed-throughs for the signal and power leads are sealed with  $0.2 \text{ g}$  of Stycast each; furthermore, the support structure for the mixing chamber heater and thermometers consists of the engineering plastic polyoxymethylene (POM) with a total mass of  $32 \text{ g}$ . POM is semi crystalline; only  $20 \%$  of the material are amorphous. The heat load on the CCDD as a function of time  $t$  (in hours) thus amounts to

$$\dot{Q}(t) = \frac{17.3}{t} \text{ nW}. \quad [4.16]$$

The heat load due to tunneling effects in amorphous materials is  $720 \text{ pW}$  after  $24 \text{ h}$  and approximately  $100 \text{ pW}$  after a week. It amounts to some  $21 \text{ pW}$  after five weeks of operation and is thus practically negligible.

*TUNNELING EFFECTS IN CRYSTALLINE SOLIDS*

The TLS model cannot be applied to crystalline solids as there are usually more than two equilibrium positions for defects in the crystal structure. The tunneling states can thus only be described by multiple potential wells.

The total number of tunneling states in crystalline materials is roughly equal to the number of impurities. In germanium and silicon, these impurities are mainly oxygen and carbon, and typically amount to 1 ppm. The defect density is in the range of  $5 \cdot 10^{37} \text{ J}^{-1} \text{ cm}^{-3}$  for high purity silicon [74], which is used as a detector material in some dark matter searches such as CDMS. Similar effects resulting in a heat load must be expected for germanium detectors.

The average level separation and the distribution of relaxation times is however not well known and thus does not allow for a reliable calculation of the heat load to be expected from germanium or silicon crystals. As a consequence, it is of uttermost importance to perform calorimetric tests on samples of the semiconductor materials which are intended to be used in large cold masses. For the baseline design presented in chapter 6, it is assumed that the level separation and distribution is of comparable magnitude in crystalline and amorphous materials.

Gloos et al. [56] attributed the heat load on the two stages in the nuclear demagnetization refrigerator in Bayreuth to the existence of tunneling states in the crystalline copper stage. The heat load on the stages has been experimentally determined and amounts to 6 pW/g in the first stage and to 27 pW/g in the second stage after a measuring time of one day. The difference is thought to originate from the fact that the two stages are made of two different types of copper with different impurity concentrations. Huiku et al. [67] report a time dependent heat load on the two stages of the Otaniemi nuclear demagnetization refrigerator. This heat load is also thought to originate from the relaxation of tunneling states in copper. The heat load amounts to 17 pW/g after one day and to 440 fW/g after 20 days.

Tunneling states might exist in the stainless steel body of the CCDR's mixing chamber, whose mass amounts to 1892 g. If a tunneling state distribution and density similar to the one in copper is assumed, the following time dependent heat load has to be expected:

$$\dot{Q}(t) = \frac{1220}{t} \text{ nW}, \quad [4.17]$$

where  $t$  is the time in hours. After 24 h, the heat load due to tunneling effects in crystalline materials amounts to 51 nW and drops to 7.3 nW after a week. The relaxation of tunneling effects in the body of the mixing chamber accounts for some 1.5 nW of the total heat leak after five weeks.

### *STRUCTURAL RELAXATION AND CREEP*

Structural relaxation is the time dependent reduction of stress at constant deformation, which gives rise to a time dependent heat load. Structural relaxation occurs, for instance, in a spring which is compressed for an extended period of time: it loses its strength. Structural relaxation has been quoted several times as a heat source in low temperature equipment [109].

The origin of stress in materials used at low temperatures is twofold. Firstly, anisotropic thermal expansion coefficients of the grains and the boundary regions cause internal thermoelastic stress during cool-down; this type of stress develops only when the temperature of a sample changes. Its magnitude depends on material parameters such as grain size and Young's modulus. Secondly, internal stress may already be present in a sample before cool-down. Stress is introduced by many manufacturing processes, such as cold deformation of metal parts. Stress caused by mechanical loads, such as in support structures, may also relax with time and give rise to a time dependent heat release.

Neganov and Trofimov [97] conducted measurements on the heat release attributed to the relaxation of thermo-elastic tension at the grain-boundaries in polycrystalline copper. They observed an exponential dependence of the heat load on time:

$$\dot{Q}(t) = W_0 \cdot e^{-\frac{t}{\tau}}. \quad [4.18]$$

$W_0$  amounts to 500 pW/g. The relaxation time  $\tau$  was approximately 100 h. The measurements were carried out at a temperature of 1 K. Neganov's and Trofimov's work was criticized for not taking into account the ortho-para conversion of hydrogen which might have been dissolved in their samples. The time dependence of the heat

load does not obey a  $t^{-2}$  law, however, which indicates that hydrogen conversion is not the source of heat and hints at structural relaxation mechanisms. Furthermore, the observed heat load could only be explained by a fairly high hydrogen contamination of some 13 ppm, which was ruled out by the authors of the study [132].

Trofimov [132] has developed a model to calculate  $W_0$ . The sample is assumed to have a locally anisotropic thermal expansion coefficient. This is the case in polycrystalline structures, where the thermal expansion coefficient  $\alpha_g$  of the grains varies from the thermal expansion coefficient  $\alpha_b$  of the boundary regions. The elastic properties of the sample, Young's modulus  $E$  and Poisson's ratio  $\nu$  are the same for the grains and the boundaries. The characteristic dimension of the grains is  $a$ , and the thickness of the boundary layer is  $d$ . When the sample is cooled from  $T_0$  to  $T_1$ , the different expansion coefficients of the grains and the boundaries lead to internal thermoelastic stress, which relaxes with time according to [4.18]. This relaxation goes with a relaxation of Young's modulus, which changes from  $E_U$  to  $E_R$ . Trofimov obtained the following equation for  $W_0$ :

$$W_0 = \frac{2}{(1-2\nu)^2} \cdot \left[ \int_{T_0}^{T_1} \alpha_g dT \right]^2 \cdot \frac{2+\Delta}{1+\Delta} \cdot \frac{\delta E}{\rho \tau} \cdot \frac{d}{a}, \quad [4.19]$$

where  $\rho$  is the density of the sample,  $\delta E = E_U - E_R$  and  $\Delta = E_U/E_R$ . With typical values for copper, namely  $\nu = 0.3$ ,  $\rho = 8920 \text{ kg/m}^3$ ,  $E = 1.1 \cdot 10^5 \text{ N/mm}^2$ ,  $\Delta = 0.2$ ,  $\tau = 100 \text{ h}$ ,  $d/a = 5 \cdot 10^{-4}$ , and  $\int_{300\text{K}}^{1\text{K}} \alpha_g dT = -3 \cdot 10^{-3}$ , the initial heat release  $W_0$  can be calculated to be 700 pW/g, which is in good agreement with the values obtained by experiment.

Frossati attributes the 50  $\mu\text{W}$  (37 pW/g) heat load of the MiniGRAIL sphere mainly to relaxation of thermoelastic stress.<sup>15</sup> Annealing the sphere at 750 °C instead of 450 °C reduced the heat load by a factor of 2 to 25  $\mu\text{W}$  [36]. This heat load was measured two weeks after cool down. If the heat load is attributed completely to relaxation of thermoelastic stress,  $W_0$  would be 540 pW/g. It is however suspected that the measured heat load results at least partly from the ortho-para conversion of  $\text{H}_2$ .

---

<sup>15</sup> Private communication from Prof. Giorgio Frossati (Leiden University), 2006

In addition to internal thermoelastic stress, heat may be generated by the relaxation of stress of external origin. Fox [47] and Feltham [45] conducted stress relaxation tests on brass and copper. Fox found that stress relaxes logarithmically obeying the following law:

$$\frac{\Delta\sigma}{\sigma_0} = K(T) \cdot \ln(1 + \nu \cdot t), \quad [4.20]$$

where  $\Delta\sigma/\sigma_0$  is the stress relaxation (in percent of the initial stress  $\sigma_0$ ), and  $t$  the time.  $K$  and  $\nu$  are material properties.  $K(T)$  depends on temperature. Experimental values for annealed oxygen free high purity copper at 77 K can be fitted with the parameters  $K = 8.58$  and  $\nu = 5.58 \text{ h}^{-1}$ . Glenn [55] and Mott [94] found that at temperatures below approximately 1 K, dislocation motion is not thermally activated but due to tunnelling. The resulting time dependence of stress relaxation is the same as given in [4.20], but  $K$  is independent of temperature.

In order to quantitatively determine the heat load originating from stress relaxation in a copper sample, the initial imperfection density has to be known. Cold plastic deformation of metals introduces imperfections such as edge dislocations and vacancy defects in the crystalline structure of the grains. The energy content of the metal is thus greatly increased; the stored energy consists mainly of the strain energy of edge dislocations, whose density rises from  $10^5 \text{ mm/mm}^3$  to  $10^{10} \text{ mm/mm}^3$  during cold deformation. The energy of an edge dislocation with a length of 1 mm amounts to approximately  $E = 10^{-12} \text{ J}$  [13]. The energy content of a copper sample thus rises by 1.1 mJ/g during cold deformation. It has to be noticed that heat dissipation starts immediately after the process of deformation and not after cool-down. As a consequence, and due to the low absolute values, this heat release mechanism can be neglected as a potential source of heat to a dilution refrigerator. This is confirmed by experiments of Sahling et al. [119], who have measured the heat release of an aluminium sample which had been subjected to plastic deformation of 2%. At a temperature of 1.3 K, no time dependent heat load could be observed, which allows putting an upper limit of 2.3 pW/g to the heat release of their sample.

In addition to stress relaxation, which takes place at constant deformation, creep occurs in metals. Creep is defined as the tendency of a material to deform permanently as a result of long term exposure to levels of stress below the material's



yield strength. It occurs due to the movement of dislocations, and at low temperatures is driven by tunnelling effects. At moderate stresses, the strain  $\varepsilon = \Delta L / L$  obeys a time dependence which is very similar to the one given in equation [4.20]:

$$\frac{\Delta L}{L} = K(T) \cdot \ln(1 + \nu \cdot t), \quad [4.21]$$

where  $t$  is the time and  $K$  and  $\nu$  material properties. Similar to Glenn's [55] and Mott's [94] results for stress relaxation, Startsev [77, 129] found that below a certain temperature, which typically amounts to 1 K, tunnelling effects drive dislocation movements and  $K(T)$  obeys the following law:

$$K(T) = K_0 \cdot \ln(1 + A \cdot T^2). \quad [4.22]$$

At very low temperatures which are typically encountered in a dilution refrigerator, it is possible to simplify equation [4.22] to obtain  $K = K_0$ . There must be some stress dependence in  $K_0$ , which is unfortunately neither reported in [129] nor in [77]. For copper, a single experimental result is given, namely  $K_0 = 5 \cdot 10^{-3}$  at a constant stress of 24 MPa. No value is given for  $\nu$ . By fitting equation [4.21] to experimental data given in [77], a value of  $\nu = 1.2 \text{ h}^{-1}$  could be deducted, however.

The heat load emerging from a support rod of length  $L$ , which is subjected to an axial tension force  $F$ , can now easily be calculated by multiplying  $F$  with the rate  $L \cdot \dot{\varepsilon}$  at which the rod lengthens:

$$\dot{Q}(t) = F \cdot L \cdot \dot{\varepsilon}(t) = F \cdot K_0 \cdot L \cdot \frac{\nu}{1 + \nu \cdot t}. \quad [4.23]$$

Judging from photographs of the gravitational wave antenna MiniGRAIL, the sphere is suspended from a rod with a length of approximately 10 cm and a diameter of roughly 25 mm. The force acting on the rod is due to the weight of the sphere and amounts to some 11300 N. This is equal to a stress of some 23 MPa. The material data reported in [129] and [77] should thus be applicable to the case of MiniGRAIL. Equation [4.23] suggests that the heat load due to creep in the support rod amounts to some 2.2  $\mu\text{W}$  after 30 days and to 360 nW after half a year.

It should be noted that the material starts to creep as soon as it is subjected to a structural load and not when cooling is started. The result obtained from [4.23] will

thus overestimate the actual heat load due to creep. This heat load can most likely be reduced by reducing the stress on the material, as  $K_0$  will decrease. Furthermore, lightweight design principles should be employed.

Another part of the heat load on the mixing chamber of the CCDR may result from the relaxation of thermoelastic stress. The initial heat load  $W_0$  for AISI 316LN stainless steel can be calculated from Trofimov's equation [4.19] and amounts to 770 pW/g. The resulting heat load on the CCDR is

$$\dot{Q}(t) = 2914 \cdot e^{-\frac{t}{100}} \text{ nW}, \quad [4.24]$$

where  $t$  is the time in hours. The heat load amounts to 264 nW after ten days and to 655 pW after five weeks. Again, it should be noted that the better part of the heat is dissipated during precooling to 4 K before the dilution refrigerator operates. It seems unlikely that creep causes a substantial heat load in the CCDR as the support structure is only mildly stressed.

#### *DECAY OF RADIOACTIVE NUCLEI*

Every material is contaminated with radioactive nuclei which decay and release heat by doing so. The amount of contamination depends on the provenance of the material as well as the manufacturing and storage it underwent. Materials which were kept on the earth's surface for extended periods, for instance, feature higher activation than materials which have been stored and processed underground. The heat load resulting from radioactive decay processes depends on the number of nuclei which decay per unit time and on the energy  $E$  released upon decay:

$$\dot{Q}(t) = E \cdot K \cdot N_0 \cdot e^{-K \cdot t}. \quad [4.25]$$

$N_0$  is the initial number of nuclei at  $t = 0$  and  $K$  the decay constant, which can easily be calculated from the half-life  $T$  by

$$K = \frac{\ln(2)}{T}. \quad [4.26]$$

The nuclei's half-life can be as high as some  $10^9$  years and is thus very long compared to experiment durations. For large values of  $T$ , the decay constant  $K$  and the variation of the decay rate with time  $(dN/dt)/N_0$  are close to zero:

$$\frac{dN/dt}{N_0} = -K \cdot e^{-K \cdot t}. \quad [4.27]$$

As a consequence, the residual heat due to radioactive decay can be considered as almost constant in time. Typical decay energies  $E$  for heavy nuclei lie in the range from 4 to 5 MeV (4.679 MeV for  $^{235}\text{U}$ , 4.27 MeV for  $^{238}\text{U}$  or 4.083 MeV for  $^{232}\text{Th}$ ). Activity levels of uranium and thorium contaminations in standard construction materials typically amount to some 10 Bq/kg. Potassium-40 contaminations, which have an activity of up to 1000 Bq/kg [86], dissipate an average 1.33 MeV upon decay. An estimate for the heat deposited by radioactive nuclides thus yields approximately 230 fW/g in a cold mass made from standard construction materials.

The materials which are used in the cold masses of low-background experiments are of special, extremely radiopure type with activity levels below 0.005 Bq/kg. As a consequence, a significant heat load from the decay of radioactive nuclei is not to be expected for large low background experiments. The heat load on the mixing chamber of the CCDR resulting from the decay of radioactive nuclei in the metal parts of the mixing chamber is estimated to 1.3 nW.

### ***4.3 Heat Dissipation in Vibrating Structures***

Both eddy current heating of a conductor vibrating in a magnetic field and dissipative structural damping of vibrational movement in the cold mass give rise to a heat load on a very low temperature apparatus. Pobell [108], for instance, measured a heat load of 15 pW on the nuclear stage of the Jülich demagnetization refrigerator during refills of the helium dewar, which subjected the nuclear stage to vibration.

Measurements have been performed on the CCDR to investigate the heat load resulting from vibrations in more detail. The vibration environment of the cryostat has been measured with a Honeywell<sup>16</sup> PA (AG714) accelerometer capable of measuring

---

<sup>16</sup> Honeywell Sensing and Control, Freeport (Illinois), USA.

accelerations of up to  $\pm 5$  g in a frequency range from 3 to 5000 Hz. The acceleration signal has been digitally recorded with a National Instruments<sup>17</sup> NI PCI-6221 Multifunction Data Acquisition Card with a sampling rate of 100 kS/s and a resolution of 16 bit. The signal has been analyzed using a National Instruments Labview program. The measured signal can be classified as stationary random data [15]. It is convenient to treat this data in the frequency rather than the time domain. Discrete Fourier transforms (DFT) are used to effect this transformation. The most common algorithm is the Fast Fourier Transform (FFT) proposed by Cooley and Tukey [29].

Aliasing is a problem often encountered when analogue data is digitally sampled. Aliasing errors occur when the highest frequency contained in the signal is twice the sampling frequency or larger. The maximum allowable signal frequency for a given sampling rate is called Nyquist frequency. The only sure way to avoid aliasing errors is to safely remove data at frequencies higher than the Nyquist frequency from the analogue signal by means of a low-pass filter. According to Bendat [15] it is sufficient to oversample analogue data (i.e. to choose a sampling rate much higher than theoretically necessary) and apply digital filtering before reducing the amount of data to a reasonable amount for further processing. This solution has been chosen for the vibration measurements on the CCDR. Furthermore, the recorded sequence of samples has been windowed with a Hamming function to reduce the leakage effect.

In normal operation the power spectral density (PSD) function of the displacement measured at the top flange mainly consists of a peak with an amplitude of  $99.5 \mu\text{m}^2/\text{Hz}$  at 33 Hz which results from the vibrations generated by the  $^3\text{He}$  pump.

The CCDR was deliberately subjected to a high level of vibrations of different frequencies and amplitudes by spinning an unbalanced rotor which had been mounted on the top flange of the cryostat. The vibrations were measured close to the rotor. No correlation between the vibrational environment and the heat load on the mixing chamber could be observed. As a consequence, it is only possible to determine an upper threshold of 335 nW for the heat load due to vibrations.

Three mechanisms with the potential to convert vibrations into heat could be identified. They are discussed in more detail in the following.

---

<sup>17</sup> National Instruments Corporation, Austin (Texas), USA.

*EDDY CURRENT HEATING*

Eddy current heating is one of the major heat sources in demagnetization cryostats where fairly large time dependent fields are applied to the cold mass. Eddy current heating in a conductor of volume  $V$  and electrical resistivity  $\rho$ , which is situated in a time-varying magnetic field, can be estimated to be

$$\dot{Q} = \frac{\dot{B}^2 \cdot P \cdot V}{\rho}, \quad [4.28]$$

where  $B$  is the field strength and  $P$  a geometry factor. For a cylinder with radius  $r$ , the geometry factor  $P$  amounts to  $r^2/8$  [109].

For a large dark matter detector array, only the earth's magnetic field has to be taken into account, which has a field strength in the range of 30  $\mu\text{T}$  to 60  $\mu\text{T}$  and does not change with time. A structure vibrating in this field experiences a changing magnetic flux and is thus heated by eddy currents. The heat dissipation is a complicated function of the velocity  $w$  of the vibration and its mode shape with respect to the field lines. A very simplified model can be derived from the law of induction and yields the following equation for the heat dissipation  $\dot{Q}$  of a rod vibrating in a magnetic field with the mean velocity  $\bar{w}$ :

$$\dot{Q} = \frac{B^2 \cdot \bar{w}^2 \cdot V}{\rho}. \quad [4.29]$$

$V$  is the volume of the rod and  $\rho$  its resistivity. With an average value for the strength of the earth's magnetic field, i.e.  $B = 45 \mu\text{T}$ , a resistivity  $\rho = 2 \cdot 10^{-7} \Omega\text{m}$  and a mean velocity of  $\bar{w} = 8 \cdot 10^{-5} \text{ m/s}$  (this is equal to a sine vibration with an amplitude of 1  $\mu\text{m}$  and a frequency of 20 Hz), the resulting heat load can be estimated to a negligibly low 7.3 aW/g - even though equation [4.29] always yields conservative results.

The heat load due to eddy current heating is most important in cryostats with magnetic fields applied, such as magnetic refrigerators, and can be neglected in dark matter searches and gravitational wave detectors, which typically use dilution refrigerators for cooling.

*STRUCTURAL DAMPING OF VIBRATIONS*

Structural damping is defined as the dissipation of energy during vibration. The harmonic movement of an oscillator would go on forever without damping. Undamped, ideally elastic structures do not exist in reality. Real-life structures are often modeled by including viscous damping, i.e. a damping force which resists vibration and is proportional to velocity. An oscillating system which is excited by the force  $F(t)$  and consists of a mass  $m$ , a spring with the spring-constant  $k$  and a viscous damper with a damping constant  $c$  can be mathematically described as

$$m\ddot{x}(t) + c\dot{x}(t) + kx(t) = F(t), \quad [4.30]$$

where  $x$  is the displacement of the mass. The critical damping factor  $c_c$  is the value of  $c$  which allows the mass – once disturbed – to return to its initial position without going past it. The critical damping factor is calculated by

$$c_c = 4\pi \cdot m \cdot f_n, \quad [4.31]$$

with  $f_n$  being the natural frequency of the undamped system, which amounts to

$$f_n = \frac{1}{2\pi} \sqrt{\frac{k}{m}}. \quad [4.32]$$

To express the damping of a structure, the damping ratio  $\mathcal{G}$  is used, which is the ratio of actual damping  $c$  and critical damping  $c_c$ :

$$\mathcal{G} = \frac{c}{c_c}. \quad [4.33]$$

Damping ratios of real-life structures at room temperature are typically in the range from 0.002 to 0.1 [121]. Damping also affects the natural frequency of a system. The damped natural frequency  $f_d$  is calculated from the undamped natural frequency  $f_n$  by

$$f_d = f_n \cdot \sqrt{1 - \mathcal{G}^2}. \quad [4.34]$$

For low damping ratios,  $f_d$  is roughly equal to  $f_n$ . A system which is excited by a time dependent force  $F(t)$  does not oscillate with its natural frequency, however. After some time, the system's damped free response becomes negligible and oscillation

occurs with the excitation frequency  $f$  and – in the case of damping – with a phase shift  $\varphi$ , which amounts to

$$\varphi = \frac{2 \cdot \vartheta \cdot \left( \frac{f}{f_d} \right)}{1 - \left( \frac{f}{f_d} \right)^2}. \quad [4.35]$$

The amplitude of the vibration reaches its maximum when the driving frequency is exactly equal to the system's damped natural frequency. The ratio of the response amplitude  $a$  and the excitation amplitude  $a_e$  is shown for various damping ratios as a function of the normalized frequency  $f/f_d$  in Figure 38. In order to keep  $a/a_e$  dimensionless, the excitation amplitude  $a_e$  is defined as the displacement induced by a constant force  $F$ , i.e.  $a_e = F/k$ .

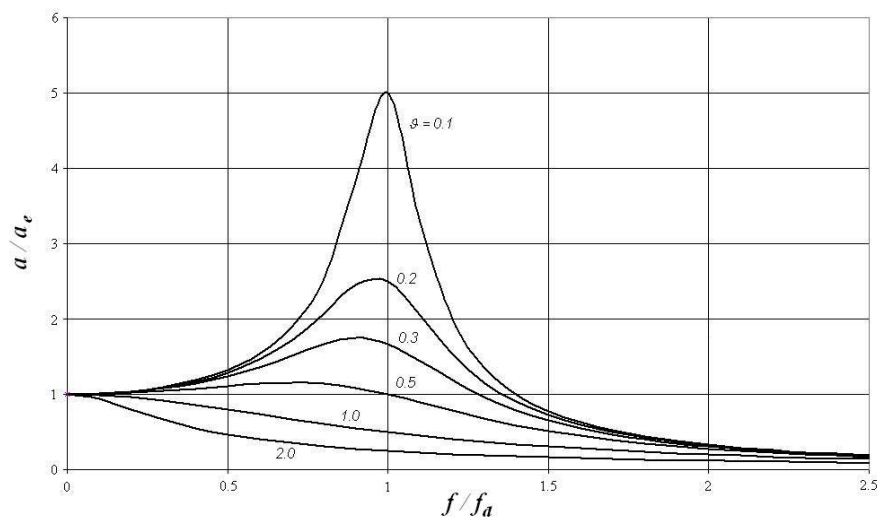


**Figure 38: Resonance curves for various damping ratios**

The system's highest possible response ratio which occurs at  $f/f_d = 1$  is called quality factor  $\bar{Q}$  (the bar is introduced to avoid confusion with the heat  $Q$ ):

$$\bar{Q} = \frac{1}{2\vartheta} = 2\pi \cdot \frac{\text{Energy Stored}}{\text{Energy Lost per Cycle}}. \quad [4.36]$$

$\bar{Q}$  is a material property which characterizes internal friction. Dependency on the type of stress, on absolute temperature, on the frequency and amplitude of the vibration, and – in ferromagnetic substances – on the magnetization has been reported.

The origin of internal friction can almost entirely be described by dislocation theory. Dislocations are local deviations from the perfect lattice structure and can move through the solid under stress. A semiquantitative theory to explain internal friction by the motion of dislocations has been derived by Granato and Lücke [58, 59]. It is based on a model by Koehler in which dislocations are pinned by point defects and bow out between these pinning points under stress. The moving dislocations experience a damping force. Churochkin et al. [26] recently extended this theory to lower temperatures by taking into account defects left in the wake of a moving dislocation, which are called dislocation dipoles. They show that at low temperatures,  $\bar{Q}$  does not depend on frequency or amplitude, but solely on the dislocations density, which depends mainly on the amount of cold deformation the material underwent. Lawson [83] reported that the dislocation density was greatly increased by improper sample handling; he observed an increase in internal friction in copper samples which had been dropped onto a hard surface. Annealing results in recrystallization and a reduction in dislocation density and internal friction by a factor of 5 [40].

Coccia and Niinikoski [27] measured the quality factor of an aluminum alloy at very low temperatures. They obtained a value of  $4 \cdot 10^7$  for Al-5056. Duffy [40] measured the quality factor of different copper alloys; at 50 mK, the quality factor amounts to  $3.7 \cdot 10^7$  for Cu-Be, and to  $8.7 \cdot 10^6$  for phosphor bronze, for instance.

A great increase in heat dissipation can be observed in samples which are simultaneously subjected to vibration and a constant mechanical load such that the vibration induces stress beyond the elastic limit. Easton et al. [42] measured the heating of copper samples subjected to deformation in the plastic region at cryogenic temperatures. A stress of 87 MPa, for instance, caused a heat input of 8.5 mJ/g. The support structure of a VLT apparatus should thus be designed such that static stress levels are well below the elastic limit.

If the principles described above are to be applied to a real-life structure, such as the cold mass inside a dilution refrigerator, it is sufficient to focus on the vibrational modes with the highest absolute energy loss between two cycles. For real life structures, the total amount of energy  $\dot{Q}(t)$  dissipated in all modes can best be evaluated with finite element methods (FEM).



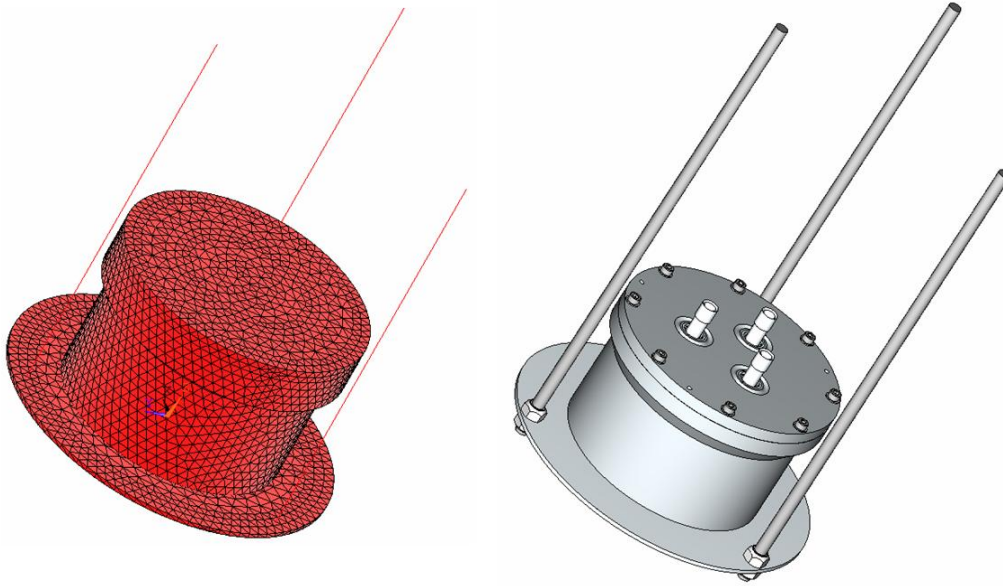


**Figure 39: The FEM and CAD models of the CCCR's mixing chamber**

In the following, this will be demonstrated for the CCCR. The FEM model of its cold mass is shown in Figure 39 above. The material properties of the model are  $\rho = 7800 \text{ kg/m}^3$ ,  $E = 2.1 \cdot 10^5 \text{ N/mm}^2$ ,  $\nu = 0.29$  and  $\bar{Q} = 8 \cdot 10^7$ . In a first step, the resonant frequencies of the mixing chamber and its support plate are evaluated. Different parts of the mixing chamber body resonate at different frequencies, resulting in local mode shape deformations. The FEM model yields two resonance frequencies at 10.3 Hz. The mode shapes consist of an axial movement of the support rods and a pendulum like movement of the whole mixing chamber. Mode shapes in the range of 145 Hz, 345 Hz and 645 Hz comprise the bending of the support plate, while bending of the rods occurs at 659.6 Hz.

In order to estimate the heat load resulting from damping due to internal friction, the mixing chamber in the FEM model was subjected to a sinusoidal displacement  $x(t)$ :

$$x(t) = A_X \cdot \sin(\omega \cdot t). \quad [4.37]$$

The velocity  $w(t)$  of the interface points can easily be obtained by deriving  $x(t)$ :

$$w(t) = \dot{x}(t) = -A_X \cdot \omega \cdot \cos(\omega \cdot t). \quad [4.38]$$

The FEM software yields the amplitude  $A_F$  and the phase angle  $\varphi$  of the harmonic force  $F(t)$  required to achieve the displacement  $x(t)$ :

$$F(t) = A_F(\omega) \cdot \sin(\omega \cdot t + \varphi). \quad [4.39]$$

The energy passing through the mechanical interface points per unit time is obtained by multiplying formulas [4.64] and [4.65]. Averaging over a sufficiently long time span  $t_E$  yields the total amount of dissipated heat:

$$\dot{Q} = -A_F(\omega) \cdot A_X \cdot \omega \cdot \frac{1}{t_E} \cdot \int_0^{t_E} \sin(\omega \cdot t + \varphi) \cdot \cos(\omega \cdot t) \cdot dt. \quad [4.40]$$

The force amplitude  $A_F(\omega)$  is linearly proportional to the displacement amplitude  $A_X$  for a given frequency  $\omega$ . Equation [4.66] can thus be written as

$$\dot{Q} = A_X^2 \cdot P(\omega), \quad [4.41]$$

where  $P(\omega)$  can be calculated from data yielded by the FEM simulation.  $P(\omega)$  has the unit  $\text{W/m}^2$ :

$$P(\omega) = -\omega \cdot \frac{A_F(\omega)}{A_X} \cdot \frac{1}{t_E} \cdot \int_0^{t_E} \sin(\omega \cdot t) \cdot \cos(\omega \cdot t + \varphi) \cdot dt. \quad [4.42]$$

This function is depicted in Figure 40 for the mixing chamber of the CCDR (instead of the angular frequency  $\omega$ , the frequency  $f$  has been chosen as independent variable).

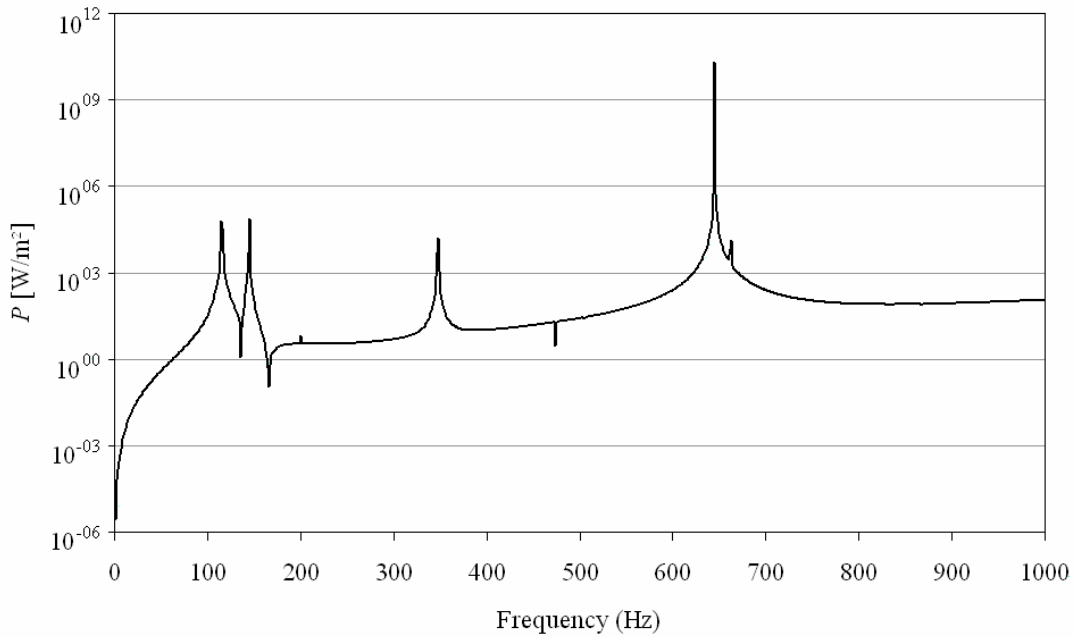


**Figure 40:** The function  $P(f)$  for the CCDR mixing chamber

$P(f)$  features pronounced peaks at the resonant frequencies of the structure in question. A structure should thus be designed such that its resonant frequencies are away from the frequencies predominant in the excitation spectrum. The function  $P(f)$  is characteristic for every structure and could be calculated for the cold mass of a large dark matter detector array in a very similar manner as calculated for the CCDD mixing chamber.

For the calculation of the resulting heat load on the CCDD, it is assumed that the cryostat is ideally rigid so that the mixing chamber vibrations are identical to the vibrations measured at the top flange. More precise results can be obtained by directly measuring the vibration spectrum at the mixing chamber. The heat load resulting from structural damping in the mixing chamber can be calculated by multiplying  $P(f)$  with the PSD function  $W(f)$  and integrating over the frequency spectrum:

$$\dot{Q} = \int_0^{\infty} P(f) \cdot W(f) \cdot df . \quad [4.43]$$

For the CCDD,  $\dot{Q}$  amounts to  $1.25 \cdot 10^{-22}$  W. This value is low enough to be neglected.

### VISCOUS DISSIPATION IN LIQUIDS

The FEM calculation method described above does not take into account the movement of the helium liquids inside the mixing chamber, which are put into motion if the cryostat is vibrating. The most likely movement seems to be swaying of the phase boundary, which induces circular flow patterns as shown in Figure 41.

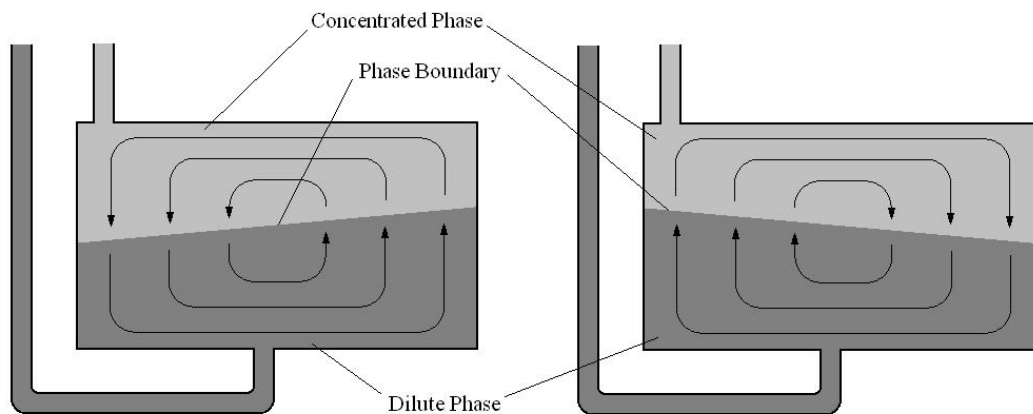


**Figure 41: Flow pattern of the liquids in the mixing chamber induced by vibration**

The viscosity of  $^3\text{He}$  at millikelvin temperatures is considerable and may thus lead to substantial heating. It is believed by the author that the heat generated by viscous dissipation in the helium liquids inside the mixing chamber is much larger than the heat generated due to internal friction in the solid parts of the mixing chamber. If the measured residual heat load on the CCDR is attributed entirely to viscous dissipation in the mixture, an upper threshold of 16 nW/g can be deducted.

The motion of fluids cannot be easily simulated. First of all, the flow in the mixing chamber is influenced by several factors, namely the injection of concentrated solution, the motion of  $^3\text{He}$  through the dilute solution to the dilute stream channel of the heat exchanger, convection eddies and currents induced by mechanical vibrations. Furthermore, simulation of two-phase systems and especially liquid-liquid interfaces has not been very successful in the past.

The heat load certainly depends on the vibrational environment, but may possibly be reduced by optimizing the mixing chamber design in this regard. The amount of  $^3\text{He}$  in the mixing chamber should be minimized. Barriers may be introduced to inhibit swaying of the phase boundary.

This experimental result clearly highlights the importance of vibration control for equipment operating at very low temperatures. Future tests should focus on the determination of the heat load which is caused by vibration. An effort should be undertaken to investigate if any of these effects can cause substantial heating and which mechanism is the most important (i.e. whether internal friction in metals or viscous dissipation in the helium liquids is dominating).

#### ***4.4 Heat Transport by Residual Gas***

Conduction through residual gas in the vacuum space of a cryostat is another source of residual heat in very low temperature systems. Gas particles which do not stick to a surface bounce around in the vacuum space and collide both with hot and cold surfaces. Energy is exchanged during these gas-wall collisions. The resulting heat flux depends – among other parameters – on the pressure of the residual gas. This pressure is determined by the equilibrium of ad- and desorption. The following section sets out to estimate the heat load due to conduction through residual gas.

The mean free path  $\lambda$  of a molecule is given by equation [4.44] where  $k_B$  is the Boltzmann constant,  $T$  the temperature,  $\xi$  the diameter of the gas molecule and  $p$  the pressure [116]:

$$\lambda = \frac{k_B T}{\sqrt{2} \cdot \pi \cdot \xi^2 \cdot p} . \quad [4.44]$$

For  $T = 4$  K,  $p = 10^{-7}$  mbar and typical atoms and molecules found in cryogenic equipment, such as  $^4\text{He}$  ( $\xi = 2.61 \cdot 10^{-8}$  cm) or  $\text{H}_2$  ( $\xi = 2.76 \cdot 10^{-8}$  cm),  $\lambda$  lies in the range of several meters. The Knudsen number  $\text{Kn}$  is defined as the ratio of the gas particles' mean free path and a characteristic geometric length  $L$ :

$$\text{Kn} = \frac{\lambda}{L} . \quad [4.45]$$

In a cryostat, the characteristic length  $L$  is most likely much smaller than the mean free path of the molecules, i.e.  $\text{Kn} \gg 1$  and the molecules travel in straight trajectories directly from one surface to the other. The average kinetic energy  $\bar{E}$  and the average velocity  $\bar{w}$  of a gas particle of mass  $m_g$  are defined by the following two relations:

$$\bar{E} = \frac{3}{2} k_B T , \quad [4.46]$$

$$\bar{w} = \sqrt{\frac{3k_B T}{m_g}} . \quad [4.47]$$

The constant occurrence of collisions produces a wide distribution of velocities which follows the Maxwell–Boltzmann law, where  $f_v$  is the probability of a molecule to travel with speed  $w$  [116]:

$$f_v = \frac{4}{\sqrt{\pi}} \cdot \left( \frac{m_g}{2k_B T} \right)^{\frac{3}{2}} \cdot w^2 \cdot e^{-\frac{m_g w^2}{2k_B T}} . \quad [4.48]$$

Molecules and atoms which impact on a surface can be scattered or trapped by the surface or might stick on it. These three mechanisms determine the amount of free particles in the vacuum space of a cryostat. The pressure depends on the local gas temperature and cannot be directly measured in the low temperature region.

Scattering is characterized by the accommodation coefficient  $\alpha$ , which is a measure of how much energy is exchanged between the surface and the impacting particle. The accommodation coefficient is usually investigated in molecular beam experiments and is defined as

$$\alpha = \frac{E_i - E_o}{E_i - E_s} \quad [4.49]$$

with  $E_i$  being the average energy of the impacting gas particles,  $E_o$  the average energy of the particles leaving the surface and  $E_s$  the energy of a particle which has thermally accommodated with a surface.  $E_s$  amounts to  $2kT$  if the molecule has only translational energy. The accommodation coefficient  $\alpha$  between a surface and a gas with particles of mass  $m_s$  and  $m_g$  respectively can be estimated from Baule's Hard Sphere Model, which has been improved by Goodman [93]:

$$\alpha = \frac{2.4 \cdot \left( \frac{m_g}{m_s} \right)}{\left( \frac{m_g}{m_s} + 1 \right)^2}. \quad [4.50]$$

If a molecule is trapped by a surface, it loses enough energy for being able to leave that surface again. Trapped particles can leave a surface when thermal motions of the surface molecules cause them to desorb. Typical sojourn times are in the range of a few hundred microseconds. The process of trapping can be treated similarly to the process of scattering by assuming an accommodation coefficient  $\alpha = 1$ . Trapping also occurs in molecular beam experiments and thus influences the measured accommodation coefficient  $\alpha$ .

Sticking is very different from trapping as the impacting gas particle actually bonds with the surface. In a typical cryogenic apparatus, gas particles are adsorbed in multilayers with liquid-like density as described by the BET model [19]:

$$\frac{p}{V \cdot (p_0 - p)} = \frac{1}{V_m \cdot c} + \frac{c-1}{V_m \cdot c} \cdot \frac{p}{p_{sat}}, \quad [4.51]$$

where  $V$  is the volume of adsorbed gas,  $p$  the given pressure and  $p_{sat}$  the saturation pressure of the gas at the given temperature. The volume of gas in a complete

monolayer is given by  $V_m$  and is constant for any temperature. It can be estimated from the number of possible adsorption sites in a monolayer, which lies in the range of  $10^{15} \text{ cm}^{-2}$ . The thickness of a monomolecular layer is roughly equal to the diameter of the absorbed particles. Furthermore, the ratio between the true area and the geometric area of a surface has to be taken into account. For copper plates, the ratio between the true and the geometric surface has been measured to amount to 14 [116]. The constant  $c$  in equation [4.51] is a function of temperature and given by

$$c = e^{\frac{E_A - E_L}{R \cdot T}}, \quad [4.52]$$

where  $E_A$  and  $E_L$  are the molar energy of adsorption of a monolayer and the energy of condensation of the adsorbed gas respectively. As the BET theory does not take into account surface tension, experimental values correspond well to the theory only close to monolayer coverage. The energy of adsorption is greatly influenced by atoms and molecules which are already present on the surface. Surfaces inside a cryostat are usually covered by some layers of water molecules and helium atoms. It is clear that the total amount of free gas particles inside the cryostat must be minimized to reduce the residual gas pressure. This can be achieved by implementing charcoal traps, which greatly increase the surface available for binding particles by adsorption. As a consequence, more gas particles are bound to the surface. This enters into equations [4.51] as the volume of one absorbed monolayer  $V_m$ .

Typical cryostats are equipped with a vacuum gauge at room temperature. If the mean free path of the molecules is much larger than a characteristic geometry of the passage connecting the vacuum space with the gauge, the pressure at low temperature can be calculated from the relation for the thermal transpiration effect [30]:

$$\frac{p}{\sqrt{T}} = \text{const}. \quad [4.53]$$

If the condition  $\text{Kn} \gg 1$  is not fulfilled in the passage, the values obtained from [4.53] for the pressure in the low temperature region overestimate actual pressures – sometimes excessively. With the gas pressure being determined, the heat flux  $\dot{Q}$  between two parallel surfaces of temperatures  $T_1$  and  $T_2$  and areas  $A_1$  and  $A_2$  caused by residues of the gas with temperature  $T$ , pressure  $p$  and molecular weight  $M$  can be calculated from equation [4.54] which is known as Kennard's law [72]:

$$\dot{Q} = A_2 \cdot \alpha_0 \cdot \frac{\kappa + 1}{\kappa - 1} \cdot \sqrt{\frac{R}{8 \cdot M \cdot \pi}} \cdot \frac{p}{\sqrt{T}} \cdot (T_2 - T_1), \quad [4.54]$$

where  $R$  is the ideal gas constant and  $\kappa$  is the ratio of the specific heats.  $T$  is the temperature of the gas and can – in a rough simplification – be assumed to be the mean between  $T_1$  and  $T_2$ . As  $p$  varies locally with temperature, the constant ratio  $p \cdot T^{-0.5}$  from relation [4.53] should be used in [4.54].

If the residual gas inside the cryostat is not a single gas but a mixture, the partial pressure of each gas has to be used in [4.53] and [4.54]. The total conduction of the residual gas then is the sum of the conductions calculated for each component. This is easily justified by the definition of molecular flow, i.e. that the gas molecules interact primarily with the walls and not with each other.

The value for  $\alpha_0$  in [4.54] can be calculated from the surface areas and accommodation coefficients  $\alpha_1$  and  $\alpha_2$  between the gas and surface 1 and 2 respectively:

$$\alpha_0 = \frac{\alpha_1 \cdot \alpha_2}{\alpha_2 + \frac{A_1}{A_2} \cdot (1 - \alpha_2) \cdot \alpha_1}. \quad [4.55]$$

Heat transfer in a cryogenic apparatus is more complex than the simplified case of two parallel surfaces. Heat is exchanged between several surfaces of different temperatures and geometric orientations to each other. It is thus suggested to enhance equation [4.54] by a view factor which takes into account the cryostat's geometry. As gas particles travel in straight trajectories very much like photons do, it seems reasonable to use the same view factors as for the calculation of thermal radiation. View factors for standard geometries are given in [134].

The composition of the residual gas influences the heat load as material properties such as molecular weight, energy of absorption and energy of condensation enter into the equations. Helium is often used as an exchange gas and is thus abundant in the vacuum space of a cryostat. Hydrogen – both in atomic and molecular form – results from cracking hydrocarbons and water molecules. Vacuum gauges based on



ionization can be sources for this cracking process<sup>18</sup>. Water, nitrogen and oxygen molecules resulting from air residues in the cryostat may exist in the vacuum space. For future investigations of the heat load due to residual gas it is suggested to analyze gas samples from the vacuum space of a cryostat with regard to their composition.

For a preliminary estimate, it seems sufficient to neglect all substances but helium, nitrogen, oxygen, molecular and atomic hydrogen, and water vapor and assume that the residual gas is made up of equal fractions of these constituents.

Due to the large number of gas particles impacting on a surface per unit time, the time constant of the adsorption process is rather small compared to typical experiment durations. The number of molecules  $N$  with mass  $m_g$  impacting on a surface per unit area and time is given by

$$N = \frac{p}{\sqrt{2\pi \cdot k_B \cdot T \cdot m_g}}, \quad [4.56]$$

where  $T$  is the gas temperature defining the average kinetic energy of a gas particle and  $p$  its pressure. In typical cryogenic systems, the number of particles impacting on a surface per second is in the same order of magnitude as the number of particles absorbed on the surface. It is thus not believed that the heat load due to conduction in residual gas varies in time scales comparable to typical experiment durations.

Typical values for the variables in equation [4.54] are given in Table 8 on the following page. They are valid for typical residual gas molecules, which might be encountered in a dilution refrigeration system between a surface at 200 mK and a surface at 10 mK.

The accommodation coefficient  $\alpha$  was calculated from Goodman's model. It was assumed that the surfaces are covered by water molecules, i.e.  $m_s$  in equation [4.50] amounts to 18 g/mol. The specific heat ratio was assumed to amount to  $\kappa = 1.66$  for ideal monoatomic gases and to  $\kappa = 1.4$  for ideal diatomic gases. For water vapor,  $\kappa$  was assumed to amount to 1.33.

---

<sup>18</sup> Private communication from Dr. Tapio O. Niinikoski (CERN), 2006

Gas	$M$ [g/mol]	$\kappa$ [1]	$\alpha$ [1]	$\frac{\kappa+1}{\kappa-1} \cdot \sqrt{\frac{R}{8 \cdot M \cdot \pi}}$ [(J/(kg·K)) <sup>0.5</sup> ]
<sup>4</sup> He	4	1.66	0.36	36.65
<sup>3</sup> He	3	1.66	0.29	42.32
N <sub>2</sub>	28	1.4	0.57	20.62
O <sub>2</sub>	32	1.4	0.55	19.29
H	1	1.66	0.12	73.30
H <sub>2</sub>	2	1.4	0.22	77.17
H <sub>2</sub> O	18	1.33	0.6	30.27

**Table 8: Important parameters for the calculation of heat transfer by conduction in residual gas**

For the calculation of the heat load due to conduction in residual gas, the constant  $p \cdot T^{-0.5}$  has to be known. It seems unlikely that a quantitative value can be obtained by measuring the residual gas pressure as the condition  $\text{Kn} \gg 1$  can hardly be fulfilled in the passage between the gauge and the vacuum space around the mixing chamber. An upper threshold of  $p \cdot T^{-0.5} = 7.3 \cdot 10^{-7} \text{ Pa} \cdot \text{K}^{-0.5}$  can however be derived from data gained in measurements with the CCDR:

The heat load on the mixing chamber was measured after the two innermost thermal screens were removed, so that the mixing chamber faced the thermal screen heat sunk to the 1 K pot. The temperature of this screen was 1.7 K. The mixing chamber temperature was 11.2 mK at a flow rate of 220  $\mu\text{mol/s}$ . This corresponds to an additional heat load of 430 nW. The upper threshold for  $p \cdot T^{-0.5}$  stated above can be calculated from equation [4.54] by assuming that the entire additional heat load results from conduction in residual gas.

The heat load due to conduction in residual gas can be minimized by several means; implementing a large number of shields, which prevent the gas particles from traveling from hot to cold parts in straight trajectories, is a first step. The temperature of the last shield surrounding the mixing chamber should be as low as possible. Secondly, the total amount of gas inside the cryostat should be minimized to reduce the residual gas pressure. This can be achieved by improving the vacuum pumping system and – as already mentioned - by implementing charcoal traps. As a third measure, the gas composition should be optimized. This can be achieved by refraining from using H<sub>2</sub> as heat exchange gas for cool-down, and using He instead. Furthermore, the surfaces inside the vacuum vessel should be carefully cleaned to remove contaminations with a high vapor pressure.

It seems likely residual gas conduction is one of the most important sources of residual heat to the mixing chamber of the CCDR. Further research on this subject is thus suggested. An additional shield, whose temperature is closer to the temperature of the mixing chamber, could be added to the cryostat. In addition, measures to improve the vacuum inside the IVC could be taken.

#### ***4.5 Radiative Heat Transfer at Very Low Temperatures***

The total energy  $\dot{Q}$  emitted by a black body of temperature  $T$  is given by the Stefan-Boltzmann law

$$\dot{Q} = \sigma \cdot T^4, \quad [4.57]$$

where  $\sigma$  is the Stefan-Boltzmann constant. Radiation is emitted in the whole bandwidth of frequencies  $f$ , with the intensity distribution  $M(f, T)$  described by Planck's law:

$$M(f, T) = \frac{2\pi \cdot h \cdot f^3}{c^2} \cdot \frac{1}{e^{hf/k_B T} - 1}, \quad [4.58]$$

where  $h$  is Planck's constant,  $c$  the speed of light and  $k_B$  the Boltzmann constant. The unit of  $M(f, T)$  is  $\text{W}(\text{m}^2 \cdot \text{Hz})$ . A characteristic wavelength, which is characterized by an intensity maximum, exists for each temperature. For typical temperatures of a dilution refrigerator, this wavelength lies in the centimeter range (some 30 cm at 10 mK, 15 cm at 20 mK and 3 cm at 100 mK, for instance).

Real bodies do not necessarily obey Boltzmann's law; they emit less energy than a black body. The ratio between the energy emitted by such a "grey body" and the energy emitted by a black body of the same temperature is called emissivity  $\varepsilon(T, f, \Omega)$  and depends on the body temperature  $T$ , the frequency  $f$  of the emitted radiation and the solid angle  $\Omega$  into which energy is emitted. By integrating over the hemisphere and the frequency spectrum, the emissivity  $\varepsilon(T)$  can be obtained. In general, the emissivity decreases with lower temperatures and polished surfaces. The absorptivity  $\alpha(T)$  can be defined as the ratio of energy absorbed by a surface to the total energy incident on that surface. In thermal equilibrium, i.e. when the impinging radiation is

emitted by a black body with the same temperature as the absorbing body, it follows from Kirchhoff's law that

$$\varepsilon(T) = \alpha(T). \quad [4.59]$$

For dielectric materials, this relation even holds under non-equilibrium conditions. In pure metals, however, the impinging electromagnetic waves penetrate only a few hundred nm into the solid. Ashby and Schocken [10] accounted for that effect and obtained the result that the emissivity of ideal metals depends on the temperature of the absorbing black body. A very hot metallic body in a very cold environment, for instance, emits only 93 % of the energy it would emit in thermal equilibrium.

At moderate temperatures, the absorptivity  $\alpha(T)$  of an ideal metal can be calculated from the Hagen-Rubens relation [62], which is based on classical electrodynamics:

$$\alpha(\lambda) = 4 \cdot \sqrt{\pi \cdot \varepsilon_0 \cdot c \cdot \frac{\rho(T)}{\lambda}} = 0.365 \cdot \sqrt{\frac{\rho(T)}{\lambda}}. \quad [4.60]$$

The constant  $\varepsilon_0$  is the permittivity of free space,  $c$  the vacuum speed of light,  $\lambda$  the wavelength of the incident radiation in m and  $\rho(T)$  the temperature dependent specific resistance of the metal in  $\Omega \cdot \text{m}$ .

Aschkinass [9] combined this relation with Wien's displacement law and integrated it over the spectrum. The result is the following equation for the total normal absorptivity  $\alpha_n$ , which depends on temperature  $T$ :

$$\alpha_n(T) = 0.578 \cdot \sqrt{\rho(T) \cdot T}. \quad [4.61]$$

This relation only holds at sufficiently large wavelengths and completely fails at wavelengths below 10  $\mu\text{m}$  and at low temperatures [125]. Drude [39] extended the theory to smaller wavelengths by taking into account the interaction of the electromagnetic waves and the free conduction electrons in a metal. Still, theory fails at low temperatures.

Shin [125] developed a comprehensive model which takes into account the anomalous skin effect, electron-electron and electron-phonon collisions as well as impurity scattering processes in the metal. The anomalous skin effect describes the fact that the distance traveled by an electron between two collisions with the lattice is in the range of or even larger than the penetration depth of the electromagnetic waves in the metal

(skin depth). Electron-electron and electron-phonon collisions and impurity scattering also influence the motion of the free electrons in the metal which are accelerated by the electromagnetic waves. The total absorptivity  $\alpha$  can be calculated as the sum of the bulk absorptivity  $\alpha_B$  and the skin absorptivity  $\alpha_S$ :

$$\alpha = \alpha_B + \alpha_S. \quad [4.62]$$

The skin absorptivity can be calculated from the Fermi velocity  $w_F$  of the electrons, which is the average velocity of an electron with mass  $m_e$  at absolute zero. This value depends on the metal's Fermi temperature  $T_F$ :

$$\alpha_S = \frac{3}{4 \cdot c} \cdot w_F = \frac{3}{4 \cdot c} \cdot \sqrt{\frac{2 \cdot k_B \cdot T_F}{m_e}}. \quad [4.63]$$

The bulk absorptivity is considerably more difficult to calculate. For transition metals, such as Cu, Fe, Au and Ag, and at temperatures below  $\sim 10$  K, the following equation applies:

$$\alpha_B = \sqrt{\frac{m^*}{\pi \cdot n_e \cdot e^2}} \cdot \left[ \frac{\chi}{2} \cdot \frac{R_{sd}}{24} \cdot \left( \frac{\hbar \cdot \omega}{k_B \cdot \Theta} \right)^3 + \frac{1}{4\pi} \cdot \left( \frac{\hbar \cdot \omega}{k_B \cdot \Theta} \right)^2 + \Gamma_M^0 \right], \quad [4.64]$$

where  $m^*$  is the effective mass of an electron,  $n_e$  the electron density,  $e$  the electronic charge,  $\omega$  the frequency of the incident radiation, and  $\Theta$  the metal's Debye temperature. For ferromagnetic metals,  $\chi$  amounts to 1, for paramagnetic metals  $\chi = 2$ .  $R_{sd}$  is a constant characteristic of electron-phonon damping and is independent of frequency and temperature.  $\Gamma_M^0$  characterizes electron-impurity scattering and is also independent of frequency and temperature. Equation [4.64] shows that  $\alpha$  does not depend on temperature if the absolute temperature is sufficiently low.

Oxide layers and surface contaminations, which are always present, alter a metal's emissivity and absorptivity, and may render it more similar to a dielectric material. Due to this, and to the fact that the density of impurities and surface irregularities, which influences the emissivity, is usually not well known for engineering materials, one should mainly rely on experimental values for design calculations. Obert et al. conducted measurements on emissivities of metallic surfaces at cryogenic temperatures [102]. Some examples are given in Table 9.

Material	77 K	4.2 K
Anodized Aluminum	0.94	0.78
Copper, Untreated	0.12	0.062
Copper, Mechanically Polished	0.06	0.023
Stainless Steel, Untreated	0.34	0.12
Stainless Steel, Mechanically Polished	0.1	0.074
Stainless Steel, Silver Plated	0.092	0.013

**Table 9: Experimental values for the emissivity of some materials [102]**

The radiative heat transfer  $\dot{Q}_{12}$  between two grey bodies (index 1 and 2) of area  $A$ , temperature  $T$  and of emissivity  $\varepsilon$  thus amounts to

$$\dot{Q}_{12} = \varphi_{12} \cdot A_1 \cdot \varepsilon_1 \cdot \varepsilon_2 \cdot \sigma \cdot (T_1^4 - T_2^4). \quad [4.65]$$

The view factor  $\varphi_{12}$  depends solely on the geometry. A fairly complete list of view factors for technically important geometries is given in [134]. The view factor for two parallel surfaces of identical size whose linear dimensions are considerably larger than their distance from each other is  $\varphi_{12} = 1$ . Parallel cylinders can be treated like two flat parallel surfaces if their radius is large compared to their distance from each other. View factors can also be calculated numerically with special software packages. In most cases, the view factors given in [134] will be sufficient, however.

Due to the low temperatures involved, the heat load radiated to the mixing chamber of a properly designed dilution refrigerator is extremely small. If the surfaces are considered to behave like black bodies, equation [4.57] yields a heat load of 91 pW/m<sup>2</sup> from a surface at 200 mK, a heat load of 13.6 nW/m<sup>2</sup> from a surface at 0.7 K and a heat load of 56.7 nW/m<sup>2</sup> from a surface of 1 K. These values show that thermal radiation can most likely be neglected if the last thermal shield around the mixing chamber is heat sunk to the dilute stream.

Theoretical work done by Levin et al. [84], Polder and van Hove [110] and Loomis and Maris [88] suggests that heat transfer between two very closely spaced surfaces exceeds by far the value expected due to blackbody radiation. The external field propagating from a body can be divided in far-field black body radiation and near-field evanescent waves. If the gap  $l$  between two bodies is sufficiently small, energy can be transferred across the gap not only by black-body radiation, but also by evanescent waves. The critical gap size depends on the temperature  $T$ :

$$l \ll \frac{\hbar \cdot c \cdot \pi}{k_B \cdot T}. \quad [4.66]$$

Hargreaves [64] measured the heat transfer between two parallel plates as a function of their distance at ambient temperature, where – according to equation [4.66] – the gap size  $l$  must be considerably smaller than roughly 25  $\mu\text{m}$ . At distances below 2  $\mu\text{m}$ , a proximity effect became strongly visible as heat transfer was enhanced by a factor of 2.

According to equation [4.66], the critical gap size at temperature levels typical for dilution refrigerators is in the range of a few centimeters (for instance 3.6 cm at 200 mK, 14.4 cm at 50 mK and 72 cm at 10 mK). Levin et al. [84] derived an equation for the heat transfer enhancement factor, which is defined as the ratio of the actual heat transfer  $\dot{Q}$  across a small gap of width  $l$  and the value expected from blackbody radiation  $\dot{Q}_{BB}$ :

$$\frac{\dot{Q}}{\dot{Q}_{BB}} = 0.1082 \cdot \frac{\pi \cdot c \cdot \hbar}{l \cdot k_B} \cdot \frac{T_1^{11/3} - T_2^{11/3}}{T_1^{14/3} - T_2^{14/3}}. \quad [4.67]$$

Equation [4.67] is valid in the region defined by [4.66], for metals whose permittivity has a value much larger than unity, and at temperatures low enough for the anomalous skin effect to set in. If the anomalous skin effect is not taken into account, equation [4.67] changes to

$$\frac{\dot{Q}}{\dot{Q}_{BB}} = 0.1450 \cdot \frac{\pi \cdot c \cdot \hbar}{l \cdot k_B} \cdot \frac{T_1^{3.5} - T_2^{3.5}}{T_1^{4.5} - T_2^{4.5}}. \quad [4.68]$$

The near field effect described above is clearly of great theoretical interest; it is doubted, however, that it has to be taken into account for engineering calculations of large cold masses: The enhancement factor for heat transfer between a metallic surface at 50 mK and a metallic surface at 7 mK, which are separated by 1 mm, amounts to 15.6, for instance (the total resulting heat flux is 5.5 pW/m<sup>2</sup>). It drops to 2 (700 fW/m<sup>2</sup>), if the distance is increased to 8 mm and approaches unity (350 fW/m<sup>2</sup>) at a distance of 15 mm. Even if radiation heat transfer is enhanced by one order of magnitude, the absolute value of the resulting heat load is still small compared to other sources.

The equations given above can now be used to estimate the heat load on the mixing chamber of the CCDR originating from thermal radiation: The minimum distance between the mixing chamber and the surrounding shield is 66 mm. This is sufficiently large to render the proximity effect negligibly small. The view factor is calculated from the geometry, which can be modeled as two concentric cylinders. The surface area  $A_2$  of the heat shield amounts to  $0.5 \text{ m}^2$ . The view factor  $\varphi_{21}$  has been calculated with the equation given in [134] and amounts to 0.088. As the shield is made from untreated copper, it is slightly oxidized. The emissivity  $\varepsilon_1$  is in the range of 0.06, while the stainless steel body of the mixing chamber has an emissivity of  $\varepsilon_2 = 0.12$ . As already stated above, the temperature of the mixing chamber is  $T_1 = 15.7 \text{ mK}$ , while the temperature of the heat shield is  $T_2 = 55 \text{ mK}$ . The resulting heat load on the dilution refrigerator is

$$\dot{Q}_{12} = \varphi_{21} \cdot A_2 \cdot \varepsilon_1 \cdot \varepsilon_2 \cdot \sigma \cdot (T_2^4 - T_1^4) = 163 \text{ aW}. \quad [4.69]$$

#### ***4.6 Heat Load due to Cosmic Rays***

Cosmic rays originate from solar particle events (SPEs) and sources located outside the solar system. Above the atmosphere, cosmic rays mainly consist of free protons, electrons and helium nuclei. These primary cosmic rays interact with the gas in the atmosphere, which results in showers of secondary particles. Muons and neutrinos, which are the most numerous charged particles at sea level, are decay products of charged mesons, while electrons, positrons and photons primarily originate from the decay of neutral mesons. Only muons and neutrinos can penetrate to typical depths of underground laboratories, where they directly interact with the cold mass or produce tertiary particles (photons, electrons or hadrons) upon interaction with adjacent matter such as rock [53].

Cosmic rays penetrating the cold mass of a very low temperature experiment (such as a detector crystal or a gravitational wave antenna) cause a time constant heat load, whose magnitude depends on the particle flux, the spectral distribution of the cosmic rays and the target material. The decay and energy loss processes of particles passing through matter can best be evaluated by Monte Carlo simulation. In the following, a brief estimation is carried out to determine the order of magnitude of the heat load to



be expected. It is evident that this number highly depends on the location of an experiment, i.e. a much higher energy deposit must be expected for cold masses installed on spacecraft than for cold masses in underground laboratories, for instance. At the earth's surface, muons are the primary heat source resulting from cosmic rays.

The integral intensity of vertical muons at sea level amounts to approximately  $70 \text{ m}^{-2}\text{s}^{-1}\text{sr}^{-1}$  or roughly  $1 \text{ cm}^{-2}\text{min}^{-1}$  for horizontal surfaces. The intensity depends on the geomagnetic latitude, the muons' interaction mean free path and the solar cycle [4]. The mean energy of cosmic muons at sea level is approximately 4 GeV [53].

Rastin has performed measurements of the sea-level muon differential spectrum  $I_d(p)$  in the momentum range from  $p_1 = 0.35 \text{ GeV}/c$  to  $p_2 = 3000 \text{ GeV}/c$  [113]. In order to calculate the heat deposit of these particles in a certain target, the stopping power  $dE/dx$  has to be known. It can be found in the literature for various materials. The differential muon intensity on the earth's surface can now be multiplied with the stopping power and with  $2\pi$ , the solid angle for a hemisphere. This simplification yields conservative results. By integrating this product over the muon momentum range, an upper limit for the heat load in a mass  $m$  due to cosmic rays is obtained:

$$\frac{\dot{Q}}{m} = 2\pi \cdot \int_{p_1}^{p_2} I_d(p) \cdot \frac{dE}{dx}(p) \cdot dp. \quad [4.70]$$

The energy dissipated per second in one gram of copper, for instance, can be calculated to be  $1.8 \cdot 10^{-14} \text{ W/g}$ . The value for stainless steel is very similar, namely  $1.86 \cdot 10^{-14} \text{ W/g}$ . Due to the higher stopping power, some  $2.37 \cdot 10^{-14} \text{ W/g}$  are dissipated in liquid helium. These results correspond fairly well to values stated by Pobell [108, 109] and Neganov [97], who report an energy deposit of approximately  $10^{-14} \text{ W/g}$ . Niinikoski<sup>19</sup> has given a similar value of  $3 \cdot 10^{-14} \text{ W/g}$ . Due to these low values, the energy deposit is not expected to be dangerous to the performance of a dilution refrigerator, even if the detector is of high mass. Bugaev et al. [20] give data on the total muon flux in many underground laboratories, which is in the range of  $2 \cdot 10^{-5} \text{ m}^{-2}\text{s}^{-1}\text{sr}^{-1}$ . It is thus concluded that the residual heat load due to cosmic rays can be completely neglected in experiments operated underground.

---

<sup>19</sup> Private communication from Dr. Tapio O. Niinikoski (CERN), 2006

The mixing chamber of the CCDR is made of stainless steel and has a mass of 1870 g. It has a volume of 151 cm<sup>3</sup>, which corresponds to 21 g of He. The <sup>3</sup>He trap, which is made from copper, has a mass of 27 g. With the values given above, this results in a heat load of 36 pW resulting from the interaction with muons.

#### ***4.7 Summary and Scaling Laws***

Table 10 and Table 11 summarize the time dependent and constant sources of residual heat and list the parameters on which their magnitude depends. The decay laws are given for time dependent heat loads. Approximate absolute values are stated for the magnitude of each heat source. The mixing chamber temperature was assumed to be in the low mK range. The values are valid for experiments which do not feature special shielding against cosmic rays and are constructed from standard materials with normal radioactive contamination.

Time dependent heat loads are most likely dominated by the ortho-para conversion of hydrogen and by relaxation of thermoelastic stress. The heat loads resulting from these two sources can be reduced considerably by annealing. For very large, integral cold masses – such as the bars and spheres used in gravitational wave detectors - annealing might not always be possible. Materials should thus be screened for a low hydrogen contamination and impurity concentration.

More experimental work should be performed on the relaxation of thermoelastic stress. This could be done by comparing the time dependent heat release of samples which underwent different thermal treatments to change the grain size of the metal.

The constant heat load is most likely dominated by heat transport due to conduction in residual gas, especially in the case of multi-ton cold masses with surface areas of several m<sup>2</sup>. More experimental work should be performed to study this effect more thoroughly. It is suggested to add additional thermal screens around the mixing chamber of the CCDR and study whether the heat load drops further.

The heat load resulting from radioactive decays and the interaction of the cold mass with cosmic rays can be neglected in most cases, especially in dark matter detector arrays which are constructed from extremely radiopure materials and operated underground.

Based on the data presented above, a list of recommendations for the minimization of the residual heat load on VLT cooling systems has been established:

- The mass of the cold parts in a VLT apparatus should be minimized. While this is not an option for gravitational wave antennas or the target material of dark matter detector arrays, supporting structures should be carefully designed for low mass.
- Metals, which are used for the construction of the cold mass, must be annealed for several hours close to their melting temperature. In order to allow for large grains to form, cool-down to ambient temperature should be effected as slowly as possible.
- Amorphous materials should not be used excessively in the cold mass. In dark matter detector arrays, polyethylene (PE) is sometimes used as a neutron shield. These PE shields should be located away from the mixing chamber and heat-sunk at a higher temperature stage.
- The temperature of the last shield around the cold mass should be as low as possible, preferably in the range from 50 to 100 mK. This measure is expected to reduce the heat load due to conduction in residual gas and due to thermal radiation. Sufficient spacing between the shields avoids heat transfer by evanescent waves.
- A further reduction of the heat load due to conduction in residual gas can be achieved by improving the vacuum levels inside the cryostat. All surfaces should be kept clean and not be touched with bare hands. Charcoal traps must be foreseen in the vacuum space. Metallic seals should be preferred to O-rings.
- The cold mass must be mechanically decoupled from vibrating equipment by a well designed support structure and flexible connection lines.

Time Dependent Heat Loads				
Source	Scales with	Time Dependence	Typical Value after 24 h	Means of Reduction
Ortho-para conversion of hydrogen	<ul style="list-style-type: none"> <li>• Mass</li> <li>• Hydrogen contamination</li> </ul>	$(1 + k \cdot t)^{-2}$ $k = 1.4 \cdot 10^{-2} \text{ h}^{-1}$	Copper: 18 pW/(g·ppm)	<ul style="list-style-type: none"> <li>• Lightweight design</li> <li>• Annealing of metal parts</li> <li>• Screen construction materials for hydrogen contamination</li> </ul>
Tunneling affects in amorphous materials	<ul style="list-style-type: none"> <li>• Total mass of amorphous materials</li> </ul>	$t^{-k}$ $k \approx 1$	Vitreous silica: 100 pW/g	<ul style="list-style-type: none"> <li>• Minimize use of amorphous materials</li> </ul>
Tunneling effects in crystalline materials	<ul style="list-style-type: none"> <li>• Mass</li> <li>• Density of impurities in crystalline materials</li> <li>• Dislocation density in metals</li> </ul>	$t^{-k}$ $k \approx 1$	Copper: 17 pW/g	<ul style="list-style-type: none"> <li>• Lightweight design</li> <li>• Minimize impurity density in crystalline materials (screen materials)</li> <li>• Minimize dislocation density in metals (annealing)</li> </ul>
Relaxation of thermoelastic stress	<ul style="list-style-type: none"> <li>• Mass</li> <li>• Grain size</li> <li>• Thickness of boundary layer</li> </ul>	$e^{-\frac{t}{k}}$ $k = 100 \text{ h}$	Copper: 400 pW/g	<ul style="list-style-type: none"> <li>• Lightweight design</li> <li>• Thermal treatment to increase grain size and reduce thickness of boundary layer (annealing followed by slow cool-down)</li> </ul>
Structural Relaxation	<ul style="list-style-type: none"> <li>• Stress levels in support structure</li> <li>• Amount of cold working</li> </ul>	$\ln(1 + \text{const} \cdot t)$	< 2.3 pW/g	<ul style="list-style-type: none"> <li>• Anneal metals after cold working (minimize dislocation density)</li> <li>• Avoid highly stressed structures</li> </ul>

Table 10: Summary of time dependent residual heat sources and scaling laws

Constant Heat Loads			
Source	Scales with	Typical Value	Means of Reduction
Thermal conduction	<ul style="list-style-type: none"> <li>Thermal conductivity of support structure material</li> <li>Geometry of support structure</li> <li>Heat sink temperature</li> </ul>	$\theta = 72.5 \text{ mW}/(\text{mK}^2)$ for 200 mK $\Delta T$ : 2.9 mW/m for 100 mK $\Delta T$ : 725 $\mu\text{W}/\text{m}$ for 50 mK $\Delta T$ : 181 $\mu\text{W}/\text{m}$	<ul style="list-style-type: none"> <li>Thermal conductivity of support structure</li> <li>Geometry of support structure</li> <li>Heat sink temperature</li> </ul>
Vibrating structures	<ul style="list-style-type: none"> <li>Internal friction of cold mass material</li> <li>Vibration environment</li> </ul>	$< 25 \text{ fW/g}$ in metallic structures $< 16 \text{ nW/g}$ in liquid helium	<ul style="list-style-type: none"> <li>Rigid support structure</li> <li>Vibration environment</li> </ul>
Heat transport by residual gas	<ul style="list-style-type: none"> <li>Surface of cold mass</li> <li>Residual gas pressure</li> <li>Residual gas composition</li> <li>Temperature of last shield</li> </ul>	$8 \mu\text{W}/(\text{m}^2\text{K})$ for 200 mK $\Delta T$ : 1.6 $\mu\text{W}/\text{m}^2$ for 100 mK $\Delta T$ : 800 nW/m <sup>2</sup> for 50 mK $\Delta T$ : 400 nW/m <sup>2</sup>	<ul style="list-style-type: none"> <li>Use <sup>3</sup>He as exchange gas</li> <li>Reduce hydrogen abundance in vacuum space</li> <li>Reduce temperature of last heat shield</li> </ul>
Thermal radiation	<ul style="list-style-type: none"> <li>Surface area of cold mass and shield</li> <li>Temperature of last shield</li> <li>Shield distance (due to proximity effect)</li> <li>Emissivity</li> </ul>	$7 \text{ nW}/(\text{m}^2\text{K}^4)$ for last shield @ 200 mK: 11 pW/m <sup>2</sup> for last shield @ 100 mK: 700 fW/m <sup>2</sup> for last shield @ 50 mK: 44 fW/m <sup>2</sup>	<ul style="list-style-type: none"> <li>Reduce temperature of last heat shield</li> <li>Sufficient spacing between shields</li> <li>Choose materials for low emissivity</li> </ul>
Radioactive decay	<ul style="list-style-type: none"> <li>Mass</li> <li>Radioactive contamination</li> </ul>	230 fW/g	<ul style="list-style-type: none"> <li>Lightweight design</li> <li>Material selection (radiopurity)</li> </ul>
Cosmic rays	<ul style="list-style-type: none"> <li>Mass</li> <li>Cosmic ray flux</li> </ul>	20 fW/g	<ul style="list-style-type: none"> <li>Lightweight design</li> <li>Improved shielding</li> </ul>

Table 11: Summary of constant and quasi-constant residual heat sources and scaling laws

## 5. Principles of Dilution Refrigerator Design

### 5.1 Design of Precooling Heat Exchangers

A typical dilution refrigeration system comprises several heat exchangers for the cooling of  $^3\text{He}$  and  $^4\text{He}$  in both their gaseous and liquid state. The definition of the efficiency  $\varepsilon$  of a heat exchanger according to [14] has already been given above:

$$\varepsilon = \frac{\text{Actual Energy Transfer}}{\text{Ideal Energy Transfer}}. \quad [5.1]$$

The ideal energy transfer is achieved by a heat exchanger which cools the hot stream to the exact temperature of the cold stream, which is not possible in reality. The efficiency  $\varepsilon$  can thus never reach unity. A well designed heat exchanger in a cryogenic apparatus should have an efficiency  $\varepsilon > 99\%$ . Efficiency can be gained at the cost of increased pressure drop. Heat exchanger design thus always involves finding a good balance between efficiency and flow impedance.

Heat exchangers for cryogenic applications mostly work over temperature ranges which are too large to justify the assumption of constant fluid properties. As a consequence, heat exchangers usually have to be split in several sections, which are then treated separately. While co-current flow heat exchangers and heat exchangers where one fluid is at constant temperature (such as heat exchangers submersed in a boiling liquid) can be treated straightforwardly, iteration is necessary for counterflow heat exchangers.

A tube-in-tube geometry is often used for heat exchangers carrying gases at pressures high enough for viscous flow. The inner flow channel is confined by a circular tube; the outer flow channel is of annular cross-section. Heat exchangers operating at lower pressures, such as in pump lines, often consist of a helical tube wound inside a larger tube which carries the low pressure gas. Heat transfer on the outer surface of the helical tube can be calculated with the correlations for a cylinder in transversal flow. The surface area available for heat transfer can be enhanced by adding fins to the tube. These fins can be modeled by plates. Heat transfer coefficients and friction factors for these most common geometries are given below.

*HEAT TRANSFER COEFFICIENTS*

In most cases, heat exchangers rely on forced convection heat transfer. Forced convection is characterized by the Nusselt number  $Nu$ . The heat transfer coefficient  $\alpha$  can be calculated from the Nusselt number  $Nu$  as follows:

$$\alpha = \frac{\lambda}{l} \cdot Nu. \quad [5.2]$$

The dimension of  $\alpha$  in SI units is  $W/(m^2 \cdot K)$ ;  $\lambda$  is the thermal conductivity of the fluid and  $l$  is a characteristic dimension. For circular tubes,  $l$  is equal to the tube diameter  $d$ . In annular gaps,  $l$  is equal to the hydraulic diameter  $d_h$ , which is the difference between the outer diameter  $d_o$  and the inner diameter  $d_i$ . For plates,  $l$  is the dimension of the plate in the direction of fluid flow. For cylinders with diameter  $d$ , which are subjected to transversal flow,  $l$  amounts to  $d \cdot \pi/2$ . Heat transfer heavily depends on the flow regime, which can be laminar or turbulent. The flow regime is characterized by the dimensionless Reynolds number  $Re$ , which is defined as

$$Re = \frac{w \cdot l}{\nu}, \quad [5.3]$$

where  $w$  is the fluid velocity,  $l$  the characteristic dimension (as defined above) and  $\nu$  the kinematic viscosity of the fluid. Laminar flow in circular and annular tubes and across cylinders is characterized by Reynolds numbers below 2300. At higher  $Re$ , flow is turbulent. For flow along flat plates, the critical Reynolds number amounts to  $10^5$ . The characteristic dimension in equation [5.3] depends on the geometry. Formulas for the Reynolds number for typical geometries are given in Table 12.

Heat transfer also depends on the direction of heat flux, i.e. whether heat flows from the fluid to the wall or from the wall to the fluid. This can be accounted for by equation [5.4].  $Pr$  is the Prandtl number of the fluid at its actual temperature, and  $Pr_w$  is the Prandtl number of the fluid if it were at wall temperature.

$$Nu = Nu_0 \cdot \left( \frac{Pr}{Pr_w} \right)^{0.11}. \quad [5.4]$$

A compilation of the most important formulas for  $Nu_0$ , which are discussed in great detail in [57], is presented in Table 12.

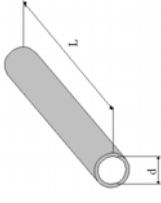
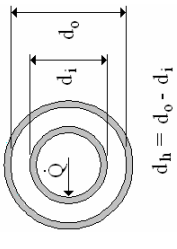
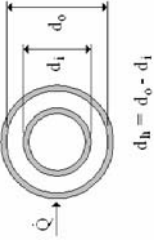
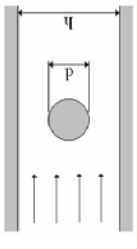
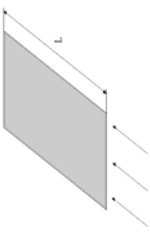
Geometry	Re	Laminar Flow (Re < 2300)	Turbulent Flow (Re > 2300)
	$\text{Re} = \frac{w \cdot d}{\nu}$	$\text{Nu}_0 = \sqrt[3]{3.66^3 + 1.61^3 \cdot \text{Re} \cdot \text{Pr} \cdot \frac{d}{l}}$	$\text{Nu}_0 = \frac{\frac{\xi}{8} \cdot (\text{Re} - 1000) \cdot \text{Pr}}{1 + 12.7 \cdot \sqrt{\frac{\xi}{8}} \cdot \left( \text{Pr}^{\frac{2}{3}} - 1 \right)} \cdot \left[ 1 + \left( \frac{d}{l} \right)^{\frac{2}{3}} \right]$ with $\frac{\xi}{\text{Re}} = \frac{1}{(1.82 \cdot \log_{10} \text{Re} - 1.64)^2}$
	$\text{Re} = \frac{w \cdot (d_o - d_i)}{\nu}$	$\text{Nu}_0 = 3.66 + 1.2 \cdot \left( \frac{d_o}{d_i} \right)^{0.8} + \left( 1 + 0.14 \cdot \sqrt{\frac{d_o}{d_i}} \right) \cdot \frac{0.19 \cdot \left( \text{Re} \cdot \text{Pr} \cdot \frac{d_h}{l} \right)^{0.8}}{1 + 0.117 \cdot \left( \text{Re} \cdot \text{Pr} \cdot \frac{d_h}{l} \right)^{0.467}}$	$\text{Nu}_0 = \frac{\frac{\xi}{8} \cdot (\text{Re} - 1000) \cdot \text{Pr}}{1 + 12.7 \cdot \sqrt{\frac{\xi}{8}} \cdot \left( \text{Pr}^{\frac{2}{3}} - 1 \right)} \cdot \left[ 1 + \left( \frac{d_l}{l} \right)^{\frac{2}{3}} \right] \cdot 0.86 \cdot \left( \frac{d_a}{d_i} \right)^{0.16}$
	$\text{Re} = \frac{w \cdot (d_o - d_i)}{\nu}$	$\text{Nu}_0 = 3.66 + 1.2 \cdot \left( \frac{d_l}{d_o} \right)^{0.8} + \left( 1 + 0.14 \cdot \sqrt{\frac{d_o}{d_l}} \right) \cdot \frac{0.19 \cdot \left( \text{Re} \cdot \text{Pr} \cdot \frac{d_h}{l} \right)^{0.8}}{1 + 0.117 \cdot \left( \text{Re} \cdot \text{Pr} \cdot \frac{d_h}{l} \right)^{0.467}}$	$\text{Nu}_0 = \frac{\frac{\xi}{8} \cdot (\text{Re} - 1000) \cdot \text{Pr}}{1 + 12.7 \cdot \sqrt{\frac{\xi}{8}} \cdot \left( \text{Pr}^{\frac{2}{3}} - 1 \right)} \cdot \left[ 1 + \left( \frac{d_l}{l} \right)^{\frac{2}{3}} \right] \cdot \left( 1 - 0.14 \cdot \left( \frac{d_l}{d_a} \right)^{0.6} \right)$
	$\text{Re} = \frac{w \cdot d}{\nu} \cdot \frac{\pi}{2}$	$\text{Nu}_0 = \sqrt{\text{Nu}_{\text{lam}}^2 + \text{Nu}_{\text{turb}}^2}$ with $\text{Nu}_{\text{lam}} = 0.664 \cdot \sqrt{\text{Re}} \cdot \sqrt[3]{\text{Pr}}$ and $\text{Nu}_{\text{turb}} = \frac{0.037 \cdot \text{Re}^{0.8} \cdot \text{Pr}}{1 + 2.443 \cdot \text{Re}^{-0.1} \cdot (\text{Pr}^{2/3} - 1)}$	
	$\text{Re} = \frac{w \cdot L}{\nu}$	$\text{Re} < 10^5: \text{Nu}_0 = 0.664 \cdot \sqrt{\text{Re}} \cdot \sqrt[3]{\text{Pr}}$	$\text{Re} > 10^5: \text{Nu}_0 = \frac{0.037 \cdot \text{Re}^{0.8} \cdot \text{Pr}}{1 + 2.443 \cdot \text{Re}^{-0.1} \cdot (\text{Pr}^{2/3} - 1)}$

Table 12: Reynolds and Nusselt numbers for typical heat exchanger geometries [57]



*PRESSURE DROP*

The frictional pressure drop  $\Delta p$  in a flow channel is given by relation [5.5], where  $\rho$  is the fluid density and  $w$  the fluid velocity:

$$\Delta p = \xi \cdot \frac{\rho \cdot w^2}{2}. \quad [5.5]$$

The variable  $\xi$  is the dimensionless friction factor. For laminar flow in circular tubes with Reynolds numbers below 2300,  $\xi$  amounts to

$$\xi = \frac{l}{d} \cdot \frac{64}{\text{Re}}, \quad [5.6]$$

where  $l$  is the length of the flow channel and  $d$  its diameter. In non-circular cross-sections,  $\xi$  must be calculated as above and multiplied by a factor  $\varphi$ , which depends on the geometry of the cross-section and can be obtained from the viewgraphs in [71]. The factor  $\varphi$  is usually smaller than 1.5. The characteristic length  $l$  for the calculation of the Reynolds number for non-circular cross-sections is

$$l = 4 \cdot \frac{A}{p}, \quad [5.7]$$

where  $A$  is the free surface area of the flow channel and  $p$  its perimeter. The friction factor for turbulent flow in tubes of all cross-sections can be calculated from Blasius' equation:

$$\xi = \frac{l}{d} \cdot \frac{0.3164}{\sqrt[4]{\text{Re}}}. \quad [5.8]$$

The pressure drop along a bank of tubes can also be evaluated with equation [5.5]. The friction factor depends on the geometry of the bank as outlined in [71].

*FLUID PROPERTIES*

It is convenient to evaluate the heat transfer and friction factors automatically with the aid of a computer, as such calculations are often iterative and have to be repeated several times in the course of a design optimization process. For such calculations it is practical to use explicit functions which describe a certain material property as a

function of one or several parameters. A compilation for the material properties of gaseous  $^3\text{He}$  and  $^4\text{He}$  is given in Table 13 and Table 14. The unit of  $T$  in the formulas is K. The deviation between experimental values from [33] and [136] and the results yielded by the formulas is sometimes fairly high due to the fact that a large temperature range is covered by a single equation. However, a designer will always include some margin of safety in his calculations, which will compensate for these deviations. As experimental values could not always be found for comparison, values for the range and maximum deviation are sometimes not available (N/A).

Property	Symbol and Unit	Equation	Range	max. deviation	Ref.
Thermal conductivity	$\lambda$ [W/(m·K)]	$\lambda = 0.00328 \cdot T^{0.675}$	$p \approx 1$ bar $4.3 \text{ K} < T < 300 \text{ K}$	8.6 %	[136]
Kinematic viscosity	$\nu$ [m <sup>2</sup> /s]	$\nu = 9.613 \cdot 10^{-9} \cdot T^{1.659}$	$p \approx 1$ bar $6 \text{ K} < T < 300 \text{ K}$	6.7 %	[136]
Density	$\rho$ [kg/m <sup>3</sup> ]	$\rho = \frac{T}{0.02172 \cdot T^2 - 0.1238}$	$p \approx 1$ bar $4.3 \text{ K} < T < 300 \text{ K}$	4.5 %	[136]
		$\rho = \frac{p}{2077 \cdot T}$	$8 \text{ K} < T < 300 \text{ K}$	5.5 %	Ideal Gas
Prandtl Number	Pr [1]	$Pr = 0.667$	$12 \text{ K} < T < 300 \text{ K}$	7.8 %	Ideal Gas
Specific Heat	$c_p$ [J/(kg·K)]	$c_p = \frac{48200}{T^2} + 5144$	$p \approx 1$ bar $4.3 \text{ K} < T < 300 \text{ K}$	8.9 %	[136]
		$c_p = \frac{5}{2} \cdot \frac{R}{M} = 5196.5$	$20 \text{ K} < T < 300 \text{ K}$	1.1 %	Ideal Gas

**Table 13: Fitted functions for material properties of gaseous  $^4\text{He}$**

Property	Symbol and Unit	Equation	Range	max. deviation	Ref.
Thermal conductivity	$\lambda$ [W/(m·K)]	$\lambda = 0.00427 \cdot T^{0.658}$	$p \approx 1$ bar $4 \text{ K} < T < 300 \text{ K}$	5.4 %	[33]
Kinematic viscosity	$\nu$ [m <sup>2</sup> /s]	$\nu = \frac{1.182 \cdot 10^{-3} \cdot T^{1.651}}{p}$	$8 \text{ K} < T < 300 \text{ K}$	2.4 %	[33]
Density	$\rho$ [kg/m <sup>3</sup> ]	$\rho = \frac{p}{2771 \cdot T}$	N/A	N/A	Ideal Gas
Prandtl Number	Pr [1]	$Pr = 0.667$	N/A	N/A	Ideal Gas
Specific Heat	$c_p$ [J/(kg·K)]	$c_p = \frac{5}{2} \cdot \frac{R}{M} = 6928.7$	N/A	N/A	Ideal Gas

**Table 14: Fitted functions for material properties of gaseous  $^3\text{He}$**

## 5.2 Heat Transfer in the 1 K Pot and the Still

In a typical dilution refrigerator,  $^3\text{He}$  is condensed in a tube located in the 1 K pot. In the first section of this condenser, gaseous  $^3\text{He}$  is precooled to its condensation temperature. In the mid section, the phase change takes place, and in the last section, the liquid  $^3\text{He}$  stream is subcooled to the temperature of the 1 K pot.

The liquid  $^4\text{He}$  in the 1K pot is in its superfluid state. The heat transfer between the liquid in the pot and solid surfaces - such as the condenser tube or the wall of the pot - is dominated by Kapitza conductance which obeys the law given in equation [1.8]. The specific heat flux  $\dot{q}$  thus amounts to:

$$\dot{q} = S \cdot (T_1^4 - T_2^4), \quad [5.9]$$

where  $S$  is an empirically determined constant. For the heat transfer between Cu and  $^4\text{He}$ ,  $S$  amounts to  $225 \text{ W}/(\text{m}^2 \cdot \text{K}^4)$ , and for CuNi and  $^4\text{He}$  to  $170 \text{ W}/(\text{m}^2 \cdot \text{K}^4)$  [128]. These values are valid in the temperature region between 1.1 K and 2.1 K. The heat flux does not depend on fluid velocity. At heat fluxes typically encountered in the 1 K pot, boiling does not occur on the heated surfaces as the  $^4\text{He}$  in the 1 K pot is superfluid.

Heat transfer inside the condenser tube is dominated by three different regimes. In the first tube section, the  $^3\text{He}$  is in the gaseous state and the equations from section 5.1 may be used. As soon as the fluid reaches its pressure dependent condensation temperature, two-phase flow develops. Kuzmenko [82] measured heat transfer coefficients for the condensation of  $^3\text{He}$  in vertical tubes, which amount to a few hundred  $\text{W}/(\text{m}^2 \cdot \text{K})$ . He found that experimental results are in excellent agreement with Nusselt's theory. It may be concluded that the same is true for the condensation heat transfer coefficient in horizontal tubes, which can be calculated from

$$\alpha = 0.725 \cdot \sqrt[4]{\frac{\lambda^3 \cdot L \cdot g \cdot \rho \cdot (1 - \rho_D / \rho)}{d \cdot \nu \cdot (T_D - T_w)}}, \quad [5.10]$$

where  $\lambda$  is the thermal conductivity of the liquid phase,  $\nu$  its kinematic viscosity,  $\rho$  its density, and  $c_p$  its specific heat;  $\rho_G$  is the density of the gaseous phase, and  $T_G$  its temperature [16]. The gravitational acceleration  $g$  amounts to  $9.81 \text{ m/s}^2$ .  $L$  is the latent heat of evaporation and  $T_w$  the wall temperature of the tube. The tube diameter is  $d$ .

Typical values encountered in the condenser of a dilution refrigerator are  $d = 2$  mm and  $T_W = 1.2$  K. At fairly low flow rates,  $^3\text{He}$  is at a pressure of some 100 mbar and thus condenses at a temperature  $T_G = 1.7$  K. Using the values given in Table 14 and Table 15 (page 102), the condensation heat transfer coefficient can be calculated to be  $710 \text{ W}/(\text{m}^2 \cdot \text{K})$ .

The value yielded by equation [5.10] needs to be multiplied by a factor  $f$  to take into account the reduced heat transfer coefficient in the areas where a layer of liquid helium is covering the walls of the condenser [16]. The quality factor  $\dot{x}$  is the ratio between the mass flow of the vapor and the total mass flow of the fluid:

$$f = \left( 1 + \frac{1 - \dot{x}}{\dot{x}} \cdot \left( \frac{\rho_D}{\rho} \right)^{\frac{2}{3}} \right)^{-\frac{3}{4}}. \quad [5.11]$$

The last section of the condenser is completely filled with liquid  $^3\text{He}$ , which is subcooled and approaches the temperature of the 1 K pot along the length of the condenser. For this third section, equation [5.9] may be used to calculate the heat transfer. The constant  $S$  amounts to  $20 \text{ W}/(\text{m}^2 \cdot \text{K}^4)$  for the heat transfer between  $^3\text{He}$  and Cu and to  $100 \text{ W}/(\text{m}^2 \cdot \text{K}^4)$  between  $^3\text{He}$  and CuNi [91]. The same values can be used for the heat exchanger in the still, where the concentrated stream is further subcooled before entering the main heat exchanger.

The dilute solution in the still is in the regime of nucleate boiling. The heat transfer coefficient between the still heat exchanger and the dilute solution boiling in the still is  $50 \text{ W}/(\text{m}^2 \cdot \text{K})$  according to Niinikoski. If the heat flux exceeds a critical value, film boiling commences. The gas layer resulting from film boiling blankets the surface, acts as an insulator and may increase the temperature difference to some 5 K. The heat flux should be kept below  $30 \text{ W}/\text{m}^2$  and the temperature difference below 0.6 K to avoid such burnout conditions.<sup>20</sup> Dorey [37] measured similar values ( $30 \text{ W}/\text{m}^2$  at 0.8 K) for the heat flux to liquid He.

Heat transfer in two-phase flow is the least understood process of the phenomena discussed above and experiments on the heat transfer in the condenser and the still are

---

<sup>20</sup> Private communication from Dr. Tapio O. Niinikoski (CERN), 2006

encouraged. The material properties of  $^3\text{He}$ , which are needed for the calculations outlined above, are given in Table 15. They have been fitted from data given in [33].

Property	Symbol and Unit	Equation	Range	max. deviation
Thermal conductivity	$\lambda$ [W/mK]	$\lambda = 0.6 + 0.4 \cdot T$	0.5 K < T < 3 K	N/A
Kinematic viscosity	$\nu$ [m <sup>2</sup> /s]	$\nu = 1.73 \cdot 10^{-8} \cdot \frac{e^{0.51 \cdot T}}{T}$	0.5 K < T < 3 K	1.6 %
Density	$\rho$ [kg/m <sup>3</sup> ]	$\rho = -2.31 \cdot T^2 + 85.2$	0.6 K < T < 3 K	2.9 %
Specific Heat	$c_p$ [J/(kg·K)]	$c_p = 407.7 \cdot T^2 + 1014$	0.4 K < T < 2.4 K	2.0 %
Latent Heat	$L$ [J/kg]	$L = \frac{10^5}{1.85 \cdot (T - 1.94)^2 + 6.45}$	0.4 K < T < 2.8 K	2.9 %
Vapor Pressure	$p$ [Pa]	$p = 1213 \cdot T^{4.453 - 0.532 \cdot \ln(T)}$	0.9 K < T < 3 K	11 %

**Table 15: Fitted functions for material properties of liquid  $^3\text{He}$**

### 5.3 Optimization of Sintered Heat Exchangers

The sintered main heat exchanger is without doubt the component which influences the performance of a dilution refrigerator most. Special attention has to be paid to its design. The most important parameter characterizing a sintered heat exchanger is the surface area available for heat exchange.

Once this value has been determined from the required cooling power and mixing chamber temperature [99], the number of sintered elements has to be fixed. The upper limit of the number of elements is set by practical considerations such as increased manufacturing costs. The lower limit is set by the necessity of approximating a temperature profile along the heat exchanger which resembles the temperature profile along an ideal, continuous heat exchanger; otherwise, the performance of the dilution refrigerator will be seriously impaired.

The numerical methods presented in chapter 3 can be used to take into account the negative impact of a finite number of heat exchanger elements and may thus be a useful tool for the optimization of a heat exchanger design. In the following, a few additional aspects of sintered heat exchangers will be discussed.

*METAL POWDERS AND SINTERING*

The large heat exchange surface areas required for powerful dilution refrigerators are best achieved with sintered metal powders. The surface area  $A$  of a sintered sponge with volume  $V$  can be calculated with equation [5.12]

$$A = \frac{6 \cdot \psi \cdot V}{d_e}, \quad [5.12]$$

where  $\psi$  is the filling factor and  $d_e$  the effective diameter of the powder. It is obvious that a smaller grain diameter leads to larger surface areas; while copper powder with an effective diameter of  $d_e = 18 \mu\text{m}$  and  $\psi = 0.4$  has been used for the CCDR, powders with  $d_e = 1.8 \mu\text{m}$  are commercially available.

The parameters of the sintering process influence the sponge's thermal performance, which is characterized both by the available surface area and by the thermal contact between the sponge and the solid substrate onto which it is sintered. In addition, the thermal contact between the grains, which can also be expressed as the thermal conductivity of the sponge, is influenced. Higher temperatures and longer sintering durations decrease the available surface area but improve the thermal contact between the sintered grains and between the sponge and the solid substrate. Niinikoski recommends sintering copper powder for 45 minutes at 850 °C. The first 25 minutes of sintering should be done in a gas mixture of 6 % H<sub>2</sub> and 94 % Ar at a pressure of 500 mbar to remove the oxide layer from the grains, followed by 20 minutes of sintering under vacuum to remove H<sub>2</sub> which may have dissolved in the copper. Prior pressing of the powder is not necessary.<sup>21</sup>

A good thermal contact between the solid and the sponge can be achieved by first sintering a thin layer of powder to the solid; this is done at high temperature and long duration. A second, thicker layer is then sintered onto the first, this time at lower temperature. This second layer has a fairly high surface area and ensures a good thermal contact to the liquid, while the first layer has a rather small surface and provides a good thermal contact between the sponge and the solid. Roughening the surface of the solid substrate also improves the thermal contact to the sponge.

---

<sup>21</sup> Private communication from Dr. Tapio O. Niinikoski (CERN), 2005

*DIFFERENT TYPES OF SINTERED ELEMENTS*

Sintered elements for a heat exchanger can be manufactured in many ways which differ in complexity and cost, but also in performance. Figure 42 shows some of these design options. The heat exchanger elements named (a), (b), and (c) are shown without the copper powder which has to be sintered to the outside of the tube to provide a good thermal contact to the dilute stream. The elements used in the CCDR are of design (a). Their main advantage is the ease of manufacture.

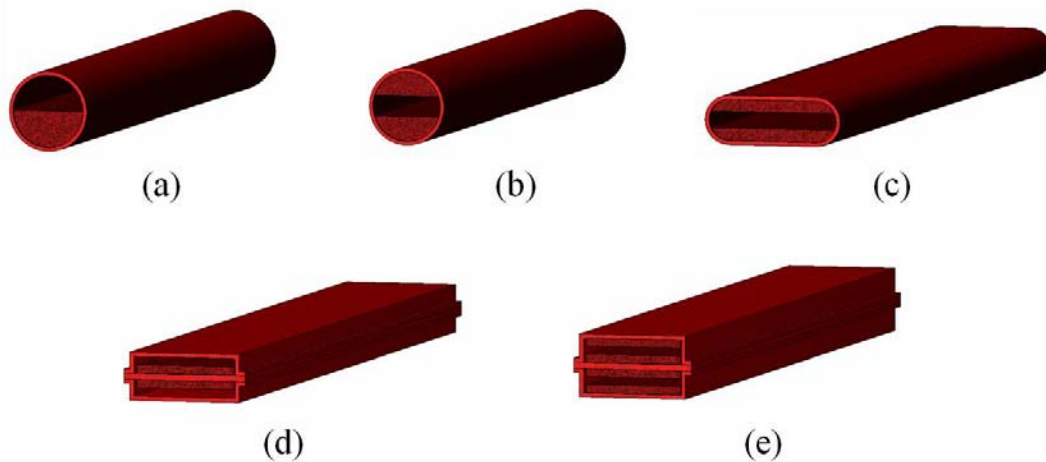


**Figure 42: Examples for sintered heat exchanger geometries**

Increased performance is achieved by reducing the thickness of the sintered sponge while keeping the total volume of the sintered sponge constant. This can be accomplished by splitting the sponge in two as shown in Figure 42 (b), and even better by rolling – and thus flattening - the tube as shown in (c). Elements (d) and (e) are considerably more complicated to manufacture, but are expected to feature superior performance.

Important parameters for the design of a heat exchanger are the cross sections of the concentrated and dilute streams. The concentrated stream must be dimensioned such that neither viscous heating nor axial conduction in the liquid impair the performance of the dilution refrigerator. Formulas for the ideal dimensions are given in [99]. In addition, the dilute stream must be dimensioned such that mutual friction does not occur. When mutual friction occurs,  $^4\text{He}$  is dragged into the still from the mixing chamber by the moving  $^3\text{He}$  and increases the  $^4\text{He}$  contamination of the concentrated stream. Castelijns [23, 24] derived the following relation for the critical  $^3\text{He}$  flow rate  $\dot{n}_{3,crit}$  which determines the onset of mutual friction:

$$\dot{n}_{3,crit} = \frac{D^2 \pi}{4} \cdot \left( \frac{x_m}{\gamma \cdot L} \right)^{\frac{1}{2.8}}, \quad [5.13]$$

where  $L$  is the length of the dilute stream,  $D$  is its diameter and  $x_m$  is the  $^3\text{He}$  concentration in the dilute solution. This amounts to 0.07 at low temperatures. The constant  $\gamma$  is  $35 \cdot 10^{-9} \text{ m}^{4.6} \cdot \text{s}^{2.8} \cdot \text{mol}^{-2.8}$ .

A prototype for the heat exchanger element (e), which is planned for the EURECA dilution refrigerator, has been manufactured at CERN. It is shown in Figure 43. The element consists of two identical copper shells and a separation plate. Copper powder is sintered to the inside surfaces of the shells and to both sides of the plate (Figure 43 a). In the next step, the two shells and the plate are welded together (b). The two volumes between the shells and the plate are for the concentrated and dilute stream respectively. The heat exchanger is built by connecting several such elements with tubes of a low-conductivity material, such as CuNi (c).

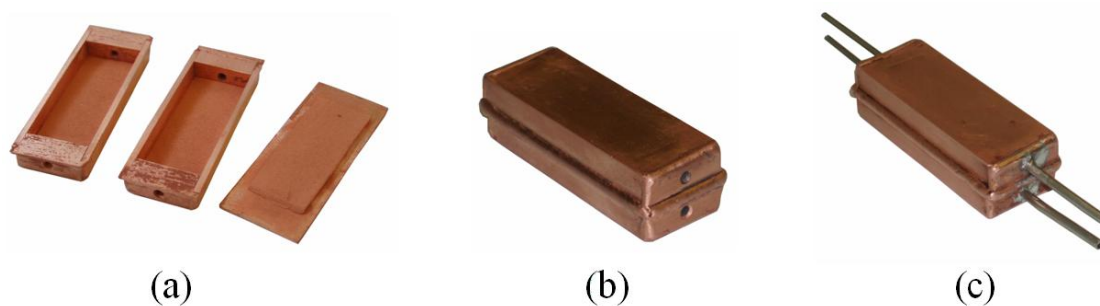


**Figure 43: A prototype for the EURECA heat exchanger elements**

Quality assurance needs to be applied to the manufacturing process of heat exchanger elements for a high performance dilution refrigerator. It is suggested to sinter special samples which are dedicated to quality assurance tests with every batch of heat exchanger elements. The surface to volume ratio of the sintered sponge can then be determined from hydraulic flow measurements.  $\text{N}_2$  with dynamic viscosity  $\eta = 1.795 \cdot 10^{-5} \text{ Pa} \cdot \text{s}$  at room temperature is streamed through the sponge sample of length  $L$  and diameter  $d$  with approach velocity  $w$ , and the pressure drop  $\Delta p$  is measured. Equation [5.14] gives the pressure drop through porous media [71]:



$$\Delta p = \frac{32 \cdot \eta \cdot L \cdot w}{d} \cdot \frac{\psi}{d_e}. \quad [5.14]$$

The pressure drop is linearly proportional to the ratio  $\psi/d_e$ , which was also used in equation [5.12]. In order to assure that the measurement is not distorted by local turbulences, the Reynolds number  $Re$  must be smaller than 2.0 [71].  $Re$  is defined as

$$Re = \frac{w \cdot d_e}{\psi \cdot \nu}, \quad [5.15]$$

where  $\nu$  is the kinematic viscosity of the gas. In addition to measurements of the surface area, mechanical tests may be used to determine whether the sponge adheres sufficiently to the substrate.

#### *THE ORIENTATION OF HEAT EXCHANGERS*

A certain amount of  $^4\text{He}$  usually contaminates the  $^3\text{He}$  circulating in a dilution refrigerator. At low temperature, the two phases separate and may move under the force of gravity in addition to the motion induced by the pressure gradient created by the pump. Bubbles or pools of one phase may develop in the heat exchanger and drop suddenly into the mixing chamber. Temperature oscillations can be the result. It is certain that the geometry of the heat exchanger – especially the tilt angle – plays a large role in these convectional instability phenomena.

Figure 44 shows the temperature of the CCDR mixing chamber as a function of time. This graph was recorded with the first version of the CCDR heat exchanger, which featured a vertical section with a length of approximately 20 cm. The oscillations resulting from convectional instabilities in this section of the heat exchanger are clearly visible. They occurred with a period of approximately 19 h. The oscillations could be triggered early by events such as mechanical shock and helium refilling. After the vertical section had been removed from the heat exchanger, no further oscillations were observed. The fact that the temperature appears considerably less stable at temperatures below 27 mK is due to the deterioration of the signal-to-noise ratio of the thermometry signal when the resistance bridge switches to a higher measurement range. It is not related to the convectional instabilities.

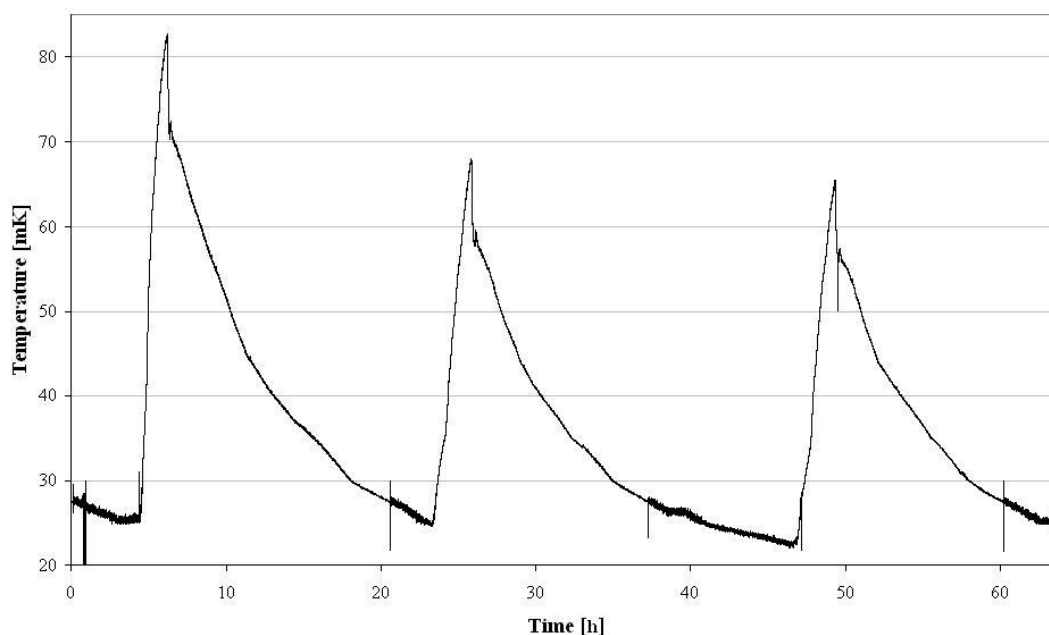


**Figure 44: Temperature oscillations due to convective instability occurring in the CCDR with the first version of the main heat exchanger**

As a consequence, vertical sections should be avoided in the main heat exchanger of a dilution refrigerator. For EURECA, it is recommended to install the heat exchanger horizontally. This is detailed in chapter 6.

### ***5.4 Optimum Pump Line Dimensions***

The  $^4\text{He}$  pump line from the 1 K pot and the  $^3\text{He}$  pump line from the still need to be designed with great care to optimize important design parameters such as diameter and length. These parameters have to be determined by trading off the following effects:

- Pressure drop in the pump line
- Compressible flow effects
- Thermoacoustic (“Taconis”) oscillations of the gas column
- Superfluid film flow

These effects are briefly discussed in the following. They influence the pipe diameter and length. The wall thickness of the pump line must be evaluated by trading thermal conduction, structural stability and manufacturing cost.

*PRESSURE DROP*

The pressure drop in the pump lines can be calculated from the formulas given in section 5.1. The flow regime in the pump lines is usually laminar. Radiation baffles, which are used to block thermal radiation, induce an additional pressure drop. This is taken care of in equation [5.5] by increasing the friction factor  $\xi$  by the value  $\xi_V$ , which depends on the fraction of the tube's cross-section which is blocked by the radiation baffle. In most cases, the radiation baffle blocks slightly more than half of the cross-section, and  $\xi_V$  amounts to 2.5 [71].

*COMPRESSIBLE FLOW EFFECTS*

In pipes of constant cross-section, the Mach number  $\text{Ma} = 1$  characterizes the highest achievable velocity as subsonic gas can only be accelerated to  $\text{Ma} > 1$  in converging/diverging nozzles. As a consequence, the diameter of a pump line must be chosen such that the velocity  $w$  of the fluid at the desired flow rate does not exceed the speed of sound  $a$ , which depends solely on the temperature  $T$  and can be calculated by

$$a = \frac{w}{\text{Ma}} = \sqrt{\frac{\kappa \cdot R \cdot T}{M}}, \quad [5.16]$$

where  $\kappa = 5/3$  for an ideal monoatomic gas.  $M$  is the molar mass of the gas. Close to the still, for instance, where the temperature is in the range of 800 mK and  $M = 3$  g/mol, the speed of sound  $a$  is 60.8 m/s.

The limit given by the speed of sound is especially important for orifices, which are sometimes used in cryogenic pump lines to limit superfluid film flow. The speed of sound in an orifice is reached if the ratio of the pressures  $p_1$  and  $p_2$  before and after the orifice is at its critical value of

$$\frac{p_1}{p_2} = \left( \frac{\kappa + 1}{2} \right)^{\frac{\kappa}{\kappa - 1}}, \quad [5.17]$$

which amounts to 2.05 for an ideal monoatomic gas such as He. The flow through the orifice cannot be augmented by further increasing this pressure ratio.

*THERMOACOUSTIC OSCILLATIONS*

The gas column inside a pipe with a non-uniform temperature distribution featuring large gradients along its axis can start to oscillate under certain conditions. These oscillations may cause a heat flow from the warm end of the pump line to its cold end and can lead to a detrimental heat load on a liquid helium bath, for instance. Taconis [130] first gave a qualitative description of such vibrations in a gas column. They are maintained as a consequence of a phase shift between the pressure and the mass oscillations in the pipe. This phase shift is influenced by the heat transfer from the wall to the gas, which entirely takes place in the so-called boundary layer.

Rott [117, 118] has done theoretical work to find the stability limits of these oscillations. His model is based on a tube whose radius  $r$  is small compared to its length  $L$ . The cold end of the tube is open, while the warm end is closed. The temperature of the tube is assumed to be constant in the cold and the warm section, with a step-change between the two parts as shown in Figure 45.

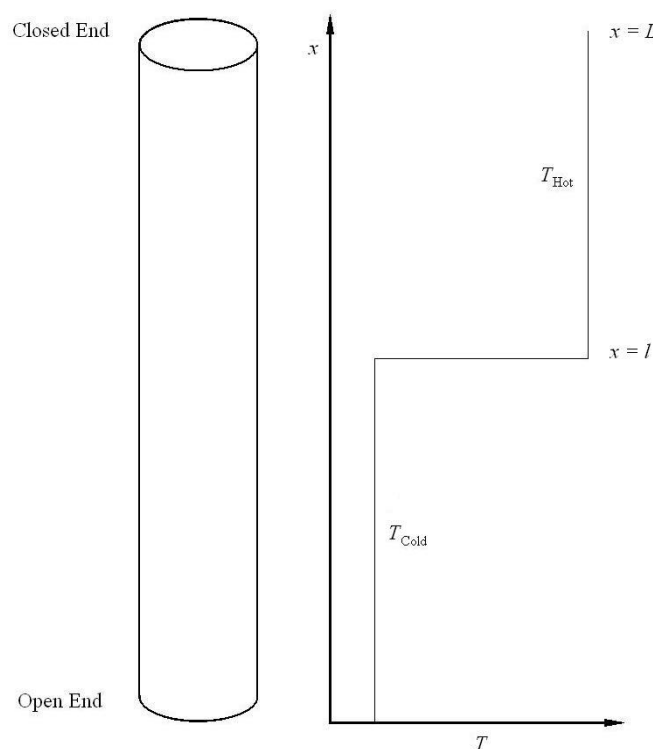


**Figure 45: The geometry and temperature distribution treated in Rott's model for the stability of thermoacoustic oscillations in pipes**

The advantage of Rott's theory over previous calculations is that he takes into account the finite size of the boundary layer between the gas and the tube, which can range

from very small values to the full tube radius. Rott's results are in very good agreement with experimentally obtained values as shown by Yazaki et al. [139] and von Hoffmann et al. [66]. In the following, a simplified version of Rott's theory is given. It can be used to eliminate Taconis vibrations already in the design phase by correctly dimensioning pump tubes. The theory is simplified insofar as only asymptotic values for the stability threshold are considered. This always yields conservative results. Furthermore, heat conduction along the pipe wall is neglected.

First, the values  $\alpha$  and  $\xi$  have to be calculated from equations [5.18] and [5.19].  $T_{\text{Hot}}$  is the temperature of the warm end of the tube,  $T_{\text{Cold}}$  the temperature of the cold end.  $L$  is the total length of the tube, while  $l$  is the axial coordinate where the temperature step occurs:

$$\alpha = \frac{T_{\text{Hot}}}{T_{\text{Cold}}}, \quad [5.18]$$

$$\xi = \frac{L-l}{l}. \quad [5.19]$$

In the next step, the two worst-case values for the dimensionless frequency parameter  $\lambda_C$  are determined. The upper value  $\lambda_{C,1}$  always amounts to  $\pi/2$ , while the lower value  $\lambda_{C,2}$  can be calculated from

$$\frac{\cot \lambda_{c,2}}{\lambda_{c,2}} = \xi. \quad [5.20]$$

This equation cannot be solved analytically. The values for  $\lambda_{C,2}$  are thus given as a function of  $\xi$  in Figure 46 on the following page.

The two values  $\lambda_{C,1}$  and  $\lambda_{C,2}$  are used to calculate the lower and the upper value for the parameter  $Y_C$  from equation [5.21]:

$$Y_{C1,2} = r \cdot \sqrt{\frac{\lambda_{C1,2} \cdot a_c}{l \cdot \nu_c}}, \quad [5.21]$$

where  $r$  is the radius of the tube,  $a_c$  the speed of sound and  $\nu_c$  the kinematic viscosity of the fluid at the temperature of the cold part of the tube.  $Y_{C,1}$  is always larger than  $Y_{C,2}$ .

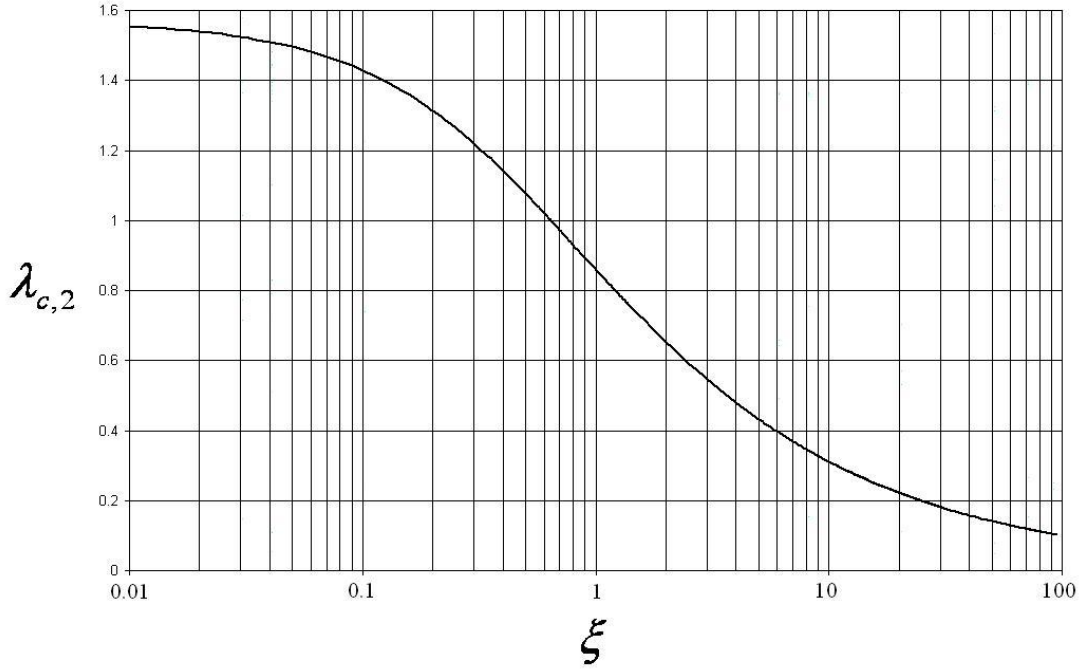


**Figure 46: The lower worst-case dimensionless frequency parameter  $\lambda_{c,2}$  as a function of  $\xi$**

It can now be determined whether oscillations in the pump tube can occur. This is the case when either  $Y_{C,1}$  or  $Y_{C,2}$  are between the lower stability limit  $L_1$  and the upper stability limit  $L_2$ . Equations [5.22] and [5.23] are used to calculate the lower limit  $L_1$ :

$$\text{for } \xi \leq 1: \quad L_1 = \left( \frac{\alpha}{G \cdot \xi} \right)^{\frac{1+\beta}{3+\beta}}, \quad [5.22]$$

$$\text{for } \xi > 1: \quad L_1 = \left( \frac{\alpha}{H} \right)^{\frac{1+\beta}{4}}. \quad [5.23]$$

The variables  $G$  and  $H$  are material parameters. The value  $\beta$  is the exponent of the temperature  $T$  in the power-law dependence of the viscosity. For both  $^3\text{He}$  and  $^4\text{He}$ , these values amount to  $G = 0.228$ ,  $H = 0.0264$  and  $\beta = 0.647$ . The upper stability limit  $L_2$  is given by equation [5.24]:

$$L_2 = \frac{2D}{1 + \frac{1}{\xi} + \lambda_{c,2}^2 \cdot \xi} \cdot \alpha^{1+\beta}. \quad [5.24]$$

$D$  is a material parameter and amounts to 1.191 for  $^3\text{He}$  and  $^4\text{He}$ . Pump tubes in dilution refrigerators do not always correspond to the tube considered by Rott. On the

one hand, the temperature does not rise in a single step but continuously, and on the other hand it might not always be possible to treat the tube as closed at the warm, and open at the cold end. These cases have not yet been treated analytically but can be solved for a given geometry by means of Computational Fluid Dynamics (CFD).

Taconis oscillations were experienced in two pipes leading into the atmospheric  $^4\text{He}$  bath of the CCDR. Both pipes are used as guides for He transfer lines. They have a diameter of 13 mm and a length of 680 mm and 440 mm respectively. The oscillation in the longer pipe had an amplitude of 100 mbar and a frequency of 2.5 Hz. The heat load resulting from these oscillations amounted to approximately 1.5 W. The oscillations were eliminated by drilling holes into the tube. The oscillations in the shorter line could be stopped by connecting its upper, warm end to the He recovery line of the laboratory. This changed the geometry from a closed to an open end.<sup>22</sup>

### *SUPERFLUID FILM FLOW*

If the pump line is used to reduce the vapor pressure above a bath below the Lambda point, a superfluid film creeps up the pump wall to warmer areas where it evaporates. This is the case in the 1 K pot and the still of a dilution refrigerator. The volume  $V_{\text{liq}}$  of liquid  $^4\text{He}$  escaping the pot can be calculated by multiplying the cross section of the film by its flow speed:

$$V_{\text{liq}} = 2\pi \cdot r \cdot t \cdot f \cdot w_{\text{crit}}, \quad [5.25]$$

where  $r$  is the radius of the tube and  $w_{\text{crit}}$  the velocity of the superfluid film (approximately 30 cm/s). The factor  $f$  accounts for the difference between the geometric and the effective perimeter of the tube; it amounts to approximately 3 if no special measures (such as electropolishing) are taken. The thickness  $t$  of the superfluid film can be estimated as

$$t \approx 30 \cdot h^{\frac{1}{3}}, \quad [5.26]$$

---

<sup>22</sup> This solution was suggested by Prof. Franz Sauerzopf (Vienna University of Technology), 2006

where  $h$  is the height above the free surface of the bulk liquid in cm [109]. The film thickness  $t$  is yielded in nm. The amount of liquid lost due to superfluid film flow can easily be converted into an equivalent heat load by multiplying by the latent heat of evaporation for  $^4\text{He}$ .

### 5.5 Mechanical Design Principles

Standard engineering solutions are not always suitable for use at low temperatures or in cryogenic equipment where leak tightness for superfluid He is required. Some manufacturing techniques and design options have proven more successful than others. In the following, a brief description of some important techniques is given.

#### INDIUM SEALS

Indium seals provide a reliable and demountable means of sealing at low temperatures. In the CCDR, indium seals have been used for the IVC, the 1 K pot, the still and the mixing chamber. As shown in Figure 47, the seat for the indium wire is a step with the width of the wire (usually in the range of 1 mm). Sealing is achieved in the gap between the vertical surfaces, into which the indium is forced as soon as the two parts are bolted together. The radial gap size between these two vertical surfaces should be  $(50 \pm 10) \mu\text{m}$ . These dimensions have proven to work in the past.

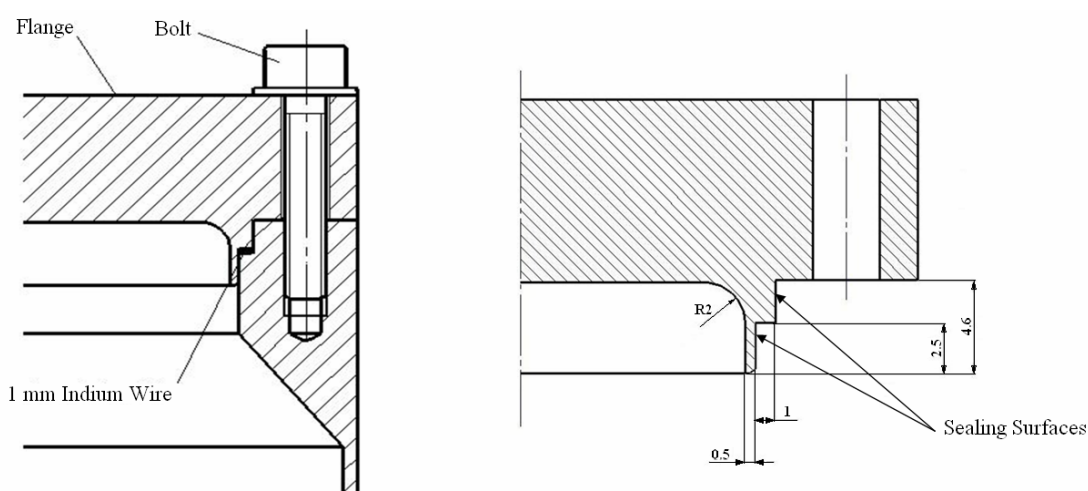
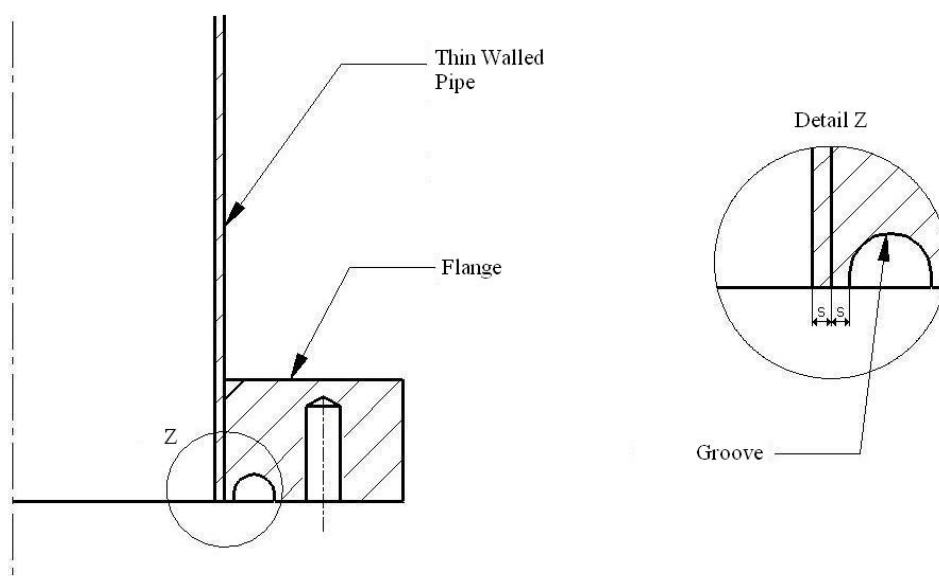


Figure 47: Dimensions for the seats of indium joints



### WELDING

The correct use of joining techniques is mandatory to avoid corrosion and leak problems and to ensure good thermal contact between parts. Welding is the best joining technique for stainless steel parts. To avoid overheating during welding, the pieces which have to be joined should be of equal thickness. This is especially important if thin-walled parts (such as pump lines) are welded. A design example is given in Figure 48.



**Figure 48: Welding joint between a thin walled pipe and a flange**

### SOLDERING AND BRAZING

Soft soldering is suitable for copper, brass and CuNi. For joints which are to be made with a soldering iron, thermal conduction away from the joint has to be minimized, as sufficient heating of the piece is otherwise impossible. A design example is shown in Figure 49. A copper tube is soft soldered to a copper insert, which in turn is brazed to a stainless steel piece. The copper insert is fairly small and can thus be heated easily with a soldering iron. The heat flux conducted along the stainless steel piece is small.

If copper, brass or CuNi have to be joined with a stainless steel piece, brazing should be used. If a connection has to be made in-situ, flame brazing has to be employed. A solution with higher reliability and better corrosion resistance is vacuum brazing. This technique is carried out in a vacuum furnace and can thus not always be used.

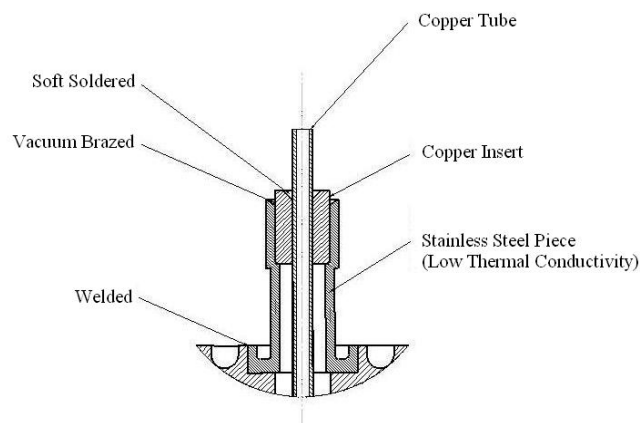


**Figure 49: The design of a joint which is to be made by in-situ soft soldering**

### *BOLTED JOINTS*

When screw connections are used, threaded holes in copper pieces should be avoided. Due to the softness of the material, threads quickly wear which might render the whole part useless. If a threaded hole cannot be avoided, it is recommended to use a threaded insert<sup>23</sup>. Attention has to be paid to the material choice for the fasteners. If a bolted connection ensures a thermal contact, it is useful to choose a fastener material with a larger thermal expansion coefficient than the bulk material. This results in an improved thermal contact at low temperatures due to the greater force pressing the parts together. To further enhance this effect, spring washers can be used. Washers with very low thermal expansion may also be added [109]. A bolt must never have a smaller thermal expansion coefficient than the bulk material as the connection would loosen when being cooled.

### *HERMETIC FEED-THROUGHS*

Hermetic feed-throughs are needed in several locations in a dilution refrigerator, for instance to pass wires from the  $^4\text{He}$  bath into the IVC or to pass wires into the still and mixing chamber. For the CCDR, hermetic feed-throughs have been manufactured by inserting up to 18 copper leads into a 2.2/2.0 CuNi tube. One end of the tube is then

---

<sup>23</sup> such as Helicoil®, produced by Böllhoff GmbH (Bielefeld, Germany)

sealed with Stycast<sup>24</sup> epoxy resin as shown in Figure 50. To reduce mechanical stress, the tube diameter should be as small as possible. Furthermore, the epoxy bulb should be as small as possible and feature a smooth surface to avoid micro-cracks. The CuNi tube can then be soft soldered to a copper insert similar to the assembly in Figure 49.

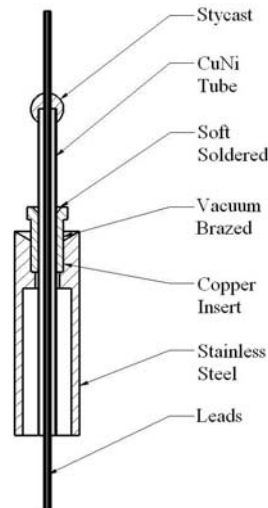


**Figure 50: Design of a hermetic wire feed-through**

### NEEDLE VALVES

In the CCDR, needle valves are used to control the flow to the 1 K pot and to change the impedance of the flow constriction in the  $^3\text{He}$  stream. This facilitates thorough adjustment of the pressure drop to a wide range of flow rates. A needle valve with an orifice diameter of 0.7 mm is used in the 1 K pot, and a needle valve with an orifice of 0.4 mm as  $^3\text{He}$  flow constriction. The design of a needle is shown in Figure 51. The needle is made from stainless steel, the valve body from brass.

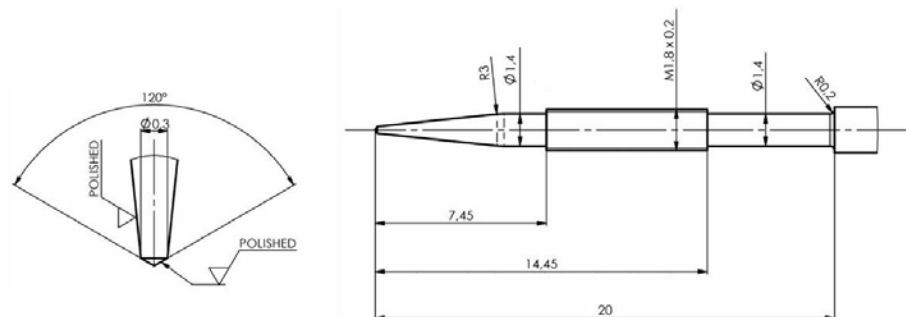


**Figure 51: Needle valve design**

<sup>24</sup> Stycast®, Lake Shore Cryotronics, Inc. (Westerville, Ohio, USA)

## 6. A Dilution Refrigerator for a Multi-Ton Cold Mass

The results from the previous chapters have been used for a design study of the refrigeration system for the multi-ton cold mass experiment EURECA. This experiment has already been described very briefly in the introduction of this thesis. The design principles used in the following can also be applied to other, similar experiments such as gravitational wave antennas.

### 6.1 The European Dark Matter Search EURECA

Cryogenic detectors are believed to be the most suitable means for direct detection of weakly interacting massive dark matter candidate particles (WIMPs). One of the cryogenic  $\text{CaWO}_4$  detector elements which are currently used in the CRESST dark matter search is shown in Figure 52.

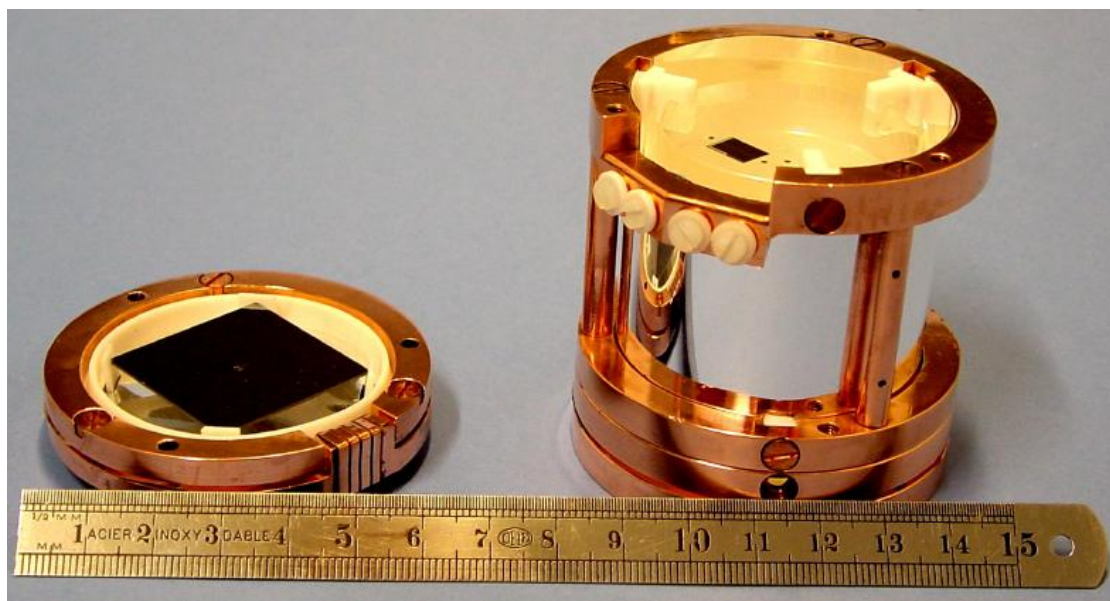


Figure 52: A  $\text{CaWO}_4$  detector element currently used by CRESST

It has already been mentioned in the introduction of this thesis that cryogenic detectors make use of the vanishingly small specific heat of the target material at low temperature. Interaction with a single WIMP leads to a measurable increase in temperature. The size of this temperature peak allows determining the energy of the impacting particle. Absorber crystals of a few hundred grams have an energy threshold of approximately 1 keV and a resolution a few hundred eV. Discrimination

between electron and nuclear recoil events is achieved by ionization or scintillation, depending on the type of detector used.

EURECA [78, 79, 80] is the successor of the European cryogenic dark matter searches CRESST [127] and EDELWEISS [85]. It aims at exploring scalar cross sections in the region from  $10^{-9}$  to  $10^{-10}$  picobarn with a target consisting of a few thousand detector elements and a total mass of one ton. A considerable amount of additional material will be used as mechanical support and to enhance thermal conduction, putting EURECA in the class of multi-ton cold mass experiments.

Apart from the substantial increase in cold mass, an important feature of EURECA is its multi-material target. The detector will be made up of several columns, which in turn consist of several hundred detector elements each. It is possible to use different target materials for each column. The preliminary layout of the cold mass is shown in Figure 53, where the arrangement of the detector elements, their grouping into columns and the corresponding support and shielding structure is visible. The detector elements are shaded blue, the front end electronics are white. The thermal shields, which will most likely be made from copper, are red.

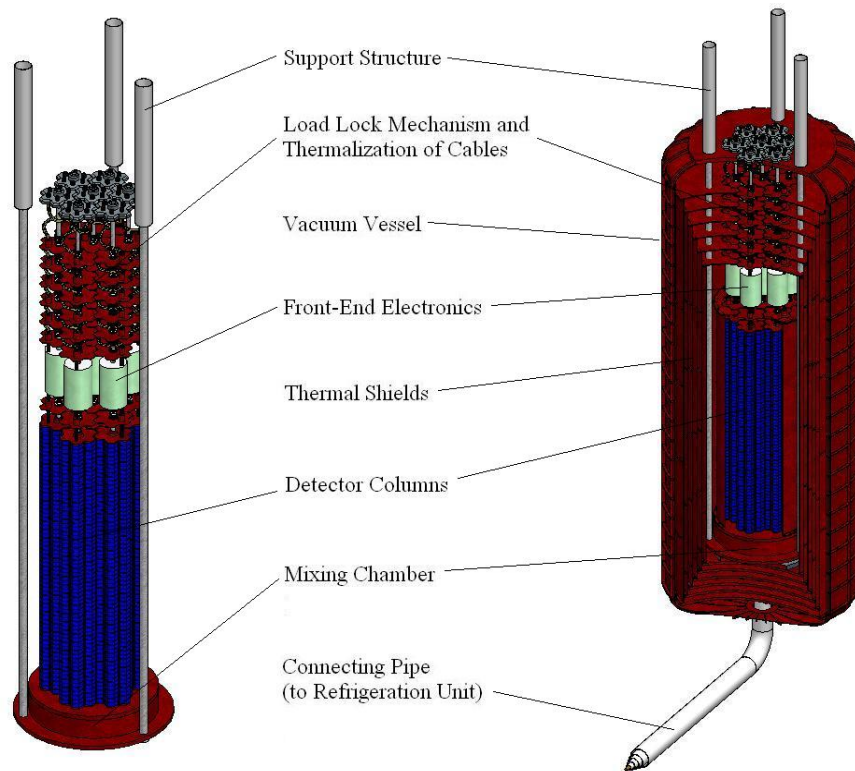


**Figure 53: Preliminary cold mass layout for the European multi-ton dark matter detector array EURECA**

It is envisioned to incorporate a load-lock system for the exchange of the columns. Data taking with the remaining columns shall not be interrupted for more than 60 hours by such an exchange operation. Grouping the target mass into a large number of smaller detector elements offers the advantage of being able to rule out events which are not caused by a WIMP. A neutron, for instance, may leave a signature very similar to that of a WIMP, but would interact with several detector elements. Non-WIMP interactions can thus be easily vetoed by coincidences.

The high sensitivity of EURECA requires an ultra-low radioactive background. In addition to operation in an underground laboratory, sophisticated shielding and the exclusive use of radiopure construction materials are necessary to reduce radioactivity levels, especially in the keV range.

The design of the EURECA cold mass on which this study is based is only preliminary and will certainly be subject to future changes. It is assumed, however, that important design parameters, such as cold mass size and the surface area of thermal shields, are in the right order of magnitude.

## **6.2 System Engineering**

Scaling the relatively small experiments CRESST and EDELWEISS by several orders of magnitude is a considerable technological challenge, which must be met by an interdisciplinary, integrated engineering approach taking into account all aspects of a system as complicated as a dark matter detector array.

This approach is called system engineering. System engineering is defined as “*a logical process of activities which transforms a set of requirements arising from a specific [...] objective into a full description of a system which fulfills the objective in an optimum way. It ensures that all aspects of a project have been considered and integrated into a consistent whole*” [135]. The first step in system engineering is to transform experiment objectives into quantitative experiment requirements and constraints. Fortescue [46] defines the techniques to be used in system engineering as “*requirements identification and analysis, options identification, experiment assessments, trade-off studies and budget (including cost) allocation*”.

In the R&D phase of a project, requirements remain flexible and are iterated several times. They are traded as the experiment concept is developed to avoid keeping old and inappropriate requirements. System requirements typically cover the areas of performance, lifetime, coverage, reliability and cost. In [121], Doukas groups key requirements into functional requirements, operational requirements and constraints.

Functional requirements characterize the task which has to be carried out by a system. For EURECA, functional requirements state that the detector must be capable of detecting WIMPs in the desired mass and cross section range. Operational requirements describe the task to be carried out in a quantitative manner. They define the cross section range in which EURECA is searching, which in turn determines the detector mass and sensitivity and the duration of the experiment. Constraints are imposed by the limited availability of resources, the project schedule or physical characteristics of the hardware. Constraints for the EURECA cooling system mainly result from the fact that operation takes place in a deep underground laboratory. This, for example, excludes design options featuring large amounts of cryogenes due to the safety risks resulting from the presence of liquefied gas in confined spaces. Further constraints result from the very nature of low background experiments, which puts limits to the use of non-radiopure materials and to tolerable mechanical vibration and electrical noise levels.

From the requirements defined on system level, requirements may be derived for all lower levels, such as the refrigeration subsystem. For the EURECA refrigeration subsystem, functional requirements put down that the subsystem must be capable of cooling the cold mass from room temperature to a certain base temperature in a given time, and maintain that base temperature. Operational requirements for the refrigeration subsystem must state the required base temperature, put an upper limit to allowable temperature oscillations and define a maximum cool-down time. The base temperature is determined by the detectors, which need to be held at a certain temperature to function well. The cooling power required at this temperature depends on the layout of the overall system and must be calculated thoroughly.

The definition of the preliminary requirements for EURECA led to the identification and evaluation of design options. The preliminary system layout resulting from these trade-offs is presented in the following. It is subsequently used to derive requirements for the refrigeration subsystem.

### ***6.3 The EURECA System Concept***

The baseline design for the EURECA refrigeration system presented in this section will serve as a starting point for future design iterations. It has been elaborated in collaboration with experts from the Experiment Cryogenics (ECR) group at CERN. The chosen design option is ideal from a scientific point of view, but is certainly not the optimum choice when it comes to cost and development time. It is however believed by the author that a design study should start from the solution yielding the highest scientific benefit, and be subsequently developed towards a technically feasible, affordable system concept.

To yield the highest scientific benefit, the detectors are located in the same cold volume, with no thermal shields between them. This allows for close packing of the detector elements, which facilitates kinematic event discrimination. A load lock system is envisioned to change a detector column while the others remain cold. These features maximize the scientific yield of the detector array.

As dark matter searches are low background experiments, they have to be thoroughly shielded from sources leaving a trace similar to the one of a WIMP in the detector modules. While CRESST and EDELWEISS rely on lead, copper and polyethylene, a layer of water with a thickness of several meters is currently envisioned for EURECA. Inside this shielded volume, only extremely radiopure materials may be used.

It thus seems reasonable to spatially separate the refrigeration subsystem from the detector subsystem housing the target crystals. While radiopurity and electromagnetic interference requirements can be relaxed for the refrigeration unit, which is placed outside the shielded volume, the number of access openings required in the neutron and gamma shielding is greatly reduced as all pump and helium transfer lines interface with the refrigeration system only. In addition, the cryogenic system can be more easily maintained as it is not submersed in water. Heat is transported from the cold parts of the detector unit to the refrigeration unit by forced convection fluid flow. The cooling fluids are led through the connecting pipe, which is also designed to serve as a barrier for electromagnetic interferences (EMI) and mechanical vibrations. The mixing chamber is accommodated in the detector unit.

In addition, the number of design interfaces between the dilution refrigerator and the cold mass is minimized, allowing for distributed development. Furthermore, late



design changes – such as a different shielding system or a different cold mass layout – only have a small impact on the design of the refrigeration system. The proposed system concept is shown in Figure 54. The detector unit housing the absorber crystals is suspended in a water tank. It is connected to the cryostat by the connecting pipe. The cryostat houses a 4 K phase separator, the 1 K pot and the still. The pumps for  $^3\text{He}$  and  $^4\text{He}$ , the compressor, the liquefier and the He recovery system are not shown. The cryostat and the detector unit will most likely be located in the same underground cavern. The gas handling system will be installed in an adjacent cavern, which also houses all necessary control equipment. Noisy machinery, such as compressors and pumps, will be accommodated in a third cavern.

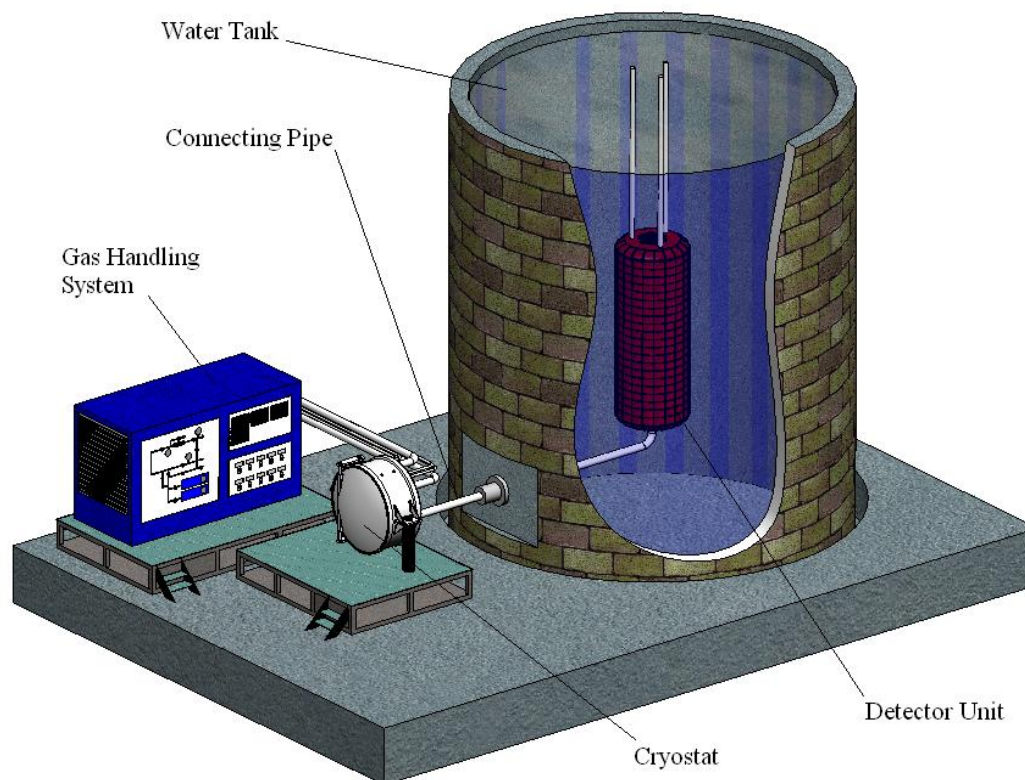


**Figure 54: The EURECA system concept**

#### ***6.4 Preliminary Temperature and Heat Load Requirements***

The  $\text{CaWO}_4$ , Si and Ge targets, which are used to search for WIMPs, must be operated at a temperature of approximately 10 mK to function properly. A description of the  $\text{CaWO}_4$  detector design is given in [7]. It is assumed that the target support structure and mixing chamber interface can be built such that the temperature gradient

between the detector and the liquid does not exceed 3 mK at the projected heat load. The requirement for the liquid temperature in the mixing chamber is thus set to 7 mK.

In order to dimension the dilution refrigerator for EURECA, the heat load on the mixing chamber has to be known. It is estimated in the following. The heat load which is to be removed from the detector elements mainly results from transition edge thermometers and heaters, which subject the thermometers to heat pulses for testing, calibration and temperature stabilization. Furthermore, conduction along the signal leads and internal heat release of the target material lead to an additional heat load.

The transition edge thermometers and the heaters dissipate some 60 pW per element. Conduction along the NbTi leads of a single element gives rise to a heat load of 560 fW, if the leads are heat sunk at 100 mK. A total of 3136 detector modules is necessary to achieve a target mass of 1 ton; the total heat load on the dilution refrigerator resulting from the thermometers, the heaters and from conduction along the signal leads thus amounts to approximately 1.8 nW.

The internal heat release of typical target materials is dominated by the relaxation of tunneling states and thus varies with time. As the exchange of one detector column must not interrupt the data taking process for more than 60 hours, the dilution refrigerator for EURECA must be capable of reaching its operating temperature with the heat load originating from the newly added detector modules after this time span. Each column will be precooled to the temperature of the array before being inserted into the shielded volume. This requires an external dilution refrigerator which is used for precooling. The mechanical operations necessary for the exchange of a column must be conducted such that no significant heating of the detector elements occurs. This assures that the mixing chamber of the dilution refrigerator will only be subjected to the heat load originating from the detector material. Assuming that the detector crystals have tunneling states with level separations and relaxation times similar to those in amorphous materials but with a density two orders of magnitude lower [74], this internal heat load amounts to 400 fW/g after 60 hours. With the mass of a detector amounting to some 320 g, the internal heat release of a single detector module thus amounts to 128 pW after 60 h. One column consists of 448 detector modules. As a consequence, a heat load of 57 nW has to be expected. It is assumed that the interval between two column exchanges is not less than two weeks. As the heat release from the relaxation of tunneling states follows a  $t^{-1}$  dependence, the heat

load from the other detectors at the time of column exchange amounts to 22.7 nW in the worst case.

The support structure holding the detector modules is made from high-purity copper. The total mass of the support structure is estimated to amount to approximately 700 kg, i.e. some 100 kg per column. The heat load originating from the ortho-para conversion of hydrogen from a single column after 60 hours amounts to approximately 807 nW, if the hydrogen contamination is close to 1 ppm. With a minimum column exchange interval of two weeks, the heat load resulting from ortho-para conversion in the remaining six columns does not exceed 85 nW.

Relaxation of thermoelastic stress will occur in the parts supporting the detectors and must also be taken into account. With the values given in chapter 4, the heat load due to structural relaxation of the support structure of a single column calculates to an enormous 27.5  $\mu$ W some 60 hours after cool down. Only after some ten days it drops to a more acceptable value of 4.5  $\mu$ W. It is thus suggested to precool each detector column inside the load-lock for several days before inserting it into the cold mass. The heat dissipated by the other columns will be below 170 nW, if the interval between two column exchanges is two weeks.

The cold mass is surrounded by a thermal shield which is heat sunk to the mixing chamber. The overall surface of this shield is approximately 12 m<sup>2</sup> [22]; the succeeding shield is heat sunk to the dilute stream and has a temperature of roughly 100 mK. If the two shields are treated as black bodies, the heat load radiated to the shield at mixing chamber temperature amounts to 70 pW.

Heat transferred by residual gas particles amounts to 8.6  $\mu$ W if the worst-case estimate given in chapter 4 is scaled with the surface area  $A$  and temperature difference  $\Delta T$  according to equation [4.54].

The detector modules rest on the mixing chamber which is supported by three AISI 316 stainless steel pipes with a diameter of 40 mm, a wall thickness of 0.75 mm, and a length of 2 m. Their upper end is heat sunk at 100 mK. Conduction along these pipes leads to a heat load of 102 nW. Each detector column is inserted into the cold volume with a stainless steel rod of 0.5 mm wall thickness, a diameter of 20 mm and a length of 50 cm. Heat conducted along these pipes amounts to 320 nW. It remains to be assessed whether stainless steel fulfills the demanding radiopurity requirements.

It is assumed that the vibrational environment of EURECA will – in the worst case – be equal to the one of the CCDR. It has been suggested in chapter 4 that the heat load caused by vibrations is mainly due to viscous motion of the He liquids in the mixing chamber. If this assumption proves correct, the vibrational heat load will be of comparable size in machines of similar mixing chamber volume. It is thus assumed that the vibrational heat load in EURECA will not exceed twice the maximum value measured with the CCDR. This – admittedly rough – estimate amounts to 670 nW.

The theoretical value for the heat load which needs to be absorbed by the mixing chamber of the EURECA dilution refrigerator can now be obtained by summing up the values stated above and amounts to 15.4  $\mu\text{W}$ . This value is considerably higher than the value calculated by another group for an experiment of roughly similar size, namely the future rare event observatory CUORE, which will use  $\text{TeO}_2$  crystals with an overall mass of 760 kg to detect the neutrinoless double-beta decay of  $^{130}\text{Te}$  [8]. CUORE can be compared to EURECA in terms of cold mass and volume. The CUORE team estimates a heat load of 1  $\mu\text{W}$  to their cold mass. Experimental results from several other experiments cooling multi-ton masses to millikelvin temperatures, however, suggest a heat load of several tens of  $\mu\text{W}$  – in spite of contrary predictions. MiniGRAIL, which has already been mentioned in chapter 4, is subjected to a heat load of 25  $\mu\text{W}$  resulting from a 1350 kg copper sphere [36]. Another example is the Nautilus gravitational wave antenna, which consists of a 2350 kg aluminum bar and exhibits an unexpectedly high heat load of 10  $\mu\text{W}$  [8]. It seems unlikely that EURECA will lie much below these values.

Even though the assumptions underlying the estimate of 15.4  $\mu\text{W}$  are worst-case values, a factor of safety is applied to the result to provide some margin for future design changes and uncertainties in the estimates. The baseline design of the EURECA dilution refrigerator is based on a heat load of 20  $\mu\text{W}$  at 7 mK. The heat load to be absorbed at the mixing chamber mainly results from the relaxation of thermoelastic stress and conduction in residual gas. These effects must thus be studied in greater detail.

The front end electronics for the detector array must be cooled to some 100 mK. The electronics will thus be thermally anchored to the dilute stream of the main heat exchanger. This additional heat load on the dilute stream must also be evaluated. The front end electronics consist of two flux locked DC SQUIDS for each detector

element. The heat load from a single DC SQUID lies in the range of 20 pW [137]. Furthermore, some 5 pW are dissipated due to ohmic losses in a 50 m $\Omega$  resistor, which is needed for the read-out circuit of the transition edge thermometers. The heat conducted along the wires connecting to a single SQUID amounts to 1.35 nW. The total number of read out channels is 6272. Conduction along the support structure causes a heat load of 422  $\mu$ W. The heat load resulting from conduction in residual gas between the 100 mK stage and the surrounding shield at 1.5 K amounts to 133  $\mu$ W. Thermal radiation amounts to another 3.5  $\mu$ W. The total heat load which has to be absorbed by the dilute stream at a temperature of 100 mK thus amounts to 567  $\mu$ W.

The cooling power requirements which have been used for the baseline design of the EURECA refrigeration system are summarized in Table 16 and Table 17 below. When stating requirements, it must also be determined how these requirements can be verified. For the design study presented below, verification is effected by analysis only, and experimental verification can be obtained by dedicated tests in the CRESST and EDELWEISS experiments.

Requirement	Value	
	nW	$\mu$ W
Electrical load from detectors	188	
Conduction along leads	1.8	
Tunneling states in detector material	80	
Heat release from Cu support structure (H <sub>2</sub> )	890	
Vibration induced dissipation	670	
Structural relaxation in Cu support structure		4.5
Conduction along support rods	422	
Conduction in residual gas		8.6
Thermal radiation	0.07	

**Table 16: Cooling power requirements at 7 mK**

Requirement	Value	
	nW	$\mu$ W
Electrical load from front end electronics	157	
Conduction along leads		8.5
Conduction along support rods		422
Conduction in residual gas		133
Thermal radiation		3.5

**Table 17: Cooling power requirements at 100 mK**

### 6.5 Dilution Refrigerator Design Parameters

The required surface area  $A$  of the main heat exchanger for the EURECA dilution refrigerator can be estimated from Niinikoski's theory [99]<sup>25</sup>. For a maximum heat load  $\dot{Q} = 20 \text{ } \mu\text{W}$ , which needs to be absorbed at a mixing chamber temperature  $T = 7 \text{ mK}$ , equation [1.13] yields a surface area of

$$A = \frac{\dot{Q}}{12.5 \cdot S \cdot T^4} = 39.2 \text{ m}^2. \quad [6.1]$$

The constant  $S$  was assumed to amount to  $17.0 \text{ W}/(\text{m}^2 \cdot \text{K}^4)$  – this is a safe value for copper. It seems impossible to use sintered silver heat exchangers due to radiopurity considerations. A surface area of  $39.2 \text{ m}^2$  is roughly equal to  $130 \text{ g}$  or  $31 \text{ cm}^3$  of copper powder<sup>26</sup> with a grain size of  $1.8 \text{ } \mu\text{m}$  and a filling factor of  $\eta = 0.4$ , if 100 % of the available surface can be used for heat exchange. A dilution refrigerator with a copper heat exchange surface area of  $39.2 \text{ m}^2$  would have a maximum cooling power of  $83 \text{ } \mu\text{W}$  at  $10 \text{ mK}$ . This value can be compared to the extremely powerful dilution refrigerator in Leiden which has been built by Frossati. This machine has a cooling power of  $20 \text{ } \mu\text{W}$  at  $10 \text{ mK}$  [133, 105] and a maximum  $^3\text{He}$  flow rate in excess of  $10 \text{ mmol/s}$ . Another very powerful machine existing today is the dilution refrigerator in Lancaster built by Pickett et al. [17, 21]. It has a comparably large heat exchange surface area and a low base temperature of approximately  $2 \text{ mK}$ ; high cooling powers away from the base temperature are however not achievable as the maximum  $^3\text{He}$  flow rate is limited to  $600 \text{ } \mu\text{mol/s}$ . The EURECA dilution refrigerator will thus be more than four times as powerful as the most sophisticated machine existing today. The optimum flow rate  $\text{opt}\{\dot{n}_3\}$  can again be estimated from Niinikoski's theory [99]:

$$\text{opt}\{\dot{n}_3\} = 0.27 \cdot A \cdot S \cdot T_m^2 \text{ (K}^2 \cdot \text{mol/J)} = 8.3 \text{ mmol/s}. \quad [6.2]$$

This flow rate is achievable with the CCDR. It will thus be possible to qualify a heat exchanger design for the EURECA dilution refrigerator at the CERN Cryolab by simply adding one or two additional roots blowers to the  $^3\text{He}$  primary pump.

---

<sup>25</sup> The numerical values which are used for the calculations in this section correspond to a  $^4\text{He}$  contamination in the concentrated stream of 10 %.

<sup>26</sup> Such powders are available from Ferro Corporation (Cleveland, Ohio, USA), Umicor Canada, Inc. (Fort Saskatchewan, Canada) and NanoDynamics, Inc. (Buffalo, New York, USA).

## 6.6 The Refrigeration Unit

The refrigeration unit consists of the cryostat, the unit housing the  $^3\text{He}$  gas handling and control systems, and the proximity cryogenics (i.e. the pumps, the compressor, the  $^4\text{He}$  liquefier and the  $^4\text{He}$  recovery system). The cryostat provides cooling to the detector unit via the connecting pipe at three different temperature levels. Gaseous  $^4\text{He}$  at 20 K and superfluid  $^4\text{He}$  at 1.5 K are led to the detector unit to cool thermal shields. In addition, liquid  $^3\text{He}$  is supplied which is used for the dilution refrigerator.

The cryostat itself is supplied with liquid helium at 4 K and gaseous helium at 20 K from the proximity cryogenics. Warm helium is returned to the proximity cryogenics via the recovery line. Furthermore, the cryostat is connected to the gas handling system, which houses the purifiers and gas tanks for the  $^3\text{He}/^4\text{He}$  mixture as well as a vacuum generator. The gas handling system and proximity cryogenics, which are mainly based on commercially available items, are described more thoroughly below.

Figure 55 outlines the synoptic diagram of the EURECA cooling system. The dilution refrigerator is only partly housed by the cryostat, as the main heat exchanger is located in the connecting pipe and the mixing chamber is accommodated in the detector unit.

The three outermost thermal shields of the cryostat and the detector unit are cooled by a continuous flow of gaseous  $^4\text{He}$ . The cold, pressurized gas is supplied by the refrigeration unit. Inside the cryostat, this stream is split into two, one cooling the shield of the detector unit, the other cooling the shields of the cryostat. The 4 K stage is formed by a pot filled with liquid  $^4\text{He}$  at atmospheric pressure. The pot is connected to a thermal shield. Liquid is drawn from the 4 K pot to produce cooling in the 1 K stage by means of Joule-Thompson expansion. The 1 K stage serves as a heat sink for another thermal shield and for the condensation of the  $^3\text{He}$ , and is used to subcool a stream of  $^4\text{He}$  at atmospheric pressure below the Lambda point (“Lambda plate H/X”). The resulting superfluid is used to cool thermal shields in the detector unit.

The third pot in the cryostat is the still. It houses a heat exchanger for  $^3\text{He}$  and is connected to the main heat exchanger of the dilution refrigerator. This main heat exchanger, however, is not accommodated in the cryostat but in the connecting pipe between the cryostat and the detector unit and inside the detector unit itself. The physical layout of the EURECA cryostat is shown in Figure 56.

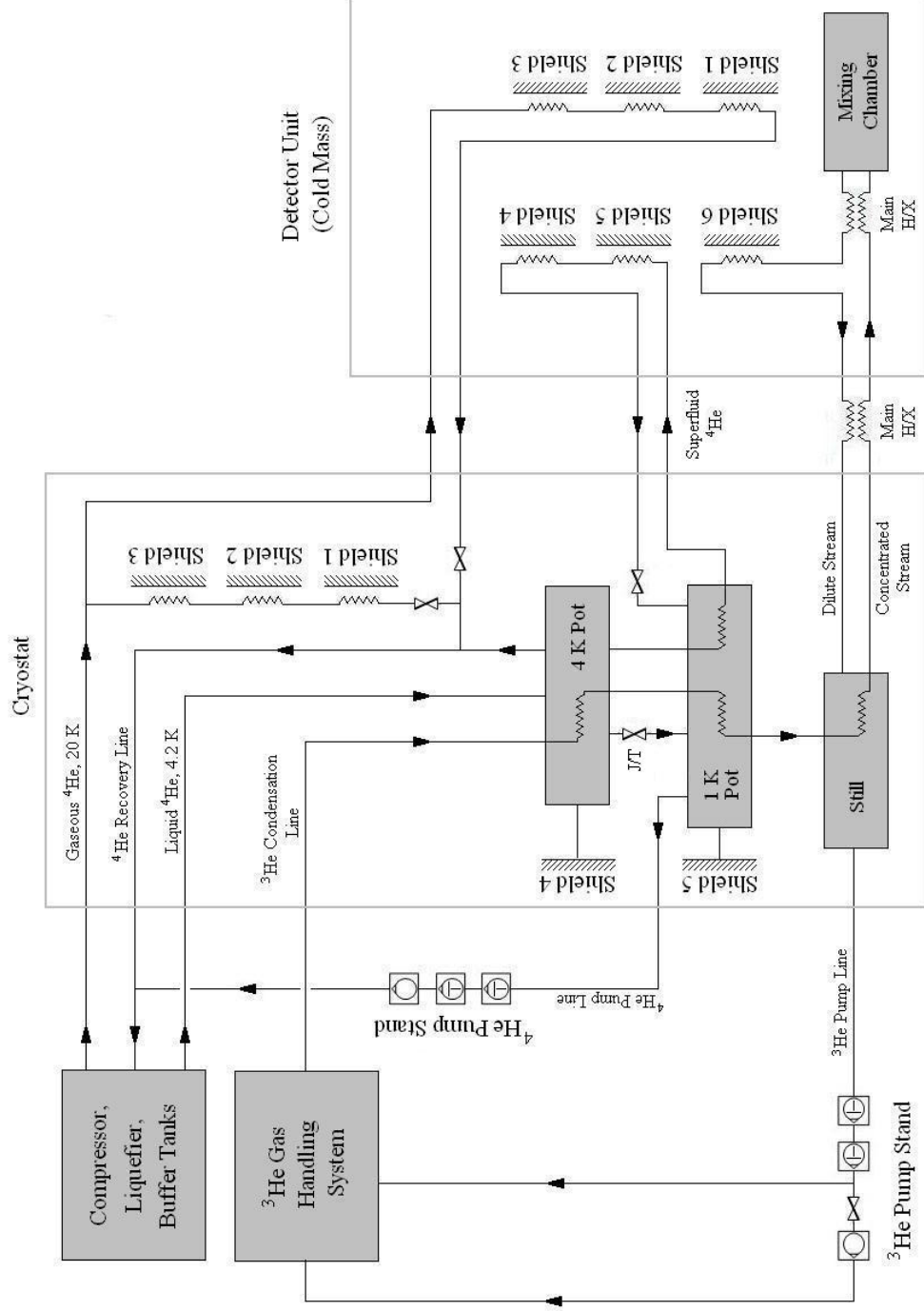
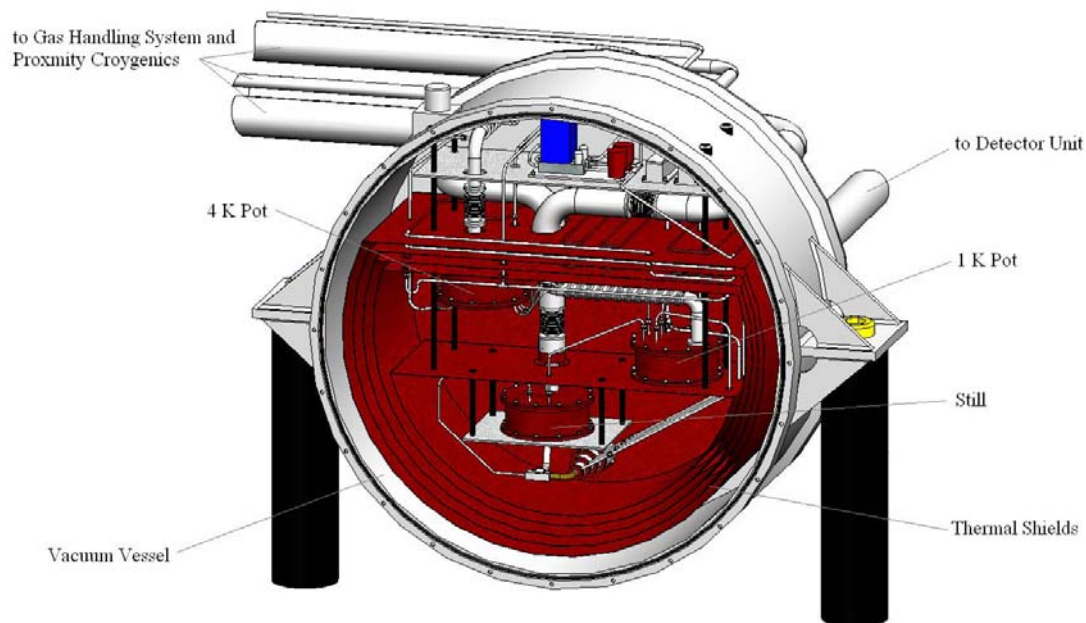


Figure 55: Synoptic diagram of the EURECA cooling system outlining the fluid flow between the cryostat, the detector unit and the proximity cryogenics





**Figure 56: The EURECA cryostat, which - for clarity - is depicted with the vacuum tight front cover and the lids of the thermal shields removed**

The EURECA cryostat has been designed to facilitate maintenance and enhance reliability. All components are accommodated in a single vacuum space of cylindrical shape such that all parts can be maintained through the front hatch without performing any disassembly work. Tube connections will be made with demountable fittings.<sup>27</sup>

#### *VACUUM SPACE TOPOLOGY AND THERMAL SHIELDING*

The cryostat vacuum vessel consists of a stainless steel ring, which is sealed by a domed bulkhead on its rear side. On its front side, a door allows for access to the subsystems installed inside. The vacuum vessel and the thermal shields are shown in Figure 57. In the image, the thermal shields are cut open.

Mechanical stability under the load of 1 bar external pressure must be guaranteed. The required wall thickness for the vacuum vessel has been calculated with the engineering formulas given in [73] for cylinders under external pressure.

---

<sup>27</sup> A system which has proven reliable at very low temperatures is Kenol by CEFILAC (Saint-Etienne, France)

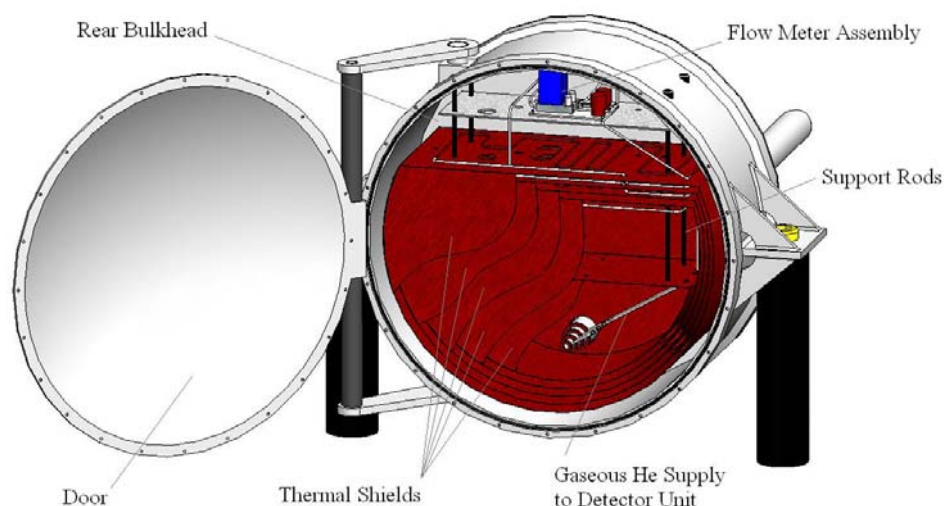


**Figure 57: The vacuum vessel and thermal shielding for the EURECA cryostat**

It amounts to 6 mm and provides a margin of safety (MoS) of 3.2 against plastic deformation. Stiffening ribs must be foreseen to prevent from elastic instability. If no stiffening ribs are used, the wall thickness must amount to 45 mm [112]. The rear bulkhead and the door are of domed shape. The required wall thickness depends on the exact shape of the parts and lies in the range of 8 mm with a MoS of 2.0 against plastic deformation [73]. Again, stiffening ribs must be added to prevent buckling. A detailed finite elements analysis of the vacuum vessel should be performed before freezing the design.

For simplicity, leak tightness of the vacuum vessel's door is ensured by an elastomer gasket. Diffusion through the gasket will not permit to reach ultra-high vacuum levels. As the very low temperature parts (i.e. the mixing chamber and the heat exchanger) of the dilution refrigerator are accommodated in a different vacuum space, this is not deemed problematic, though.

Commercial hermetic feed-throughs are used for all electrical cables which have to be led into the Faraday cage formed by the vacuum vessel. Low-pass filters reduce electromagnetic interferences by some 60 dB. Electrical cables for equipment inside the 4 K pot, the 1 K pot and the still (such as thermometers and heaters) are routed inside the pump lines. Hermetic feed-throughs are installed at room-temperature levels. This avoids the use of low-temperature hermetic feed-throughs and thus increases the reliability of the system.

#### *4 KELVIN SUBSYSTEM*

The amount of liquid  $^4\text{He}$  which needs to be supplied by the proximity cryogenics is determined by the heat losses to the 4 K stage and the  $^4\text{He}$  flow rates to the lambda plate and the 1 K system respectively. The heat load on the 4 K stage results from the incoming  $^3\text{He}$ , thermal radiation on the 4 K shield and from conduction along the support rods. It amounts to 2.36 W and causes a boil-off rate of 26.2 mmol/s. A heat exchanger must be incorporated to precool the incoming  $^3\text{He}$  with the boil-off vapors.

A level gauge, a heater and a thermometer are located inside the 4 K pot in addition to the  $^3\text{He}$  precooling heat exchanger, which is immersed in the liquid phase. The pipes connecting to this heat exchanger enter the pot from below; this simplifies the assembly of the cryostat and makes it less susceptible to variations of the liquid level in the 4 K pot. A flexible bellows in the boil-off line avoids excessive mechanical stress due to mechanical overdetermination.

#### *1 KELVIN SUBSYSTEM*

The 1 K subsystem provides a heat sink for the thermal shield surrounding the still and serves as condenser for  $^3\text{He}$ . An additional heat load arises from subcooling  $^4\text{He}$  for the lambda plate heat exchanger, from flash evaporation and from superfluid film creep. The cold vapors pumped from the 1 K pot are used to precool the incoming  $^3\text{He}$ , to precool  $^4\text{He}$  in the lambda plate heat exchanger and the  $^4\text{He}$  used for Joule-Thompson expansion. The boil-off rate from the 1 K pot amounts to 27.5 mmol/s. Superfluid film creep can be neglected if compared to the amount of  $^4\text{He}$  which is evaporated from the pot. However, the outlet of the 1 K pot may be electropolished to minimize the effective perimeter of the line.

The  $^4\text{He}$  flow rate of 27.5 mmol/s calls for a pump with a pumping speed of 700  $\text{m}^3/\text{h}$ , if the pump line has a length of several meters and a diameter of some 200 mm. To provide for sufficient MoS, a pump with a speed of approximately 1000  $\text{m}^3/\text{h}$  should be chosen. Such machines are available commercially, usually as a combination of a rotary vane pump and a roots blower<sup>28</sup>.

---

<sup>28</sup> Such as the combination Sogevac SV 1200 and RUVAC WSU 2001 (Leybold Vacuum, Köln, Germany) or the combination DUO 250 and WKP 1000 (Pfeiffer Vacuum, Asslar, Germany)

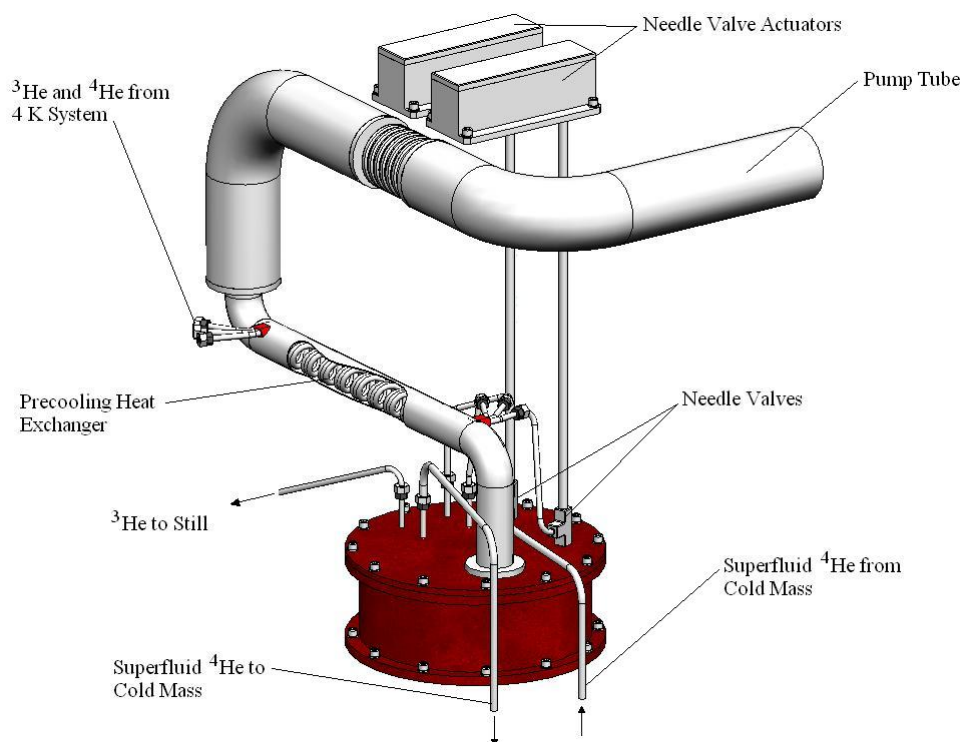


**Figure 58: The 1 K stage of the EURECA refrigeration subsystem**

The design of the 1 K subsystem is shown in Figure 58. The pump line is equipped with a flexible bellows to minimize mechanical stress. Due to the fairly high flow rate, the pump line must be vacuum isolated for a length of several meters. An indium seal is used to hermetically close the pot. The level in the 1 K bath is controlled by an automatic system developed by Burghart [22]. This control system actuates a needle valve. A similar system is used to control the flow of superfluid  $^4\text{He}$  through the cold mass.

### *STILL SUBSYSTEM*

The still design is driven by the need to minimize the  $^4\text{He}$  contamination in the  $^3\text{He}$  stream. This calls for an efficient film burner and a fairly low still temperature. It is assumed that the  $^3\text{He}$  concentration in the liquid inside the still amounts to 1 %; at a temperature of 800 mK, the concentration of  $^3\text{He}$  in the vapor above the liquid then amounts to 93 % [111]. In order to achieve this temperature, the still needs to be pumped to a pressure of 0.24 mbar. With a pump line of 260 mm diameter and a

length of roughly 6 m, a pump speed of 3800 m<sup>3</sup>/h is required.<sup>29</sup> Reducing the still temperature further improves the performance of the cryostat as the <sup>3</sup>He concentration in the vapor above the dilute solution would increase. At a still temperature of 700 mK, for instance, the <sup>3</sup>He concentration in the vapor rises to 97.6 % [111]. A pump with a speed of approximately 12000 m<sup>3</sup>/h would be needed to reach this temperature.<sup>30</sup> It is doubted, however, that the benefits resulting from a lower still temperature justify the considerably higher cost of such a large pumping system.

The <sup>4</sup>He contamination of the concentrated stream is not only caused by the fraction of <sup>4</sup>He in the vapor above the dilute solution, but also by superfluid film creep inside the <sup>3</sup>He pump line. In analogy to the 1 K pot, the outlet of the still should be electropolished to minimize the effective perimeter. The pump line diameter close to the still should not be smaller than 10 mm to avoid fluid velocities approaching the speed of sound. A film burner with a design similar to the one used for the CCDR is foreseen. The <sup>3</sup>He pump line is equipped with a bellows to accommodate thermal dilatation and is vacuum isolated to avoid freezing and dewing on the pipe.

The heat exchanger used to cool the <sup>3</sup>He is located in the bottom part of the pot to assure that it is always completely immersed in dilute solution. The still heater is located well above this heat exchanger to avoid that vapor bubbles, which form on the surface of the heater, impair the heat transfer on the heat exchanger's surface. Furthermore, a thermometer is accommodated in the still.

The dilution refrigerator is optimized for a rather narrow range of <sup>3</sup>He flow rates of approximately 8 - 10 mmol/s. As this requires a heating power of 300 mW at a typical still temperature of 800 mK, no special measures need to be taken to minimize the heat load on the still. Furthermore, a flow impedance needs to be accommodated between the 1 K stage and the still. It does not seem necessary to use an adjustable impedance such as a needle valve, as the range of required flow rates is not very large.

---

<sup>29</sup> Available technical solutions are, for instance, a serial combination of the WKP 6000AM and WKP 1000AM roots pumps followed by a DUO 65M rotary vane pump (Pfeiffer Vacuum, Asslar, Germany)

<sup>30</sup> Such as a serial combination of three parallel WKP 6000AM, one WKP 2000AM and two parallel DUO 65M (Pfeiffer Vacuum, Asslar, Germany)

### 6.7 Connecting Pipe and Main Heat Exchanger

The connecting pipe is the link between the refrigeration unit and the detector unit. It has a length of 5 to 6 m and houses a part of the main heat exchanger of the dilution refrigerator. The connecting pipe is made of several concentric tubes. The outermost tube confines the vacuum space. The annular gap between the next two tubes forms the flow channel for the return stream of gaseous  $^4\text{He}$ , which is used to cool the three outermost shields in the detector unit. The return stream serves as a thermal shield for the supply stream, which is led through the annular gap formed by the next two tubes. The very same principle is employed for the superfluid  $^4\text{He}$ , which is used to cool the forth and the fifth shield of the detector unit. The superfluid  $^4\text{He}$  supply stream serves as a thermal shield for the main heat exchanger of the dilution refrigerator, which is located in the very center of the connecting pipe.

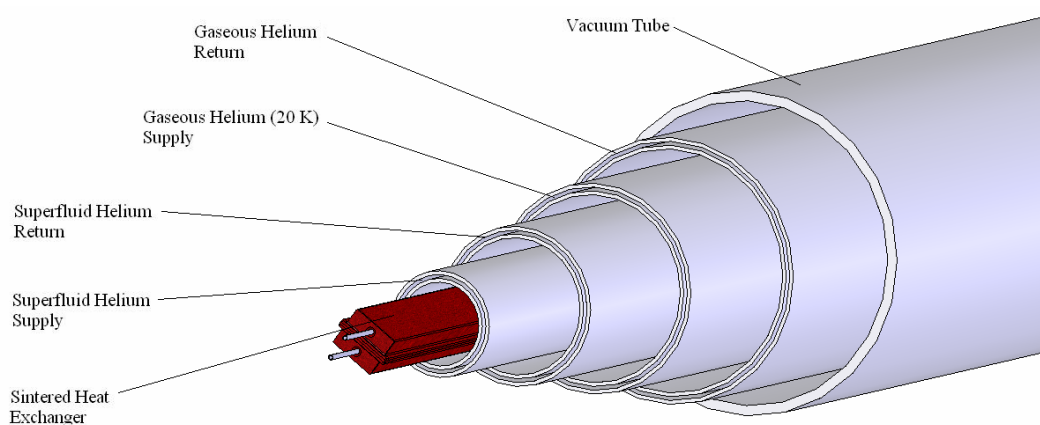


**Figure 59:** Cross-section of the connecting pipe between the cryostat and the detector unit of the EURECA dark matter detector array.

The connecting pipe may be inclined a little to adjust the appropriate level difference between the mixing chamber and the still. Bends – in the horizontal plane – may be incorporated to avoid the existence of a direct line of sight through which neutrons or other detrimental particles might travel to the target mass.

The connecting pipe also serves as a barrier for mechanical vibrations and electromagnetic interferences. Mechanical vibrations are attenuated by several bellows, which are also used to compensate for the thermal dilatation of the tubes.

Electromagnetic interferences between the detector unit and the electrical equipment in the refrigeration unit must be avoided at all cost. Both interferences conducted along the metallic pipes and radiated interferences, which are caused by the residual

electromagnetic stray fields passing through the low pass filters in the cryostat, have to be blocked from the shielded volume. Ceramic discs could be used to interrupt the electrical conduction path between the cryostat and the detector unit, through which low-frequency interferences could be transmitted. In order to avoid that these discs create an unacceptable opening in the faraday cage formed by the all-metal vessel surrounding the detectors, metallic membranes can be welded between the tubes. These membranes also separate the vacuum space of the refrigeration unit from the vacuum space of the detector unit. They must be made from a metal of rather low thermal conductivity, such as titanium. Inside the fluid flow channels, copper meshes serve as a barrier for radiated electromagnetic interferences. Stray magnetic fields, which can influence the SQUID read-out electronics, can be shielded by making one of the connection tubes from superconducting material; axial magnetic fields are attenuated by a factor  $10^4$  within a distance of three radii from the connection tube's end, while radial fields are attenuated by the same factor within six tube radii [54]. The bellows, the ceramic discs and the membranes are accommodated in a single assembly, which is shown in Figure 60. The main heat exchanger is not depicted.

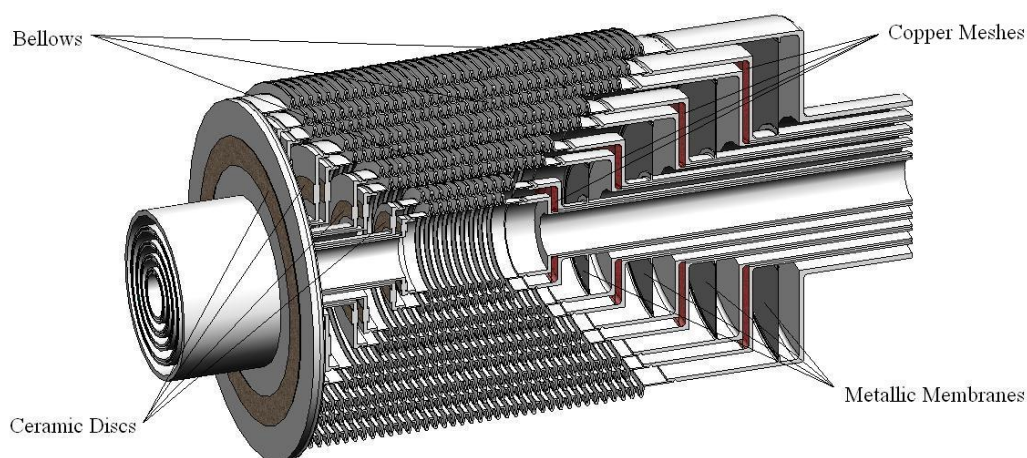


**Figure 60: The separator assembly for attenuation of mechanical vibrations and EMI**

The main heat exchanger of the EURECA dilution refrigerator is one of the most crucial items of the whole machine. It has to precool the  $^3\text{He}$  stream to a temperature of some 13 mK. In addition, the dilute stream is used as a heat sink for a thermal shield surrounding the detectors and for the front end electronics. The dilute stream of the heat exchanger must be sufficiently large to allow for  $^3\text{He}$  transport without mutual friction. Furthermore, it must be large enough to guarantee a  $^3\text{He}$  concentration of at least 1 % in the dilute solution in the still.



The concentrated stream must be large enough to avoid substantial frictional heating. At such high cooling powers, axial conduction in the fluid is hardly of concern.

As the effective surface area is usually considerably smaller than the geometric surface area of the powder used for sintering, it is recommended to put several times as much sintered copper powder as needed in the heat exchanger. The ideal continuous heat exchanger is sufficiently approximated if the powder is arranged in 12 discrete elements. For the sake of simplicity, it is suggested to design and manufacture three types of elements, with different heat exchange surface areas and stream cross sections. The elements with the highest surface area and cross section must be placed close to the mixing chamber, while the elements with the smallest surface area and cross section must be placed close to the still.

### 6.8 The Mixing Chamber

The mixing chamber is located in the detector unit and lies directly below the detector columns. It is one of the main components of the cold mass and the only part of the dilution refrigerator located inside the shielded volume. As a consequence, the detailed design of the mixing chamber must be established in close coordination with the cold mass design. The preliminary design of the mixing chamber is outlined in Figure 61.

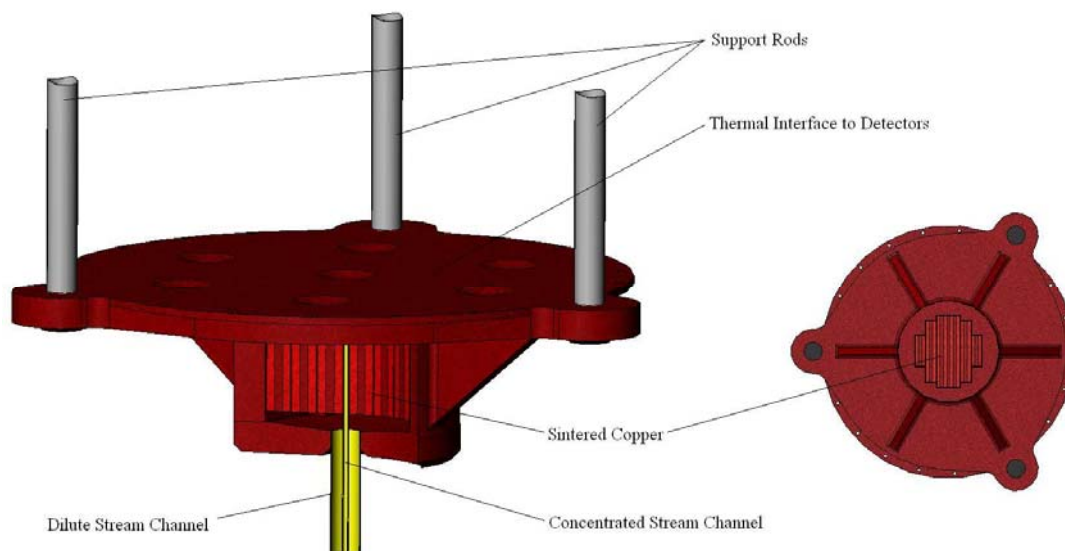


**Figure 61: The preliminary design of the mixing chamber of the EURECA dilution refrigerator**



The mixing chamber is connected to a large copper plate which serves as thermal interface and mechanical support for the detector columns. This plate has a diameter of roughly 700 mm and a thickness of 40 mm which is required to provide sufficient mechanical strength and to minimize the temperature gradient developing along the plate. As the low temperature thermal conductivity of high purity copper is two to three orders of magnitude larger than that of the liquid helium isotopes [91], thermal paths should rely on conduction in copper and not in liquid helium.

It is desirable to keep the thermal mass of the mixing chamber small to minimize the reaction time of the dilution refrigerator. The amount of liquid in the mixing chamber should thus be as small as possible. On the other hand, enough volume must be available to accommodate the required amount of copper powder needed for a good thermal contact between the liquid and the solid. Niinikoski [99] calculated that the surface inside the mixing chamber should be ten times larger than the surface in the heat exchanger. For the EURECA dilution refrigerator, at least 1.3 kg of copper powder with a grain size of 1.8  $\mu\text{m}$  and a filling factor of  $\psi = 0.4$  have to be located in the mixing chamber. The thermal penetration depth of this copper powder amounts to 23 mm at a temperature of 7 mK. The copper powder will be sintered to fins which are welded to the plate supporting the detectors. To improve the thermal contact at higher temperatures – such as during cool-down – the sintered layer should be as thin as possible. The location of the phase boundary should be directly above the fins.

As no gamma shielding is accommodated between the absorber crystals and the mixing chamber, only radiopure materials may be used for its construction. Indium joints and soldered connections must thus be replaced by welding. Electrical cables, which have to be routed to the thermometer and the heater inside the mixing chamber, will be led through the dilute stream. This helps to avoid the use of low-temperature hermetic wire feed-throughs which are a potential source of leaks.

## ***6.9 Gas Handling System and Proximity Cryogenics***

The proximity cryogenics comprise a  $^4\text{He}$  liquefier with a compressor, helium buffer tanks and a helium recovery system. The gas handling system consists of the vacuum generators, the  $^3\text{He}$  and  $^4\text{He}$  pumps and all equipment needed to operate the closed  $^3\text{He}$  circuit, such as gas reservoirs and purification equipment.

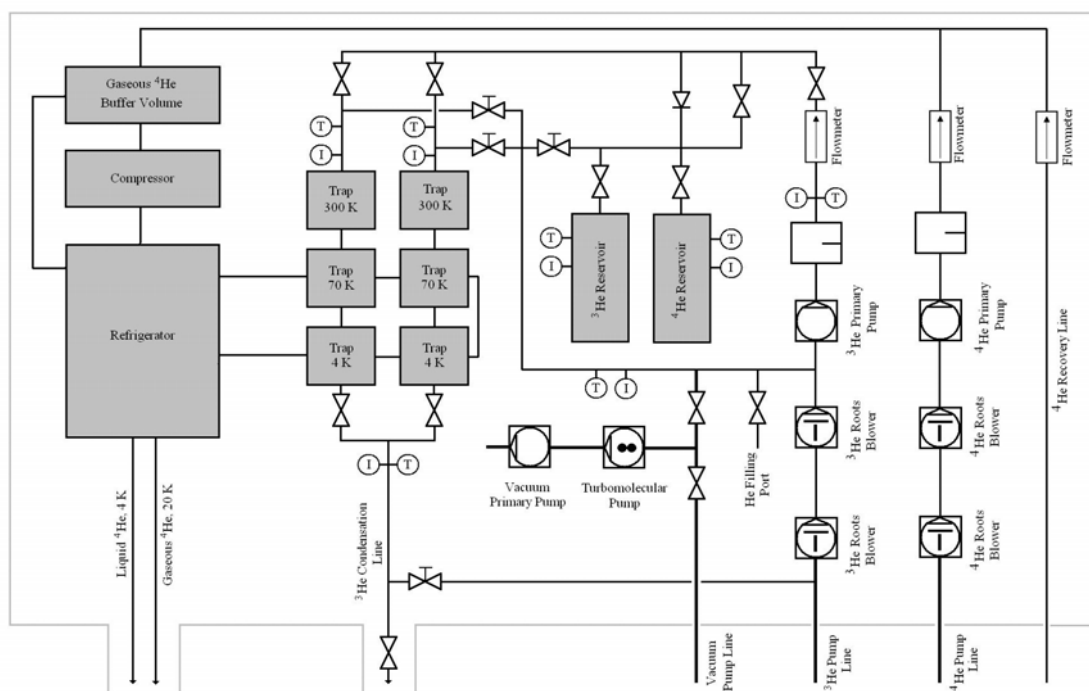


**Figure 62: Synoptic diagram of the  $^3\text{He}$  gas handling system and proximity cryogenics**

The synoptic diagram of the gas handling system and of the proximity cryogenics is shown in Figure 62. The refrigerator supplies gaseous  $^4\text{He}$  at 20 K and liquid  $^4\text{He}$  at 4 K to the cryostat. Furthermore, liquid helium is supplied to cool the charcoal traps. The  $^3\text{He}$  circuit is very similar to that of the CCDR. The most important difference is that two roots blowers are used instead of one and that a line is provided which allows shunting the cryostat. This line is used to circle gas in the  $^3\text{He}$  circuit and through the traps to purge the oil in the pumps and to remove impurities from the mixture before routing it to the cryostat. The condensation line is vacuum insulated so that the  $^3\text{He}$  is not warmed after leaving the traps and enters the cryostat as cold as possible. Furthermore, both electrical pressure transducers and mechanical pressure indicators are installed. This allows for digital data acquisition while maintaining the possibility to manually perform recovery operations in case of a power cut. All pumps are equipped with temperature and overpressure sensors to initiate automatic shut-down in case of a malfunction. These sensors are not displayed in Figure 62.

The gas handling system features charcoal traps at room temperature, 70 K and 4 K. Two units are foreseen at each temperature level to allow for alternating operation, which is necessary for trap regeneration without interruption of the  $^3\text{He}$  circulation. All traps are cooled by He to avoid the additional infrastructure needed to produce liquid  $\text{N}_2$ . Alternatively, cryocoolers may be used to cool the traps.

The main requirements for the proximity cryogenics are the desired flow rate of liquid  $^4\text{He}$  and the temperature, pressure head and flow rate of cold shielding gas which have to be supplied to the cryostat.

Three copper shields are accommodated inside the vacuum vessel of the cryostat. They are soldered to a pipe through which cold, gaseous helium is flown. The flow rate has to be chosen such that dewing does not occur on the wall of the vacuum vessel. The heat transfer coefficient between the vacuum vessel and air at ambient temperature was calculated with free convection correlations and amounts to  $3.4 \text{ W}/(\text{m}^2 \cdot \text{K})$ . A flow rate of 50 mmol/s has proven suitable in thermal simulation. The resulting pressure drop is 475 mbar. The shield temperatures are 238 K, 166 K and 61 K respectively.

For cooling the three outermost shields of the cold mass, 250 mmol/s of gaseous  $^4\text{He}$  at 20 K and a pressure head of 2.2 bar need to be supplied. The resulting shield temperatures are 220 K, 91 K and 23 K respectively. It is desirable to make the copper shields as thin as possible to reduce the amount of matter inside the shielded volume. As a consequence, conduction along the shield is limited and the  $^4\text{He}$  tube should be thermally linked to the shield at several locations. The temperature of the vacuum vessel around the first shield is close to ambient. The thermal contact between the vacuum vessel and the water in which it is submerged was determined with the aid of free convection correlations and amounts to  $80 \text{ W}/(\text{m}^2 \cdot \text{K})$ .

The next two shields inside the cold mass are cooled by superfluid  $^4\text{He}$  at atmospheric pressure. They are connected serially and separated by a capillary which is dimensioned such that the critical flow velocity of superfluid  $^4\text{He}$  is exceeded. This allows for a larger temperature gradient between the two shields as the thermal conduction in the liquid is greatly reduced. The fact that  $^4\text{He}$  in the supply line is in its superfluid state positively affects heat transport from the refrigeration unit to the detector unit. The flow of liquid  $^4\text{He}$  required to cool the two shields is chosen such that the return stream does not turn normalfluid to keep the pressure drop low. With a flow rate of 6 mmol/s, the shield temperatures amount to 1.5 and 2.13 K.

In steady state operation, the liquefier must provide approximately 60 mmol/s of liquid  $^4\text{He}$  for the 4 K and 1 K stages of the cryostat and roughly 12 mmol/s for the cold charcoal traps. Furthermore, it must provide 300 mmol/s of gaseous  $^4\text{He}$  at a

temperature of 20 K as shield gas for the cryostat and the detector unit. Liquefaction systems fulfilling these requirements are available commercially.<sup>31</sup>

The required flow rates of gaseous  $^4\text{He}$  at 20 K and of superfluid  $^4\text{He}$  have been evaluated by means of numeric thermal simulation. The thermodynamic data of  $^4\text{He}$  was taken from [136]. The heat transfer and pressure drop correlations for forced and free convection are given in [57] and [115].

Water cooling must be provided for the  $^3\text{He}$  and  $^4\text{He}$  pumping systems, for the compressor and for the liquefier. The  $^3\text{He}$  pumps will dissipate some 20 kW if a system with a pumping speed of 4000 m<sup>3</sup>/h is chosen; the pumps for the 12000 m<sup>3</sup>/h alternative would dissipate some 55 kW. The  $^4\text{He}$  pumps with a pumping speed of 1000 m<sup>3</sup>/h will reject some 9 kW to the water cooling loop. The compressor and liquefier required for continuous supply with liquid  $^4\text{He}$  dissipate some 90 kW. All electronic components will be placed in racks, which are equipped with air/water heat exchangers. Rack internal cooling is effected by circulating cold air, which in turn rejects heat to the laboratory's water cooling loop.

### ***6.10 Design Risks and Alternatives***

Numerical thermal simulation has been used to evaluate and verify the performance of the proposed dilution refrigeration system. Figure 63 shows the mixing chamber temperature as a function of cooling power at a  $^3\text{He}$  flow rate of 8.3 mmol/s. This chart may be used to determine the influence of an unexpectedly high heat load. It seems unlikely that much higher flow rates than the projected one will be achievable, as this would imply installing new pumps and redesigning the whole  $^3\text{He}$  circuit. It may however be possible to replace the heat exchanger by a larger one, and operate the refrigerator at suboptimum flow. Figure 63 gives data for the projected heat exchanger with a surface area of some 40 m<sup>2</sup> and for a possible replacement by 48 m<sup>2</sup>. In addition, Figure 63 illustrates the difference between ideal and real heat exchangers and the resulting necessity to include sufficient MoS in preliminary design calculations: The desired mixing chamber temperature of 7 mK is only achieved at heat loads below 8  $\mu\text{W}$ , a considerably lower value than that used in section 6.5.

---

<sup>31</sup> Such as the L140 liquefier with DSD171 compressor of Linde Kryotechnik (Wiesbaden, Germany)

The numerical model underlying the data in Figure 63 and Figure 64 does not take into account the limited efficiency of sintered sponges. As a consequence, considerably more sintered copper powder than theoretically necessary should be accommodated.

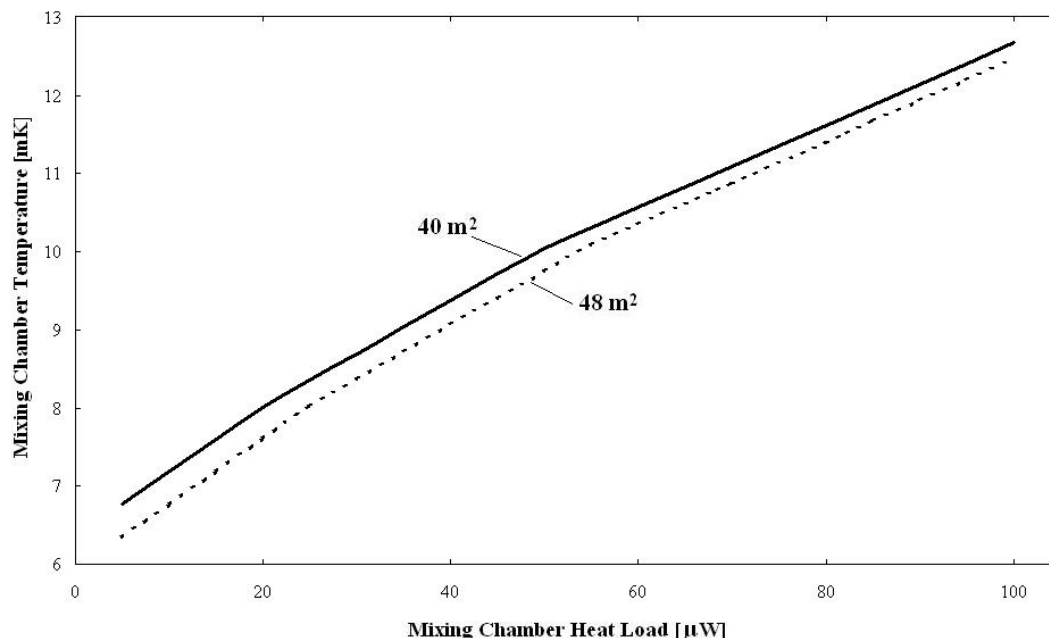


**Figure 63:** The EURECA mixing chamber temperature for  $\dot{n}_3 = 8.3 \text{ mmol/s}$  as a function of the heat load for two different heat exchange surfaces, namely  $A = 40 \text{ m}^2$  and  $A = 48 \text{ m}^2$ .

Figure 64 on page 143 shows the performance of the EURECA dilution refrigerator if the heat exchanger has a smaller surface area than expected. The mixing chamber temperature is shown for a heat load of  $20 \mu\text{W}$  as a function of the  $^3\text{He}$  flow rate for three heat exchangers with 50 %, 30 % and 10 % of the projected surface area respectively. The highest acceptable detector temperature is most likely determined by the transition edge thermometers and remains to be defined.

In case the development risk associated with such a large dilution refrigeration system should be deemed too high, a design alternative featuring eight dilution refrigerators of more common size can be considered. Each detector column would be cooled by a single dilution refrigerator; the eighth unit would be used to cool the thermal shields. Closely spaced thermal shields would have to be placed between the detector columns to avoid interferences between two given refrigerators. A detector column could possibly be replaced without influencing the temperature of the others at all.

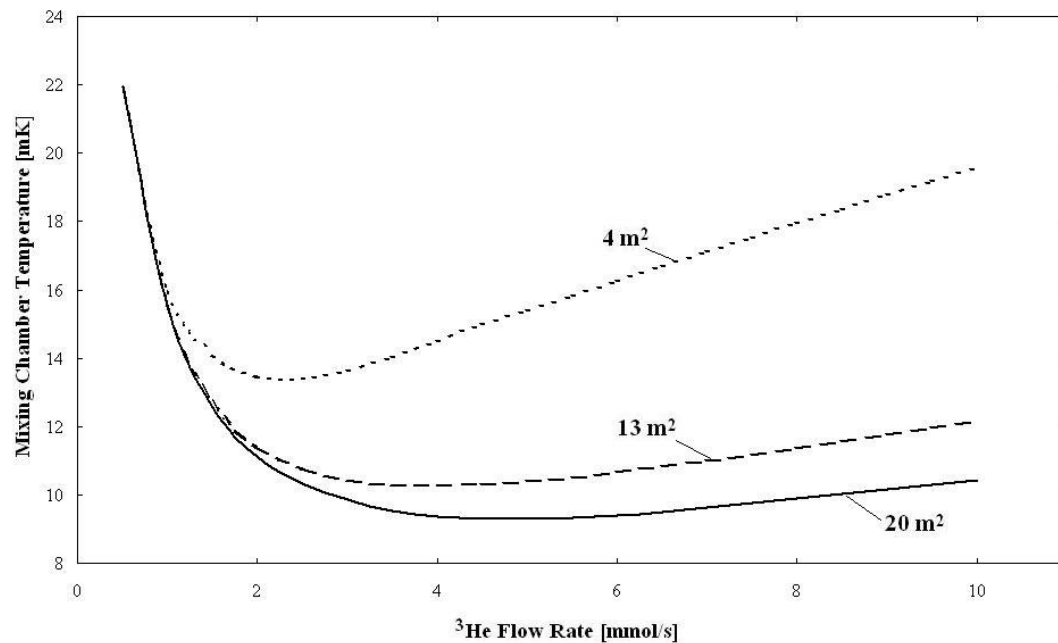


**Figure 64:** The EURECA mixing chamber temperature as a function of  $^3\text{He}$  flow rate for heat exchangers with insufficiently large surface areas, namely  $A = 20 \text{ m}^2$ ,  $A = 13 \text{ m}^2$  and  $A = 4 \text{ m}^2$

Due to the fact that the amount of auxiliary equipment – such as pumps, gas reservoirs and control systems - is increased accordingly, the production cost of such a system is estimated to be considerably higher than the production cost of a single, large system. A well designed system consisting of a single dilution refrigerator will also feature higher reliability than an array of several smaller refrigerators.

Furthermore, it seems desirable to push the state of the art of dilution refrigeration to new levels. Other experiments, such as the gravitational wave detectors described in chapter 1, would benefit from such developments.

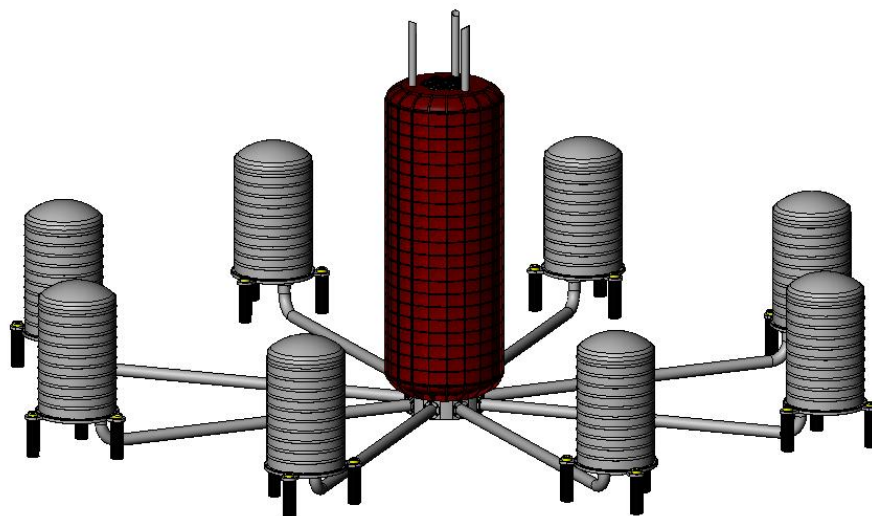


**Figure 65:** A design alternative for EURECA featuring 8 dilution refrigerators

## 7. Conclusions and Outlook

### 7.1 Summary

This thesis project was set out to develop a reliable and precise method for the calculation of the cooling power of a dilution refrigerator of a given design and to determine the residual heat load on devices operated at very low temperatures.

A thermal model of a dilution refrigerator has been established using numerical simulation. The results yielded by this model were compared to experimental data obtained from measurements performed with the CCDR, a dilution refrigerator which has been designed, built and tested in the framework of this thesis project. The simulation agrees well with experiments, which proves its suitability for the engineering of VLT machines. Further work is however necessary on the characterization of the heat transfer between sintered sponges and liquid He.

The sources of residual heat on very low temperature equipment were identified and studied. The magnitude of each source was either derived from theory, from experimental results published by other groups, or from measurements performed with the CCDR. It is concluded that conduction in residual gas and the relaxation of thermoelastic stress are the most dominant sources of residual heat in multi-ton cold mass experiments.

Building on the findings listed above, a design study for a multi-ton cold mass experiment has been performed. A high performance dilution refrigeration system is required to absorb a heat load of  $20 \mu\text{W}$  at a temperature of  $7 \text{ mK}$ . The underlying concept serves as a baseline for EURECA, a future European dark matter search.

### 7.2 Suggestions for Future Work

Several topics remain to be addressed before claiming that the refrigeration of multi-ton cold masses can be undertaken without substantial risk of failure. Suggestions for future work on this subject can be grouped into three categories, namely the extension of the cooling power measurements, further experimental work on the residual heat loads and the development of key components for multi-ton cold mass experiments.

*EXTENSION OF COOLING POWER MEASUREMENTS*

- The cooling power measurements should be extended to temperatures below 30 mK and compared to the results of the numerical model.
- The thermal performance of sintered sponges must be studied in more detail. It would be useful to conduct measurements on dedicated sponge samples of different thickness and grain size in the mixing chamber.
- The construction and test of a large heat exchanger is recommended in order to explore the feasibility of a dilution refrigerator with the performance outlined in chapter 6 of this thesis. The CCDR is capable of reaching the required flow rates if one or two Roots blowers are added to the  $^3\text{He}$  pump stand.

*EXPERIMENTAL WORK ON RESIDUAL HEAT LOADS*

- It is suggested to rigorously test the equations and numbers given in chapter 4, focusing on the potentially large heat sources, i.e. the conduction in solids and residual gas, vibrations and the relaxation of thermoelastic stress. Such measurements will benefit from improved thermometry, such as Pt-NMR.
- For EURECA, it will be important to establish a catalogue of materials which may be used in the cold mass. These materials must fulfill radiopurity requirements and have a low internal heat release. The internal heat release of typical materials to be used in the cold mass of a dark matter detector should be studied (among others, radiopure copper, stainless steel, nickel and PE are considered important).

*KEY COMPONENTS FOR MULTI-TON COLD MASS EXPERIMENTS*

- The load lock mechanism for the detector columns in the detector unit of EURECA is an issue of major criticality. A prototype should be built and tested.
- The thermal link between the mixing chamber and the detector modules should be characterized experimentally. It is suggested to measure the  $\Delta T$  which develops across the link as a function of pressing force.

Some of these items will be addressed by Burghart [22].



## Appendices

### A. Thermal Simulation Model for the CCDD

The TAK 2000 code listing which has been used to simulate the CCDD is given below. In total, 12 sintered elements are modeled, along with a straight and a coiled tube-in-tube heat exchanger. The most important operating parameters, namely the  $^3\text{He}$  flow rate, the still temperature, the heat load on the mixing chamber and the surface area efficiency of the heat exchanger can be adjusted by changing the variables in section “Boundary Conditions”.

```

C-----
HEADER OPTIONS DATA
C-----

UID      = SI          $ Model Units
SOLRTN   = FWDWRD     $ Solution routine
Logic    = On         $ User logic

QPrint   = Off        $ Print impressed heat rates
GPrint   = Off        $ Print conductor values
CPrint   = Off        $ Print nodal thermal masses
CSGDump  = Off        $ Print nodal CSG values
NCVPrint = Off        $ Print NCV conductor status
HPrint   = Off        $ Print heater status
LPrint   = Off        $ Print thermal louver status

QDump    = Off        $ Print network map
PlotQ    = Off        $ Create ,PLQ plot file of heat rates (SS Only)
LodTmp   = Off        $ Load initial temperatures from ,INI file
AutoDamp = On         $ Automatic solution damping function (SS Only)

Dictionaries = On      $ Print actual/relative data dictionaries

C-----
HEADER CONTROL DATA
C-----

C  ----- Program Control Constants -----

ABSZRO   = 0.0          $ Absolute Zero
SIGMA    = 1.0          $ Stefan-Boltzmann Constant
IFC      = 3            $ Output Units Flag

C  ----- Transient Constants -----

TIMEO    = 0.0          $ Transient start time
TIMEND   = 10.0         $ Transient stop time
PLOT     = 1.0          $ Plot file output interval
TRCRIT   = 0.0000000001 $ Transient convergence criteria
NLOOPT   = 999999       $ Max number of iterations per step
OUTPUT   = 20.0         $ Transient output interval
DTIMEI   = 0.0001      $ Maximum Time Step

C  ----- Boundary Conditions -----

FLOW     = 0.0001       $ He3 Flow Rate [mol/s]
ST       = 800.0         $ Still Temperature [mK]
HL       = 500.0         $ Heat Load due to Mixing Chamber Heater [microW]
EA       = 0.01         $ Heat Exchanger Surface Efficiency

```

```

C ----- Geometric Parameters -----
C   Straight Tube-in-Tube H/X
      SDIAI = 0.65          $ Inner Diameter of CuNi Tube [mm]
      SDIAO = 1.0          $ Outer Diameter of CuNi Tube [mm]
      SL = 500.0           $ Total Length of Straight H/X [mm]
      DilAS = 27.5         $ Cross Section of Dilute Stream [mm^2]

C   Coiled Tube-in-Tube H/X
      CDIAI = 0.65          $ Inner Diameter of CuNi Tube [mm]
      CDIAO = 1.0          $ Outer Diameter of CuNi Tube [mm]
      CLCon = 1200.0        $ Total Length of Coiled H/X - Concentrated Stream
      CLDil = 700.0        $ Total Length of Coiled H/X - Dilute Stream
      DilAC = 27.5         $ Cross Section of Dilute Stream [mm^2]

C   Sintered H/X
      FLC = EA*167.0        $ Surface Area in Concentrated Stream per Element [cm2]
      FLD = EA*983.0        $ Surface Area in Dilute Stream per Element [cm2]
      SinL = 80.0          $ Length of a single Element [mm]
      DilASin = 26.5       $ Cross Section of Dilute Stream [mm^2]
      ConASin = 1.6        $ Cross Section of Concentrated Stream [mm^2]

C   Connection between HX and Mixing Chamber
      ConnL = 150.0         $ Total Length of Connection Piece [mm]
      ConnDIAI = 0.65      $ Diameter of Conc. Stream of Connection Piece [mm]
      DilAConn = 27.5      $ Cross Section of Dilute Stream [mm^2]

C ----- Thermodynamic Parameters -----
      CuCon = 20.0          $ Kapitza Cu - Con. Sol. 20 [W/(K^4*m^2)] (Niinikoski)
      CuDil = 25.0          $ Kapitza Cu - Dil. Sol. 25 [W/(K^4*m^2)] (Niinikoski)

      CNCon = 67.0          $ Kapitza CuNi - Con. Sol. 67.0 [W/(K^4*m^2)] (estimate)
      CNDil = 67.0          $ Kapitza CuNi - Dil. Sol. 67.0 [W/(K^4*m^2)] (Snyder)

C-----
HEADER NODE DATA
C-----
      BAS -10, ST, -0.0     $ Still Liquid (Boundary Node)
      BAS 30, ST, 0.1       $ Mixing Chamber Liquid

      GEN 1100, 20, 1, ST, 0.0 $ Straight Tube-in-Tube H/X Concentrated Stream
      GEN 1120, 20, 1, ST, 0.0 $ Coiled Tube-in-Tube H/X Concentrated Stream
      GEN 1140, 96, 1, ST, 0.0 $ Sintered H/X Concentrated Stream

      GEN 1400, 20, 1, ST, 0.0 $ Straight Tube-in-Tube H/X Dilute Stream
      GEN 1420, 20, 1, ST, 0.0 $ Coiled Tube-in-Tube H/X Dilute Stream
      GEN 1440, 96, 1, ST, 0.0 $ Sintered H/X Dilute Stream

      GEN 1700, 20, 1, ST, 0.0 $ Straight Tube-in-Tube CuNi Tube
      GEN 1800, 20, 1, ST, 0.0 $ Coiled Tube-in-Tube CuNi Tube
      GEN 3500, 12, 1, ST, 0.0 $ Sintered Copper Tubes

      BAS 5000, 1.0, -0.0    $ To Store FLOW Variable

C-----
HEADER CONDUCTOR DATA
C-----
      BAS 1, -10, 1100, 1.0  $ Flow from Still into Tube-in-Tube H/X
      GEN 1100, 135, 1, -1100, 1, 1101, 1, 1.0 $ Flow in Concentrated Stream
      BAS 1236, -1235, 30, 1.0 $ Flow from Concentrated Stream to MC

      GEN 1400, 135, 1, 1400, 1, -1401, 1, 1.0 $ Flow in Dilute Stream
      BAS 1536, -30, 1535, 1.0 $ Flow from MC to Dil. Stream

C ----- Straight Tube-in-Tube H/X -----
      GEN -1700, 20, 1, 1100, 1, 1700, 1, SDIAI*SL/20.0*3.1415*CNCon*1.0E-12
      GEN -1800, 20, 1, 1400, 1, 1700, 1, SDIAO*SL/20.0*3.1415*CNDil*1.0E-12

C ----- Coiled Tube-in-Tube H/X -----
      GEN -1900, 20, 1, 1120, 1, 1800, 1, CDIAI*CLCon/20.0*3.1415*CNCon*1.0E-12
      GEN -2000, 20, 1, 1420, 1, 1800, 1, CDIAO*CLCon/20.0*3.1415*CNDil*1.0E-12

```

```

C ----- Sintered H/X -----
C The first block defines the Kapitza conductances between the sintered
C powder and the concentrated stream. The second block defines the Kapitza
C conductance between the sintered powder and the dilute stream. One line
C stands for one element. Radiation conductors are used to account for the
C T^4 dependence.

```

```

GEN -2100, 8, 1, 3500, 0, 1140, 1, CuCon*FLC/16.0*1.0E-10
GEN -2108, 8, 1, 3501, 0, 1148, 1, CuCon*FLC/16.0*1.0E-10
GEN -2116, 8, 1, 3502, 0, 1156, 1, CuCon*FLC/16.0*1.0E-10
GEN -2124, 8, 1, 3503, 0, 1164, 1, CuCon*FLC/8.0/1.0E-10
GEN -2132, 8, 1, 3504, 0, 1172, 1, CuCon*FLC/8.0/1.0E-10
GEN -2140, 8, 1, 3505, 0, 1180, 1, CuCon*FLC/8.0/1.0E-10
GEN -2148, 8, 1, 3506, 0, 1188, 1, CuCon*FLC/8.0/1.0E-10
GEN -2156, 8, 1, 3507, 0, 1196, 1, CuCon*FLC/8.0/1.0E-10
GEN -2164, 8, 1, 3508, 0, 1204, 1, CuCon*FLC/8.0/1.0E-10
GEN -2172, 8, 1, 3509, 0, 1212, 1, CuCon*FLC/8.0/1.0E-10
GEN -2180, 8, 1, 3510, 0, 1220, 1, CuCon*FLC/8.0/1.0E-10
GEN -2188, 8, 1, 3511, 0, 1228, 1, CuCon*FLC/8.0/1.0E-10

```

```

GEN -2300, 8, 1, 3500, 0, 1440, 1, CuDil*FLD/16.0*1.0E-10
GEN -2308, 8, 1, 3501, 0, 1448, 1, CuDil*FLD/16.0*1.0E-10
GEN -2316, 8, 1, 3502, 0, 1456, 1, CuDil*FLD/16.0*1.0E-10
GEN -2324, 8, 1, 3503, 0, 1464, 1, CuDil*FLD/8.0*1.0E-10
GEN -2332, 8, 1, 3504, 0, 1472, 1, CuDil*FLD/8.0*1.0E-10
GEN -2340, 8, 1, 3505, 0, 1480, 1, CuDil*FLD/8.0*1.0E-10
GEN -2348, 8, 1, 3506, 0, 1488, 1, CuDil*FLD/8.0*1.0E-10
GEN -2356, 8, 1, 3507, 0, 1496, 1, CuDil*FLD/8.0*1.0E-10
GEN -2364, 8, 1, 3508, 0, 1504, 1, CuDil*FLD/8.0*1.0E-10
GEN -2372, 8, 1, 3509, 0, 1512, 1, CuDil*FLD/8.0*1.0E-10
GEN -2380, 8, 1, 3510, 0, 1520, 1, CuDil*FLD/8.0*1.0E-10
GEN -2388, 8, 1, 3511, 0, 1528, 1, CuDil*FLD/8.0*1.0E-10

```

```

C ----- Link FLOW Node to Still -----
C The 3he flow Variable is stored as the temperature of node 5000. To
C avoid error messages, this node must be thermally anchored to another
C node. As a consequence, it is connected to the still with a linear
C conductor of conductance 0:

```

```

BAS 5000, -10, 5000, 0.0

```

```

C-----
HEADER ARRAY DATA
C-----

```

```

10      $ Cooling Power (Radebaugh)
C Temp  J/mol  (T)
0.      ,      0.00000000
1.      ,      0.00008188
2.      ,      0.00032770
4.      ,      0.001312
6.      ,      0.002954
8.      ,      0.005254
10.     ,      0.008214
15.     ,      0.01850
20.     ,      0.03288
25.     ,      0.05132
30.     ,      0.07377
35.     ,      0.10012
40.     ,      0.13028
45.     ,      0.16410
50.     ,      0.2014
60.     ,      0.2857
70.     ,      0.3813
80.     ,      0.4865
90.     ,      0.5995
100.    ,      0.7186
120.    ,      0.9699
140.    ,      1.2328
160.    ,      1.5020
180.    ,      1.7740
200.    ,      2.0460
250.    ,      2.7180
300.    ,      3.3640
350.    ,      3.9750
400.    ,      4.5410
450.    ,      5.0610
500.    ,      5.4780
550.    ,      5.9160
600.    ,      6.2160, END

```

```

100      $ Specific Heat for Concentrated Stream (Greywall)
C Temp  (J/mol*K)
0.      ,      0.
10.     ,      0.2278036
20.     ,      0.4514502
40.     ,      0.8779584
60.     ,      1.2562454
80.     ,      1.5788286
100.    ,      1.858179
150.    ,      2.4085658
200.    ,      2.7203408
300.    ,      3.0329472
400.    ,      3.1875876
500.    ,      3.2973324
600.    ,      3.417054
700.    ,      3.5716944
800.    ,      3.762085
900.    ,      3.9774176, END

```

C The following, two dimensional array gives the data for the  
C specific heat of the dilute stream, which does not only  
C depend on the temperature of the dilute solution, but also  
C on the temperature of the mixing chamber:

```

C Specific Heat for Dilute Stream (Radebaugh)
C Temp  (J/mol*K)
200., 7., 0.,      10.,      20.,      50.,      100.,      200.,      400.
0.,    0.,    0.,    0.,    0.,    0.,    0.,    0.,    0.
10.,   1.0777, 1.0745, 0.,    0.,    0.,    0.,    0.,    0.
20.,   2.1907, 2.1842, 2.1645, 0.,    0.,    0.,    0.,    0.
40.,   4.6282, 4.6146, 4.5742, 0.,    0.,    0.,    0.,    0.
60.,   7.3202, 7.3009, 7.2435, 6.8655, 0.,    0.,    0.,    0.
80.,   9.9790, 9.9571, 9.8921, 9.4606, 0.,    0.,    0.,    0.
100.,  12.3295, 12.3082, 12.2446, 11.8185, 10.7161, 0.,    0.
120.,  14.1442, 14.1265, 14.0840, 13.7293, 12.6129, 0.,    0.
140.,  15.6269, 16.2838, 16.1448, 15.6793, 14.6070, 0.,    0.
160.,  16.4656, 16.5749, 16.5830, 16.3652, 15.5667, 0.,    0.
200.,  18.1627, 18.1539, 18.1273, 17.9369, 17.3821, 16.4768, 0.
300.,  19.7727, 19.7703, 19.7634, 19.7137, 19.4075, 18.8660, 0.
400.,  20.3670, 20.3647, 20.3580, 20.2994, 20.1291, 19.7611, 23.1794
500.,  20.7311, 20.7267, 20.7124, 20.6535, 20.4712, 20.1931, 20.9547
600.,  21.1960, 21.1917, 21.1778, 21.0771, 20.8861, 20.4920, 20.6270
700.,  21.8847, 21.8781, 21.8554, 21.6978, 21.3002, 20.7636, 20.6054
800.,  23.3202, 23.3033, 23.2577, 22.9486, 22.2308, 21.2345, 20.7156
900.,  26.8309, 26.7920, 26.6765, 25.9657, 24.3589, 22.3342, 21.0216, END

```

```

300      $ Thermal Conductivity for 3He (Niinikoski)
C Temp  (W/mK)
0.      ,      0.36
10.     ,      0.036
20.     ,      0.018
40.     ,      0.009
60.     ,      0.006
80.     ,      0.004
100.    ,      0.007
200.    ,      0.006
300.    ,      0.00643
400.    ,      0.00686
500.    ,      0.00729
600.    ,      0.00771
700.    ,      0.00814
800.    ,      0.00857
900.    ,      0.009, END

```

```

400      $ Thermal Conductivity for Dilute Solution (Niinikoski)
C Temp  (W/mK)
0.      ,      0.3
10.     ,      0.03
20.     ,      0.03
40.     ,      0.07
60.     ,      0.11
80.     ,      0.15
100.    ,      0.18
150.    ,      0.28
200.    ,      0.25
300.    ,      0.2
400.    ,      0.2
500.    ,      0.2
600.    ,      0.2
700.    ,      0.2
800.    ,      0.2
900.    ,      0.2, END

```

```

500          $ Dynamic Viscosity of 3He (Niinikoski)
C Temp      (kg/(m*s))
10.         ,      0.001978
20.         ,      0.000520
40.         ,      0.000144
60.         ,      0.000070
80.         ,      0.000044
100.        ,      0.000031
150.        ,      0.000017
200.        ,      0.000012
300.        ,      0.000008
400.        ,      0.000006
500.        ,      0.000005
600.        ,      0.000004
700.        ,      0.000004
800.        ,      0.000004
900.        ,      0.000004, END

```

```

C-----
HEADER OPERATIONS
C-----

```

```

C This is the main routine of the program. First, a file
C (C:\result.txt) is opened. The heat load is written in
C the file. Each run through the loop DR executes the simulation
C with a certain flow rate. The loop ends as soon as a flow of
C 0.003 is exceeded.

```

```

      OPEN(20, FILE='c:\result.txt', IOSTAT=STAT)
      WRITE(20,*) 'Heat Load: ', HL
      WRITE(20,*) ''

```

```

      DR: DO WHILE (FLW .LT. 0.003)
      TIMEO = 0
      FLW = FLW + 0.0002
      T5000 = FLW

```

```

      CALL FWDWRD
      CALL NETMAP
      CALL COLTMP

```

```

      WRITE(20,*) , FLW*1000.0, T(30)
      ENDDO DR

```

```

      CLOSE(20)

```

```

C-----
HEADER OUTPUT CALLS
C-----

```

```

C Empty Header to Avoid Automatic Generation by TAK

```

```

C-----
HEADER VARIABLES 1
C-----

```

```

      FLOW = T5000

```

```

C Assign Cooling Power to Mixing Chamber

```

```

F      X = T(2)
      CALL D1DEG1(X, A10, S)
F      Q(2) = (-1000000.0*FLOW*S)+HL

```

```

C Assign Conductances to Concentrated Stream (Still to HX)

```

```

F      X = T(10)
      CALL D1DEG1(X, A100, S)
F      G(1) = FLOW*(S)*1000

```

```

C Assign Conductances to Concentrated Stream (Straight Tube-in-Tube HX)

```

```

      Conductor = 2
      Concl: DO WHILE (Conductor .LT. 23)
F      X = T(Conductor + 1)
      CALL D1DEG1(X, A100, S)
      CALL D1DEG1(X, A300, P)
      P = P*(3.1415/4.0*(SDIAI**2)/(SL/20.0))/1000.0
F      G(Conductor) = (FLOW*S+P)*1000
      Conductor = Conductor + 1
      ENDDO Concl

```

## C Assign Conductances to Concentrated Stream (Coiled Tube-in-Tube HX)

```

Conc2: DO WHILE (Conductor .LT. 43)
F      X = T(Conductor + 1)
        CALL D1DEG1(X, A100, S)
        CALL D1DEG1(X, A300, P)
        P = P*(3.1415/4.0*(CDIAI**2)/(CLCon/20.0))/1000.0
F      G(Conductor) = (FLOW*S+P)*1000
        Conductor = Conductor + 1
ENDDO Conc2

```

## C Assign Conductances to Concentrated Stream (Sintered HX)

```

Conc3: DO WHILE (Conductor .LT. 137)
F      X = T(Conductor + 1)
        CALL D1DEG1(X, A100, S)
        CALL D1DEG1(X, A300, P)
        P = P*(ConASin/(SinL/8.0))/1000.0
F      G(Conductor) = (FLOW*S+P)*1000
        Conductor = Conductor + 1
ENDDO Conc3

```

## C Conductor into Mixing Chamber

```

F      X = T(138)
        CALL D1DEG1(X, A100, S)
        CALL D1DEG1(X, A300, P)
        P = P*(3.1415/4.0*(ConnDIAI**2)/ConnL)/1000.0
F      G(137) = (FLOW*S+P)*1000

```

## C Assign Viscous Heating Rates to Concentrated Stream (Straight Tube-in-Tube HX)

```

Conductor = 2
Conc4: DO WHILE (Conductor .LT. 23)
F      X = T(Conductor + 1)
        CALL D1DEG1(X, A500, S)
        P = 128*S*((SL/1000)/20)/3.1415/((SDIAI/1000)**4)
        P = P*(FLOW**2)*((36.83/1E6)**2)*1.E6
F      Q(Conductor+1) = P
        Conductor = Conductor + 1
ENDDO Conc4

```

## C Assign Viscous Heating Rates to Concentrated Stream (Coiled Tube-in-Tube HX)

```

Conc5: DO WHILE (Conductor .LT. 43)
F      X = T(Conductor + 1)
        CALL D1DEG1(X, A500, S)
        P = 128*S*((CLCon/1000)/20)/3.1415/((CDIAI/1000)**4)
        P = P*(FLOW**2)*((36.83/1E6)**2)*1.E6
F      Q(Conductor+1) = P
        Conductor = Conductor + 1
ENDDO Conc5

```

## C Assign Viscous Heating Rates to Concentrated Stream (Sintered HX)

```

Conc6: DO WHILE (Conductor .LT. 137)
F      X = T(Conductor + 1)
        CALL D1DEG1(X, A500, S)
        P = P*(ConASin/(SinL/8.0))/1000.0
        P = 128*S*((SinL/1000)/8)/3.1415/((ConASin*4/3.1415/1.E6)**2)
        P = P*(FLOW**2)*((36.83/1E6)**2)*1.E6
F      Q(Conductor+1) = P
        Conductor = Conductor + 1
ENDDO Conc6

```

## C Assign Viscous Heating Rates to Concentrated Stream (into Mixing Chamber)

```

F      X = T(138)
        CALL D1DEG1(X, A500, S)
        P = 128*S*((ConnL/1000)/20)/3.1415/((ConnDIAI/1000)**4)
        P = P*(FLOW**2)*((36.83/1E6)**2)*1.E6
F      Q(138) = P

```

## C Assign Conductances to Dilute Stream (Straight Tube-in-Tube HX)

```

Conductor = 138
Dilute1: DO WHILE (Conductor .LT. 158)
F   X = T(Conductor + 1)
F   Y = T(2)
    CALL D2DEG1(Y, X, A200, S)
    CALL D1DEG1(X, A400, P)
    P = P*(DilAS/(SL/20.0))/1000.0
    IF (P .GE. FLOW*S) THEN P = 0
F   G(Conductor) = (FLOW*S-P)*1000
    Conductor = Conductor + 1
ENDDO Dilute1

```

## C Assign Conductances to Dilute Stream (Coiled Tube-in-Tube HX)

```

Dilute2: DO WHILE (Conductor .LT. 178)
F   X = T(Conductor + 1)
F   Y = T(2)
    CALL D2DEG1(Y, X, A200, S)
    CALL D1DEG1(X, A400, P)
    P = P*(DilAC/(CLDil/20.0))/1000.0
    IF (P .GE. FLOW*S) THEN P = 0
F   G(Conductor) = (FLOW*S-P)*1000
    Conductor = Conductor + 1
ENDDO Dilute2

```

## C Assign Conductances to Dilute Stream (Sintered HX)

```

Dilute3: DO WHILE (Conductor .LT. 273)
F   X = T(Conductor + 1)
F   Y = T(2)
    CALL D2DEG1(Y, X, A200, S)
    CALL D1DEG1(X, A400, P)
    P = P*(DilASin/(SinL/8.0))/1000.0
    IF (P .GE. FLOW*S) THEN P = 0
F   G(Conductor) = (FLOW*S-P)*1000
    Conductor = Conductor + 1
ENDDO Dilute3

```

## C Conductor from Mixing Chamber

```

F   X = T(2)
F   Y = T(2)
    CALL D2DEG1(Y, X, A200, S)
    CALL D1DEG1(X, A400, P)
    P = P*(DilAConn/ConnL)/1000.0
    IF (P .GE. FLOW*S) THEN P = 0
F   G(273) = ((FLOW*S)-P)*1000

```

## C Assign Viscous Heating Rates to Dilute Stream (Straight Tube-in-Tube HX)

```

Conductor = 138
Dilute4: DO WHILE (Conductor .LT. 158)
F   X = T(Conductor + 1)
    P = 128*5.E-8*((SL/20.0)/1000)*(FLOW**2)*((36.83/1E6)**2)/3.1415
    P = P/((X/1000)**2)/((DilAS*4/3.1415/1.E6)**2)*1.E6
F   Q(Conductor+1) = P
    Conductor = Conductor + 1
ENDDO Dilute4

```

## C Assign Viscous Heating Rates to Dilute Stream (Coiled Tube-in-Tube HX)

```

Dilute5: DO WHILE (Conductor .LT. 178)
F   X = T(Conductor + 1)
    P = 128*5.E-8*((CLDil/20.0)/1000)*(FLOW**2)*((36.83/1E6)**2)/3.1415
    P = P/((X/1000)**2)/((DilAC*4/3.1415/1.E6)**2)*1.E6
F   Q(Conductor+1) = P
    Conductor = Conductor + 1
ENDDO Dilute5

```

## C Assign Viscous Heating Rates to Dilute Stream (Sintered HX)

```

Dilute6: DO WHILE (Conductor .LT. 273)
F   X = T(Conductor + 1)
    P = 128*5.E-8*((SinL/8.0)/1000)*(FLOW**2)*((36.83/1E6)**2)/3.1415
    P = P/((X/1000)**2)/((DilASin*4/3.1415/1.E6)**2)*1.E6
F   Q(Conductor+1) = P
    Conductor = Conductor + 1
ENDDO Dilute6

```

## C Kapitza Conductors in Small Sintered Elements

```

Conductor = 354
KapitzaSmallC: DO WHILE (Conductor .LT. 378)
F   G(Conductor) = CuCon*FLC/16.0*1.0E-10
    Conductor = Conductor + 1
ENDDO KapitzaSmallC

Conductor = 450
KapitzaSmallD: DO WHILE (Conductor .LT. 474)
F   G(Conductor) = CuDil*FLD/16.0*1.0E-10
    Conductor = Conductor + 1
ENDDO KapitzaSmallD

```

## C Kapitza Conductors in Large Sintered Elements

```

Conductor = 378
KapitzaLargeC: DO WHILE (Conductor .LT. 450)
F   G(Conductor) = CuCon*FLC/8.0*1.0E-10
    Conductor = Conductor + 1
ENDDO KapitzaLargeC

Conductor = 474
KapitzaLargeD: DO WHILE (Conductor .LT. 546)
F   G(Conductor) = CuDil*FLD/8.0*1.0E-10
    Conductor = Conductor + 1
ENDDO KapitzaLargeD

```

## C Output Data

```

IF (TIMEN .EQ. DTIMEI) THEN
WRITE(IWIN,*) 'Flow: ', FLOW
CALL SCRNRWRITE(IWIN)
ENDIF

```

```

C-----
END OF DATA
C-----

```

The thermal network model above contains the values used for the calculation of the mixing chamber as a function of  $^3\text{He}$  flow rate for a cooling power of 500  $\mu\text{W}$ . Other data can be calculated by changing the program section called “HEADER OPERATIONS”.

### ***B. Thermal Simulation Model for Sintered Sponges***

The following thermal network has been used to calculate the efficiency of sintered heat exchangers as presented in section 3.6. It contains material properties of pure  $^3\text{He}$  and can thus only be used for the calculation of the surface area efficiency of the concentrated stream of a sintered heat exchanger. The model can however easily be changed to allow for calculations of the dilute side of the main heat exchanger.



C-----  
 HEADER OPTIONS DATA  
 C-----

UID	= SI	\$ Model Units
SOLRTN	= FWDWRD	\$ Solution routine
Logic	= On	\$ User logic
QPrint	= Off	\$ Print impressed heat rates
GPrint	= Off	\$ Print conductor values
CPrint	= Off	\$ Print nodal thermal masses
CSGDump	= Off	\$ Print nodal CSG values
NCVPrint	= Off	\$ Print NCV conductor status
HPrint	= Off	\$ Print heater status
LPrint	= Off	\$ Print thermal louver status
QDump	= Off	\$ Print network map
PlotQ	= Off	\$ Create ,PLQ plot file of heat rates (SS Only)
LodTmp	= Off	\$ Load initial temperatures from ,INI file
AutoDamp	= On	\$ Automatic solution damping function (SS Only)
Dictionaries	= On	\$ Print actual/relative data dictionaries

C-----  
 HEADER CONTROL DATA  
 C-----

C ----- Program Control Constants -----

ABSZRO	= 0.	\$ Absolute Zero
SIGMA	= 1.0	\$ Stefan-Boltzmann Constant
IFC	= 3	\$ Output Units Flag

C ----- Transient Constants -----

TIMEO	= 0.0	\$ Transient start time
TIMEND	= 5.0	\$ Transient stop time
PLOT	= 0.7	\$ Plot file output interval
TRCRIT	= 0.0000000001	\$ Transient convergence criteria
NLOOPT	= 999999	\$ Max number of iterations per step
OUTPUT	= 20.0	\$ Transient output interval
DTIMEI	= 0.0001	\$ Maximum Time Step

C ----- User Data -----

XLT	= 0.0	\$ Lowest Sponge Temp
YLT	= 400.0	\$ Highest Liquid Temp
ST	= 250.0	\$ Highest Sponge Temp
FL	= 167.0/8.0	\$ Surface Area per Element per Node [cm2]
SPT	= 0.7	\$ Sponge Thickness [mm]
SPA	= 1.6/8.0	\$ Free Surface Area per Element per Node [cm2]
CuCon	= 20.0	\$ Kapitza Cu Sinter - Conc. Sol. 20.0 [W/(K^4*m^2)]

C-----  
 HEADER NODE DATA  
 C-----

BAS -10, ST, -0.0	\$ Copper (Boundary Node)
BAS -100, ST, -0.0	\$ Concentrated Liquid in Stream
GEN 101, 19, 1, ST, -0.0	\$ Concentrated Liquid in Pore
GEN 200, 19, 1, ST, -0.0	\$ Sponge

C-----  
 HEADER CONDUCTOR DATA  
 C-----

C Conduction in Liquid  
 SIM 100, 19, 1, 100, 1, 101, 1, 10, 0.6\*(SPA/10000.0)/(SPT/1000.0/19.0)\*1.E3

C Kapitza Conduction between Liquid and Sponge  
 GEN -200, 19, 1, 101, 1, 200, 1, CuCon\*(FL/10000.0)/19.0\*1.E-6

C Conduction in Sponge  
 SIM 300, 18, 1, 200, 1, 201, 1, 20, 0.4\*(SPA/10000.0)/(SPT/1000.0/19.0)\*1.E3  
 SIV 400, 218, 10, 20, 0.4\*(SPA/10000.0)/(SPT/1000.0/19.0)\*1.E3

C Ideal Conductor between the two boundary nodes  
 -1000, 10, 100, CuCon\*(FL/10000.0)\*1.E-6

```

C-----
HEADER ARRAY DATA
C-----

10          $ Thermal Conductivity for 3He
C          Temp (W/mK)
0.          ,      0.36
10.         ,      0.036
20.         ,      0.018
40.         ,      0.009
60.         ,      0.006
80.         ,      0.004
100.        ,      0.007
200.        ,      0.006
300.        ,      0.00643
400.        ,      0.00686
500.        ,      0.00729
600.        ,      0.00771
700.        ,      0.00814
800.        ,      0.00857
900.        ,      0.009, END

20          $ Thermal Conductivity for Copper
C          Temp (W/mK)
0.          ,      0.
10.         ,      0.1
20.         ,      0.2
40.         ,      0.4
60.         ,      0.6
80.         ,      0.8
100.        ,      10.
200.        ,      20.
300.        ,      30.
400.        ,      40.
500.        ,      50.
600.        ,      60.
700.        ,      70.
800.        ,      80.
900.        ,      90.
1000.       ,      100., END

C-----
HEADER OPERATIONS
C-----

C Program Main Routine. First, the output file (C:\result.txt) is
C opened. The first loop (designated MN) changes the sponge temperature.
C The second loop (designated DR) changes the liquid temperature.

OPEN(20, FILE='c:\result.txt', IOSTAT=STAT)

      MN: DO WHILE (XLT .LT. ST)
      IF (XLT .GT. 140) THEN
      XLT = XLT + 10.0
      END IF
      IF (XLT .GT. 190) THEN
      XLT = XLT + 30.0
      END IF
      XLT = XLT + 10.0
      T10 = XLT
      WRITE(20,*) 'Sponge Temp: ', T10
      HLT = T10

      DR: DO WHILE (HLT .LT. YLT)
      TIMEO = 0
      HLT = HLT + 10.0
      T100 = HLT
      CALL FWDWRD
      CALL NETMAP
      CALL COLTMP
      F = G100*(T100-T101)
      H = G1000*((T100**4) - (T10**4))
      WRITE(20,*) , T100, F/H
      ENDDO DR

      HLT = 0.0
      WRITE(20,*) ''
      ENDDO MN

CLOSE(20)

C-----
END OF DATA
C-----

```

## Bibliography

- [1] Abel W.R., Johnson R.T. Wheatley J.C. and Zimmermann W., Jr. (1967). *Phys. Rev. Lett.* **18**, 737
- [2] Akerib D.S. and the CDMS Collaboration (2006). *Phys. Rev. Lett.* **96**, 011302
- [3] Alcock C. and the MACHO Collaboration (2000). *Astrophys. J.* **542**, 281
- [4] Allkofer O.C. and Grieder P.K.F. (1983). *Cosmic Rays on Earth*. Karlsruhe Fachinformationszent. Kernforsch. Zentralstelle At. Energ., Karlsruhe
- [5] ALSTOM Power Technology Centre (2004). *ESATAN Engineering Manual, EM-ESATAN-056*
- [6] Anderson P.W., Halperin B.I. and Varma C.M. (1972). *Phys. Mag.* **25**, 1
- [7] Angloher G. et al. (2005). *Astroparticle Physics* **23**, 325
- [8] Arnaboldi C. and the CUORE Collaboration (2004). *Nucl. Instr. and Meth. in Phys. Res. A* **518**, 775
- [9] Aschkinass, E. (1905). *Ann. Phys.* **17**, 960
- [10] Ashby N. and Schocken K. (1965). *Thermal Radiation of Solids*. Scientific and Technical Information Division, NASA, Washington, DC
- [11] Astone P. et al. (1997). *Proc. 7<sup>th</sup> Int. Workshop on Low Temp. Detectors*. Max Planck Institute of Physics, Munich, 206
- [12] Bacher J.-P., Benvenuti C., Chiggiato P., Reinert M.-P., Sgobba S. and A.-M. Brass (2003). *J. Vac. Sci. Technol. A* **21**, 167
- [13] Bargel H.J., Schulze G., ed. (2000). *Werkstoffkunde*. Springer, Berlin, Heidelberg, New York
- [14] Barron R. (1966). *Cryogenic Systems*. McGraw-Hill, New York, St. Louis, San Francisco, Toronto, London, Sydney
- [15] Bendat J.S., Piersol A.G. (2000). *Random Data – Analysis and Measurement Procedures*. Wiley, New York, Chichester, Weinheim, Brisbane, Singapore, Toronto
- [16] Blangetti, F. (1988). *Filmkondensation reiner Dämpfe*. In *VDI Wärmeatlas*, 5<sup>th</sup> ed., VDI-Verlag, Düsseldorf
- [17] Bradley D.I. et al. (1982). *Cryogenics* **22**, 296
- [18] Briggs A. (1991). *Cryogenics* **31**, 932
- [19] Brunauer S., Emmett P.H. and Teller E. (1938). *J. of the American Chem. Soc.* **60**, 309
- [20] Bugaev E.V. et al. (1998). *Phys. Rev. D* **58**, 054001-1
- [21] Bunkov Yu. M. et al. (1990). *J. of Low Temp. Phys.* **83**, 257
- [22] Burghart G. (forthcoming). *Studies of the Key Components for a Large Cryogenic Dark Matter Detector Array (Working Title)*. Ph.D. Thesis, Vienna University of Technology, Austria
- [23] Castelijns C.A.M, Kuerten J.G.M, De Waele A.T.A.M, Gijsman H.M. (1985). *Phys. Rev. B* **32**, 2870

- [24] Castelijns C.A.M (1986). *Flow Properties of  $^3\text{He}$  in Dilute  $^3\text{He}$ - $^4\text{He}$  Mixtures at Temperatures between 10 and 150 mK*. Ph.D. Thesis, Eindhoven University of Technology, Eindhoven, The Netherlands
- [25] Cerdonio M. et al. (1997). *Class. Quantum Grav.* **14**, 1491
- [26] Churochkin D.V., Sahling S. and Osipov V.A. (2005). *Phys. Rev. B* **72**, 014116
- [27] Coccia E. and Niinikoski T.O. (1984). *Lettere al Nuovo Cimento* **41**, 242
- [28] Coccia, E. et al. (1998). *Grav. Waves, Proc. 2<sup>nd</sup> Edoardo Amaldi Conference*. World Scientific, 551
- [29] Cooley J.W. and Tukey J.W. (1965). *Math. Comput.* **19**, 297
- [30] Corrucini R. J. (1959). *Vacuum* **7-8**, 19
- [31] Cousins D.J, Fisher S.N., Guénault A.M., Picket G.R., Smith E.N. and Turner R.P. (1994). *Phys. Rev. Lett.* **73**, 2583
- [32] Cousins D.J, Guénault A.M., Picket G.R., Thibault P. and Turner R.P. (1995). *J. of Low. Temp. Phys.* **101**, 259
- [33] Coyler B. (1966). *Cryogenic Properties of Helium-3 and Helium-4*. Report RHEL/R 138, Rutherford High Energy Laboratory, Chilton, UK
- [34] Das P., De Bruyn R. and Taconis K.W. (1965). *Proc. 9<sup>th</sup> Int. Conf. on Low Temp. Phys.* Plenum Press, London, 1253
- [35] De Waard A., Gottardi L. and Frossati G. (2002). *Class. Quantum Grav.* **19**, 1935
- [36] De Waard A. et al. (2005). *Proceedings of the 6<sup>th</sup> Edoardo Amaldi Conference on Gravitational Waves*. Bankoku Shinryoukan Kise Nago, Okinawa
- [37] Dorey A.P. (1964). *Cryogenics* **5**, 146
- [38] Doshita N. et al. (2004). *Nucl. Instr. and Meth. in Phys. Res. A* **526**, 138
- [39] Drude, P. (1904). *Ann. Phys.* **14**, 677
- [40] Duffy W. (1999). *J. Appl. Phys.* **86**, 2483
- [41] Dupré A., van Itterbeek A. and Michiels L. (1963). *Phys. Lett.* **8**, 99
- [42] Easton D.S., Kroeger D.M. and Moazed A. (1976). *Appl. Phys. Lett.* **29**, 382
- [43] Enss C. and Hunklinger S. (2000). *Tiefertemperaturphysik*. Springer, Berlin, Heidelberg, New York
- [44] Fairbank H.A. and Lee D.M. (1960). *Rev. Sci. Instrum.* **31**, 660
- [45] Feltham, P. (1960). *Journal of the Institute of Metals* **89**, 210
- [46] Fortescue P. and Stark J., ed. (1995). *Spacecraft Systems Engineering, 2nd edition*. John Wiley & Sons, Inc., Chichester, New York, Brisbane, Toronto, Singapore
- [47] Fox A. (1974). *Journal of Testing and Evaluation, JTEVA*, **Vol. 2**, 32
- [48] Frossati G., Godfrin H., Hebral B., Schumacher G. and Thoulouze D. (1977). *Proc. U.L.T. Hakoné Symp.* Phys. Soc. Japan, Tokyo, 205
- [49] Frossati G. (1978). *J. de Phys. (Paris)* **39**, C6-1578
- [50] Frosatti G. (1992). *J. of Low Temp. Phys.* **87**, 595

- [51] Frossati G. and Coccia E (1994). *Cryogenics* **34**, 9
- [52] Frosatti G. (1995). *J. of Low Temp. Phys.* **101**, 81
- [53] Gaisser T.K. and Stanev T. (2002) in Weinberg E.J. et al, ed., *Phys. Rev. D* **66**, *Particles and Fields, Part I*. The American Physical Society
- [54] Gallop J.C. (1991). *SQUIDS, the Josephson Effects and Superconducting Electronics*. IOP Publishing Ltd, Bristol
- [55] Glenn J. W. (1956). *Phil. Mag.* **1**, 400
- [56] Gloos K., Smeibidl P., Kennedy C., Singsaas A., Sekowski P., Mueller R.M. and Pobell F. (1988). *J. of Low Temp. Phys.* **73**, 101
- [57] Gnielinski, V. (1988). *Wärmeübertragung bei erzwungener einphasiger Strömung*. In *VDI Wärmeatlas*, 5<sup>th</sup> ed., VDI-Verlag, Düsseldorf
- [58] Granato A. and Lücke K. (1956). *J. App. Phys.* **27**, 583
- [59] Granato A. and Lücke K. (1956). *J. App. Phys.* **27**, 789
- [60] Greywall D. S. (1983). *Phys. Rev. B* **27**, 2747
- [61] Haasbroek J. N. (1971). *Thermal conductivity at very low temperatures*. Ph.D. Thesis, Rijksuniversiteit te Leiden, The Netherlands.
- [62] Hagen E. and Rubens H. (1903). *Ann. Phys.* **11**, 873
- [63] Hall H.E., Ford P.J. and Thompson, K. (1966). *Cryogenics* **6**, 80
- [64] Hargreaves C.M. (1969). *Phys. Lett. A* **30**, 491
- [65] Harrison J.P. and McCol D.B. (1977). *J. Phys. C: Solid State Phys.* **10**, L297
- [66] Hoffmann T., Lienert U., Quack H. (1973). *Cryogenics* **13**, 490
- [67] Huiku M.T., Jyrkkiö T.A., Kyynäräinen J.M., Lopenen M.T., Lounasmaa O.V. and Oja A.S. (1985). *J. of Low Temp. Phys.* **62**, 433
- [68] Jenson J.E., Tuttle W.A., Stewart R.B., Brechna H. and Prodell A.G. (1980). *Selected Cryogenic Data Notebook*. BNL 10200-R. Brookhaven National Laboratory, Upton (NY)
- [69] Jungmann G., Kamionkowski M, Griest K. (1996). *Phys. Rep.* **267**, p. 195
- [70] K&K Associates, *TAK 2000 Manual*, Rel. 3.2.
- [71] Kast, W. (1988). *Druckverlust bei der Strömung durch Rohre*. In *VDI Wärmeatlas*, 5<sup>th</sup> ed., VDI-Verlag, Düsseldorf
- [72] Kennard E.H (1938). *Kinetic Theory of Gases with an Introduction to Statistical Mechanics*. McGraw-Hill, New York, London
- [73] Klapp E. and Lambrecht D. (1981) *Thermischer Apparatebau*. In *Dubbel, Taschenbuch für den Maschinenbau*, 14<sup>th</sup> ed., Springer, Berlin, Heidelberg, New York
- [74] Kleiman R.N., Agnolet G. and Bishop D.J. (1987). *Phys. Rev. Lett.* **59**, 2079
- [75] Koláč M., Neganov B.S. and Sahling S. (1984). *J. of Low Temp. Phys.* **59**, 547
- [76] Kosterlitz J.M. and Thouless D.J. (1973). *J. of Phys. C* **6**, 1181
- [77] Koval V.A., Osetski A.I., Soldatov V.P and Startsev V.I. (1978) *Adv. in Cryo. Eng.* **24**, 249

- [78] Kraus H. et al. (2005). EURECA: The European Future of Cryogenic Dark Matter Searches, Proceedings of the TAUP (Topics in Astroparticle and Underground Physics) Workshop, Zaragoza, Spain
- [79] Kraus H. et al. (2006). EURECA - The European Future of Dark Matter Searches with Cryogenic Detectors, Proceedings of the 7<sup>th</sup> International Symposium on Sources and Detection of Dark Matter in the Universe, Marina del Rey (CA), USA
- [80] Kraus H. et al. (2006). EURECA - The European Underground Rare Event Calorimeter Array, Proceedings of the 6<sup>th</sup> International Workshop on the Identification of Dark Matter, Rhodes, Greece
- [81] Krusius M., Paulson D.N. and Wheatley J.C. (1978). *Cryogenics* **18**, 649
- [82] Kuzmenko I. F. (1995). *Cryogenics* **35**, 219
- [83] Lawson A. W. (1941). *Phys. Rev.* **60**, 330
- [84] Levin M. L., Polevoi V. G and Rytov S. M. (1980). *Sov. Phys. JETP* **52**, 1054
- [85] L'Hôte D. et al. (1997). *Proc. 7<sup>th</sup> Int. Workshop on Low Temp. Detectors*. Max Planck Institute of Physics, Munich, 237
- [86] Loewenthal G.C. and Airey P.L (2001). *Practical Applications of Radioactivity and Nuclear Radiations*. Cambridge University Press, Cambridge, New York
- [87] London H., Clarke G.R. and Mendoza E. (1962). *Phys. Rev.* **128**, 1992
- [88] Loomis J.L. and Maris J.H. (1994). *Phys. Rev. B* **50**, 18517
- [89] Loponen M.T., Dynes R.C., Narayanamurti V. and Garno J.P (1980). *Phys. Rev. Lett.* **45**, 457
- [90] Loponen M.T., Dynes R.C., Narayanamurti V. and Garno J.P (1981). *Phys. Rev. B* **25**, 1161
- [91] Lounasmaa O.V. (1974). *Experimental Principles and Methods below 1 K*. Academic Press, London, New York
- [92] Maps J. and Hallock R.B. (1981). *Phys. Rev. Lett.* **47**, 1533
- [93] Masel R.I. (1996). *Principles of Adsorption and Reaction on Solid Surfaces*. Wiley, New York, Chichester, Brisbane, Toronto, Singapore
- [94] Mott N. F. (1956). *Phil. Mag.* **1**, 568
- [95] Narayanamurti V. and Pohl R.O. (1970). *Rev. Mod. Phys.* **42**, 201
- [96] Neganov B.S., Borisov N. and Liburg, M. (1966). *Pis'ma Zh. Eksp. Teor. Fiz.* **50**, 1445; translation: *Sov. Phys. - JETP Letters* **29**, 959
- [97] Neganov B.S. and Trofimov V.N. (1978). *Pis'ma Zh. Eksp. Teor. Fiz.* **28**, 356; translation: *Sov. Phys. - JETP Letters* **28**, 328
- [98] Niinikoski T.O. (1971). *Nucl. Instr. and Methods* **97**, 95
- [99] Niinikoski T.O. (1976). *Proc. 6<sup>th</sup> Int. Cryo. Engin. Conf.* IPC Science and Technology Press, Guilford, 102
- [100] Niinikoski T.O. (1982). *Nucl. Instr. and Methods* **192**, 151
- [101] Nittke A., Scherl M., Esquinazi P., Lorenz W., Junyun L., and Pobell F. (1995). *J. of Low Temp. Phys.* **98**, 517

- [102] Obert W., Coupland J.R., Hammond D.P., Cook T. and Harwood K. (1982). *Adv. in Cry. Eng.* **27**, 293
- [103] Oda Y., Fujii G. and Nagano H. (1974). *Cryogenics* **14**, 84
- [104] Olson, J.R. (1992). *Cryogenics* **33**, 729
- [105] Pennings N.H, de Bruyn Ouboter R. and Taconis K.W. (1976). *Physica B* **81**, 101
- [106] Philipps W.A. (1970). *Proc. Roy. Soc.* **A319**, 565
- [107] Philipps W.A. (1971). *J. of Low Temp. Phys.* **7**, 351
- [108] Pobell, F. (1982). *Physica B* **109 & 110**, 1485
- [109] Pobell F. (1995). *Matter and Methods at Low Temperatures*. Springer, Berlin, Heidelberg, New York
- [110] Polder D. and van Hove M. (1971). *Phys. Rev. B* **4**, 3303
- [111] Radebaugh R. (1967). *Thermodynamic Properties of the  $^3\text{He}$ - $^4\text{He}$  Solutions with Applications to the  $^3\text{He}$ - $^4\text{He}$  Dilution Refrigerator*. NBS Technical Note 362
- [112] Rammerstorfer, F.G. (1992). *Repetitorium Leichtbau*. Oldenbourg Verlag, Wien, München
- [113] Rastin B.C. (1984). *J. Phys. G: Nucl. Phys.* **10**, 1609
- [114] Ratnam B. and Mochel J. (1970). *J. of Low Temp. Phys.* **3**, 239
- [115] Rheinländer, J. (1988). *Wärmeübertragung bei freier und bei Überlagerung von freier und erzwungener Umströmung von Körpern*. In *VDI Wärmeatlas*, 5<sup>th</sup> ed., VDI-Verlag, Düsseldorf
- [116] Roth A. (1982). *Vacuum Technology*. North Holland, Amsterdam, New York, Oxford
- [117] Rott N. (1969). *J. Appl. Math. Phys. (ZAMP)* **20**, 230
- [118] Rott N. (1973). *J. Appl. Math. Phys. (ZAMP)* **24**, 54
- [119] Sahling S. and Abens S. (2001). *Solid State Communications* **120**, 249
- [120] Sanglard V. et al. (2005). *arXiv:astro-ph/0503265 v3*.
- [121] Sarafin T.P. (1995). *Spacecraft Structures and Mechanisms*. Kluwer Academic Publishers, Dordrecht, Boston, London
- [122] Schmidt F. (1973). *Phys. Rev. B* **10**, 4480
- [123] Schwark M., Pobell F., Halperin W.P., Buchal C., Hanssen J., Kubota M. and Mueller R.M. (1983). *J. Low Temp. Phys.* **53**, 685
- [124] Schwark M., Pobell F., Kubota M. and Mueller R.M. (1984). *J. of Low Temp. Phys.* **58**, 171
- [125] Shin N. (1961). *The Theory of Optical and Infrared Properties of Metals*. Technical Note C-62081, NASA, Washington, DC
- [126] Siqueira M.L., Viana R.J. and Rapp R.E. (1991). *Cryogenics* **31**, 796
- [127] Sisti M. et al. (1997). *Proc. 7<sup>th</sup> Int. Workshop on Low Temp. Detectors*. Max Planck Institute of Physics, Munich, 232

- [128] Snyder N.S. (1969). *Thermal Conductance at the Interface of a Solid and Helium II (Kapitza Conductance)*. NBS Technical Note 385, US National Bureau of Standards, Boulder, Colorado
- [129] Startsev V. I. (1981). *Czech. J. Phys. B* **31**, 115
- [130] Taconis K.W., Beenakker J.J.M, Nier A.O.C. and Aldrich L.T. (1949). *Physica* **XV**, 733
- [131] Takano Y. (1994). *Rev. Sci. Instrum.* **65**, 1667
- [132] Trofimov V.N. (1983). *J. of Low Temp. Phys.* **54**, 555
- [133] Vermeulen G.A. and Frossati G. (1987). *Cryogenics* **27**, 139
- [134] Vortmeyer, D. (1988). *Strahlung Technischer Oberflächen*. In *VDI Wärmeatlas*, 5<sup>th</sup> ed., VDI-Verlag, Düsseldorf
- [135] Walker P.M.B., ed. (1988). *Chambers Science and Technology Dictionary*. W&R Chambers Ltd and Cambridge University Press, Edinburgh, Cambridge, New York, Melbourne
- [136] Weisend J.G., ed. (1998). *Handbook of Cryogenic Engineering*. Taylor & Francis, Philadelphia, Bristol, London
- [137] Wellstood F.C., Urbina C. and Clarke J. (1994). *Phys. Rev. B* **49**, 4952
- [138] Willekers R.W., mathu F., Meijer H.C. and Postma H. (1990). *Cryogenics* **30**, 351
- [139] Yazaki T, Tominaga A., Narahara A. (1980), *J. of Low Temp. Phys.* **41**, 45
- [140] Zeegers, J. (1991). *Critical Velocities and Mutual Friction in <sup>3</sup>He-<sup>4</sup>He II Mixtures at Temperatures below 100 mK*. Ph.D. Thesis, Eindhoven University of Technology, Eindhoven, The Netherlands
- [141] Zimmermann J. and Weber G. (1980). *Phys Rev. Lett.* **46**, 661



## Curriculum Vitae

### *Personal Data*

Name: Patrick Wikus  
Date of Birth: 02.05.1979  
Nationality: Austrian  
Marital Status: Single  
e-mail: wikus@chello.at

### *Education*

1998 – 2002 Vienna University of Technology, Mechanical Engineering (Master of Science). Internships at Daimler Steyr Puch, Airbus and EADS Astrium.  
1998 Military Service in the 4<sup>th</sup> Signal Battalion in Vienna  
Commander of a patrol of 4  
1997 – 1998 Stay-abroad in Phoenix, Arizona (USA); studies at the Mesa Community College  
1989 – 1997 Albertus Magnus Highschool in Vienna  
Graduation with honors

### *Professional Experience*

2005 – 2007 Doctoral Student at CERN (Switzerland)  
Work in the field of cryogenic technology - especially dilution refrigeration - in the framework of the European dark matter experiment EURECA  
2002 – 2004 System Engineer at EADS Space Transportation (Germany)  
Development of hardware for microgravity applications (International Space Station, Sounding Rockets, Parabolic Flights)

### *Relevant Knowledge*

Language Skills: German, English, French (all fluent in writing and speaking) and Russian (beginner)  
Engineering Software: ANSYS, NASTRAN, TAK2000, Labview, Mathematica, MATLAB, Origin, CATIA and SolidWorks

### ***Talks & Publications***

Kraus H. et al. (2006). *EURECA - The European Future of Dark Matter Searches with Cryogenic Detectors*, Proceedings of the 7<sup>th</sup> International Symposium on Sources and Detection of Dark Matter in the Universe, Marina del Rey (CA), USA

Kraus H. et al. (2006). *EURECA - The European Underground Rare Event Calorimeter Array*, Proceedings of the 6<sup>th</sup> International Workshop on the Identification of Dark Matter, Rhodes, Greece

Wikus P. (2006). Talk at the 3<sup>rd</sup> EADS Junior's Day: *Microgravity Research and Parabolic Flight*. Bremen, Germany

Kraus H. et al. (2005). *EURECA: The European Future of Cryogenic Dark Matter Searches*, Proceedings of the TAUP (Topics in Astroparticle and Underground Physics) Workshop, Zaragoza, Spain

Wikus P., Winter J., Hummel T., Tailhades J., Dariol L. and Dewandre T. (2004). Talk at the 5<sup>th</sup> European Conference on Foams, Emulsions and Applications (EUFOAM): *Aqueous Foams in Microgravity: ESA Projects Investigate Bubble Dynamics, Rheology and Drainage Effects*. Marne la Vallée, France

Wikus P. (2002). Diploma Thesis: *Designing for Manned Spaceflight on the example of the ISS Crew Refrigerator/Freezer Rack (RFR)*. Vienna University of Technology

### ***Hobbies***

Scuba Diving, Mountaineering, Basketball, Jogging, Golf, Traveling, Reading and RC Helicopters